

**ADVANCED CHARACTERIZATION OF  
CEMENTITIOUS MATERIALS**

**ADVANCED CHARACTERIZATION OF  
CEMENTITIOUS MATERIALS**

**PENG DONG, B.ENG., M.ENG**

A Thesis Submitted to the School of Graduate Studies in Partial  
Fulfilment of the Requirements for the Degree

Doctor of Philosophy

McMaster University © Copyright by Peng Dong, June 2020

DOCTOR OF PHILOSOPHY (2020)

McMaster University

(Materials Science and Engineering)

Hamilton, Ontario

TITLE: Advanced Characterization of Cementitious Materials

AUTHOR: Peng Dong, B.Eng., M.Eng.

SUPERVISOR: Professor Nabil Bassim

NUMBER OF PAGES: xvi, 256

# Lay Abstract

Cement is the binding material for concrete, which “glues” pieces of fine and coarse aggregate into concrete, which is the most widely used human-made material on the planet. Cement hydration consists of early-age and late-age chemical reactions that transform unhydrated powder into the binding medium upon which concrete is based. This work is focused on researching structure evolution and phase transformation as well as hydration kinetics of early hydration reactions up to 24 h, and characterizing 3D structure and pore systems of mortar samples. The liquid-based reactions up to 24 h are achieved using liquid cell transmission electron microscopy, which provides insights into real-time structural evolution of main hydrated products, especially C-S-H nucleation and growth. The effects of adding nano-silica on early hydration reactions up to 24 h are also evaluated. Furthermore, the reconstruction models of pore systems show transport pathways of mortar sample.

# Abstract

Early-age hydration reactions contribute to early structure and strength development, which is closely related to transportation and concrete placing on site in real practice. The in-situ hydration reactions of nano Portland cement (PC) and nano PC with nano-silica up to 24 h were realized using liquid cell transmission electron microscopy (LC-TEM). The main hydrated product, calcium silicate hydrate (C-S-H) was found to shed light on a complex early stage process, where C-S-H develops according to both layered structure morphology and aggregation of building blocks. These experiments are the first application of the LC-TEM technique in real-time imaging reaction process of cementitious materials.

Also, the effects of nano-silica on microstructure evolution, phase transformation and heat release, especially in early hydration reactions up to 24 h needs further elucidation. The results indicated that the addition of nano-silica provided more nucleation sites for hydrated products leading to more well-distributed precipitates in the reaction. It was also observed that nano-silica had a strong tendency to attach to ettringite crystals and accelerated the conversion of ettringite to monosulfate.

In mortar or concrete, the pore systems and distribution of various cementitious phases were characterized using plasma focused ion beam (PFIB) and X-ray micro-computed tomography (CT) to obtain dataset of larger length scale (100s of nm to mm). A workflow working with cement mortar on PFIB was established, in which a hard Si mask was applied to minimize the curtaining effect. The 3D reconstruction models reveal fluid transport pathways through connected pores and cracks. The thickness mesh of anhydrous phases shows different dissolution rates and preferential dissolution locations. This is the first time that PFIB has been used for cementitious materials and bridges a critical mesoscale length scale that dictates some materials properties such as strength and fluid transport properties.

# Acknowledgements

I would like to express my deepest gratitude to my supervisor, Dr. Nabil Bassim for his guidance, constant support, and encouragement throughout my Ph. D study. He provided patient supervision and the opportunity for me to work with various researchers and projects, which makes me think more about the fundamental materials problem between structure and property. I am deeply impressed by his curiosity, research enthusiasm and endless pursuit that set an excellent example for my research career. I will be forever thankful to Dr. Ali Allahverdi for patiently assisting me in experiments and introducing me to the worlds of inorganic nanomaterials and cementitious materials. His solid expertise, hardworking attitude and research habit inspired me a lot. I would also like to thank Dr. Daman Panesar and Dr. Kathryn Grandfield for their helpful suggestions and discussions as members of my supervisory committee.

I wish to thank faculties, researchers and staff in Department of Materials Science and Engineering, Canadian Center for Electron Microscopy (CCEM) as well as the Graduate Studies for maintaining a friendly and cooperative environment. Many thanks to Dr. Andreas Korinek, Dr. Carmen Andrei, Dr. Hui Yuan, Chris Butcher, Andy Duft, Jhoynner Martinez for the electron microscopy training, Victoria Jarvis and Dr. James Britten for X-ray experiments, and Xiaogang Li and Doug Culley and Ed McCaffery for their technical assistance. I am very grateful to Mary-Anne Bechamp and Chelsea Gregory for having things organized, providing the best working environment.

Last but not least, I would like to thank my parents and cousins for their unconditional love, understanding and support throughout my life. I dedicate this thesis to my beloved parents: Yanwen Zhang and Yuting Dong.

# Table of Contents

Preface.....	1
1. Introduction.....	2
1.1 Research Background.....	2
1.2 Research Hypothesis and Objectives .....	4
1.2.1 Hydration Mechanisms and Kinetics in Early Hydration Reactions.....	5
1.2.2 Characterization of Pore Systems and Different Phases in Late Hydration Reactions .....	6
1.3 Thesis Outline .....	6
1.4 References .....	8
2 Literature Review.....	11
2.1 Development of Ordinary Portland Cement (OPC).....	11
2.1.1 Introduction of OPC and Its Environmental Effects .....	11
2.1.2 Hydration Reactions of OPC .....	12
2.1.3 Hypothesis of Growth Mechanisms of C-S-H.....	16
2.1.4 Reaction Stages and Kinetics of Alite/C <sub>3</sub> S.....	19
2.1.5 Reaction Stages and Kinetics of OPC .....	21
2.2 Supplementary Cementitious Materials in Concrete.....	23
2.2.1 Motivation to Add Supplementary Cementitious Materials in Cement .....	23
2.2.2 The Definition of Supplementary Cementitious Materials.....	24
2.2.3 Classification of Supplementary Cementitious Materials .....	24
2.2.4 Filler Effects of Supplementary Cementitious Materials .....	26
2.2.5 Applications of Supplementary Cementitious Materials in Cement .....	27
2.3 Nano-silica in Cement and Concrete.....	29
2.3.1 Introduction of Nano-silica.....	29
2.3.2 Strengthening Mechanisms of Nano-silica.....	30
2.3.3 Research on Effects of Nano-silica in Cement.....	30

2.4 Liquid Cell Transmission Electron Microscopy (LC-TEM).....	34
2.4.1 The Development of TEM to Image Liquids .....	34
2.4.2 Electron Beam Effects .....	36
2.4.3 Applications of LC-TEM in Different Materials Systems .....	38
2.4.4 Perspectives for Geological Materials .....	41
2.5 Focused Ion Beam (FIB) and 3D Tomography.....	42
2.5.1 Introduction to the FIB-SEM System.....	42
2.5.2 FIB Tomography and Instrumentation Setup .....	43
2.5.3 Curtaining Effect .....	45
2.5.4 Segmentation .....	47
2.5.5 FIB Tomography and Pore Characteristics .....	49
2.5.6 Perspectives of 3D Tomography in Characterizing Pore Systems in Cementitious Materials .....	50
2.6 References .....	51
3. Liquid Cell Transmission Electron Microscopy Reveals C-S-H Growth Mechanism during Portland Cement Hydration .....	65
3.1. Introduction .....	67
3.2. Methods.....	71
3.2.1 As – received OPC .....	71
3.2.2 Ball Milling and Nano PC .....	71
3.2.3 Water/cement (w/c) Ratio.....	72
3.2.4 Liquid Cell Preparation and In-situ Imaging.....	73
3.2.6 Scanning Electron Microscopy and Energy Dispersive Spectroscopy.....	74
3.3. Results .....	74
3.4. Conclusions .....	83
3.5 Acknowledgements .....	84
3.6 References .....	85

4. In-situ Observations of Different Cement Hydration Stages Using Liquid-cell Transmission Electron Microscopy .....	90
4.1. Introduction .....	93
4.2. Materials and Methods .....	97
4.2.1 As – received and Nano PC .....	97
4.2.2 Liquid Cell Assembly and In-situ Imaging .....	97
4.2.3 Isothermal Calorimetry and Heat Flow .....	98
4.2.4 Lyophilization and Quantitative XRD Analysis.....	98
4.2.5 Scanning Electron Microscopy and Energy Dispersive Spectroscopy.....	99
4.3. Results and Discussion.....	100
4.4. Conclusions .....	115
4.5 Acknowledgements .....	117
4.6 References .....	117
5. The Effects of Nano-silica on Early-age Hydration Reactions of Nano Portland Cement	123
5.1. Introduction .....	125
5.2. Experimental .....	127
5.3. Results and Discussion.....	129
5.4. Conclusions .....	143
5.5 Acknowledgements .....	144
5.6 References .....	145
6. Advanced Characterization of 3D Structure and Porosity of Ordinary Portland Cement (OPC) Mortar Using Plasma Focused Ion Beam Tomography and X-ray Computed Tomography .....	149
6.1. Introduction .....	150
6.2. Materials and Methods .....	154
6.2.1. Materials and Sample Preparation.....	154
6.2.2. Predetermination and Si Mask.....	155
6.2.3. Plasma FIB – SEM Setup and Serial Sectioning.....	156

6.2.4 Segmentation and Quantification .....	160
6.2.5. Micro – CT and 3D reconstruction on pore system.....	163
6.3. Results .....	164
6.3.1. PFIB Results .....	164
6.3.2 Micro-CT Analysis of Porosity .....	166
6.3.3 Pore Size Distribution.....	167
6.4. Discussion .....	168
6.5. Conclusions .....	170
6.6 Acknowledgements .....	171
6.7 References .....	171
7. Conclusions and Outlook.....	177
Appendix.....	182

## List of Figures

Figure 2.1 Schematic representation of interfacial transition zone from an aggregate to bulk cement paste in concrete from [1] .....	15
Figure 2.2 Proposed formation of C-S-H gel by Jennings [13]. a) One relatively small volume fractal region, formed from contacting ~ 5 nm globules of C-S-H. b) The same volume fractal region (shown in white) has grown into a larger, self-similar structure with a reduced packing density. c) Adjacent fractal regions have grown into each other to form a relatively uniform structure with a range of gel pore sizes. The largest pores are greater than 10 nm. Upon drying these pores collapse to form a structure with a packing density of about 0.64. ....	17
Figure 2.3 Adopted from Gartner [20]. Schematic of growth process with three separate sheets of C-S-H emanating from a common nucleation point which can be considered a nanocrystalline region .....	19
Figure 2.4 Rate of alite hydration as a function of time given by isothermal calorimetry measurements [24].....	20
Figure 2.5 Schematic diagram of a liquid cell for transmission electron microscope [77].....	35
Figure 2.6 Schematic of dual-beam FIB-SEM system and geometry between columns and sample [102].....	42
Figure 2.7 FIB tomography setup and serial sectioning direction using dual-beam system [110] .....	44
Figure 3.1 Schematic of liquid cell configuration within the TEM demonstrating C-S-H nucleation and growth on the SiN membranes during cement hydration:  stands for silica tetrahedra,  for CaO,  for water, the blue particles away from SiN membranes are dissolving cement particles. .	71
Figure 3.2 Needle-like ettringite crystals in liquid cell TEM (a) 1 h 47 min, (b) 2 h 29 min and (c) 2 h 45 min (scale bars, 0.5µm).....	75
Figure 3.3 C-S-H nucleation and primary growth on the membrane of liquid cell chips during induction period: (a) at 3 h 09 min, some newly formed embryos in the microwell, (b) higher magnification of C-S-H embryos from (a) AOI 1 with sizes as small as 5 nm to 10 nm. (c) Continued C-S-H nucleation and growth at 3 h 48 min, and (d) some embryos from (c) AOI 2 were as small as 5 nm to 10 nm, while some grew quickly to 20 nm to 30 nm, and (e) TEM image from LC chip after opening and drying, showing individual and joined C-S-H precipitates at their primary growth stage with completely disordered microstructures, (f) LC-TEM image showing early growth and coalescence of C-S-H disk-like precipitates with sizes of 0.6 µm to 0.8 µm in their intermediate stage. ....	77
Figure 3.4 Ex-situ TEM imaging of C-S-H at the intermediate stage (a) Bright field (BF) image of C-S-H precipitate, (b) HR image of nanocrystalline and disordered C-S-H in boxed area of (a). The marked areas show the presence of C-S-H nanocrystals inside the amorphous C-S-H matrix.....	78

Figure 3.5 The main growth stage of sheet-like C-S-H precipitates at different time intervals (a video is attached as V. 3.A1) (a) 2 h 42 min, (b) 2 h 54 min, (c) 3 h 03 min, (d) 3 h 09 min, (e) 3 h 14 min, (f) 3 h 29 min, (g) 4 h 08 min and (h) 4 h 46 min (scale bars, 0.5  $\mu\text{m}$ ) ..... 80

Figure 3.6 Confirmation of C-S-H formed during in-situ reactions s(a) BF image and SAD patterns with d-spacings of 0.3190 nm, 0.2786 nm, 0.1994 nm and 0.1677 nm, indicating a polycrystalline structure similar to tobermorite structure, (b) C-S-H microcrystal inside layered structure with d-spacings of 0.3277 nm, 0.3197 nm and 0.2837 nm structure..... 82

Figure 4.1 BF images showing growth and collapse of C-S-H precipitates with time a) at 2 h 31 min and b) 2 h 39 min ..... 100

Figure 4.2 Contract variance of images in the same area showing thickness change and 3D growth of C-S-H precipitates a) 3 h 05 min, b) 3 h 10 min and c) 3 h 23 min..... 102

Figure 4.3 C-S-H precipitates from a) induction period, at 2 h 10 min, b) induction period, at 3 h 30 min, c) acceleration period, at 15 h 53 min and d) deceleration period, at 23 h 48 min. Scale bars, 0.5  $\mu\text{m}$ . ..... 104

Figure 4.4 Post-situ TEM experiment on C-S-H precipitates a) BF image, b) DF image and c) BF image and diffraction pattern of selected area ..... 105

Figure 4.5 The dissolution of ettringite from the same position (a video of aligned images is attached V. 4.A2). a) at 1 h 59 min, b) at 2 h 08 min, c) 2 h 11 min, and d) at 2 h 16 min. Scale bars, 0.5  $\mu\text{m}$ 107

Figure 4.6 Heat flow and cumulative curves of nano PC and OPC hydration within 24 h under the circumstance of 25 °C in solid and dashed lines, respectively. Three peaks of nano PC heat flow curve are A1, A2 and A3. Four different hydration stages: I – initial or dissolution period (red line), containing dissolution of cement particles, II – induction period (green line), involving slow reaction, III – acceleration stage (yellow line), and IV – deceleration stage (blue line)..... 109

Figure 4.7 Phase contents of main anhydrous and hydrated phases of hydration reactions within 24 h from Rietveld refinement; a)  $\text{C}_3\text{S}$ , C-S-H, and portlandite, b)  $\text{C}_3\text{A}$ , ettringite, and anhydrite. .... 111

Figure 5.1 Schematic of hydration reactions in NPC and OPC with NS ..... 127

Figure 5.2 Heat flow and cumulative heat curves of nano PC and nano PC with NS (yellows lines indicate the end of induction period and the silicate peak of nano PC with NS, respectively)..... 130

Figure 5.3 Heat flow and cumulative heat curves of OPC and OPC with NS (blue arrow show aluminate peak of OPC and yellow arrow show aluminate peak of PC with NS)..... 132

Figure 5.4 Phase evolution of plain NPC (a & b), NPC with nano silica (c & d) and phase contents of C-S-H and ettringite in the two systems (e). .... 135

Figure 5.5 LC-TEM images showing microstructure of different areas and time scales in NPC a) 1 h 35 min, b) 3 h 10 min, c) 4 h 52 min, d) 14 h 06 min and e) 24 h 21 min ..... 137

Figure 5.6 LC-TEM images showing microstructure at different time scale in NPC with NS, a) 1 h 48 min, b) 2 h 47 min (same area as first image), c) 4 h 36 min, d) 14 h 16 min and e) 23 h 58 min ..... 138

Figure 5.7 a) NS attachment to needle-like ettringite crystals and b) subsequent C-S-H nucleation and growth inside chips without plasma cleaning in advance .....	139
Figure 6.1 The SE image of sample surface by JEOL 6610, and schematic of hard single-crystal Si masks (M1, M2, M3 and M4) on top of possible VOIs, which were indicated in blue rectangles and their distances to selected features were measured to be L1, L2, L3 and L4. Milling front and milling directions are shown by the cross and arrow on left side.....	156
Figure 6.2 Experimental setup of FIB-SEM dual-beam system. a) 52-degree secondary electron image showing a prepared VOI with two trenches on both sides. b) Top-view ion beam image after trench milling. c) Top-view ion beam image showing deposition layer and a fiducial on top for rocking milling as well as sectioning direction. d) Backscattered electron image of the first slice of serial sectioned image stack, 79.8 $\mu\text{m}$ by 88.3 $\mu\text{m}$ , pixel size = 25 nm in both x and y direction.....	159
Figure 6.3 Deep learning trainset. a) The manual segmentation consisting of 3 phases, namely, anhydrous phases, pores, and matrix. b) The generated train (blue), validation(yellow) and test(red) masks. ....	160
Figure 6.4 The accuracy of segmentation by varying (a) Modality, (b) Architecture, (c) Slice count and (d) spacing.....	163
Figure 6.5 3D reconstruction of 631 BSE images after cropping, with the dimension of 79.8 $\mu\text{m}$ by 88.3 $\mu\text{m}$ by 63.1 $\mu\text{m}$ .....	164
Figure 6.6 3D Segmentation models of cement mortar a) Skeletonization of connected pores, b) thickness mesh of anhydrous phases.....	166
Figure 6.7 X-ray micro-CT and reconstruction models of air voids and large capillary pores of OPC mortar in different viewing directions .....	167
Figure 6.8 Pore size distribution of a) capillary pores from PFIB reconstruction and b) air voids and large capillary pores from micro-CT reconstruction.....	168
Figure 3.A1. Particle size distribution of nano PC after three-step ball milling .....	183
Figure 3.A2. SEM image and EDS spectra showing ettringite (spectrum 1) and calcium monosulfate (spectrum) .....	184
Figure 3.A3 Secondary electron image of (a) C-S-H precipitates and (b) C-S-H precipitates and ettringite crystals inside liquid reaction cell after opening the chips, indicating enough room of liquid cell for 3D structure development.....	185
Figure 3.A4 Post-situ characterization of Portlandite (a) SEM and (b) EDS spectra from the positions marked in Figure 3-A3 (a) .....	186
Figure 4.A1 Particle size distribution of nano OPC.....	188
Figure 5.A1 Microstructure and morphology of nano-silica .....	189
Figure 5.A2 SEM showing morphology of hydrated products in nano PC, a) sheet-like C-S-H and b) embedded portlandite in C-S-H precipitates.....	190

Figure 5.A3 SEM images showing morphology of hydrated products in nano PC with nano-silica, a) more distributed sheet-like C-S-H and b) embedded portlandite..... 191

## List of Tables

Table 2.1 Common compounds in cementitious materials .....	13
Table 6.1 Chemical, Bogue’s potential phase compositions and physical properties of the as – received OPC .....	154
Table 3.A1 Chemical, Bogue’s potential phase compositions and physical properties of as – received OPC.....	186
Table 3.A2 Elemental analysis of Portlandite by EDS .....	187
Table 4.A1 Chemical, Bogue’s potential phase compositions and physical properties of as – received OPC.....	188

## List of Abbreviations

OPC	Ordinary Portland cement
SCM	Supplementary cementitious materials
SEM	Scanning electron microscopy
EDS	Energy dispersive spectroscopy
FTIR	Fourier transform infrared spectroscopy
QXRD	Quantitative X-ray diffraction
LC-TEM	Liquid cell transmission electron microscopy
MIP	Mercury intrusion porosimetry
$\mu$ -CT	Micro-computed tomography
PFIB	Plasma focused ion beam
C <sub>3</sub> S	Tricalcium silicate
C <sub>2</sub> S	Dicalcium silicate
C <sub>3</sub> A	Tricalcium aluminate
C <sub>4</sub> AF	Tetracalcium aluminoferrite
C-S-H	Calcium silicate hydrate
C-A-H	Calcium aluminate hydrates
AS	Aluminate silicate
W/c	Water to cement ratio
W/b	Water to binder ratio
Afm	Monosulfate
EBSD	Electron backscattered diffraction
VOI	Volume of interest
BF	Bright field
DF	Dark field
NPC	Nano Portland cement
NS	Nano-silica
HPC	High-performance concrete

# Declaration of Academic Achievements

This dissertation is written to fulfill the requirement for the degree Doctor of Philosophy in Materials Science and Engineering at McMaster University. All work described was undertaken from May 2017 to May 2020. Over the course of this study, I explored the application of liquid cell transmission electron microscopy (LC-TEM) technique on the hydration reactions of two nano cement systems, namely, nano Portland cement (PC) and nano PC with nano-silica (NS). The new insights of real-time structural evolution, especially C-S-H nucleation, and growth, and partial ettringite dissolution are provided. These works are the first attempts of the LC-TEM technique to study cement hydration reactions in early age up to 24 h, which opens up possibilities for studying structure evolution and reaction dynamics of different cementitious materials. Furthermore, I designed a workflow of working with plasma focused ion beam (PFIB) and mortar samples, which enables good image quality for later segmentation and quantification. The major contribution of this study came from myself, with helpful discussions with my supervisor and Prof. Ali Allahverdi. The results of my studies will be published in a set of four peer-reviewed journal articles that I prepared as the leading author. I was also the third author in another four peer-reviewed journal articles from collaborative work, in which three were published between 2018 and 2019, and one was under review. The four journal articles that form this “sandwich” thesis include the following:

1. Peng Dong, Ali Allahverdi, Carmen M. Andrei and Nabil D. Bassim: Liquid Cell Transmission Electron Microscopy Reveals C-S-H Growth Mechanism during Portland Cement Hydration, *Nature Communications*, under review.
2. Peng Dong, Ali Allahverdi, Carmen M. Andrei and Nabil D. Bassim: In-situ Observations of Different Cement Hydration Stages Using Liquid-cell Transmission Electron Microscopy, *Materials Characterization*, submitted.

3. Peng Dong, Ali Allahverdi, Carmen M. Andrei and Nabil D. Bassim: The effects of nano-silica on early-age hydration reactions of nano Portland cement, *Nanoscale*, submitted.
4. Peng Dong, Hui Yuan, Ali Allahverdi, Jatheeshan Raveenthiran, Nicolas Piché, Benjamin Provencher, and Nabil D. Bassim: Advanced Characterization of 3D Structure and Porosity of Ordinary Portland Cement (OPC) Mortar Using Plasma Focused Ion Beam Tomography and X-ray Computed Tomography, *Microscopy and Microanalysis*, major revision.

## **Preface**

In this collective work, hydration reactions including microstructure evolution, hydration kinetics and phase transformation in early stage, and 3D distribution of different phases, pore systems in late stage were examined using advanced characterization techniques. This thesis is written as “sandwich” thesis consisting of seven chapters. Chapter 1 briefly outlines the research background, hypothesis and objectives and the overall layout of the thesis. Chapter 2 summarizes the competing theories under discussion and knowledge states with respect to C-S-H nucleation and growth mechanisms, the effects of supplementary cementitious materials and characterization techniques to evaluate pore systems. Chapters 3-6 present four manuscripts that have been written based on the research work. Chapter 7 draws the major conclusions of the collective work and provide insights for future work. The appendix adds 3 additional published works and 1 work currently under review at *Journal of Building Engineering* for which the author has been a contributor.

# 1. Introduction

## 1.1 Research Background

Cement is the material that binds together aggregates such as sand and rocks into a structural composite known as concrete. Ordinary Portland cement (OPC) and concrete materials that use OPC as its binder are the most widely used formulations of cement in the construction industry. It is a multiphase mixture that constitutes several phases that react in a complex manner upon hydration (i.e. reaction with water) designed to give special properties, such as early strength, durability, controlled heat of formation and other properties. It is used to bind aggregate particles in a strong composite that is durable and performs well under many different operating conditions. These hydration reactions occur at first over the span of minutes but can continue within a concrete microstructure over the span of decades, in a complex evolution of chemistry and physical structure, including developing important internal pore structures and networks. Since it was introduced in 1824 [1], OPC has been playing a crucial role in the modern infrastructure that defines our way of life: buildings, bridges and dams, sidewalks, and more. However, the production of OPC requires an enormous amount of energy, and releases almost one ton of carbon dioxide for every ton of cement produced [2]. One way to reduce the lifetime carbon release is to improve concrete strength and durability by adding supplementary cementitious materials (SCM) to the design of cement. Recently, addition of amorphous nano-silica particles between 1 nm to 500 nm has attracted much attention because its higher surface area and reactivity accelerates hydration reactions and promises to make high performance concrete [3]. Hydration reactions and microstructure evolution of both early and late ages are important in cementitious materials because the state of hydration and pore network geometry and chemistry contribute to the strength and durability of the composite. Thus, understanding reaction mechanisms, microstructure evolution and pore systems are necessary in designing strong and durable concrete.

Many efforts have been devoted to characterizing early hydration reactions that are related to early strength. Some techniques including scanning electron microscopy (SEM) [4-6], Fourier transform infrared spectroscopy (FTIR) [7], quantitative in-situ X-ray diffraction (XRD) [8-11], calorimetry and thermodynamic modelling [12, 13], have been used for measuring such properties as heat evolution, chemical bonding and phase evolution and distribution at different time and length scales. These are indirect methods of analysis that infer the chemical and structural changes happening at the nanoscale and do not provide direct observation of microstructural evolution at relevant length scales. With the development of micro-electro-mechanical system (MEMs) technology (from the semiconductor industry), direct observation of liquid-phase chemical reactions at the nanoscale can now be achieved in a within a transmission electron microscope (TEM) with both nanometer and temporal resolution [14]. The liquid cell TEM (LC-TEM) is a powerful new tool to research mechanisms and microstructure of early hydration reactions in cementitious materials.

The relationship between microstructure and materials properties is critical for optimizing materials processing and lifetime. The microstructure of cementitious materials is tremendously complex due to the presence in the cement mixture of many compounds, with both of hydrated and anhydrous phases, amorphous and crystalline phases and pore networks that form between these reacting phases [15]. The porosity in mortar (defined as the mixture of cement and fine aggregate (from 75  $\mu\text{m}$  to 4.75 mm)) and concrete (cement plus fine plus coarse (> 4.75 mm) aggregates) is linked to strength and durability [16]. The pore network is a hierarchical structure, and pores range from nanoscale to cm-scale, with mechanical behaviour defined by the mesoscale interplay between the pore networks, the composition of the still-hydrated solution in the pore networks and the adjacent evolving materials phases near the pore network [17]. Because the pore network is so hierarchical, it is difficult to directly measure and analyze porosity simultaneously at many length scales. Researchers have been trying to study

and quantify concrete and mortar porosity and pore structures using various methods, such as gas absorption, mercury intrusion porosimetry (MIP), X-ray micro computed tomography (X-CT), and focused ion beam (FIB) tomography. Recently, a new variant of focused ion beam (PFIB) that employs a plasma Xe<sup>+</sup> source has been developed and promises to acquire nano to meso- scale and, 3-dimensional microstructural information in porous materials simultaneously [18]. Therefore, it is possible to measure later hydration reactions, microstructure and pore network by three-dimensional tomography using PFIB.

This work is focused on employing new techniques in electron and ion microscopy that have been recently developed for materials science applications to measure hydration reactions in cements and microstructure evolution of early and late stages of cements and mortars. The reaction mechanisms, reaction kinetics and real-time microstructural evolution in the early stage are researched using advanced characterization techniques, such as liquid cell transmission electron microscopy (LCTEM), transmission electron microscopy (TEM), X-ray diffraction (XRD), scanning electron microscopy (SEM) and energy dispersive spectroscopy (EDS), and isothermal calorimetry. For hydration reactions in later stages, FIB-SEM serial sectioning tomography and subsequent image processing are applied to distinguish the microstructure and pore systems of OPC mortar. Some complimentary experiments such as  $\mu$ -CT x-ray tomography are also performed to be compared with FIB tomography.

## **1.2 Research Hypothesis and Objectives**

This research is based on two kinds of cementitious materials formulations: OPC and OPC with nano silica additives. OPC is in most common building material cement formulation at present. However, despite a 200-year successful practical use, the nucleation and growth mechanisms of main hydrated products at the nanoscale are still unclear and some formation mechanisms are the object debate. Meanwhile, the addition of nano-silica in cementitious materials has attracted much attention while the effects of nano-silica on modifying

microstructure and hydration kinetics in early age up to 24 h needs further clarification. In mature OPC mortar, it is important to investigate pore networks and various phases within a representative volume. In sum, this study aims at applying advanced characterization techniques to research hydration reactions of both early and late stages.

### **1.2.1 Hydration Mechanisms and Kinetics in Early Hydration Reactions**

For early hydration reactions, the focus is on the nucleation and growth mechanisms and hydration kinetics. Basically, there are two main hypotheses for early calcium silicate hydrate (C-S-H), the main cement hydration product, reaction growth mechanisms, which are modeled as 2D layers or a colloidal aggregate. The former mechanism suggests that C-S-H develops through attachment of silicate tetrahedra along the margin of embryos to form a disordered layered structure. In contrast, the colloidal model believes that C-S-H forms by the aggregation of C-S-H nanoparticles, which grow to a certain size and remain stable. This study is trying to provide new insights into hypothesis of C-S-H growth mechanisms through direct observation of a dilute nano PC after hydration reaction is started.

The kinetics of the cement hydration reaction are also crucial in early hydration reactions. This is critically important to apply experimental rigour to compare nanoscale cement hydration kinetics to realistic OPC reaction kinetics, thus identifying the aspects of nanoscale cement characterization that universal and those that are unique to the geometry of the materials system and experimental technique. Specifically, it is necessary that the four main time periods in the hydration reaction, namely, i) slow reaction stage, ii) induction stage, iii) acceleration stage and iv) deceleration stage are clarified. Besides, real-time microstructure evolution and quantitative phase contents will help to understand phase transformations in early hydration reactions.

The effects of a nano-silica addition on nucleation and growth as well as hydration kinetics are compared with those of nano PC formula. The phase transformation and hydration reactions are also evaluated qualitatively and quantitatively.

## **1.2.2 Characterization of Pore Systems and Different Phases in Late Hydration**

### **Reactions**

In this part, some important pore characteristics including porosity, pore size distribution, and connectivity of mature mortars are characterized through PFIB tomography and X-ray micro CT tomography. The sample preparation and instrumentation parameters are refined and improved in order to exploit the application and feasibility of PFIB on cementitious materials. Different porosity characterization techniques are to be compared. The hydrated and anhydrous phases are to be examined and compared as well. The complex issue of interpreting porosity from 3-D image stacks at all length scales is addressed using multi-detector integration and machine learning protocols to perform image segmentation.

## **1.3 Thesis Outline**

Chapter 1: Introduction. This chapter summarizes the overall research context, research hypothesis and objectives and the thesis outline.

Chapter 2: Literature review. This chapter presents state of the art and background in the fields of cementitious materials and advanced microscopy. Competing theories of C-S-H growth mechanisms such as colloidal model or layered structure model are introduced. The contradictory findings and effects of nano-silica on hydration reactions are also summarized. Various advanced characterization techniques that have been used to evaluate cementitious materials are presented.

Chapter 3: *Liquid cell transmission electron microscopy reveals C-S-H growth mechanism during Portland cement hydration.* This chapter presents the in-situ results of C-S-H nucleation

and growth using LC-TEM and post-situ experiments. This work aims at realizing the application of in-situ TEM to research hydration reactions of nano PC and providing direct evidence of microstructure evolution. It is found that C-S-H precipitates develop through lateral growth with an alternating nanocrystalline and amorphous structure. Evidence also suggests the other C-S-H growth mode of the aggregation of particles. This work has been submitted to *Nature Communications* and is under review.

Chapter 4: *In-situ Observations of Different Cement Hydration Stages Using Liquid-cell Transmission Electron Microscopy*. This chapter is to understand the hydration kinetics of nano PC and evaluate the applicability of nanoscale measurements to real-world applications. The different hydration stages are revealed using LC-TEM, combined with isothermal calorimetry and Rietveld refinement. The C-S-H precipitates nucleate on the SiN membrane, collapse together and grow in 3D to form a network. The real-time dissolution of needle-like ettringite was also captured, whose process releases sulfate to form monosulfate, leading to a retardation in the early acceleration stage. This work will be submitted to *Materials Characterization*.

Chapter 5: *The effects of nano-silica on early-age hydration reactions of nano Portland cement*. In this chapter, the effects of nano-silica on hydration reactions of nano PC including microstructure evolution, phase transformation and kinetics are investigated. The results show that nano-silica are easily attached to the surfaces of needle-like ettringites contributing to more nucleation sites for C-S-H precipitates. Also, a lower content of ettringite is achieved in nano PC with nano-silica due to acceleration of ettringite conversion to monosulfate. These findings will be submitted to *Nanoscale*.

Chapter 6: *Advanced Characterization of 3D Structure and Porosity of Ordinary Portland Cement (OPC) Mortar Using Plasma Focused Ion Beam Tomography and X-ray Computed Tomography*. This chapter presents results of 3D reconstruction models of mortar structure and

pore systems from nanometric to millimetric scales. A novel characterization technique, PFIB is used and the workflow working with cementitious materials is explored. The reconstruction and segmentation models employ advanced machine learning algorithms and reveal different hydration kinetics and fluid transport pathways. This has been submitted to *Microscopy and Microanalysis*.

Chapter 7: This chapter concludes the important findings from each of previous chapters and discusses the significance of these conclusions. Finally, the future work is proposed and outlined.

Appendix: This includes 3 additional publications and an additional manuscript under review at *Journal of Building Engineering* that are focused on cementitious materials and advanced characterization.

## 1.4 References

1. Elsen, J., G. Mertens, and R. Snellings, *Portland Cement and other Calcareous Hydraulic Binders*, in *Advances in the characterization of industrial minerals*. 2010. p. 441-479.
2. Andrew, R.M., *Global CO<sub>2</sub> emissions from cement production*. *Earth System Science Data*, 2018. **10**(1): p. 195-217.
3. Flores, Y.C., et al., *Performance of Portland cement pastes containing nano-silica and different types of silica*. *Construction and Building Materials*, 2017. **146**: p. 524-530.
4. Zhang, L., et al., *Hydration for the Alite mineral: Morphology evolution, reaction mechanism and the compositional influences*. *Construction and Building Materials*, 2017. **155**: p. 413-426.
5. Paiva, H., et al., *Microstructure and hardened state properties on pozzolan-containing concrete*. *Construction and Building Materials*, 2017. **140**: p. 374-384.

6. Vargas, P., O. Restrepo-Baena, and J.I. Tobón, *Microstructural analysis of interfacial transition zone (ITZ) and its impact on the compressive strength of lightweight concretes*. Construction and Building Materials, 2017. **137**: p. 381-389.
7. Ylmén, R., et al., *Early hydration and setting of Portland cement monitored by IR, SEM and Vicat techniques*. Cement and Concrete Research, 2009. **39**(5): p. 433-439.
8. Scrivener, K.L., et al., *Quantitative study of Portland cement hydration by X-ray diffraction/Rietveld analysis and independent methods*. Cement and Concrete Research, 2004. **34**(9): p. 1541-1547.
9. Merlini, M., et al., *The early hydration and the set of Portland cements: in situ X-ray powder diffraction studies*. Powder Diffraction, 2007. **22**(3): p. 201-208.
10. Hesse, C., et al., *Quantitative in situ X-ray diffraction analysis of early hydration of Portland cement at defined temperatures*. Powder Diffraction, 2009. **24**(2): p. 112-115.
11. Hesse, C., F. Goetz-Neunhoeffler, and J. Neubauer, *A new approach in quantitative in-situ XRD of cement pastes: Correlation of heat flow curves with early hydration reactions*. Cement and Concrete Research, 2011. **41**(1): p. 123-128.
12. Lothenbach, B. and F. Winnefeld, *Thermodynamic modelling of the hydration of Portland cement*. Cement and Concrete Research, 2006. **36**(2): p. 209-226.
13. Thomas, J.J., et al., *Modeling and simulation of cement hydration kinetics and microstructure development*. Cement and Concrete Research, 2011. **41**(12): p. 1257-1278.
14. Ross, F.M., *Opportunities and challenges in liquid cell electron microscopy*. Science, 2015. **350**(6267): p. aaa9886.
15. Jansen, D., et al., *Does Ordinary Portland Cement contain amorphous phase? A quantitative study using an external standard method*. Powder Diffraction, 2011. **26**(1): p. 31-38.
16. Gao, Y., et al., *The ITZ microstructure, thickness and porosity in blended cementitious composite: Effects of curing age, water to binder ratio and aggregate content*. Composites Part B: Engineering, 2014. **60**: p. 1-13.

17. Yio, M.H.N., H.S. Wong, and N.R. Buenfeld, *3D pore structure and mass transport properties of blended cementitious materials*. Cement and Concrete Research, 2019. **117**: p. 23-37.
18. Burnett, T.L., et al., *Large volume serial section tomography by Xe Plasma FIB dual beam microscopy*. Ultramicroscopy, 2016. **161**: p. 119-29.

## **2 Literature Review**

### **2.1 Development of Ordinary Portland Cement (OPC)**

#### **2.1.1 Introduction of OPC and Its Environmental Effects**

Concrete is the most widely used construction material because it is widely available, low-cost and easily shaped into various shapes and sizes. Concrete production scaled to about one ton of concrete for every living person worldwide in 2005, an amount by weight only exceeded by that of water [1]. OPC, the most important binding material of concrete, has played a crucial role in human development since it was introduced in the nineteenth century [2]. Portland cement (PC) was invented and patented by Joseph Aspdin through burning impure limestones at temperatures above 1450 °C [3]. The quality and quantity of OPC production was increased later in the 1870 – 80s due to the application of continuous shaft kilns. In the early 20th century, the implementation of rotary kilns, ball mills as well as gypsum contributed greatly to its worldwide acceptance and popularity [2, 4]. However, modern human lifestyles and infrastructural development require a large amount of Portland cement, whose production process consumes enormous amounts of energy due to synthesis at very high temperatures. It is reported that one ton of carbon dioxide is released to produce almost one tone of Portland cement, and that Portland cement industries contribute 5 to 7% of anthropogenic carbon dioxide emissions [3, 5, 6]. In recent years, society is increasingly much aware of the importance of sustainable living including reduction of energy consumption, a low carbon economy and application of new technologies. From a building and construction perspective, it is essential that new *green* buildings are utilized both environmentally and economically, with an emphasis on durability, and with a lowered energy budget for concrete production. This requires new insights into concrete and cement chemistry and the combined efforts of the research community to satisfy the demand for better concrete for construction.

### 2.1.2 Hydration Reactions of OPC

The manufacturing process of OPC involves the preparation of PC clinker, which is a sintering product of burning impure limestone, or limestone and aluminosilicate-containing materials at about 1450°C [1]. Cement is then produced by grinding PC clinker to powders under 75 µm that is usually conducted in ball mills. During the grinding process, a few percent of gypsum or other calcium sulphates are added to regulate early hydration reactions [3].

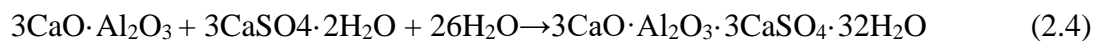
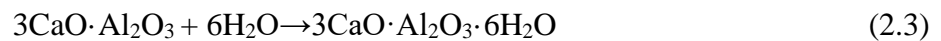
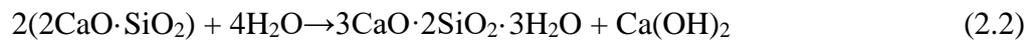
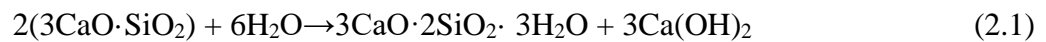
The hydration reactions of OPC are complex because of its multi-component starting compositions and many phases that evolve during the hydration reactions. Table 2.1 shows information of chemical formula, abbreviation, morphology, and crystal structure of common compounds in cementitious materials and will be referenced throughout the text of this dissertation. The starting constituents of OPC prior to hydration are tricalcium silicate ( $C_3S$  or alite), dicalcium silicate ( $C_2S$  or belite), tricalcium aluminate ( $C_3A$  or aluminate phase) and tetracalcium aluminoferrite ( $C_4AF$  or ferrite phase) and a few other minor compounds. Commercial cement mixes are usually designed by varying the content of the different phases and contain mainly 50% ~ 70% tricalcium silicate, 15% ~ 30% dicalcium silicate, 5% ~ 10% aluminate phase and 5% ~15% ferrite phase [1, 3].

Table 2.1 Common compounds in cementitious materials

	Name	Chemical formula	abbreviation	Morphology	Common Crystal structure	Note
Reactants						
1	Alite	$3\text{CaO} \cdot \text{SiO}_2$	$\text{C}_3\text{S}$	Hexagonal crystals	Triclinic, monoclinic, trigonal	Responsible for early strength
2	Belite	$2\text{Ca}_2\text{O} \cdot \text{SiO}_2$	$\text{C}_2\text{S}$	Irregular	Monoclinic	Far less reactive than alite
3	Tricalcium aluminate	$3\text{CaO} \cdot \text{Al}_2\text{O}_3$	$\text{C}_3\text{A}$	prismatic and granular	Cubic, orthorhombic	Reacts first in the hydration reaction
4	Tetracalcium aluminoferrite	$4\text{CaO} \cdot \text{Al}_2\text{O}_3 \cdot \text{Fe}_2\text{O}_3$	$\text{C}_4\text{AF}$	Hexagonal crystal	Orthorhombic	High reactivity
5	Gypsum	$\text{CaSO}_4 \cdot 2\text{H}_2\text{O}$	$\text{C}\bar{\text{S}}\text{H}_2$	Elongated and prismatic	Monoclinic	Regulates setting (fluid to solid)
6	Anhydrite	$\text{CaSO}_4$	$\text{C}\bar{\text{S}}$	cleavage masses	orthorhombic	Soluble form of gypsum
7	Alkali	$\text{OH}^-$	--	--	--	pH >7.0
8	Limestone	$\text{CaCO}_3$	--	--	--	Source for OPC
Products						
9	Ettringite	$3\text{CaO} \cdot \text{Al}_2\text{O}_3 \cdot 3\text{CaSO}_4 \cdot 32\text{H}_2\text{O}$	$\text{C}_6\text{A}\bar{\text{S}}_3\text{H}_{32}$	Needle	Hexagonal	Forms after mixing
10	Portlandite	$\text{Ca}(\text{OH})_2$	CH	Large Hexagonal-prism crystals	Hexagonal	By-product of silicate reactions
11	Calcium silicate hydrate	$3\text{CaO} \cdot 2\text{SiO}_2 \cdot 3\text{H}_2\text{O}$	C-S-H	Crystalline fibers or reticular network	Amorphous and/or Nanocrystalline	Main hydration products
12	Tobermorite	$5\text{CaO} \cdot 6\text{SiO}_2 \cdot 5\text{H}_2\text{O}$	C-S-H	Fibers and platelets	Orthorhombic	Mineral
13	Jennite	$9\text{CaO} \cdot 6\text{SiO}_2 \cdot 11\text{H}_2\text{O}$	C-S-H	Blade shaped crystals, fibrous and sheet form	Triclinic	Mineral
14	Calcium aluminate hydrate	$3\text{CaO} \cdot \text{Al}_2\text{O}_3 \cdot 6\text{H}_2\text{O}$	C-A-H	Compact faceted crystals	Hexagonal	Forms quickly
15	Monosulfate	$3\text{CaO} \cdot (\text{Al,Fe})_2\text{O}_3 \cdot \text{CaSO}_4 \cdot n\text{H}_2\text{O}$	$\text{C}_4\text{A}\bar{\text{S}}\text{H}_{18}$	Hexagonal plate	Triclinic and/or rhombohedral	Forms slowly

where C stands for CaO, S stands for SiO<sub>2</sub>, A stands for Al<sub>2</sub>O<sub>3</sub> and F stands for Fe<sub>2</sub>O<sub>3</sub>, H stands for H<sub>2</sub>O, and  $\bar{\text{S}}$  stands for SO<sub>3</sub>

Various compounds in cement react with water to form different hydrated products like calcium silicate hydrate (C-S-H), calcium aluminate hydrates (C-A-H) as well as portlandite, whose hydration reaction equations are listed below [1]. It is worth mentioning that original cement designs used to exhibit rapid or “flash” setting (or hardening) behaviour in just a few minutes, because of the fast setting (solidification of the paste) of C<sub>3</sub>A in a few minutes with water addition, thus forming calcium aluminate hydrate (C-A-H). Another drawback of this reaction is that much exothermal heat is released and causes evaporation and loss of water and subsequently a drop in compressive strength [7]. Therefore, gypsum (CaSO<sub>4</sub>·2H<sub>2</sub>O), is typically added as a retarding agent is added during the cement clinker manufacturing process to regulate the setting due to the affinity of C<sub>3</sub>A to SO<sub>3</sub>. The reaction of calcium aluminate with gypsum is shown below.



The above reaction (4) releases less heat than reaction (3), which is less harmful to the microstructure from water loss and allows further, slower hydration reactions to continue. The product of the reaction, known as ettringite (3CaO·Al<sub>2</sub>O<sub>3</sub>·3CaSO<sub>4</sub>·32H<sub>2</sub>O), to some extent accelerates hardening effects leading to higher early strength [7]. So far gypsum has proven to be the most effective hydration regulator in cement. The reaction proceeds as follows, with a change in microstructural form from a powder of anhydrous cement, with a powder size distribution under 75 μm to a hydrated network of binding material that has a specific mechanical strength. The ettringite crystals are formed after mixing cement with water. The needle-like ettringite crystals are likely to appear first in the transition zone resulting from the

forming of water films around the large aggregate particles in freshly compact concrete [1]. The main by-products, Portlandite ( $\text{Ca}(\text{OH})_2$ ) from silicate reactions and ettringite from aluminate reactions are embedded inside the matrix [1]. A schematic microstructure after hydration reactions in the presence of gypsum is shown in Figure 2.1.

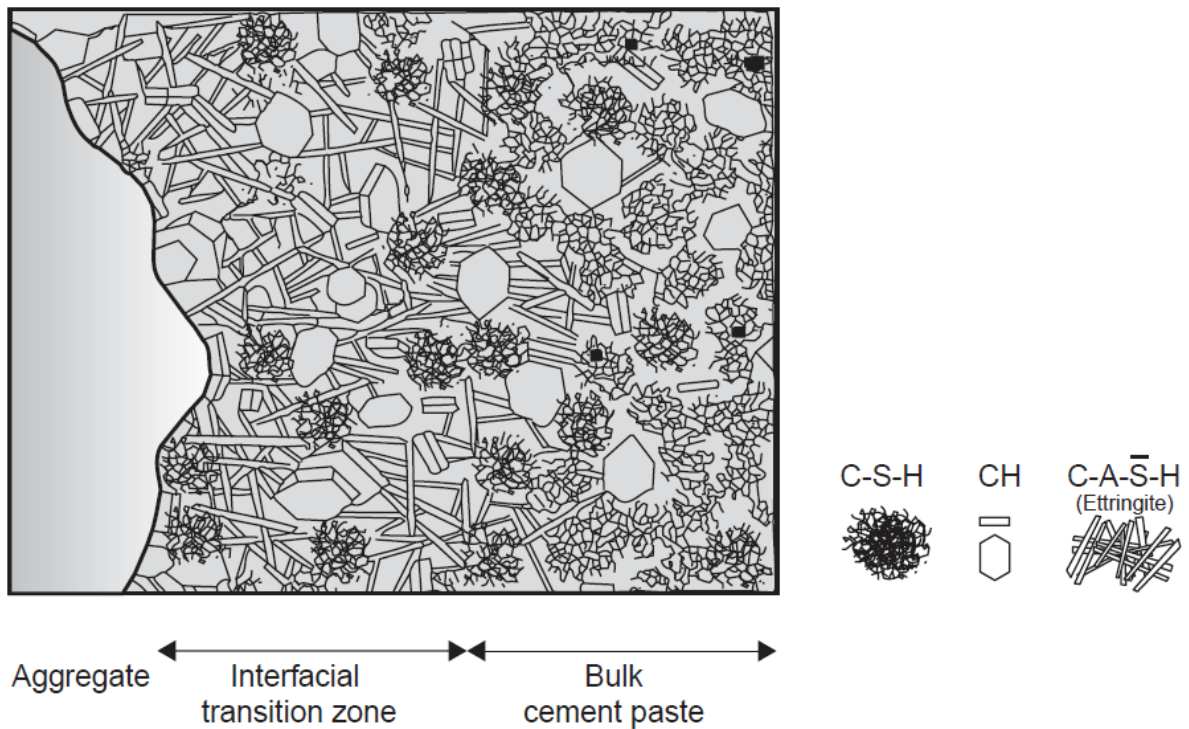


Figure 2.1 Schematic representation of interfacial transition zone from an aggregate to bulk cement paste in concrete from [1]

Generally, concrete is divided into three categories based on formulation according to compressive strength. These are low-strength concrete (less than 20 MPa), moderate-strength concrete (20 to 40 MPa) and high-strength concrete (more than 40 MPa) [1]. The compressive strength of concrete depends on various factors including water to cement ratio, aggregate type and size, admixtures (minerals, water-reducing, and air-entraining admixtures, etc.), and curing conditions (time, temperature, and humidity conditions). It is well accepted that strength is in inverse relationship with porosity in solids [1]. In cement paste, the small voids within the matrix are detrimental to strength. As for mortar and concrete, the strength is determined by the matrix, matrix-aggregate transition zone and aggregate, in which water/cement ratio-

porosity affects the porosity both of cement paste and the transition zone. This makes it very important to understand porosity in a volume when considering strength of cementitious materials.

Reactions occur at different rates and with different reaction enthalpies. Typically, the first reactions, aluminate reactions occur and ettringite crystals are formed in a few minutes after mixing cement and water, followed by the precipitation of C-S-H from alite hydration, and hydration reactions of belite happen slowly and can last for years as hydration products diffuse through a complex pore system in the concrete. Therefore, alite hydration accounts for early compressive strength and belite hydration reactions increase late strength slowly.

### **2.1.3 Hypothesis of Growth Mechanisms of C-S-H**

The most significant cement hydration product is C-S-H, which provides basic structure, and dominates subsequent mechanical properties of both cement and concrete, such as strength and durability. Research on cement hydration reactions have been performed for more than a century. However, the early-stage growth mechanisms and microstructural evolution of C-S-H and whether it conforms one of two competing theories of formation: a colloidal model or layered model are still not fully understood. The beginning of this discussion originated at the 12<sup>th</sup> international conference on cement conference in London in 1918, when the nature of cement as colloids was addressed first [8]. A colloidal model was developed by Powers and Brownyard in 1946, based on a joint research on mechanisms of shrinkage, different size of pores, and various phases and states of water [9]. They proposed that the hydrated products of OPC may be a colloidal gel by electron microscopic analysis [10, 11]. With the development of higher resolution techniques later, much information on structure was revealed on atomic scale. It is now well acceptable that C-S-H be explained as tobermorite mixed with jennite, consistent with many experimental results. In 2000, Jennings [12] proposed that C-S-H microstructure between 1 and 100 nm and ascribed the basic building block of these phases to

roughly spherical units of nearly 2 nm, which packed together to form globules. The specific surface area and packing factor were also calculated in the model, which promoted the discussion and experiments. Their later experimental results were also interpreted based on this modified colloidal model with 5 nm globules to explain nanoporosity associated with drying and heat curing (shown in Figure 2.2) [13]. The composition, mean formula and solid density of C-S-H were measured in gel particles [14]. Later studies provided insights into the evolution of tricalcium silicate after hydration using a variety of methods, including isothermal calorimetry and in-situ synchrotron measurements, which revealed more details of the hydration kinetics and crystalline nature of C-S-H gel during transformation [15].

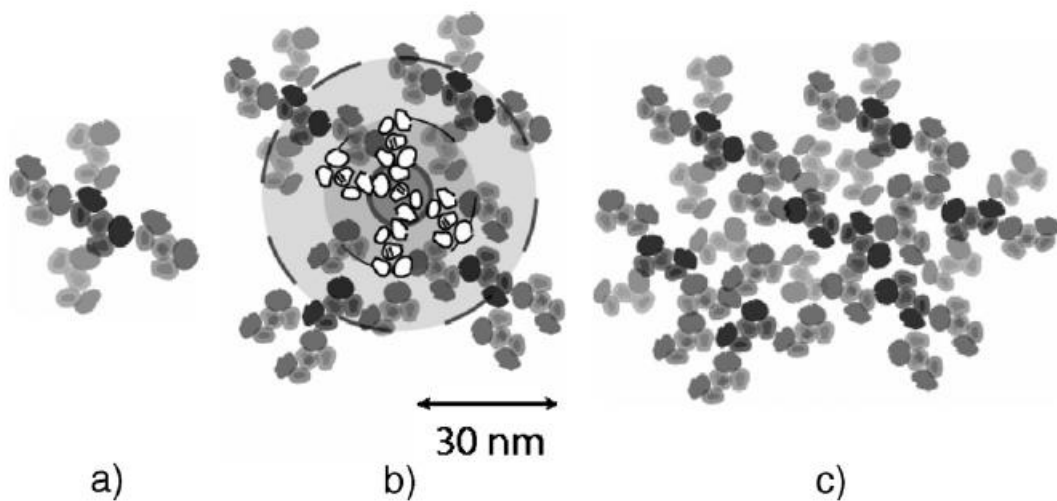


Figure 2.2 Proposed formation of C-S-H gel by Jennings [13]. a) One relatively small volume fractal region, formed from contacting  $\sim 5$  nm globules of C-S-H. b) The same volume fractal region (shown in white) has grown into a larger, self-similar structure with a reduced packing density. c) Adjacent fractal regions have grown into each other to form a relatively uniform structure with a range of gel pore sizes. The largest pores are greater than 10 nm. Upon drying these pores collapse to form a structure with a packing density of about 0.64.

An alternative hypothesis of the early stages of C-S-H formation in the form of layered structure model was first proposed based on X-ray diffraction evidence in 1952 [9]. Taylor explained the C-S-H structure as a disordered layered structure, which comprised of imperfect jennite (Table 2.1) and tobermorite (repeating distance of crystal structure 1.4 nm, Table 2.1).

The chains that construct the C-S-H structure were assumed to repeat at intervals of silicate tetrahedra [16, 17]. The nature and relative proportions of ions and molecules including calcium silicate,  $\text{Ca}(\text{OH})_2$  and water molecules, and  $\text{Al}^{3+}$ ,  $\text{Si}^{4+}$ , alkali cations and  $\text{Ca}^{2+}$  ions were discussed. A disordered layer structure was also proposed in Richardson and Groves' Model [8, 18, 19]. Gartner [20] believed that C-S-H grows as wavy or buckled sheets. These sheets are formed through the attachment of silicate tetrahedra at silicate chains along the margin of two-dimensional sheets. The well – ordered silicate sheets from growth of small two-dimensional C-S-H nuclei are within about 5 nm, beyond which more defects will probably be built in because of more defect nucleation sites inside the sheets. In the meantime, heterogeneous nucleation from the first C-S-H sheet at one point may produce a second sheet with active nucleation. In this case, several layers of sheets perpendicular to the original sheet may form, which appeared like imperfect tobermorite or jennite (Table 2.1) [20, 21]. Synchrotron-based X-ray diffraction was conducted to further reveal the feature of a tobermorite-based dimer with a layer thickness of 11.7 Å [22]. Zhang [23] also illustrated the hydration mechanisms on tricalcium silicate in a dilute slurry by characterizing hydration products after 1 day to 1 year and molecular dynamics. The relationship between Ca/Si ratio and polymerization reaction of silicate monomers and silicate chains were further clarified.

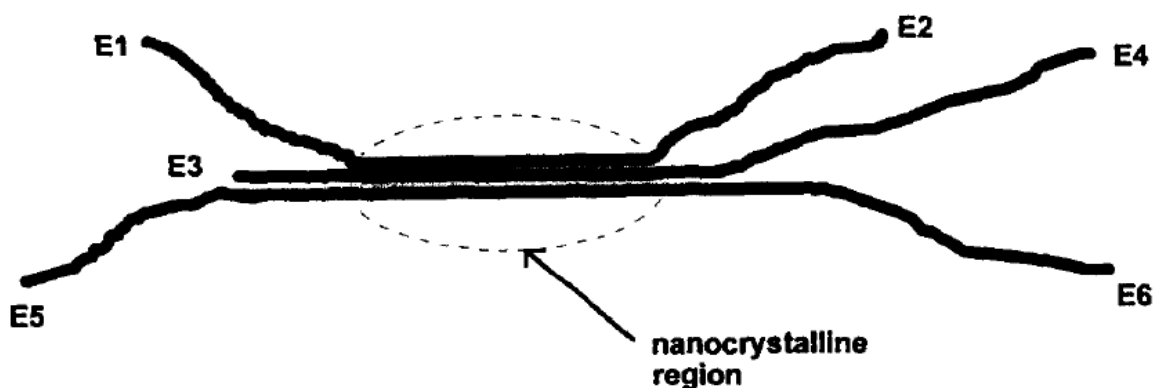


Figure 2.3 Adopted from Gartner [20]. Schematic of growth process with three separate sheets of C-S-H emanating from a common nucleation point which can be considered a nanocrystalline region

The main difference of two models is whether the microstructure evolves as growing silicate chains from the solution or globules of agglomerated nanoparticles with certain size.

The debate of C-S-H growth mechanisms has been continued for decades. Many researchers have been devoted time and effort to elucidate it at the nanoscale. However, direct evidence of microstructural evolution of C-S-H is still needed. Also, a good understanding of C-S-H growth mechanisms will benefit the control and modification of hydration reactions and thus facilitate the design of concrete with good strength and durability.

#### **2.1.4 Reaction Stages and Kinetics of Alite/C<sub>3</sub>S**

The hydration reactions of alite/C<sub>3</sub>S and even OPC vary with a wide range of timescales, but during early hydration (24 hours), most of the dominant effects take place. Many efforts have been devoted to hydration reactions of alite because it accounts for 50% to 70% of cement and dominates the early microstructure and strength development. The hydration kinetics of alite is usually analyzed by considering four hydration stages, which are stage of initial reaction, induction stage, acceleration stage and deceleration stage, indicated by heat flow calorimetry as shown in Figure 2.4 [24].

The initial reaction stage is described as an early exothermic peak during the wetting process. It is known that the rates of alite dissolution decelerate quickly before the solution of dissolved alite reaches a saturation state [25]. Some hypothesis of decelerating dissolution rates involve metastable barrier hypothesis, whereby a continuous thin layer of calcium silicate hydrate restricts further hydration of cement particles, and a slow dissolution hypothesis, where there is a near-steady state balance between C<sub>3</sub>S dissolution and slow growth of C-S-H [24, 26, 27]. The supersaturation of the hydration water with dissolving salts is reached, and the C-S-H nuclei are stable in an induction period. The acceleration period involves the accelerated

growth of hydrated products, while decelerated rate of microstructure and strength development is observed in deceleration stage. Some experiments show the relationship between alite dissolution and growth of etch pits of alite surface, which is affected by the composition of liquid [26]. Also, Nicoleau et al. [27] attributed this deceleration stage to  $C_3S$  dissolution instead of the growth of C-S-H. Gartner [28] argued that the rate of  $C_3S$  hydration cannot not be controlled by the dissolution rate other than at extremely early ages. Bergold et al. [29] studied mechanically synthesized alite and found that amorphous alite speeded up the hydration. The etch pit opening on crystalline alite increased reactive surface and enhanced the hydration degree during deceleration stage.

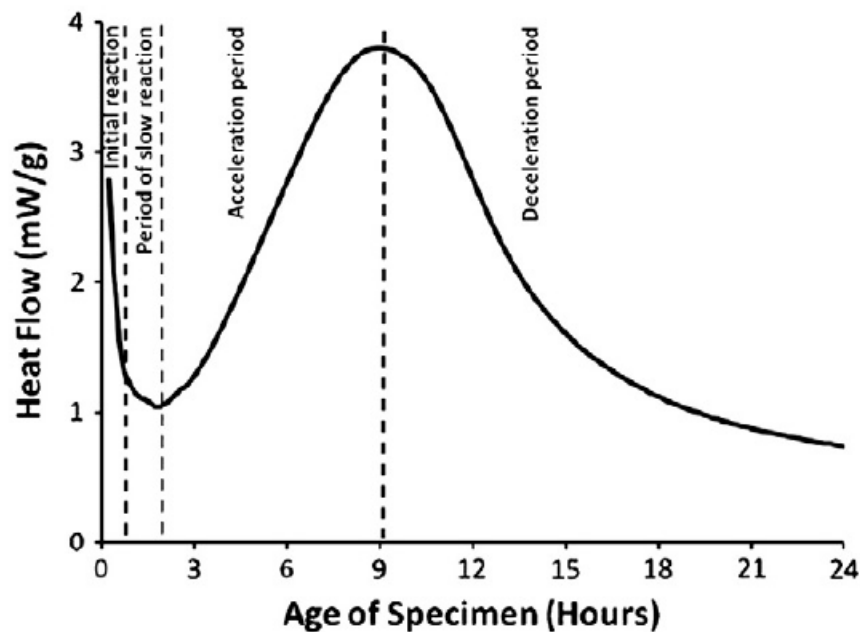


Figure 2.4 Rate of alite hydration as a function of time given by isothermal calorimetry measurements [24]

As mentioned previously, the other important category of reactions is the aluminate reactions, which influence reaction kinetics in early stages. Quennoz et al. [30] clarified the relationships between alite and  $C_3A$ -gypsum hydration in a calorimetry study, in which alite hydration reactions are accelerated with gypsum, due to interactions of sulfate ions and aluminum ions. It was also concluded that an aluminate peak appeared prior to a silicate peak

in undersulfated systems while a silicate peak occurred prior to an aluminate peak in properly sulfated systems. Heat evolution curves were compared at different setting temperatures, showing different curve shapes above 26 °C due to activation energy. Mota et al. [31] studied the effects of alkali and sulfate on hydration kinetics of alite by adding gypsum, Na<sub>2</sub>SO<sub>4</sub>, NaOH and gypsum, and NaOH separately to an alite system, in which all systems exhibited clear early acceleration of hydration. However, the silicate reactions at later ages were inhibited, resulting from increasing solubility of aluminate by alkalis. Pustovgar et al. [32] researched the influence of aluminates on hydration kinetics of alite with the addition of NaAlO<sub>2</sub>. Their experimental and simulated results showed that aluminates hindered C<sub>3</sub>S dissolution by absorbing to the hydroxylated C<sub>3</sub>S on the surface. Bergold et al. [33] further concluded from their study that sulfate accelerated alite hydration, resulting from the seeding effects of fine ettringite and more surface for alite precipitation. However, the precipitation of monosulfate phases (Afm) instead of Al inhibition lead to the slowdown of alite hydration.

### **2.1.5 Reaction Stages and Kinetics of OPC**

The hydration kinetics of the OPC mixture are much more complex than those of pure alite and requires advanced characterization techniques. Quantitative X-ray diffraction (QXRD) on cement hydration has been developed by many researchers and proved to be an effective method [34]. While calorimetry can provide information of heat evolution, QXRD reveals the information of quantitative phase content. It is achieved through the Rietveld refinement, in which measured X-ray diffraction pattern peaks are fitted and refined using a scale factor, and adjusting lattice parameters and accounting for preferred orientations [35]. Rietveld analysis gives quantitative analysis of multiphase mixtures of detected crystalline phases normalized to 100%. Adjustments to the phase calculations are also employed according to a simplified hypothesis which assumes only alite hydrates with water in early age [34].

Many studies have been conducted to understand the hydration kinetics of OPC, combining various analysis techniques. Merlini and Artioli [36] studied the phase evolution during first hours of hydration using in-situ synchrotron experiments. It showed that ettringite precipitates after mixing with water and C-S-H were formed after a few hours. The phase contents of  $C_3S$ ,  $Ca(OH)_2$ , ettringite and  $C_3A$  were quantified as well. Hesse et al. [34] researched early hydration reactions by in-situ QXRD, in which amorphous C-S-H content was calculated by using portlandite ( $Ca(OH)_2$ ) as a standard, and other crystalline phases were quantified. The formation of ettringite and portlandite indicated the process of hydration reactions. It was also concluded that the formation of ettringite was closely related to the dissolution of anhydrite ( $CaSO_4$ ) and  $C_3A$ . Jansen et al. [37] combined heat flow calorimetry and QXRD to analyze hydration kinetics and found the dissolution of anhydrite and gypsum contributed in a minor fashion to released heat. The research was conducted to compare the heat flow calculated from QXRD phase contents and measured heat flow, which exhibited a good agreement [38]. The conclusion was also reached that the first maximum peak in calorimetry data resulted from the aluminate reaction, and that the aluminate reaction, dissolution of  $C_3A$  along with the formation of ettringite accounted for a second smaller peak, as a shoulder on the maximum silicate peak. Some researchers [39] incorporated Proton nuclear magnetic resonance ( $^1H$  NMR) with heat flow and QXRD to study ion behavior during hydration reactions. It was found that the sulfate and aluminum adsorption affected sulfate depletion greatly. Other techniques have also been used in characterizing hydration reactions, such as quantitative analysis on Raman patterns [40], quantitative analysis from backscattered electron (BSE) and energy dispersive spectroscopy (EDS) [41], infrared spectroscopy (IR) and Viscat (determine water amount by measuring needle penetration) techniques [42].

Early hydration reactions of OPC are complex due to the large number of constituents and wide variety of hydrated products. Moreover, two kinds of reactions, namely, silicate reaction

and aluminate reactions interact with each other, which usually are reflected from measurements of phase transformations and heat changes. It is necessary that multiple techniques be used to analyze hydration in early age both qualitatively and quantitatively.

## **2.2 Supplementary Cementitious Materials in Concrete**

### **2.2.1 Motivation to Add Supplementary Cementitious Materials in Cement**

The attempt to add natural and artificial materials to produce blended cement, which shares comparable strength and durability to OPC, started in the late 20<sup>th</sup> century [43]. It is well known that the production of Portland clinker is an energy-intensive process, due to high reaction temperature, usually up to 1450 °C. The addition of supplementary cementitious materials in blended cements with a potential lowered carbon budget, has attracted much attention, in response to the problem of huge energy consumption and climate change.

Natural Supplementary cementitious materials are abundant and are used in many countries around the world. A significant number of industrial by-products and waste materials are becoming environmental issues because of a disposal crisis. These wastes need substantial amount of space to dispose and does harm to soil and water resources. On the other hand, these industrial wastes are potential replacement materials in the cement industry, which also lead to less consumption of PC and reduction of environmental issues. Industrial by-products including fly ash, silica fume, and ground granulated blast slag, rice husk ash and palm oil fuel ash have been researched and used in concrete for many years[44]. Another advantage to using waste materials from industries is to reduce costs. They are easy to access since there are massive production of wastes worldwide. The consumption of electricity and coal can be reduced as well.

### 2.2.2 The Definition of Supplementary Cementitious Materials

The supplementary cementitious materials are those that exhibit hydraulic or pozzolanic behavior. A hydraulic property refers to the ability of a binder to set and harden when mixed with water, such as OPC. Blast furnace slags from the steelmaking industry, however, show relatively slow hydraulic behavior compared with OPC. They can be chemically activated in the presence of alkali-hydroxides, sulfates like gypsum, and may exhibit pozzolan behavior. Pozzolan materials contain siliceous materials and show cementitious properties through the reaction of calcium hydroxide in moisture [43]. The fundamental reaction of the pozzolan reaction is the recombination of silicate or aluminate material and the formation of hydrated products. It is described as follows [1].



where C stands for CaO, S stands for SiO<sub>2</sub>, A stands for Al<sub>2</sub>O<sub>3</sub>, and H stands for H<sub>2</sub>O. This reaction is beneficial for cement mixtures. Less heat is produced from the pozzolan reactions of supplementary cementitious materials compared with that of C<sub>3</sub>S cement hydration reactions [45]. The reduction of heat release is critical to avoid cracking caused by thermal effects when it comes to a massive production.

### 2.2.3 Classification of Supplementary Cementitious Materials

Supplementary cementitious materials may be divided into two categories based on origin. The first group of materials are natural supplementary cementitious materials and can be used in their natural form, such as sedimentary rocks and diatomaceous earths (consists mainly of amorphous hydrated silica). The other group of materials are artificial supplementary cementitious materials that require further structure modification through the manufacturing or production process. Some industrial wastes including blast furnace slag, fly ash and silica fume belong to artificial supplementary cementitious materials [43].

Natural supplementary cementitious materials consist of volcanic materials and sedimentary materials. The majority of natural pozzolan originated from volcanic rocks due to the wide availability in many countries. Two kinds of volcanic pozzolan materials, volcanic ashes and pumice exhibit high activity due to their highly glassy and porous nature. Some volcanic rocks after alteration by alkaline fluids show much compact and strong structure, for example zeolites [43].

Sediments that may also serve as natural pozzolan materials include both biogenic sediments like organism skeletons and chemical precipitates. In some cases, thermal treatments are needed to improve the pozzolan activity of sediments. It is shown that clay and shales exhibit higher activity after heating to 600 °C to 900 °C. It is the amorphous or disordered aluminosilicate structure that contributes to the increase of pozzolanic activity of clay [1].

Industrial by-products and wastes are the most important sources of pozzolanic materials to substitute OPC. A variety of wastes are applicable to the cement industry. Some of the most widely used industrial wastes are discussed below.

#### 1) Blast furnace slags

Blast furnace slags from steelmaking exhibit latent hydraulic behavior, and substitute for a larger portion of cement than pozzolanic materials. They are obtained in the pig iron production process as a by-product. Blast furnace slag floats on top of molten iron and steel and contains silicate and aluminate. The glassy product is created through rapid quenching below 800 °C after separation instead of slow cooling, which only produces unreactive crystalline materials. The porous glassy structure is introduced as a supplementary cementitious material while the coarser crystalline part is treated as lightweight aggregate. Blast furnace slags are composed of 30 ~ 50% CaO, 28 ~ 38% SiO<sub>2</sub>, 8 ~ 24% Al<sub>2</sub>O<sub>3</sub>, 1 ~ 18% MgO [43]. The property of latent

hydraulic and pozzolanic reactions makes it an applicable replacement in PC up to 40 ~ 60% with a comparable compressive strength [45, 46].

## 2) Coal fly ash

Fly ash or pulverized fly ash is a product of coal combustion in modern thermal plants, and widely used as supplementary cementitious materials as well. They are materials recaptured from exhausted flue gas. The coal used contains both organic and inorganic matter. After passing through a high temperature zone, carbon-containing matter mostly transforms into volatile gases, while inorganic minerals, such as quartz and clay remain. Some minerals may undergo some chemical, physical and mineralogical changes and form amorphous structures. Like other pozzolanic materials, fly ashes share a composition of  $\text{SiO}_2$ ,  $\text{Al}_2\text{O}_3$ ,  $\text{Fe}_2\text{O}_3$  and  $\text{CaO}$  [47]. Those with low  $\text{CaO}$  content are used as supplementary cementitious materials and those with higher  $\text{CaO}$  content are considered to be a cement-replacement material.

## 3) Silica fume

Silica fume, also known as microsilica is a by-product of silicon metal industry. The silicon dioxide vapor is produced during quartz reduction process at temperature of more than 2000 °C. The vapor is then condensed into small, high-purity amorphous silica of 0.1 ~ 0.2  $\mu\text{m}$ . The advantage of silica fume is consistency in composition, which shares more than 90% silica, and a few other minor compounds of less than 1%, separately.

### **2.2.4 Filler Effects of Supplementary Cementitious Materials**

It is crucial to understand the effects of SCMs in blended cement reactions. Many studies have been conducted to clarify the effects of these materials on hydration kinetics. The most significant effect is described as a filler effect (the hydration of the clinker component is accelerated due to mineral addition in cement) [48], for which even the inert materials have on blended systems.

In general, there are two primary mechanisms leading to the filler effect. The first mechanism is that in the presence of SCMs the water to clinker ratio is higher at the same water to solid ratio, assuming the blended materials do not react, ensuring hydration reactions run to completion. The other mechanism proposes that due to SCMs, the increased internal surface area provides more nucleation sites for hydration products to precipitate [5].

Recent studies reveal that the finer microstructures were achieved in blended systems than that of OPC systems [49, 50]. The nanoscale structure of foil-like C-S-H was also evaluated. It was shown that blended cement with metakaolin (anhydrous calcined form of the clay mineral) and limestone exhibited better mechanical properties at 7 and 28 days [51] after hydration. Additionally, relatively higher amounts of portlandite was observed in these blended systems than 100% OPC system. The degree of hydration was enhanced due to the filler effect, where extra space was provided for hydrates. Mounanga et al. [52] researched the effects of limestone filler on the setting time, mechanical properties and heat release of mortars. They found that the shortest setting time was accomplished with the addition of finer particles. The mechanical properties in blended systems were enhanced while the heat released were reduced. Oey et al. [53] clarified the influencing factors of blended powders and reaction rates through experimentation and simulation. Consistent with other studies, the research demonstrated that mineral powders provided additional sites for nucleation of hydration products and accelerated reactions. The results also revealed that increasing surface area and the capacity of the filler's surface to offer favorable nucleation sites for hydrated products contributed to acceleration of hydration reactions. Further simulations also indicated that acceleration also related to the compositions of fillers and their dissociated ions to participate in exchange reactions.

### **2.2.5 Applications of Supplementary Cementitious Materials in Cement**

Supplementary cementitious materials can be added to cement to make greener concrete. It is reported that the addition of supplementary cementitious materials has an impact on water

demand, setting time, heat evolution, microstructure and properties [54]. Some applications of supplementary cementitious materials have been seen in ultra high-performance concrete (UHPC). UHPCs are composite materials with excellent static and dynamic mechanical properties as well as superior durability [55]. Tuan et al. [56] compared UHPC made with rice husk ash and silica fume, separately. The degree of hydration in later ages were increased with the addition of rice husk ash. However, it seemed that silica fume exhibited larger ability than rice husk ash to refine the pore structure, which contributed to strength increment and durability, and reduce the content of  $\text{Ca}(\text{OH})_2$  that is harmful for acidic attack. Concerning the compressive strength of UHPC, samples with rice husk ash were higher than those with silica fume. It was concluded that the long-term curing effect of storing water inside porous structure of rice husk ash contributed to higher strength. Korpa et al. [57] examined phase development in normal and UHPC without aggregate using QXRD and thermogravimetry (TG) methods. The results showed most significant changes of phase development happened within seven days, after which less changes were observed in both normal and UHPC. More of the anhydrous phase,  $\text{C}_3\text{S}$  remained in UHPC, resulting from less water for hydration. No carbonation (calcium-containing phases attacked by carbon dioxide to form calcium carbonate) was seen in UHPC sample. The role of glass powder on hydration degree and mechanical properties in UHPC was researched [58]. It showed that the 100% substitution of silica fume by glass powder gave the worst compressive strength, while the combination of silica fume and glass powder resulted in best compressive strength of 221 MPa. By careful examination of phase evolution, it was found out that the hydration was accelerated due to increasing dissolution of PC clinker in the presence of glass powder. However, the pozzolanic properties of glass powder were not as good as silica fume, which reacted with  $\text{Ca}(\text{OH})_2$  five times more than that of glass powder by weight. The role of glass powder in accelerating hydration reactions was due to increased surface area for soluble alkali.

It is promising that supplementary cementitious materials replace OPC and reduce the emission of carbon dioxide. But efforts are still needed to understand the role of supplementary cementitious materials in microstructure and properties. This is particularly important to compare different results because of inconsistency of compositions of materials, even with the same kind of supplementary cementitious materials.

## **2.3 Nano-silica in Cement and Concrete**

### **2.3.1 Introduction of Nano-silica**

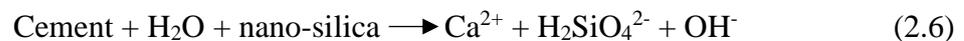
Nanotechnology is greatly changing every aspect of our life [59]. With the advancement of nanoscience and nanoengineering, it is promising to improve the microstructure and properties of concrete in two ways. The first one is to combine nano-sized building blocks in concrete, including nano-admixtures and nanoparticles. The properties of concrete, like surface functionality, can also be improved by adsorbing customized molecules onto cement particles to achieve certain surface properties [60]. Recently, nanotechnology in concrete has received more and more attention.

Among various manufactured nano materials, nano-silica with sizes from 15 to 200 nm in the beginning to see an increasing interest in concrete. Extending from microscale silica fume, which has played an effective role in improving concrete properties, nano-silica is increasingly being researched. Various forms of nano-silica can be produced via different methods, due to advances in nanoparticle synthesis [61]. Nano-silica is amorphous silica with a nanoscale structure, thus possessing a higher purity, surface area and reactivity [62]. Compared with silica fume, nano-silica is believed to be very important in cement hydration because of its high surface-to-volume ratio. Therefore, many investigations have been conducted to clarify the reaction mechanisms, kinetics and the effects of nano-silica on cement microstructure and properties.

### 2.3.2 Strengthening Mechanisms of Nano-silica

Like microscale silica fume, nano-silica has a filler effect. High surface energy results in absorption of hydrated products onto nano-silica particles and acceleration of cement hydration [63]. Furthermore, the reactivity of nano-silica is significantly improved, which is easier for nano-silica to react in the following two possible ways [64].

The first reaction type is nucleation reactions, which lead to the acceleration of hydration reactions. The C-S-H precipitates on the surface of pure C<sub>3</sub>S grains and within the pore structure, which are between cement particle, nano-silica and water. A large amount of seeds is spread between cement grains in the water, serving as seeds for the formation of more C-S-H. Then the reaction not only happens on the surface of particles, but also within the pores. Therefore, the reactions are accelerated by the formation of a large amount of seeds for further nucleation of C-S-H [59].



Furthermore, the addition of nano-silica promotes the pozzolanic reactions, which react nano-silica with Ca(OH)<sub>2</sub>. The advantage of this reaction is that the amount of Ca(OH)<sub>2</sub> is reduced [64]. It is good for properties, especially for resistance to acid attack, important for acid rain applications, or in industrial environments, because portlandite reacts easily with acids. The deterioration of cementitious materials caused by leaching in acid are reduced. Additional C-S-H results in further hydration of the microstructure and increase the strength of concrete as well.

### 2.3.3 Research on Effects of Nano-silica in Cement

Currently, many studies have been conducted to analyze the effects of nano-silica on structure and properties. Many researchers have reported that nano-silica has a positive effect on concrete. The research of addition of superplasticizer (chemically synthesized polymers as

water-reducing admixtures) and colloidal nano-silica on the hydration of pure alite and belite pastes were monitored using infrared spectroscopy (IR) [65]. The results showed that colloidal nano-silica accelerated the hydration reactions of alite and belite pastes in the presence of superplasticizer. The hydrated products were composed of C-S-H. Stefanidou and Papayianni [66] performed the tests of adding nano-silica with and without superplasticizer. It was found that the addition of nano-silica increased the amount of water needed for reaction without superplasticizer due to the higher surface area. The compressive strength increased 20 ~ 25% with the addition of 0.5 wt.% to 2 wt.% nano-silica in this case. But the addition of superplasticizer reduced the amount of water needed and the strength increment was up to 35% even with 1% addition of nano-silica. The hydration kinetics and phase contents of cement were determined by examining mortars with same replacement ratios of nano-silica for up to 28 days [67]. A larger amount of hydration products, especially C-S-H and C-A-H, was seen in mortars with higher percentages of replacement after the first day. The hydration rate and the quantity of hydrates increased significantly between 1 day and 7 days. It was also worth noting that the reactivity of nano-silica in first few hours was good because of high surface area. Almost 20% to 34% increase in C-S-H content were observed with 5% and 10% replacement of cement at 28 days. It is difficult to determine the exact amount of substitution of nano-silica particles that are suitable for cement and concrete, due to greatly varied compositions of raw materials. Many research groups are exploring their own formulas in specific research studies.

Nano-silica will see increasing applications in UHPC than traditional supplementary cementitious materials, due to superior effects on strength and durability. The nano-silica possessed better structural and properties than traditional supplementary cementitious materials, including quartz, and silica fume, and resulted in different microstructure and compressive strength with 2.5% replacement of cement [68]. Both silica fume and nano-silica

were responsible for acceleration of hydration reactions. Finer microstructures and an increase in strength increment resulted from filler effects and the pozzolanic reaction with  $\text{Ca}(\text{OH})_2$ . The strength of pastes with the addition of nano-silica had higher strength as well [68]. Zapata et al. [69] conducted research to assess the effects of micro and nano-silica in the presence of superplasticizer on PC mortars. The air contents in both systems were decreased because of the effects of these nanoparticles on improving structural compaction. However, mortar samples from nano-silica exhibited the highest compressive strength with the addition of 1% nano-silica, while the highest compressive strength of micro-silica addition was obtained at 15%. This means that the addition of nano-silica helps to save some material while achieving the same strengthening effects. Yu et al. [62] further researched the effects of nano-silica on hydration and microstructure development of UHPC. Less binder in the unit volume can be used to obtain a dense and homogeneous structure in the presence of superplasticizer. They also concluded that an optimal amount of nano-silica can be selected to have the lowest porosity, since porosity decreased with increasing addition of nano-silica at first but then increased with continuing addition. Another study was conducted by Wu et al. [55] compared the effects of nano- $\text{CaCO}_3$  and nano-silica on UHPC. Both nano materials contributed to decrease of flowability and increase of heat of hydration with increasing contents. The results showed that nano-silica led to increasing compressive strength in early age, but nano- $\text{CaCO}_3$  contributed to increase of strength after 7 days. A less porous and more homogenous structure were observed in both formulas due to the nucleation and filling effects.

However, some contradictory results have also been reported with the addition of nano-silica in cement. A study by Dolado et al. [70] on fly ash belite pastes showed that compressive strength declined at 28 days and 90 days with the addition of nano-silica. The trend went up only after 180 days. Senff et al. [71] studied the individual and combined addition of nano- $\text{SiO}_2$  and nano- $\text{TiO}_2$  in PC mortars. Unexpectedly, no significant increase of compressive

strength was observed in proposed methods of addition. But the hydration kinetics of mortars were greatly different in those with and without nano addition. The compressive strength from Shih et al. [72] also showed a complicated trend, which increased with addition of nano-silica and then decreased. The highest compressive strength was achieved at 0.6% addition of nano-silica at 56 days. Besides, the increase of compressive strength reached the largest, up to 60.6% compared with cement paste without the addition of nano-silica at the age of 14 days. But it was reduced to 43.8% at the age of 56 days. It was further clarified by nuclear magnetic resonance (NMR), nitrogen adsorption and mercury intrusion porosimetry (MIP) in which the microstructure of PC pastes with the addition of nano-silica had a denser and more stable framework. Berra et al.[73] also found that no significant improvement of compressive strength was achieved. The addition of nano-silica led to significant reduction of workability, which was overcome by the addition of superplasticizer. It was also believed that the addition of superplasticizer decreased the reactivity of nano-silica.

The studies show completely different results and the main reasons are still to be clarified. Kong et al. [74] ascribed less significant gain of compressive strength due to nano-silica agglomeration. The results showed that the addition of nano-silica and fumed silica refined the structure and pores. But the additional C-S-H that formed from agglomerates could not be treated as binder because the agglomerates that were formed were weak zones due to their low strength and elastic modulus. Further conclusions were drawn that microstructural improvement was a result of water absorption, filling and pozzolanic effects instead of seeding effects. Moreover, the large agglomerates of nano-silica absorbed less water than was predicted to improve the fluidity in pastes, instead of acting as fillers to release free water from voids [75]. The influence of primary particle size and sizes of agglomerates of amorphous nano-silica on UHPC were compared. The results confirmed that non-agglomerated silica particles

contributed to highest compressive strength at 7 days. The properties of UHPC may be improved through a better dispersion of silica., using, for example, commercial silica sols [76].

Nano-silica is a particularly new material in concrete. Increasing the surface reactivity using nano-silica can be promising in improving the structure and properties of cementitious materials. It is difficult to get a universal consistency of formula for the introduction of nano silica because size and composition of cementitious materials vary widely. Many contradictory results of strength improvement are also seen in literature reviews. This may be due to the agglomeration of nano-silica, which requires more research in the future.

## **2.4 Liquid Cell Transmission Electron Microscopy (LC-TEM)**

### **2.4.1 The Development of TEM to Image Liquids**

TEM is a powerful technique that provides structural and chemical information at the micro to atomic scale. A typical TEM sample has long been prepared as a stable solid-phase sample with a thickness of less than 100 nm, which allows electrons to transmit through the sample and scatter, giving important structural and chemical information. Recently, there has been an increasing demand to do liquid-phase analysis, which further reveals reaction mechanisms in nano scale, like nanoparticle nucleation and growth mechanisms. However, it is impossible for traditional TEM to do liquid analysis because all samples are exposed to a high vacuum environment, conducive to the free-space emission and transmission of electrons. [77].

Generally, two techniques were developed to achieve liquid imaging inside TEM while maintaining the right pressures for the electron source to operate. One method is the designed open cell that enables a high pressure in the sample region for liquid to condense by differential pumping. This is also known as environmental TEM or ETEM. The liquid sample is placed onto a supporting sample, where the sample is in contact with a large electrode [77, 78]. It is

still used in modern TEM for both gas-related and liquid reactions. The drawbacks of this technique are the uncontrolled liquid thickness and limited maximum pressure.

The second technique is designed to overcome the disadvantages of uncontrolled thickness in the open cell, as well as providing convenience of flowing liquid and heating. The idea is to separate liquid from microscope vacuum using a closed cell with robust, electron-transparent windows, which lead to good imaging resolution [79]. With the development of fabrication and thin film and MEMS technology, a closed cell can be made using thin silicon or silicon nitride windows that are deposited onto etched silicon wafers (shown in Figure 2-5). The liquid is confined between such two chips that has been glued, wafer-bonded or sealed mechanically in the holder with an O-ring [77]. Different sizes of reaction cells can be selected with different chip geometries and with various heights of spacers. Liquid flow is achieved through an inside channel, connected with inlets and outlets on the holder, which opens possibility for changing reaction chemistry. Electrochemical reaction experiments are performed using special chips as well. The system is tested for vacuum leaks before it is inserted into the microscope.

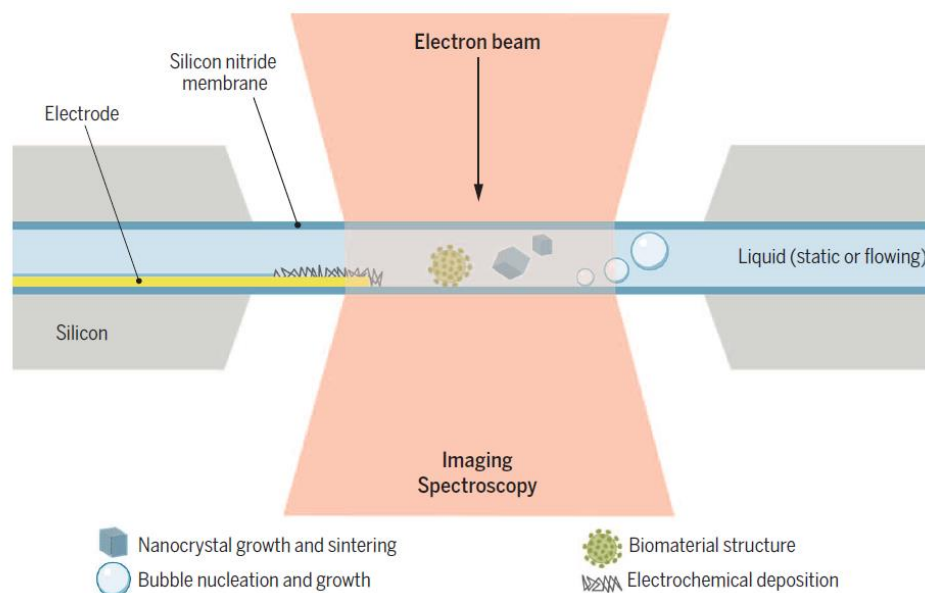


Figure 2.5 Schematic diagram of a liquid cell for transmission electron microscope [77].

New advancements make it possible to realize liquid reactions in TEM microscope. This allows more insights into the real-time transformation and reaction mechanisms in various fields, including electrochemistry, nanoparticle growth, liquid physics, and nano patterning [77, 80, 81].

#### **2.4.2 Electron Beam Effects**

The electron beam interactions with liquid sample must be understood before some conclusions are drawn from in-situ experiments in TEM. When a high-energy electron beam goes through a liquid sample, it may affect liquid reactions in several ways, including heating, radiolysis, and an imposing an electric field.

Heating is an important beam effect to take into account. Grogan et al. [82] estimated the temperature increase based on an assumption that beam-induced heat generation dissipate away from irradiated region. Then the heat is a function of the density of the irradiated medium and the volumetric dose rate, where the increase of either parameter contributes to higher heat generation. But the beam heating only leads to small temperature rises, like a few degrees or less, because a thick (hundreds of nanometers) liquid sample possesses relatively good thermal conductivity. This slight temperature rise may not be enough to cause a bubble effect [82], but the reaction kinetics observed in a liquid cell may be altered [80].

Understanding of radiolysis that involves the interactions of ionizing radiation with fluid medium is also necessary. Grogan et al. [82] also imaged bubble nucleation, growth and migration in water in the liquid cell, and quantified varying concentrations of radiolysis species with time and dimension using a simplified reaction-diffusion model. Different ionized species including hydrated electrons ( $e_h$ ),  $H_3O^+$ , H, OH,  $H_2$  and  $H_2O_2$  were considered, where gaseous products were probably responsible for bubble formation, while other products with high oxidizing and reducing properties accounted for modifying nanoscale reactions. The results

showed that the concentration of H<sub>2</sub> increased with electron beam time, and beam energy. It is found that ionized products like hydrogen and hydrated electrons achieve an equilibrium state within seconds. In the meantime, the highly reactive radiolysis product like the hydrated electron diffused only to short distance near the irradiated region, while gaseous products like H<sub>2</sub> diffused further. Schneider et al. [83] further proposed a mathematical model to compute the concentrations of radiolysis products as functions of electron beam irradiation parameters, time, space, and solution composition in typical electron microscopy. The concentrations of radiolysis products varied with time, where in homogeneous reactions, H<sub>2</sub> was formed with a higher amount than secondary product, O<sub>2</sub> with time in neat water. Also, the increase of dose rate contributed to the steady-state concentration of each type of radiolysis products. In heterogenous reactions where only a fraction of liquid in the cell was irradiated, gaseous products like H<sub>2</sub> and O<sub>2</sub> diffused out further from the center of the irradiated region while e<sub>h</sub><sup>-</sup> and H<sup>+</sup> only exhibited a high concentration within the irradiated region. The concentrations of radiolysis products were affected by the initial pH of liquid solution, especially in acidic (pH < 5) and alkaline (pH > 10) solutions. The steady-state concentrations of e<sub>h</sub><sup>-</sup> and O<sub>2</sub> decreased while H<sup>+</sup> and H<sub>2</sub> increased in acidic solution compared with that of pH = 7. In alkaline solutions, the steady state concentrations of e<sub>h</sub><sup>-</sup> and O<sub>2</sub> were lower and H<sub>2</sub> was higher. Gupta et al. [84] concluded that interfaces between water and surrounding surfaces led to a spatial variation in the energy absorbed by water near the walls. Because the walls behaved like a source of secondary and backscattered electrons to diffuse and deposit energy in water, the dose rate and local concentrations may be increased.

Another electron beam effect is the imposed electron field that varies in TEM and STEM circumstances due to different beam geometry. In a broad-beam illumination, the highest resolution of liquid cell imaging is achieved at the electron beam exit side of the sample. For STEM illumination, the highest resolution for an object within liquid sample occurs at the

entrance side of the sample [80]. Moreover, in a focused-beam STEM mode, positive charges mainly appear within the probed region, resulting in cylindrically symmetric field around the illuminated region, with a declining strength away from the region. However, in TEM mode, most positive charges accumulate in the surface region, such as the SiN membranes. The electric fields are much stronger near the surfaces and the edge of the beam [85]. In some cases, ion drift may happen if the electric field is strong enough to overcome the activation energy of the process. Then the nucleation and growth of nanoparticles are results of the relationship between self-diffusion and drift motion [86]. As a result, the variations of local compositions and supersaturation may happen due to the drifting cations and anions [85]. This will probably influence reaction chemistry and precipitation phenomenon.

In summary, the electron beam interacts with a liquid sample in the forms of heating, irradiation of radiolysis and ion drift induced by the electric field. Therefore, local concentrations and reaction kinetics may be altered in liquid cell electron microscopy. This also requires that careful attention and suitable procedures be taken to reduce the interactions between the electron beam and liquid solutions. A better understanding of electron beam effects with liquid will help interpret results and draw suitable conclusions.

### **2.4.3 Applications of LC-TEM in Different Materials Systems**

The advent of LC-TEM to achieve liquid reactions in real time allow new insights into many fundamental reactions and mechanisms. It is possible to obtain both chemical and structural information about materials, such as crystal structure from diffraction measurements, to chemical bonding from coupled energy dispersive spectroscopy (EDS) detector and electron energy loss spectroscopy (EELS) detector, though these are often hindered because of the large degree of scattering through 2 nitride windows and liquid, which often bows to a larger scattering through-thickness due to differential vacuum conditions between the SiN chip and the microscope column.

LC-TEM enables the examination of electrochemical processes including electrodeposition, interfacial electrochemical reactions in battery materials and nanoscale microstructural evolution of corrosion. Ross [87] realized the nucleation and growth of Cu nanoparticles on polycrystalline Au in the presence of complex electrolyte chemistry. The nucleation and growth were quantified based on diffusion models, which incorporated surface diffusion. Zhu et al. [88] investigated simultaneous nanocatalyst degradation and electrochemical response of Pt-Fe nanocatalysts using liquid cell electron microscopy. The coarsening processes of nanocatalyst particles are not uniform in space and time scale. The particles exhibited significantly different behavior after being attached to electrode compared with that of isolation in the electrolyte. This demonstrated that in-situ characterization of nanocatalysts with electrochemical bias were superior to ex-situ electrochemical studies. Jiang et al. [89] presented an in-situ study of dynamic dissolution process of palladium nanocrystals. The results showed that the dissolution rate increased with a decreasing radius in nanocrystals with radius lower than  $R_{critical}$ . For nanocrystals with radius of larger than  $R_{critical}$ , the dissolution rate was a constant. It is also promising for a variety of electrochemical process using liquid cell technique.

The processes of nanoparticle nucleation, growth and coalescence can be resolved. Evans et al. [90] visualized the lead sulfide nanoparticle growth using STEM imaging using LC-TEM. The overall growth rate was measured by examining different frames of a continuously acquired movie was estimated assuming growth occurs uniformly in all surfaces. The results also demonstrated that the final morphology of nanostructures was controlled based on growth mechanisms. Canepa et al. [91] clarified the growth phenomena of monodispersed size- and shape-controlled Au nanocrystals in the presence of surfactant. The role of surfactant in this process was also influenced by the STEM, where electron-induced radiolytic species acted as reductant. The results showed that the particle shape strongly depends on the surfactant at a

low dose circumstance. An increasing surfactant concentration contributed to a suppressed growth rate of Au nanocrystals. It was further concluded that nanoparticles conformed with a reaction-limited growth mechanism at low surfactant concentration, while a diffusion-limited mechanism dominated at a high surfactant concentration. Noh et al. [92] observed the dissolution of Ag and deposition of Ag under the beam in different conditions. The dissolution of Ag was caused by ionization from the primary beam, while the precipitation of Ag was through reduction of  $\text{Ag}^+$  by radiolytic electron species in the solution. The effects of activity of silver in solution and beam current density on relative rates were also incorporated into a model to describe chemical kinetics and minimize electron beam induced damage.

More in-situ experiments have been realized in biological processes as well, like biomineralization. Nielsen et al. [93] explored the process of calcium carbonate ( $\text{CaCO}_3$ ) nucleation in a liquid reaction cell. They recorded the nucleation of both metastable and stable phases that possessed the common morphologies. Various pathways of  $\text{CaCO}_3$  formation were revealed, either through solutions directly or indirectly through transformation of amorphous and crystalline precursors. The results showed real-time nucleation and growth mechanisms previously limited by characterization techniques. Smeets et al. [94] further researched into the role of matrix-immobilized acidic macromolecules in biomineralization and kinetic energy barriers of nucleation by liquid phase electron microscopy. The results exhibited that the binding of calcium ions to form Ca-PSS globules is a key step in the formation of metastable amorphous calcium carbonate (ACC). It also demonstrated that the films in both cases decreased the interfacial energy that determined the free-energy barrier to nucleate. It turned out that ion binding contributed most to the nucleation. Kröger and Verch [95] attributed the differences of the biomineralization results from in-situ TEM and those in bulk solutions to the spatial restriction of reacting within a liquid cell. 2D Finite Elements (FE) simulations were performed to study the impact of confinement on steady state concentration surrounding a

nanoparticle in a supersaturated solution. It was believed that the concentration of available ions in solutions was greatly reduced with confinement lower than a critical value, which decreased the stability of the precipitates.

Besides, the liquid physics and interactions of electron beam with liquid sample are important topics in liquid cell electron microscopy as well, as introduced in previous section. These new advances in hardware makes it possible to realize fundamental research and provide details into reaction mechanisms and kinetics.

#### **2.4.4 Perspectives for Geological Materials**

The understanding of hydration reactions is crucial for modifying reactions and designing reliable building materials. The research of geological and mineral materials with hydrated and anhydrous properties are restricted by research techniques [77]. In cement hydration reactions, the growth mechanisms of the most important hydrates, C-S-H have been debated for decades. Many researchers have devoted efforts in studying hydration reactions using various techniques, such as heat flow calorimetry, quantitative XRD, modelling, etc. One attempt of in-situ visualization technique was conducted by Katz et al. [96] using a self-designed capsule in SEM. The ettringite crystal evolution was resolved with time. However, the real-time changes of main hydrated products were not shown clearly, restricted by the resolution of SEM technique. The LC-TEM technique is promising in its ability to provide real-time structural and chemical information of hydrated products at the early stage. The research on nucleation and growth mechanisms of main hydrated products in cementitious materials is not only essential to understand hydration reactions, but also of commercial value. However, the application of LC-TEM on cement hydration reactions has not yet been reported.

## 2.5 Focused Ion Beam (FIB) and 3D Tomography

### 2.5.1 Introduction to the FIB-SEM System

FIB systems have become useful tools in last 25 years, originating from developments in semiconductor industry for mask repair and circuit edit applications. Dual beam FIB-SEM systems (Figure 2-6) that contain both an ion beam column and an electron beam column enable a site-specific ion milling and analysis in various fields of study [97]. Different dual-beam platforms have been developed, in which the ion column is typically mounted at an angle of  $45^\circ \sim 55^\circ$  from vertical electron column as well as orthogonally arranged FIB-SEM systems [98, 99]. This allows both precise site-specific sample milling and imaging through aligning two beams at a coincident point, taking the advantages of high energy ions and good resolution of electron imaging [100]. A typical ion beam resolution of 5 nm is achieved in a liquid metal  $\text{Ga}^+$  FIB instrument [101]. Coupled with an energy dispersive X-ray spectroscopy (EDS) detector or electron backscattered diffraction (EBSD) detector, more structural information can be obtained.

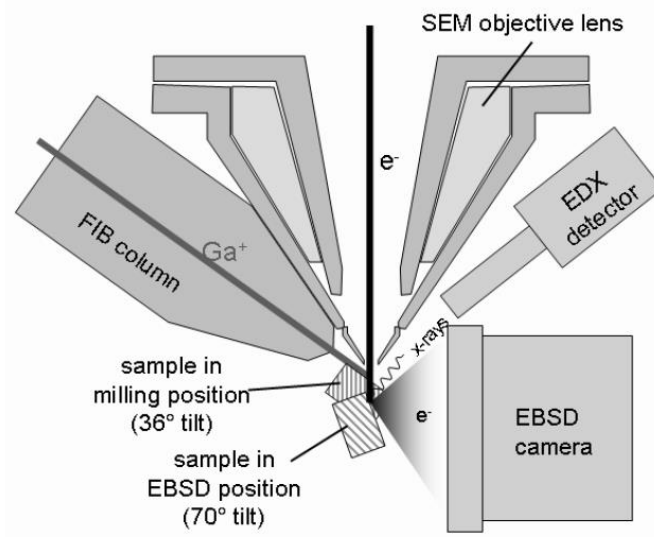


Figure 2.6 Schematic of dual-beam FIB-SEM system and geometry between columns and sample [102]

The application of FIB-SEM systems yields many advantages in localized milling and analysis, and site-specific TEM sample preparation. Secondary electron imaging is suitable to navigate to a region of interest as ion imaging may mill away the surrounding materials. Higher resolution imaging is possible using electron imaging, especially with different imaging contrast mechanisms, such as BSE electrons (sensitive to atomic number) and secondary electrons (sensitive to topography) [97]. Moreover, the preparation of polymer lamellae on glass is obtained with the advantage of a limited amount of preferential milling due to perpendicular relationship between ion beam and the sample [103].

Many studies have benefited from the site-specific FIB-SEM systems. King et al. [104] examined the surface of AA2024 and targeted corrosion products at specific sites in FIB-SEM instrument coupled with EDS detector. They concluded that the predominant attack modes were dealloying of S-phase particles, interfacial attack and grain boundary attack after characterizing FIB-prepared sample in TEM. Soldati et al. [105] prepared site-specific thin sample of cathode/electrolyte interface of intermediate temperature solid oxide fuel cells. The semi-coherent interface between LSCF and CGO was observed by TEM technique in the first time. Vieweg et al. [106] presented a FIB method by a shadow geometry of a platinum layer for site-specific cross-sectioning of nanoparticles, which were anisotropic. The nanoparticles were observed to obtain structural and chemical information with accuracy on the nanoscale. The 3D failure analysis [107] and large volume 3D imaging [108] were also proved to be applicable using FIB-SEM systems.

### **2.5.2 FIB Tomography and Instrumentation Setup**

The FIB tomography technique has been applied in various materials systems because dual beams enable both etching and subsequent imaging. This process can be repeated and is called serial sectioning. It enables the acquisition of 3-D structural and chemical information about

samples. To obtain a successful 3D tomogram, careful setups of sample geometry and software are needed.

In a typical FIB-SEM instrument, the sample is mounted at the eucentric point, where the converging angle is usually achieved by a pretilt holder and adjusted tilting angle. In this case, localized sample milling are completed through ion beam sputtering of the target material while the sectioned planes are imaged using electron beam [109]. Then a volume of interest (VOI) is prepared, in which a trench in front of the VOI and trenches on both sides must be prepared, allowing multiple acquisitions without shadowing effects. A protective layer, either Pt or C, is deposited on top of VOI and helps with surface roughness and VOI protection from ion beam damage [98]. Moreover, markers are prepared on the top and side of VOI so that a precise overlay of slices during tomogram post-acquisition image processing is guaranteed. Another layer of deposition can also be conducted to prevent markers for further erosion and reduce charging effects.

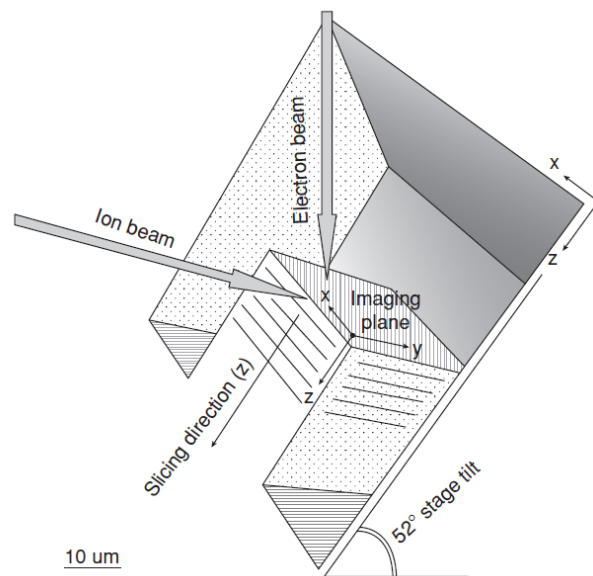


Figure 2.7 FIB tomography setup and serial sectioning direction using dual-beam system [110]

After the preparation of VOI, automated 3D sectioning setup can be performed as shown in Figure 2.7. The process of serial sectioning can be set automatically using software, where suitable parameters need be determined in advance. In some cases, a sample rotation of  $180^\circ$  to an EBSD detector is needed [111] when conducting EBSD acquisition as well, which depends on equipment setup [112]. It is also noted that a minimum number of 10 slices are required for a sufficient reconstruction of a granular texture [109]. Furthermore, it has been discussed that the BSE interaction volume has a huge influence on the effective resolution of FIB tomography. For example, a layer of 50 nm is not successfully resolved in a 5 keV BSE mode, which possesses an interaction volume of 100 nm [110]. This shows that depth penetration and imaging conditions must be considered for a reasonable step size. During serial sectioning, it is also necessary to correct beam shift, sample drift and changes in focal depth, which can be adjusted either manually or automatically [109].

The obtained image series (or stacks) need further corrections and alignment. After that, 3D reconstruction and segmentation can be performed to extract useful qualitative and quantitative information related to microstructure [113]. The images may appear to have artifacts like curtaining effects, which requires specific image processing algorithms to do some corrections before reliable results are achieved.

### **2.5.3 Curtaining Effect**

Dual-beam FIB-SEM systems provide capability for nano-tomography with nanometric resolution in mesoscale. However, one major challenge associated with ion milling or polishing is the so-called curtaining effect that refers to straight lines appearing on the cross section of the sample [98] as the result of preferential milling. If left long enough, the curtaining streaks actually change the milling front, with a 3-D wave-like morphology appearing on the surface. For serial sectioning experiments, curtaining may also give information from deeper areas of the sample (i.e. one is not imaging a planar milling front). Curtaining may result from

inhomogeneities of the material, such as internal porosity, surface roughness, or heterogeneous phases with different milling rates or ion channelling effects in different crystal orientations, as well as insufficient ion beam dose or divergent beam tail effects. [114, 115].

One solution to this problem is the application of post-acquisition curtaining removal algorithms. Early frequency-based attempts include zeroing k-space pixels in discrete Fourier space [116], which leaves an unwanted wavy pattern and smoothing of image and may not remove curtains entirely. Schankula et al. [117] introduced a flexible linear optimization model based on calculating the continuous Fourier coefficients for correcting multi-angle curtaining effects in FIB tomography. This method maybe not versatile on materials with severe porosity due to the relatively simple assumptions of the model. Fitschen et al. [118] proposed a new convex variational model for removing curtaining that the corrupted 3D image was split into a clean image and two kinds of corruptions, including a striped part and a laminar one. Recently, the low-rank-based single-image decomposition model was also implemented to separate the original image considering the structural characteristic of stripe and the image equally [116, 119].

The second solution to reduce curtains is through physical methods during the experiment. A rocking stage [120] or a goniometer stage [114] in a FIB-SEM system provide capability of sample rotating and thus the alternating of ion beam angle to effectively cut across the grain of the sample, resulting in better image quality. Also, sample preparation is crucial to obtain artifact-free image for segmentation. Taillon et al. [121] established a sample preparation workflow for porous materials that involved encasing the sample in a vacuum infiltrator, degassing under vacuum followed by epoxy impregnation to stabilize the porous structure. Gaboreau et al. [122] demonstrate that it was efficient to use methyl-methacrylate (MMA) resin to preserve the texture of a compacted clay material without modifying the pore space geometry for FIB and TEM imaging. Subramaniam et al. [123] developed a novel single-crystal

sacrificial mask method and allowed a high-quality milling finish using PFIB. The masking layer that served as a sacrificial protection tailored the beam, launched a planar milling front into the sample (thus protecting the material from materials curtaining due to sample surface roughness) and thus reduced material preferential artifacts during high current milling [123].

#### **2.5.4 Segmentation**

Segmentation is the process of identifying pixels in a 2D image or voxel in a 3D dataset and to classify them into a series of categories known as the label field. This classification can be performed based on the intensity of the pixel (for example corresponding to the backscattering coefficient, and thus the atomic number), or a combination of values associated with the pixels (such as a spectral map with windows), or based on geometric measures (the edges where large changes in contrast are detected as a gradient of the intensity adjacent to the pixels). This classification is necessary to enact, so as to extract and classify objects and to obtain statistically relevant structural information from a digitized dataset.

Image segmentation is a wide field of image processing, which is a subset of computer science and the signal processing field of electrical engineering. It is now commonly associated with medical imaging, but could be used for real-time video processing, geospatial information and many other fields. Simple image segmentation can be done by hand by a skilled operator who can identify features of interest. This is typically extremely time consuming, and generally relies on the attention span and biases of the image processor. More automated algorithms have been developed to aid in the segmentation of image. These include global and local thresholding of the images based on intensity contrast, to a more sophisticated clustering, or spatial-dependent methods, such as k-means clustering [124] and edge detection [125]. However, many of these methods suffer from intensity variance of the data, so pre-segmentation image processing is necessary to handle lighting corrections or depth-dependent intensity variations, as can occur with shadowing from redeposition in 3D FIB-SEM data

collection. A relatively new type of adaptive algorithm was developed on the idea that the boundary of an object is delineated through dynamical evolution and deformation of a curve [126, 127]. This contour-based segmentation depends on the regularity of boundary curve and corresponding grayscale values, which may lead to over-segmentation.

In recent years, the ground-breaking advancements of Convolutional Neural Networks (CNN) in deep learning have shown great promises in promoting image segmentation [128]. Machine learning typically requires a set of training data from the skilled user to identify a “correct” segmentation from training data, followed by testing of the dataset to ensure that the machine “learns” what is correct. Following an optimization of testing parameters, the machine has learned the correct method of segmenting the dataset, it can then be applied to a larger or different dataset. However, this degree of learning does inherit the biases of the training dataset.

The architecture of the CNN-based ML segmentation methods have the popular computational design of the U-Net architecture consisting of an encoder and a decoder network that are connected by skip connections [129]. U-Net and U-Net like models [129, 130] have shown impressive capability of tackling complicated segmentation problems even with a small amount of classified training data, which is promising to perform multi-modal segmentation tasks on 3D FIB-SEM dataset. Design and training of U-Net architectures are beyond the scope of the dissertation but a thorough review of machine learning as applied to microscopy data is provide here in [131]. In recent years, several software companies for image processing have integrated CNNs into user-friendly software packages, where the scientist optimizing some parameters, provides training data, and the CNN performs the segmentation in a relatively user-friendly but somewhat opaque manner.

### 2.5.5 FIB Tomography and Pore Characteristics

The development of FIB tomography facilitates the quantification of the microstructure and pore characteristics. It is crucial to characterize the pore network in different length scales, which are responsible for mass transport properties, including of salt-diffusion which leads to rebar corrosion for reinforced concrete, and mass transport of pore solution for hydration reactions in cement and concrete. Bera et al. [132] combined micro-computed tomography (CT) and focused ion beam tomography on Berea sandstone, which served as building block for precious hydrocarbon fuel and possessed interconnected micro-pores of 2 ~ 5  $\mu\text{m}$ . They concluded that small interconnected pores between 30 to 40  $\mu\text{m}$  connected with large voids between 100 to 250  $\mu\text{m}$  in the materials. Karwachi et al. [133] also characterized mesopores in steamed zeolites, which allowed a new quantitative insight into the characteristics of mesopores, such as length, width and morphology. The distribution of nanopores can also be obtained using FIB-SEM tomography [115, 134]. Porosity and pore characteristics were compared using different techniques, ranging from mercury intrusion porosimetry, micro-CT, FIB tomography, TEM tomography, where FIB tomography filled in the gap between micro-CT and TEM tomography and overcomes disadvantages of porosimetry, like ink neck-effects (a pore connected to external phase via a smaller pore, which acts as a neck ) [109, 135, 136].

The amount of information typically obtainable in a  $\text{Ga}^+$  FIB-SEM instrument is usually limited by ion milling rate. The advent of a new ion source of  $\text{Xe}^+$  ions in a plasma source configuration, allows milling at a higher current up to 2  $\mu\text{A}$ , which makes it possible for large-volume serial sectioning [137]. On the other hand,  $\text{Ga}^+$  ion source provides probe current up to several tens of nA, and the probe diameter increases dramatically after it reaches around 10 nA [98, 137]. Burnett et al. [138] concluded from comparison of serial sectioning in both  $\text{Ga}^+$  FIB and  $\text{Xe}^+$  FIB that it was 60 times faster and showed less artifacts on hard metals. VOI of hundreds of microns was achieved in less than 24h, which showed features as small as tens of

nanometers. Compared with  $\text{Ga}^+$  source,  $\text{Xe}^+$  source showed no trace of ion implantation. Xiao et al. [139] obtained higher strength of single crystalline aluminum micropillars, from  $\text{Xe}^+$  FIB operations instead of  $\text{Ga}^+$  FIB, which results in segregation of Ga at the grain boundaries and subsequent embrittlement. The advantages of emerging Plasma  $\text{Xe}^+$  FIB make it suitable for large volume 3D tomography of many kinds of materials.

### **2.5.6 Perspectives of 3D Tomography in Characterizing Pore Systems in Cementitious**

#### **Materials**

It is essential to acquire three-dimensional (3D) data for a better understanding of pore systems, which is critical to clarify microstructure-property relationship in cementitious materials. The pore structure properties, such as porosity, pore size distribution, and pore connectivity determine storage and transport characteristics of cement paste and concrete [140]. Traditionally, mercury intrusion porosimetry (MIP) has been applied to analyze pore distribution, which is strongly affected by ink-bottle effect [109, 141]. The micro computed x-ray tomography (CT) allows 3D structure visualization at micrometer resolution, where nanoscale pores cannot be visualized. 3D atom probe tomography and TEM tomography can also reconstruct structure with resolution less than 1nm [142]. However, many samples are needed since the sample for these techniques is less representative. Multiple techniques are needed to characterize multiple length scales of porosity because of the complexity and size distribution in cementitious materials.

Few studies on FIB tomography of cementitious materials have been reported. Holzer et al. [143] conducted statistical particle shape analysis of cement particles using FIB nanotomography (FIB-nt), which revealed structure information and particle-particle interface at submicrometric scale. This provided data for proposed processing method of particle size distribution, which were compared with that from laser granulometry [144]. Holzer et al. [145] also applied X-ray CT to examine 3-D shape cement particles between 20 to 60  $\mu\text{m}$  and FIB-

nt to check 3-D shape of cement particles between 0.4 to 2.0  $\mu\text{m}$ . It was found out that the shape of cement particles in the range of 0.4 to 60  $\mu\text{m}$  depended on size. However, research on hydrated cementitious materials, especially the interfaces between hydrated matrix and aggregates, and pore characteristics have not been conducted by FIB tomography. Furthermore, a reliable quantification of porosity of different scales and acquisition of pore networks are prerequisites for determining properties and designing new materials.

Focused ion beam (FIB) is a powerful technique to conduct 3D tomography with nanometric resolution. The new  $\text{Xe}^+$  plasma focused ion beam (PFIB) achieves 20-50 times higher sputtering and milling rates in given amount of time than  $\text{Ga}^+$  source machine [138]. This makes it a novel tool for material removal, serial sectioning and 3D tomography. It also remains better resolution using higher milling current compared with  $\text{Ga}^+$  FIB resulting from much stable probe size. This opens a new window for large volume serial sectioning with good resolution [98, 140]. It is very promising in making large representative 3D structures up to hundreds of microns where complex microstructures and multiscale pore networks can be analyzed in cementitious materials.

## 2.6 References

1. Mehta, P. and P. Monteiro, *M. Concrete: microstructure, properties, and materials*. 3rd. New York, 2006.
2. Pintér, F. and C. Gosselin, *The origin, composition and early age hydration mechanisms of Austrian natural Portland cement*. Cement and Concrete Research, 2018. **110**: p. 1-12.
3. Elsen, J., G. Mertens, and R. Snellings, *Portland Cement and other Calcareous Hydraulic Binders*, in *Advances in the characterization of industrial minerals*. 2010. p. 441-479.

4. Weber, J., K. Bayer, and F. Pintér, *Nineteenth century “novel” building materials: examples of various historic mortars under the microscope*, in *Historic Mortars*. 2012, Springer. p. 89-103.
5. Lothenbach, B., K. Scrivener, and R.D. Hooton, *Supplementary cementitious materials*. *Cement and Concrete Research*, 2011. **41**(12): p. 1244-1256.
6. Assi, L.N., et al., *Investigation of early compressive strength of fly ash-based geopolymer concrete*. *Construction and Building Materials*, 2016. **112**: p. 807-815.
7. Bhanumathidas, N. and N. Kalidas, *Dual role of gypsum: Set retarder and strength accelerator*. Vol. 78. 2004. 170-173.
8. Richardson, I., *The calcium silicate hydrates*. *Cement and concrete research*, 2008. **38**(2): p. 137-158.
9. Papatzani, S., K. Paine, and J. Calabria-Holley, *A comprehensive review of the models on the nanostructure of calcium silicate hydrates*. *Construction and Building Materials*, 2015. **74**: p. 219-234.
10. Scrivener, K.L., P. Juilland, and P.J.M. Monteiro, *Advances in understanding hydration of Portland cement*. *Cement and Concrete Research*, 2015. **78**: p. 38-56.
11. Brouwers, H.J.H., *The work of Powers and Brownyard revisited: Part I*. *Cement and Concrete Research*, 2004. **34**(9): p. 1697-1716.
12. Jennings, H.M., *A model for the microstructure of calcium silicate hydrate in cement paste*. *Cement and concrete research*, 2000. **30**(1): p. 101-116.
13. Jennings, H.M., et al., *A multi-technique investigation of the nanoporosity of cement paste*. *Cement and Concrete Research*, 2007. **37**(3): p. 329-336.
14. Allen, A.J., J.J. Thomas, and H.M. Jennings, *Composition and density of nanoscale calcium-silicate-hydrate in cement*. *Nat Mater*, 2007. **6**(4): p. 311-6.
15. Cuesta, A., et al., *Multiscale understanding of tricalcium silicate hydration reactions*. *Sci Rep*, 2018. **8**(1): p. 8544.
16. Taylor, H.F., *Proposed structure for calcium silicate hydrate gel*. *Journal of the American Ceramic Society*, 1986. **69**(6): p. 464-467.

17. Taylor, H.F.W., *Nanostructure of CSH: Current status*. Vol. 1. 1993. 38-46.
18. Richardson, I. and G. Groves, *Models for the composition and structure of calcium silicate hydrate (CSH) gel in hardened tricalcium silicate pastes*. cement and concrete research, 1992. **22**(6): p. 1001-1010.
19. Richardson, I. and G. Groves, *The incorporation of minor and trace elements into calcium silicate hydrate (CSH) gel in hardened cement pastes*. Cement and Concrete Research, 1993. **23**(1): p. 131-138.
20. Gartner, E.M., *A proposed mechanism for the growth of CSH during the hydration of tricalcium silicate*. Cement and concrete research, 1997. **27**(5): p. 665-672.
21. Minard, H., et al., *Mechanisms and parameters controlling the tricalcium aluminate reactivity in the presence of gypsum*. Cement and Concrete Research, 2007. **37**(10): p. 1418-1426.
22. Garbev, K., et al., *Cell Dimensions and Composition of Nanocrystalline Calcium Silicate Hydrate Solid Solutions. Part 1: Synchrotron-Based X-Ray Diffraction*. Journal of the American Ceramic Society, 2008. **91**(9): p. 3005-3014.
23. Zhang, L., et al., *Hydration for the Alite mineral: Morphology evolution, reaction mechanism and the compositional influences*. Construction and Building Materials, 2017. **155**: p. 413-426.
24. Bullard, J.W., et al., *Mechanisms of cement hydration*. Cement and Concrete Research, 2011. **41**(12): p. 1208-1223.
25. Garrault, S. and A. Nonat, *Hydrated layer formation on tricalcium and dicalcium silicate surfaces: experimental study and numerical simulations*. Langmuir, 2001. **17**(26): p. 8131-8138.
26. Nicoleau, L., M.A. Bertolim, and L. Struble, *Analytical Model for the Alite (C3S) Dissolution Topography*. Journal of the American Ceramic Society, 2016. **99**(3): p. 773-786.
27. Nicoleau, L. and A. Nonat, *A new view on the kinetics of tricalcium silicate hydration*. Cement and Concrete Research, 2016. **86**: p. 1-11.

28. Gartner, E., *Discussion of the paper "A new view on the kinetics of tricalcium silicate hydration," by L. Nicoleau and A. Nonat, Cem. Concr. Res. 86 (2016) 1–11.* Cement and Concrete Research, 2018. **104**: p. 114-117.
29. Bergold, S.T., F. Goetz-Neunhoeffler, and J. Neubauer, *Influence of the reactivity of the amorphous part of mechanically activated alite on its hydration kinetics.* Cement and Concrete Research, 2016. **88**: p. 73-81.
30. Quennoz, A. and K.L. Scrivener, *Interactions between alite and C3A-gypsum hydrations in model cements.* Cement and Concrete Research, 2013. **44**: p. 46-54.
31. Mota, B., T. Matschei, and K. Scrivener, *The influence of sodium salts and gypsum on alite hydration.* Cement and Concrete Research, 2015. **75**: p. 53-65.
32. Pustovgar, E., et al., *Influence of aluminates on the hydration kinetics of tricalcium silicate.* Cement and Concrete Research, 2017. **100**: p. 245-262.
33. Bergold, S.T., F. Goetz-Neunhoeffler, and J. Neubauer, *Interaction of silicate and aluminate reaction in a synthetic cement system: Implications for the process of alite hydration.* Cement and Concrete Research, 2017. **93**: p. 32-44.
34. Hesse, C., et al., *Quantitative in situ X-ray diffraction analysis of early hydration of Portland cement at defined temperatures.* Powder Diffraction, 2009. **24**(2): p. 112-115.
35. Álvarez-Pinazo, G., et al., *Rietveld quantitative phase analysis of Yeelimite-containing cements.* Cement and Concrete Research, 2012. **42**(7): p. 960-971.
36. Merlini, M., et al., *The early hydration and the set of Portland cements: in situ X-ray powder diffraction studies.* Powder Diffraction, 2007. **22**(3): p. 201-208.
37. Jansen, D., et al., *The early hydration of Ordinary Portland Cement (OPC): An approach comparing measured heat flow with calculated heat flow from QXRD.* Cement and Concrete Research, 2012. **42**(1): p. 134-138.
38. Hesse, C., F. Goetz-Neunhoeffler, and J. Neubauer, *A new approach in quantitative in-situ XRD of cement pastes: Correlation of heat flow curves with early hydration reactions.* Cement and Concrete Research, 2011. **41**(1): p. 123-128.

39. Ectors, D., et al., *In situ 1 H-TD-NMR: Quantification and microstructure development during the early hydration of alite and OPC*. Cement and Concrete Research, 2016. **79**: p. 366-372.
40. Hasanzadeh, B., F. Liu, and Z. Sun, *Monitoring hydration of UHPC and conventional paste by quantitative analysis on Raman patterns*. Construction and Building Materials, 2016. **114**: p. 208-214.
41. Wu, S., et al., *Quantitative invalidation characterization of Portland cement based on BSE and EDS analysis*. Construction and Building Materials, 2018. **158**: p. 700-706.
42. Ylmén, R., et al., *Early hydration and setting of Portland cement monitored by IR, SEM and Vicat techniques*. Cement and Concrete Research, 2009. **39**(5): p. 433-439.
43. Snellings, R., G. Mertens, and J. Elsen, *Supplementary Cementitious Materials*. Reviews in Mineralogy and Geochemistry, 2012. **74**(1): p. 211-278.
44. Aprianti, E., et al., *Supplementary cementitious materials origin from agricultural wastes – A review*. Construction and Building Materials, 2015. **74**: p. 176-187.
45. Paris, J.M., et al., *A review of waste products utilized as supplements to Portland cement in concrete*. Journal of Cleaner Production, 2016. **121**: p. 1-18.
46. Malagavelli, V. and P. Rao, *High performance concrete with GGBS and ROBO sand*. International journal of engineering science and technology, 2010. **2**(10): p. 5107-5113.
47. Yang, K.-H., et al., *Effect of supplementary cementitious materials on reduction of CO<sub>2</sub> emissions from concrete*. Journal of Cleaner Production, 2015. **103**: p. 774-783.
48. Berodier, E., K. Scrivener, and G. Scherer, *Understanding the Filler Effect on the Nucleation and Growth of C-S-H*. Journal of the American Ceramic Society, 2014. **97**(12): p. 3764-3773.
49. Taylor, R., I.G. Richardson, and R.M.D. Brydson, *Composition and microstructure of 20-year-old ordinary Portland cement–ground granulated blast-furnace slag blends containing 0 to 100% slag*. Cement and Concrete Research, 2010. **40**(7): p. 971-983.
50. Scrivener, K.L. and A. Nonat, *Hydration of cementitious materials, present and future*. Cement and Concrete Research, 2011. **41**(7): p. 651-665.

51. Antoni, M., et al., *Cement substitution by a combination of metakaolin and limestone*. Cement and Concrete Research, 2012. **42**(12): p. 1579-1589.
52. Mounanga, P., et al., *Improvement of the early-age reactivity of fly ash and blast furnace slag cementitious systems using limestone filler*. Materials and Structures, 2010. **44**(2): p. 437-453.
53. Oey, T., et al., *The Filler Effect: The Influence of Filler Content and Surface Area on Cementitious Reaction Rates*. Journal of the American Ceramic Society, 2013. **96**(6): p. 1978-1990.
54. Juenger, M.C.G. and R. Siddique, *Recent advances in understanding the role of supplementary cementitious materials in concrete*. Cement and Concrete Research, 2015. **78**: p. 71-80.
55. Wu, Z., et al., *Effects of different nanomaterials on hardening and performance of ultra-high strength concrete (UHSC)*. Cement and Concrete Composites, 2016. **70**: p. 24-34.
56. Van Tuan, N., et al., *Hydration and microstructure of ultra high performance concrete incorporating rice husk ash*. Cement and Concrete Research, 2011. **41**(11): p. 1104-1111.
57. Korpa, A., T. Kowald, and R. Trettin, *Phase development in normal and ultra high performance cementitious systems by quantitative X-ray analysis and thermoanalytical methods*. Cement and Concrete Research, 2009. **39**(2): p. 69-76.
58. Vaitkevičius, V., E. Šerelis, and H. Hilbig, *The effect of glass powder on the microstructure of ultra high performance concrete*. Construction and Building Materials, 2014. **68**: p. 102-109.
59. Gupta, S., *Application of Silica Fume and Nanosilica in Cement and Concrete – A Review*. Journal on Today's Ideas - Tomorrow's Technologies, 2013. **1**(2): p. 85-98.
60. Pacheco-Torgal, F. and S. Jalali, *Nanotechnology: Advantages and drawbacks in the field of construction and building materials*. Construction and Building Materials, 2011. **25**(2): p. 582-590.
61. Chen, X., et al., *A novel low temperature vapor phase hydrolysis method for the production of nano-structured silica materials using silicon tetrachloride*. RSC Advances, 2014. **4**(17).

62. Yu, R., P. Spiesz, and H.J.H. Brouwers, *Effect of nano-silica on the hydration and microstructure development of Ultra-High Performance Concrete (UHPC) with a low binder amount*. Construction and Building Materials, 2014. **65**: p. 140-150.
63. Jafarbeglou, M., M. Abdouss, and A.A. Ramezaniapour, *Nanoscience and Nano Engineering in Concrete Advances , A Review*. International Journal of Nanoscience and Nanotechnology, 2015. **11**(4): p. 263-273.
64. Singh, L.P., et al., *Beneficial role of nanosilica in cement based materials – A review*. Construction and Building Materials, 2013. **47**: p. 1069-1077.
65. Björnström, J. and I. Panas, *Antagonistic effect of superplasticizer and colloidal nano-silica in the hydration of Alite and Belite pastes*. Journal of materials science, 2007. **42**(11): p. 3901-3907.
66. Stefanidou, M. and I. Papayianni, *Influence of nano-SiO<sub>2</sub> on the Portland cement pastes*. Composites Part B: Engineering, 2012. **43**(6): p. 2706-2710.
67. Tobón, J.I., et al., *Mineralogical evolution of Portland cement blended with silica nanoparticles and its effect on mechanical strength*. Construction and Building Materials, 2012. **36**: p. 736-742.
68. Flores, Y.C., et al., *Performance of Portland cement pastes containing nano-silica and different types of silica*. Construction and Building Materials, 2017. **146**: p. 524-530.
69. Zapata, L.E., et al., *Rheological performance and compressive strength of superplasticized cementitious mixtures with micro/nano-SiO<sub>2</sub> additions*. Construction and Building Materials, 2013. **41**: p. 708-716.
70. Dolado, J.S., et al., *Effect of Nanosilica Additions on Belite Cement Pastes Held in Sulfate Solutions*. Journal of the American Ceramic Society, 2007. **0**(0): p. 070916231959005-???
71. Senff, L., et al., *Effect of nano-SiO<sub>2</sub> and nano-TiO<sub>2</sub> addition on the rheological behavior and the hardened properties of cement mortars*. Materials Science and Engineering: A, 2012. **532**: p. 354-361.
72. Shih, J.-Y., T.-P. Chang, and T.-C. Hsiao, *Effect of nanosilica on characterization of Portland cement composite*. Materials Science and Engineering: A, 2006. **424**(1-2): p. 266-274.

73. Berra, M., et al., *Effects of nanosilica addition on workability and compressive strength of Portland cement pastes*. Construction and Building Materials, 2012. **35**: p. 666-675.
74. Kong, D., et al., *Influence of nano-silica agglomeration on microstructure and properties of the hardened cement-based materials*. Construction and Building Materials, 2012. **37**: p. 707-715.
75. Kong, D., et al., *Influence of nano-silica agglomeration on fresh properties of cement pastes*. Construction and Building Materials, 2013. **43**: p. 557-562.
76. Oertel, T., et al., *Primary particle size and agglomerate size effects of amorphous silica in ultra-high performance concrete*. Cement and Concrete Composites, 2013. **37**: p. 61-67.
77. Ross, F.M., *Opportunities and challenges in liquid cell electron microscopy*. Science, 2015. **350**(6267): p. aaa9886.
78. Wang, C.-M., H.-G. Liao, and F.M. Ross, *Observation of materials processes in liquids by electron microscopy*. MRS Bulletin, 2015. **40**(01): p. 46-52.
79. Lee, H.-W., Y. Li, and Y. Cui, *Perspectives in in situ transmission electron microscopy studies on lithium battery electrodes*. Current Opinion in Chemical Engineering, 2016. **12**: p. 37-43.
80. de Jonge, N. and F.M. Ross, *Electron microscopy of specimens in liquid*. Nat Nanotechnol, 2011. **6**(11): p. 695-704.
81. Zheng, H. and Y. Zhu, *Perspectives on in situ electron microscopy*. Ultramicroscopy, 2017. **180**: p. 188-196.
82. Grogan, J.M., et al., *Bubble and pattern formation in liquid induced by an electron beam*. Nano Lett, 2014. **14**(1): p. 359-64.
83. Schneider, N.M., et al., *Electron–Water Interactions and Implications for Liquid Cell Electron Microscopy*. The Journal of Physical Chemistry C, 2014. **118**(38): p. 22373-22382.
84. Gupta, T., et al., *Spatially dependent dose rate in liquid cell transmission electron microscopy*. Nanoscale, 2018. **10**(16): p. 7702-7710.
85. Jiang, N., *Note on in situ (scanning) transmission electron microscopy study of liquid samples*. Ultramicroscopy, 2017. **179**: p. 81-83.

86. Ren, G. and Y.-T. Wang, *Saturated sodium chloride solution under an external static electric field: A molecular dynamics study*. Chinese Physics B, 2015. **24**(12).
87. Ross, F.M., *Electrochemical nucleation, growth and dendrite formation in liquid cell TEM*. Microscopy and Microanalysis, 2010. **16**(S2): p. 326-327.
88. Zhu, G.-Z., et al., *In Situ Liquid Cell TEM Study of Morphological Evolution and Degradation of Pt–Fe Nanocatalysts During Potential Cycling*. The Journal of Physical Chemistry C, 2014. **118**(38): p. 22111-22119.
89. Jiang, Y., et al., *Probing the oxidative etching induced dissolution of palladium nanocrystals in solution by liquid cell transmission electron microscopy*. Micron, 2017. **97**: p. 22-28.
90. Evans, J.E., et al., *Controlled growth of nanoparticles from solution with in situ liquid transmission electron microscopy*. Nano Lett, 2011. **11**(7): p. 2809-13.
91. Canepa, S.A., et al., *Influence of Cetyltrimethylammonium Bromide on Gold Nanocrystal Formation Studied by In Situ Liquid Cell Scanning Transmission Electron Microscopy*. The Journal of Physical Chemistry C, 2018. **122**(4): p. 2350-2357.
92. Noh, K.W., et al., *Challenges associated with in-situ TEM in environmental systems: The case of silver in aqueous solutions*. Ultramicroscopy, 2012. **116**: p. 34-38.
93. Nielsen, M.H., S. Aloni, and J.J. De Yoreo, *In situ TEM imaging of CaCO<sub>3</sub> nucleation reveals coexistence of direct and indirect pathways*. Science, 2014. **345**(6201): p. 1158-1162.
94. Smeets, P.J., et al., *Calcium carbonate nucleation driven by ion binding in a biomimetic matrix revealed by in situ electron microscopy*. Nat Mater, 2015. **14**(4): p. 394-9.
95. *Liquid Cell Transmission Electron Microscopy and the Impact of Confinement on the Precipitation from Supersaturated Solutions*. Minerals, 2018. **8**(2).
96. Katz, A., A. Bentur, and K. Kovler, *A novel system for in-situ observations of early hydration reactions in wet conditions in conventional SEM*. Cement and Concrete Research, 2007. **37**(1): p. 32-37.
97. Langford, R.M. and C. Clinton, *In situ lift-out using a FIB-SEM system*. Micron, 2004. **35**(7): p. 607-11.

98. Bassim, N., K. Scott, and L.A. Giannuzzi, *Recent advances in focused ion beam technology and applications*. MRS Bulletin, 2014. **39**(04): p. 317-325.
99. Hara, T., et al., *Application of orthogonally arranged FIB–SEM for precise microstructure analysis of materials*. Journal of Alloys and Compounds, 2013. **577**: p. S717-S721.
100. Giannuzzi, L.A., *Introduction to focused ion beams: instrumentation, theory, techniques and practice*. 2004: Springer Science & Business Media.
101. Giannuzzi, L.A. and M. Utlaut, *A review of Ga<sup>+</sup> FIB/SIMS*. Surface and Interface Analysis, 2011. **43**(1-2): p. 475-478.
102. Zaeferrer, S., S. Wright, and D. Raabe, *3D-Orientation Microscopy in a FIB SEM: A New Dimension of Microstructure Characterization*. Microscopy and Microanalysis, 2007. **13**(S02).
103. Langford, R.M., *Focused ion beams techniques for nanomaterials characterization*. Microsc Res Tech, 2006. **69**(7): p. 538-49.
104. King, P.C., et al., *FIB/SEM study of AA2024 corrosion under a seawater drop: Part I*. Corrosion Science, 2011. **53**(3): p. 1086-1096.
105. Soldati, A.L., et al., *High resolution FIB-TEM and FIB-SEM characterization of electrode/electrolyte interfaces in solid oxide fuel cells materials*. International Journal of Hydrogen Energy, 2011. **36**(15): p. 9180-9188.
106. Vieweg, B.F., et al., *TEM preparation method for site- and orientation-specific sectioning of individual anisotropic nanoparticles based on shadow-FIB geometry*. Ultramicroscopy, 2012. **113**: p. 165-170.
107. Altmann, F. and R.J. Young, *Site-specific metrology, inspection, and failure analysis of three-dimensional interconnects using focused ion beam technology*. Journal of Micro/Nanolithography, MEMS, and MOEMS, 2014. **13**(1).
108. Xu, C.S., et al., *Enhanced FIB-SEM systems for large-volume 3D imaging*. Elife, 2017. **6**.
109. Holzer, L., et al., *Three-dimensional analysis of porous BaTiO<sub>3</sub> ceramics using FIB nanotomography*. Journal of microscopy, 2004. **216**(1): p. 84-95.

110. Holzer, L. and M. Cantoni, *Review of FIB-tomography*. Nanofabrication Using Focused Ion and Electron Beams: Principles and Applications, 2012. **559201222**: p. 410-435.
111. West, G. and R. Thomson, *Combined EBSD/EDS tomography in a dual-beam FIB/FEG-SEM*. Journal of microscopy, 2009. **233**(3): p. 442-450.
112. Guyon, J., et al., *Advancing FIB assisted 3D EBSD using a static sample setup*. Ultramicroscopy, 2016. **161**: p. 161-7.
113. Salzer, M., et al., *A two-stage approach to the segmentation of FIB-SEM images of highly porous materials*. Materials Characterization, 2012. **69**: p. 115-126.
114. Loeber, T.H., et al., *Reducing curtaining effects in FIB/SEM applications by a goniometer stage and an image processing method*. Journal of Vacuum Science & Technology B, Nanotechnology and Microelectronics: Materials, Processing, Measurement, and Phenomena, 2017. **35**(6).
115. Liu, Y., et al., *Nano-Tomography of Porous Geological Materials Using Focused Ion Beam-Scanning Electron Microscopy*. Minerals, 2016. **6**(4).
116. Liu, S., et al., *A fast curtain-removal method for 3D FIB-SEM images of heterogeneous minerals*. J Microsc, 2018. **272**(1): p. 3-11.
117. Schankula, C.W., C.K. Anand, and N.D. Bassim, *Multi-Angle Plasma Focused Ion Beam (FIB) Curtaining Artifact Correction Using a Fourier-Based Linear Optimization Model*. Microscopy and Microanalysis, 2018. **24**(6): p. 657-666.
118. Fitschen, J.H., J. Ma, and S. Schuff, *Removal of curtaining effects by a variational model with directional forward differences*. Computer Vision and Image Understanding, 2017. **155**: p. 24-32.
119. Chang, Y., et al., *Remote sensing image stripe noise removal: From image decomposition perspective*. IEEE Transactions on Geoscience and Remote Sensing, 2016. **54**(12): p. 7018-7031.
120. Benkouider, A., et al. *Ultrafast nano-fabrication and analysis using Xe plasma-FIB-SEM microscope and its applications for Cu milling using the Rocking-stage*. in *European Microscopy Congress 2016: Proceedings*. 2016. Wiley Online Library.

121. Taillon, J.A., et al., *Improving microstructural quantification in FIB/SEM nanotomography*. Ultramicroscopy, 2018. **184**(Pt A): p. 24-38.
122. Gaboreau, S., J.-C. Robinet, and D. Prêt, *Optimization of pore-network characterization of a compacted clay material by TEM and FIB/SEM imaging*. Microporous and Mesoporous Materials, 2016. **224**: p. 116-128.
123. Subramaniam, S., et al., *A Comprehensive Approach Towards Optimizing the Xenon Plasma Focused Ion Beam Instrument for Semiconductor Failure Analysis Applications*. Microsc Microanal, 2017. **23**(4): p. 769-781.
124. Khalaf, W., et al., *A DC optimization-based clustering technique for edge detection*. Optimization Letters, 2016. **11**(3): p. 627-640.
125. Prill, T., et al., *Morphological segmentation of FIB-SEM data of highly porous media*. J Microsc, 2013. **250**(2): p. 77-87.
126. Imanli, H., et al., *Validation of a novel CARTOSEG segmentation module software for contrast-enhanced computed tomography-guided radiofrequency ablation in patients with atrial fibrillation*. Pacing Clin Electrophysiol, 2017. **40**(11): p. 1206-1212.
127. Lu, H., *X-ray Computed Tomography Assessment of Air Void Distribution in Concrete*. 2017.
128. Ronneberger, O., P. Fischer, and T. Brox. *U-net: Convolutional networks for biomedical image segmentation*. in *International Conference on Medical image computing and computer-assisted intervention*. 2015. Springer.
129. Ibtehaz, N. and M.S. Rahman, *MultiResUNet : Rethinking the U-Net architecture for multimodal biomedical image segmentation*. Neural Netw, 2020. **121**: p. 74-87.
130. Kohl, S., et al. *A probabilistic u-net for segmentation of ambiguous images*. in *Advances in Neural Information Processing Systems*. 2018.
131. Novikov, A.A., et al., *Deep sequential segmentation of organs in volumetric medical scans*. IEEE transactions on medical imaging, 2018. **38**(5): p. 1207-1215.
132. Bera, B., S.K. Mitra, and D. Vick, *Understanding the micro structure of Berea Sandstone by the simultaneous use of micro-computed tomography (micro-CT) and focused ion beam-scanning electron microscopy (FIB-SEM)*. Micron, 2011. **42**(5): p. 412-8.

133. Karwacki, L., et al., *Architecture-dependent distribution of mesopores in steamed zeolite crystals as visualized by FIB-SEM tomography*. *Angew Chem Int Ed Engl*, 2011. **50**(6): p. 1294-8.
134. Keller, L.M., et al., *On the application of focused ion beam nanotomography in characterizing the 3D pore space geometry of Opalinus clay*. *Physics and Chemistry of the Earth, Parts A/B/C*, 2011. **36**(17-18): p. 1539-1544.
135. Hemes, S., et al., *Multi-scale characterization of porosity in Boom Clay (HADES-level, Mol, Belgium) using a combination of X-ray  $\mu$ -CT, 2D BIB-SEM and FIB-SEM tomography*. *Microporous and Mesoporous Materials*, 2015. **208**: p. 1-20.
136. Chalmers, G.R., R.M. Bustin, and I.M. Power, *Characterization of gas shale pore systems by porosimetry, pycnometry, surface area, and field emission scanning electron microscopy/transmission electron microscopy image analyses: Examples from the Barnett, Woodford, Haynesville, Marcellus, and Doig units*. *AAPG Bulletin*, 2012. **96**(6): p. 1099-1119.
137. Jiruse, J., et al., *Combined plasma FIB-SEM*. *Microscopy and Microanalysis*, 2012. **18**(S2): p. 652-653.
138. Burnett, T.L., et al., *Large volume serial section tomography by Xe Plasma FIB dual beam microscopy*. *Ultramicroscopy*, 2016. **161**: p. 119-29.
139. Xiao, Y., et al., *Investigation of the deformation behavior of aluminum micropillars produced by focused ion beam machining using Ga and Xe ions*. *Scripta Materialia*, 2017. **127**: p. 191-194.
140. Yio, M.H., et al., *3D imaging of cement-based materials at submicron resolution by combining laser scanning confocal microscopy with serial sectioning*. *J Microsc*, 2015. **258**(2): p. 151-69.
141. Dewers, T.A., et al., *Three-dimensional pore networks and transport properties of a shale gas formation determined from focused ion beam serial imaging*. *International Journal of Oil, Gas and Coal Technology*, 2012. **5**(2-3): p. 229-248.

142. Cantoni, M. and L. Holzer, *Advances in 3D focused ion beam tomography*. MRS Bulletin, 2014. **39**(04): p. 354-360.
143. Holzer, L., et al., *FIB-Nanotomography of Particulate Systems—Part I: Particle Shape and Topology of Interfaces*. Journal of the American Ceramic Society, 2006. **89**(8): p. 2577-2585.
144. Munch, B., et al., *FIB-Nanotomography of Particulate Systems—Part II: Particle Recognition and Effect of Boundary Truncation*. Journal of the American Ceramic Society, 2006. **89**(8): p. 2586-2595.
145. Holzer, L., et al., *Shape Comparison between 0.4-2.0 and 20-60  $\mu\text{m}$  Cement Particles*. Journal of the American Ceramic Society, 2010.

### **3. Liquid Cell Transmission Electron Microscopy Reveals C-S-H Growth Mechanism during Portland Cement Hydration**

Peng Dong<sup>1</sup>, Ali Allahverdi<sup>2</sup>, Carmen M. Andrei<sup>3</sup> and Nabil D. Bassim<sup>1,3</sup>

1. Department of Materials Science and Engineering, McMaster University, 1280 Main St W, Hamilton, ON L8S 4L8, Canada

2. Cement Research Centre, School of Chemical Engineering, Iran University of Science and Technology, Narmak 16846 – 13114, Tehran, Iran

3. Canadian Centre for Electron Microscopy, McMaster University, 1280 Main St W, Hamilton, ON L8S 4L8, Canada

**Author contributions:** In chapter 3, the experiments and data analysis were conducted mostly by Mr. Peng Dong. Dr. Carmen Andrei helped with liquid cell transmission electron microscopy (LC-TEM) experiment. Dr. Ali Allahverdi and Dr. Nabil Bassim provided experimental design, important guidance, and discussion.

The manuscript was originally drafted by Mr. Peng Dong, edited, and revised to the final version by Dr. Ali Allahverdi, Dr. Nabil Bassim and Dr. Carmen Andrei. This chapter has been submitted to Nature Communications and under review.

## **Abstract**

C-S-H is the main product of the cement hydration reactions and contributes to the binding properties in concrete, in which ordinary Portland cement (OPC) reacts with water to form a solid structure. Early-stage C-S-H growth mechanisms have been debated for several decades. Many efforts have been devoted to the two main hypotheses whether C-S-H grows according to colloidal agglomeration or layered structure precipitation and growth models. We report the first application of in-situ liquid cell transmission electron microscopy (LC-TEM) to research hydration reactions of nano PC, providing nanoscale insight into early liquid-based reaction mechanisms. We demonstrate that the formation and growth of C-S-H precipitates starts through lateral growth of planar silicate sheets, but soon continues in all directions resulting in a 3D microstructure. Furthermore, nanocrystalline C-S-H structures with sizes between 5 nm to 10 nm were observed inside the amorphous or highly disordered C-S-H matrix, denoting that C-S-H growth is conformed with layered structure models. Crack formation and propagation inside C-S-H precipitates confirms the presence of increasing lattice strain due to growing defects that limits the growth of a fully crystalline structure by buckling and separating the sheets. The rolling up and crumbling of C-S-H precipitates promotes the formation of new embryos and later aggregation of building blocks, which is consistent with a colloidal model as well. The hydration reactions of nano PC in liquid cell are very similar to known reactions in real mortar and concrete samples in terms of microstructure and phase developments, lending confidence to a clearer elucidation of C-S-H formation.

**Keywords:** Liquid cell transmission electron microscopy, Portland cement, Hydration, C-S-H growth mechanism

### 3.1. Introduction

Cements and concretes are the most widely used construction materials on the planet. The chemistry and manufacturing processes have attracted much attention recently due to the energy intensive nature of their fabrication and the potential for addressing greenhouse gas emissions in the industrial materials space. Cements rely on a series of hydration reactions to convert cement powder into a strong hardened paste that binds structures together. Understanding, at the nanoscale, these hydration reaction mechanisms and the formation of its predominant product, calcium-silicate hydrates (C-S-H) can lead to new pathways to design of greener, stronger and more durable cementitious construction materials.

Hydration reactions of OPC have been studied for several centuries since Portland cement was patented in Britain in 1824. Still, they are rather complex and remain a target of optimization for materials improvement. Their complexity arises because OPC contains four main constituents, namely tricalcium silicate ( $3\text{CaO}\cdot\text{SiO}_2$ , known as  $C_3S$ , where C is CaO and S is  $\text{SiO}_2$ ), dicalcium silicate ( $2\text{CaO}\cdot\text{SiO}_2$ ,  $C_2S$ ), tricalcium aluminate ( $3\text{CaO}\cdot\text{Al}_2\text{O}_3$ ,  $C_3A$ , where A is  $\text{Al}_2\text{O}_3$ ) and tetra-calcium aluminoferrite ( $4\text{CaO}\cdot\text{Al}_2\text{O}_3\cdot\text{Fe}_2\text{O}_3$ ,  $C_4AF$ , where F is  $\text{Fe}_2\text{O}_3$ ), a few percent of gypsum which acts as set regulating agent and other minor minerals [1, 2]. Post hydration, OPC forms hydration products like calcium silicate hydrates (C-S-H), Portlandite ( $\text{Ca}(\text{OH})_2$ ), ettringite ( $(\text{CaO})_3\cdot\text{Al}_2\text{O}_3\cdot(\text{CaSO}_4)_3\cdot(\text{H}_2\text{O})_{32}$ ), and calcium monosulfate ( $(\text{CaO})_3\cdot\text{Al}_2\text{O}_3\cdot\text{CaSO}_4\cdot(\text{H}_2\text{O})_{12}$ ) or monocarbonates [2]. The initial hydration reactions of  $C_3S$  to form C-S-H are particularly crucial to early microstructure and strength development [2]. C-S-H nucleation and growth in early stages follow a known reaction pathway ( $C_3S$  dissolution, induction, acceleration, and deceleration periods) for the first few to 24 hours [3]. It is well understood that C-S-H is not completely amorphous due to precipitation and densification of silicate ions to form short chains, resulting in a short-order arrangement of atoms [4]. However,

the details of the growth mechanism of C-S-H has been debated for a century without resolution. The first attempt to clarify formation mechanisms relied on a colloidal theory in 1918 [5].

Many models of microstructural evolution are mainly based on two different hypotheses, one based on the aggregation of nano C-S-H particles or other basic building blocks together [3, 6, 7] and the other based on formation and growth of planar defective sheets of silicate layers through attachment of silicate tetrahedra from solution [3, 8]. The colloidal hypothesis proposed that C-S-H is comprised of colloidal particles with dimension between 1 and 100 nm [9-11]. The composition and mass density were calculated, which helped to figure out C-S-H gel microstructure in a fine size and high surface area [6].

By contrast, early concepts of layered structure synthesis assumed that C-S-H is similar to imperfect jennite and 1.4 nm tobermorite that are natural calcium silicate hydrate minerals, consisting of layers of Ca-O sandwiched between polymeric silicate anions. [12-14], and a constitutional model was also proposed, which is related to the nature and relative proportions of molecules and ions [13, 15, 16].

Further hypotheses and experimental work also tried to clarify the nanocrystalline nature of C-S-H [17, 18]. It has been reported that tricalcium silicate transforms during hydration into nanocrystalline C-S-H gel exhibiting disk-like morphology by transmission electron microscopy (TEM) imaging [17, 19, 20]. Both simulations [21] and ensemble measurements provide insights into silicate chains morphology in C-S-H gel [4, 17], and showed that the dominant pattern was linear silicate chain structure [22]. Locally, by combining cryo-TEM and small angle X-ray scattering, Krautwurst et al. [23] captured C-S-H metastable structure in liquid and spherical particles at nanoscale, and ascribed the formation of amorphous precursor to kinetic effects in early hydration.

To capture the microstructural evolution as it happens, soft X-ray spectromicroscopy has also been applied to in-situ alkali-silicate reaction (ASR) gel formation [24]. Gartner et al. [25]

researched C-S-H growth mechanisms using soft X-ray microscopy experiments on silica particles in saturated  $\text{Ca}(\text{OH})_2$  solution with NaOH and  $\text{CaCl}_2$  solution to study C-S-H growth, and concluded that the C-S-H dendrites were oriented about a single common axis, indicating the origination from a common initial nucleus. Juenger et al. [26] investigated the hydration reactions of  $\text{C}_3\text{S}$  in a solution containing  $\text{CaCl}_2$  using soft X-ray transmission microscopy and found that  $\text{CaCl}_2$  accelerated hydration reactions and observed fibrillar hydration products from both inside and outside the  $\text{C}_3\text{S}$  grain. However, the C-S-H growth mechanisms were discussed based on indirect evidence in model cement systems with salt addition, and the nature of hydrated products was not fully clarified. Still, the exact mechanisms of C-S-H formation in Portland cement and direct evidence in liquid reactions are yet to be revealed.

Over decades many researchers have attempted to clarify hydration products and reaction mechanisms. Thermodynamic models have been established in understanding the interactions between different cement compositions and structure of hydration products as well as cement hydration kinetics [27-29]. The application of new materials characterization techniques including quantitative (in-situ) X-ray powder diffraction (XRPD) [30-33], heat flow calorimetry [32, 34], scanning electron microscopy (SEM) [22, 35, 36] as well as other techniques [37-39] provide insight into these mechanisms. Despite these advancements, the details of nucleation and growth mechanisms with structural and chemical information in early hydration reactions *at the nanoscale* needs further elucidation.

Recent advances in TEM imaging of liquid-based nucleation and growth in solutions have found traction in such systems as lithium battery reactions and biomineralization [40-42] by embedding a reactive solution between a pair of closed silicon-based chips [42-44]. The microstructure evolution in liquid is imaged through two SiN windows, typically 20 to 100 nm thick and supported by Si [44]. This local environment is shielded from the vacuum of the electron microscope, while remaining transparent to the electron beam. LC-TEM has benefited

many research areas, including electrochemistry, nanoparticle growth, fluid physics, and biological mineralization and living cells [42, 45-50]. The authors' previous work demonstrated the feasibility of LC-TEM in cement hydration reactions [51]. Even though many liquid phase reactions have been conducted using this technique, the application of LC-TEM on hydration reactions of OPC has not yet been reported.

In this paper, we report the application of LC-TEM technique on hydration reactions of nano-PC for the first time. To perform the reactions in microchips, nano-PC was prepared in the form of a sufficiently dilute cement slurry, compatible with imaging conditions. This solution was anticipated to be a lime saturated slurry to avoid C-S-H dissolution [3]. Hydration reactions were monitored up to 24 h and real-time changes of the main hydration products, ettringite and C-S-H were captured in early-stage liquid reactions. Complementary studies by ex-situ TEM (i.e. high-resolution TEM, electron diffraction) and SEM with energy dispersive spectroscopy (EDS) were also performed to confirm the hydration products, such as ettringite, C-S-H, Portlandite and monosulfate. Figure 3.1 shows a schematic of cement hydration reactions inside liquid cell. Our results support the hypothesis that C-S-H grows in the form of defective sheets of silicate layer. The nanocrystalline C-S-H precipitates exhibit a similar structure as poorly crystallized tobermorite. This work provides direct evidence of the formation of the main hydration products and new insights into the theory of C-S-H nucleation and growth mechanisms.

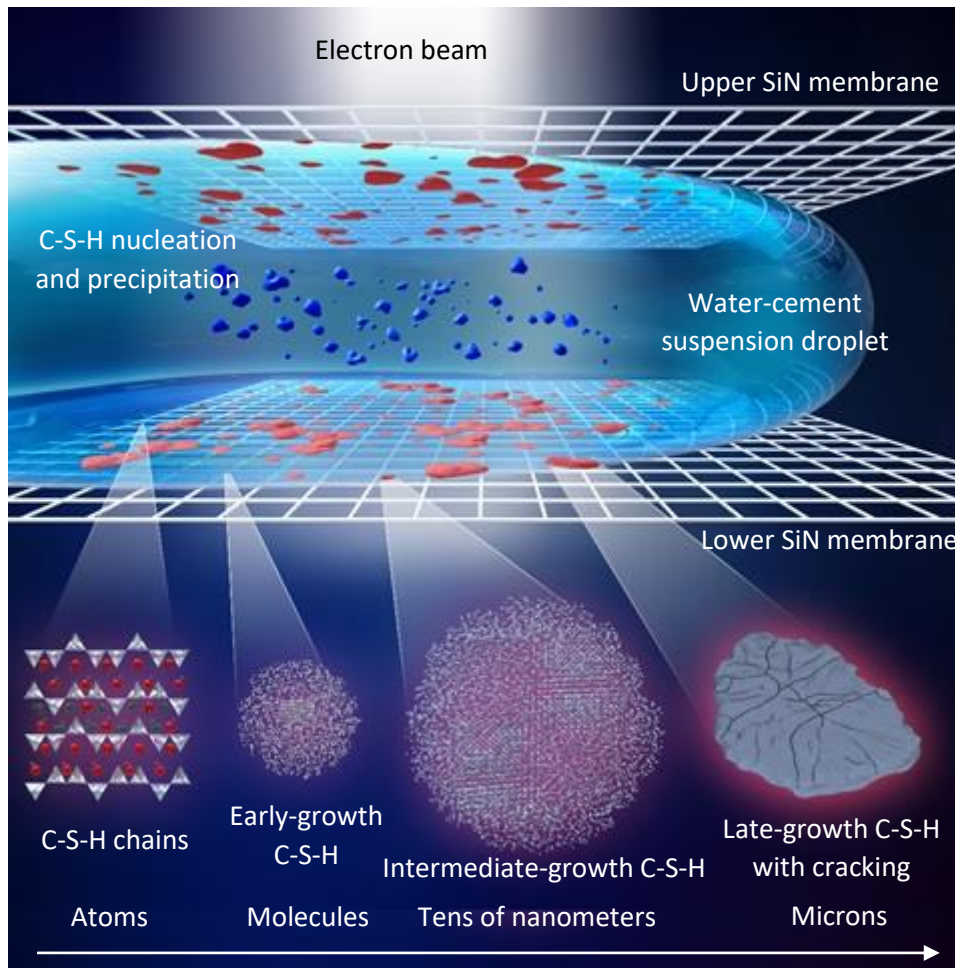


Figure 3.1 Schematic of liquid cell configuration within the TEM demonstrating C-S-H nucleation and growth on the SiN membranes during cement hydration:  $\nabla$  stands for silica tetrahedra,  $\bullet$  for CaO,  $\bullet$  for water, the blue particles away from SiN membranes are dissolving cement particles.

## 3.2. Methods

### 3.2.1 As – received OPC

The OPC with a mineralogical composition given in Table 3.A1 was from commercial product. The average particle size of 45  $\mu\text{m}$  was too large for liquid cell microchips and therefore further processing was needed to reduce the particle size.

### 3.2.2 Ball Milling and Nano PC

The purpose of ball milling is to reduce particle size, which is vital to a successful experiment. By using larger cement particles, there is a risk of breaking the SiN membranes of the chips, hence breaking the vacuum in the microscope. Furthermore, thick particles are not

electron transparent for TEM observation. By experimenting with different types of spacers and chips, we found out that using a chip – containing a microwell 4x8 array (EPT 42A2-10, Protochips Inc., Raleigh, NC, USA) as a large chip and 150 nm spacer for the small chip (EPB-55DF-10) was the best solution. A compromise of sufficient space in the cell and good resolution needs to be reached. The chips with larger spacers accommodate more reactants with the sacrifice of good resolution [40, 42, 52]. Therefore, more advantages are seen to use solid material with smaller particle size.

A three – stage ball milling operation was applied to reduce the particle size of OPC effectively. The first stage was to use relatively large corundum balls (10 mm diameter) to grind cement for 14 days. The subsequent grinding stage was achieved using smaller zirconia balls (4 mm diameter), for another 32 days. Both stages were conducted in the presence of anhydrous ethanol, which aimed at dispersing cement particles and minimizing friction heat. The particle size distribution of nano PC in terms of particle number after milling was conducted by Particle Size Analyzer (Horiba CAPA-700) followed by the confirmation of TEM imaging. After achieving a suitable particle size distribution (Figure 3.A1) at the end of the second milling stage, the cement-ethanol slurry was dried at 70 °C on a hot plate. In the last stage, the cement aggregates formed during drying were milled again with zirconia balls for up to 3 days. It appeared that 97.6% of PC particles were below 500 nm, 83.0% below 200 nm and 66.3% below 50 nm.

### **3.2.3 Water/cement (w/c) Ratio**

As mentioned, it is necessary that many strict requirements be satisfied to achieve desired reactions successfully in LC-TEM. It is commonly accepted that w/c ratio can be controlled at values as low as less than 0.20 for superplasticized cement pastes and to values as high as 0.50 for cement slurries [53-55]. In LC-TEM, however, the electron beam must transmit through the sample, which forces the sample to be a highly diluted slurry rather than a paste. After a

few attempts, we concluded that a dilute cement suspension with w/c ratio of 15 is reasonable for liquid cell tests and also is enough concentrated so that partial hydration of nano PC saturates the solution with  $\text{Ca}(\text{OH})_2$  to avoid C-S-H dissolution. Thus, 0.2 g nano PC was mixed with 3 ml deionized water in a glass vial, followed by sonication for 5 min. The mixing time that was the starting time of hydration reactions, was recorded. After large particles settled down at the bottom of the vial, a 2  $\mu\text{l}$  drop was taken using micropipette and put on the window of the small chip.

### **3.2.4 Liquid Cell Preparation and In-situ Imaging**

Both chips were rinsed in acetone and methanol for 2 min to remove a photoresist protective coating. 2  $\mu\text{l}$  drop of cement suspension was put on a small bottom chip (we already described the types of the chips above). On top, a large chip with individual microwells was used to seal the cell. This allowed a maximum liquid thickness of almost 250 nm. By aligning the microwells carefully, up to four wells were present for in-situ imaging. The liquid holder was checked for leaks under vacuum before it was inserted into the microscope. The real time imaging was performed using a Titan microscope (ThermoFisher-FEI Titan) operated at 300 kV in TEM mode. The average screen current was 1.21 nA. Different areas of interest (AOI) were tracked to study microstructure evolution in a 24-hour interval. To minimize the beam effects on hydration reactions, the beam was not kept for more than 3 s on a specific AOI. The LC-TEM experiments were performed at total of 5 times with 2 failed experiments, in which similar results were obtained with regards to microstructure evolution and timing of the reaction process in all experiments. We started from chips with spacer thickness of 5  $\mu\text{m}$ , 500 nm and arrived at optimal imaging conditions with chips with spacer thickness of 150 nm, with which the LC-TEM experiments were repeated 3 times. Among each experimental dataset, as the timing and hydrated products were observed and the data within the manuscript is representative of these repeatable experiments.

### **3.2.5 Post-situ TEM Imaging and Diffraction Patterns**

The liquid cell chips were taken out and totally dried at different time steps in the reaction process before post-situ experiment was conducted. The post-situ characterization was performed on the small chip using a JEOL 2010F operated at 200kV. TEM images of microstructures and diffraction patterns were obtained.

### **3.2.6 Scanning Electron Microscopy and Energy Dispersive Spectroscopy**

The chips were coated with 10 nm carbon and studied by scanning electron microscopy with energy-dispersive x-ray spectroscopy (SEM-EDS) in a JEOL 7000 microscope operated at 9 keV. The SEM images and EDS data were acquired on key features. The results provided information to confirm the microstructures and chemical compositions that were observed in liquid cell.

## **3.3. Results**

The hydration reactions started at the very first moment that nano PC comes in contact with water. With 150 nm spacers on small chip and 170 nm thickness of microwell in large chip, the thickness of the reaction cell is up to 320 nm without the bulging effect that provides enough room for hydrated products to develop in 3D. Needle-like ettringite crystals (shown by arrows) formed due to the aluminate reaction were clearly observed. Typical formation of ettringite crystals was captured (Figure 3.2 (a)) 1 h 47 min after mixing. More ettringite crystals with precipitates nucleated closed to the needles were observed in different regions at about 3 hours after mixing, as shown in Figure 3.2 (b) and (c). This demonstrates that ettringite crystals act as nucleation sites for other precipitates as well. The chemical compositions of a needle-like crystal and the adjoining hydration product were examined and verified to be ettringite and monosulfate by SEM and EDS (Figure 3.A2).

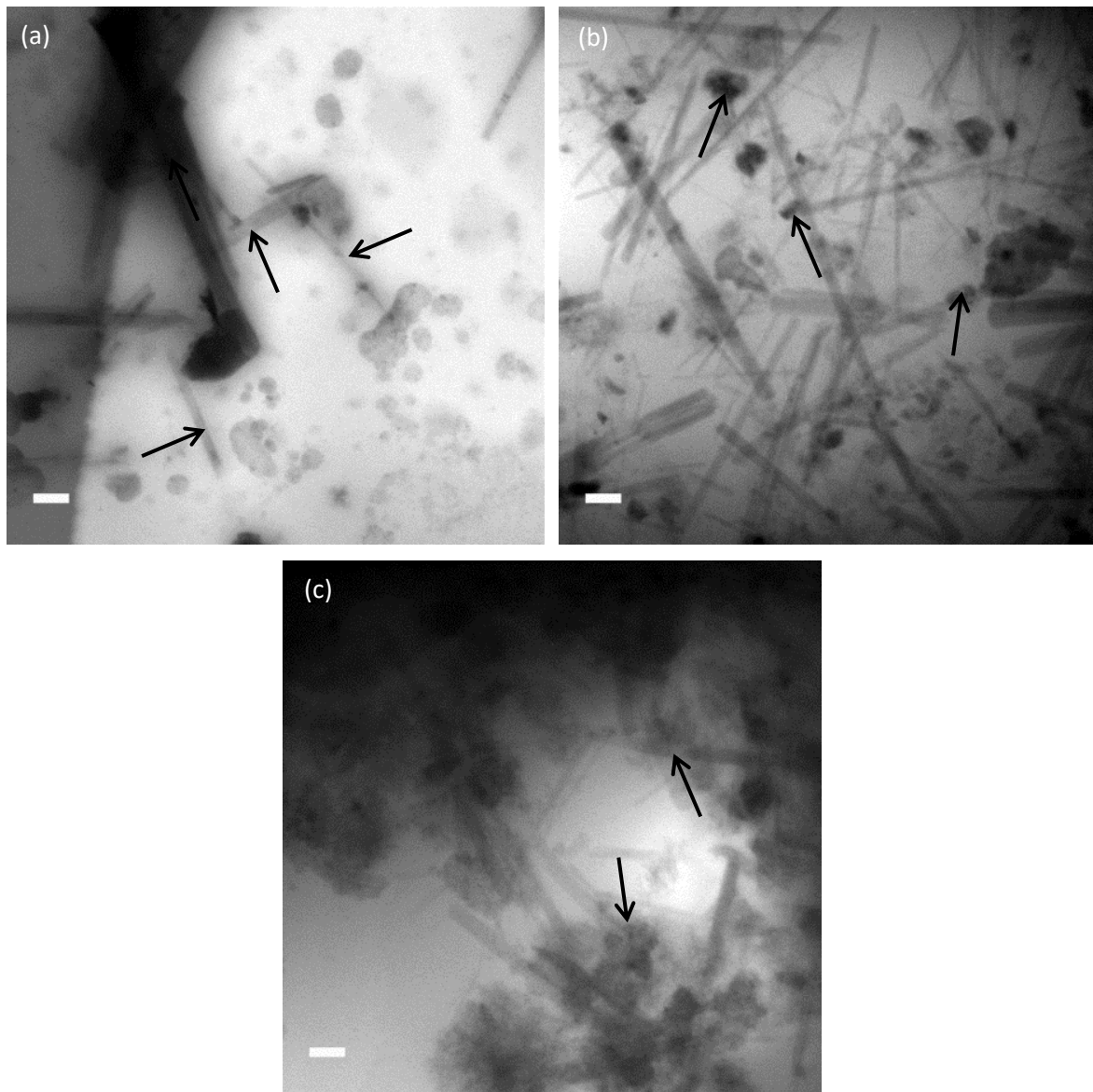
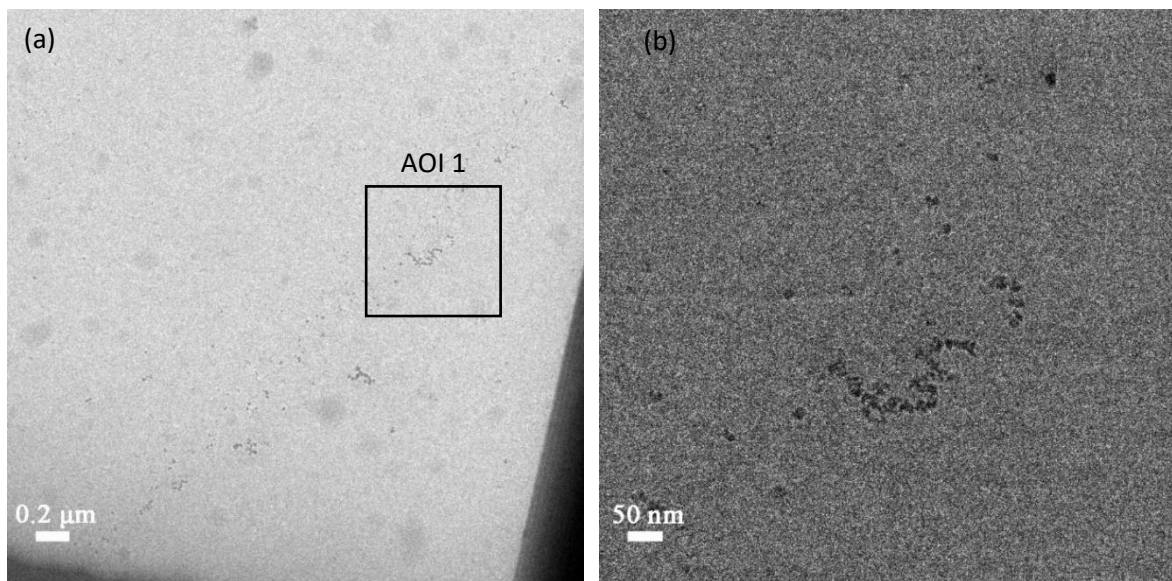


Figure 3.2 Needle-like ettringite crystals in liquid cell TEM (a) 1 h 47 min, (b) 2 h 29 min and (c) 2 h 45 min (scale bars, 0.5 $\mu$ m)

The effective nucleation of C-S-H effectively starts following an induction period from the mixing time ( $t = 0$ ). The real-time nucleation and primary growth of C-S-H precipitates at early and intermediate hydration stages were also captured and shown in Figure 3.3 (a) to (d). C-S-H nucleation started with the appearance in the microwell of a few C-S-H embryos. Figure 3.3 (b) is an enlarged image of AOI 1 in Figure 3.3 (a) showing 5 to 10 nm in size embryos. Around 3 h 50 min from mixing time, C-S-H nucleation and growth was still observed with more C-S-H precipitates nucleated on the SiN membrane (Figure 3.3 (c)). These precipitates were not observed to have drifted or agglomerated in solution and assembled colloiddally. Some

precipitates were as small as 5 nm to 10 nm, while some grew as large as 20 nm to 30 nm, as seen in Figure 3.3 (d). It was noticed that well-defined C-S-H precipitates nucleated mostly on the SiN membrane. This was because the membrane and the walls of LC chips provided more nucleation sites for heterogeneous nucleation of C-S-H by lowering the surface energy. The C-S-H precipitates were also examined post situ. After opening the microchips, we were able to obtain some individual C-S-H precipitates at their intermediate growth stage with sizes varying from 20 nm to 110 nm (Figure 3.3 (e)). However, it shows a different C-S-H morphology that is similar to particle aggregation. Also, some large C-S-H precipitates joined together to form a network. The C-S-H precipitates as large as 0.6  $\mu\text{m}$  to 0.8  $\mu\text{m}$  in their intermediate stage were observed in Figure 3.3 (f). It is worth mentioning that these precipitates were completely irregular in their microstructure.



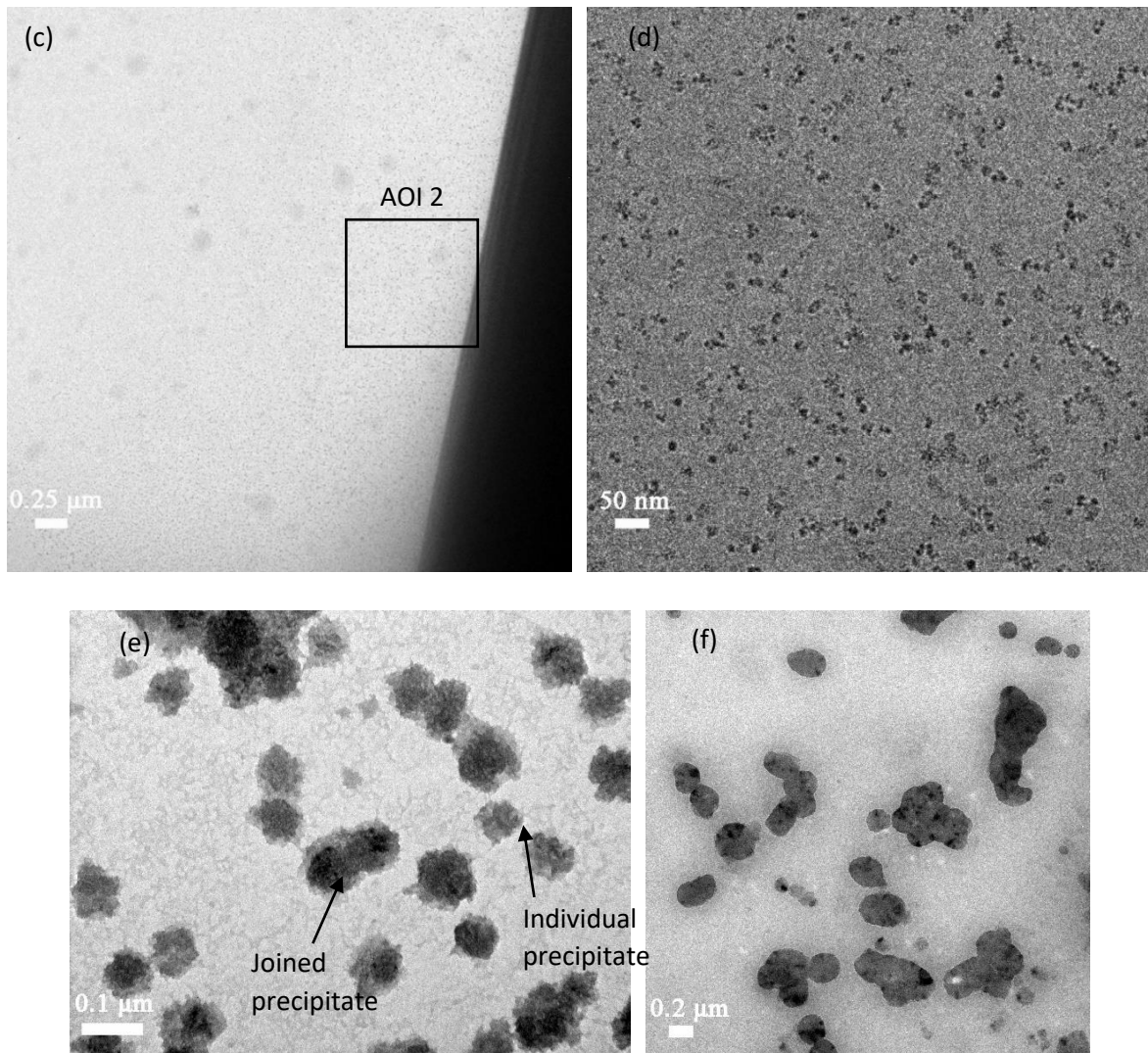


Figure 3.3 C-S-H nucleation and primary growth on the membrane of liquid cell chips during induction period: (a) at 3 h 09 min, some newly formed embryos in the microwell, (b) higher magnification of C-S-H embryos from (a) AOI 1 with sizes as small as 5 nm to 10 nm. (c) Continued C-S-H nucleation and growth at 3 h 48 min, and (d) some embryos from (c) AOI 2 were as small as 5 nm to 10 nm, while some grew quickly to 20 nm to 30 nm, and (e) TEM image from LC chip after opening and drying, showing individual and joined C-S-H precipitates at their primary growth stage with completely disordered microstructures, (f) LC-TEM image showing early growth and coalescence of C-S-H disk-like precipitates with sizes of 0.6  $\mu\text{m}$  to 0.8  $\mu\text{m}$  in their intermediate stage.

Figure 3.4 (a) shows C-S-H precipitates with two different morphology after opening the chips. The morphology of C-S-H in the center indicated that C-S-H developed through particle aggregation. The C-S-H precipitates at intermediate growth stage in the boxed area of Figure 3.4 (a) were analyzed in the HRTEM image in Figure 3.4 (b). Lattice fringes surrounded by amorphous matrix (marked areas) were observed. This indicates the presence of C-S-H nanocrystals inside the amorphous C-S-H matrix. The well-ordered structures were within the

order of 5 nm to 10 nm, beyond which disordered arrangements of atoms were built in the microstructure. These displacements and defects could provide more sites for heterogeneous nucleation. As a result, lattice strain was also built in the C-S-H precipitates. This alternation of nanocrystalline and amorphous regions confirmed the layered structure model.

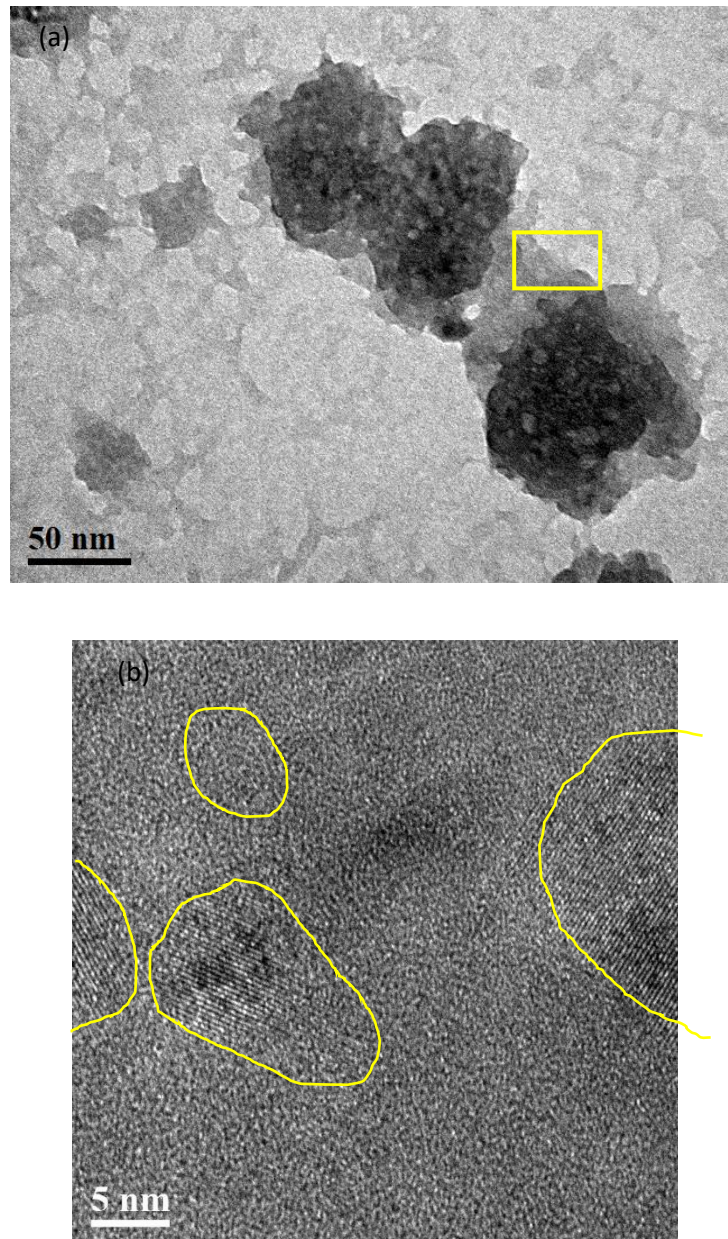


Figure 3.4 Ex-situ TEM imaging of C-S-H at the intermediate stage (a) Bright field (BF) image of C-S-H precipitate, (b) HR image of nanocrystalline and disordered C-S-H in boxed area of (a). The marked areas show the presence of C-S-H nanocrystals inside the amorphous C-S-H matrix.

The real-time direct evidence of C-S-H growth was shown in Figure 3.5, which were obtained in a separate in-situ experiment with similar experimental conditions. As exhibited in Figure 3.5 (a), the C-S-H precipitates tended to grow with a disk-like morphology. Upon further growth, some C-S-H precipitates (Figure 3.5 (b) to (g)) collapsed and impinged on each other to form a network, in which the main activation energy was the decrease of surface energy. Later (4 h 46 min), however, these C-S-H sheets started cracking in both the center and the connection edges after coalescing together (Figure 3.5 (h)). This cracking cannot be caused by C-S-H dissolution due to slurry dilution. Knowing that the solubility of  $\text{Ca}(\text{OH})_2$  in water is about 1.7 g/L at about 20 °C [28], simple stoichiometric calculations of  $\text{C}_3\text{S}$  hydration in the prepared nano-cement slurry (0.2 g nano-cement in 3 mL water) confirms formation of an amount of  $\text{Ca}(\text{OH})_2$  that is 12 times greater than the amount needed (about 0.0052 g  $\text{Ca}(\text{OH})_2$  for 3 mL water) for saturation of the slurry, so that partial hydration of the nano-cement saturates the slurry soon after mixing. This has been confirmed by measuring the pH of the slurry of 12.73 before putting the LC into TEM (30 min from mixing time). Crack formation confirms significant strain in the growing texture and indicates that structural defects exist inside C-S-H precipitates. These defects could be caused by the presence of impurities in cement [6]. We also found that the areas within the microcracks are quite empty and clear confirming that C-S-H formation and growth at the beginning starts in the form of 2D sheet-like precipitates. They are very thin in the orthogonal direction to the LC membrane. The 3D C-S-H structures (Figure 3.A3) were also observed inside the liquid cell after opening the chips, which suggested the fact that 2D sheet-like precipitates grow not only laterally, but also gradually aggregated with precipitates from other embryos in the orthogonal direction to the LC membrane. The formation of sheet-like precipitate structures at early age of hydration up to 24 h were also confirmed later by SEM imaging.

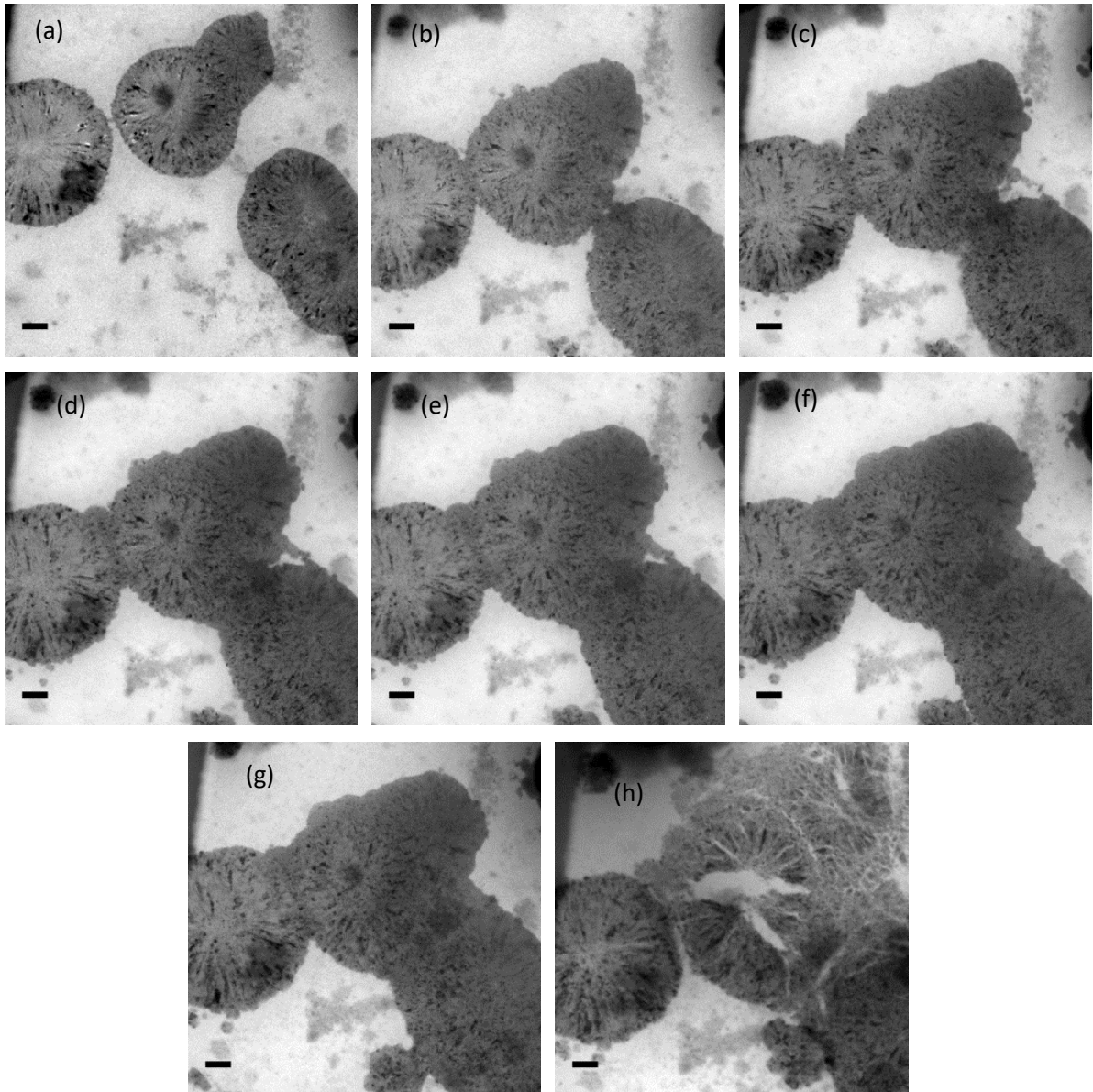


Figure 3.5 The main growth stage of sheet-like C-S-H precipitates at different time intervals (a video is attached as V. 3.A1) (a) 2 h 42 min, (b) 2 h 54 min, (c) 3 h 03 min, (d) 3 h 09 min, (e) 3 h 14 min, (f) 3 h 29 min, (g) 4 h 08 min and (h) 4 h 46 min (scale bars, 0.5  $\mu\text{m}$ )

In this work, direct evidence shows that the growing of C-S-H precipitates happens along the edge and the surface of the planar sheets (Figure 3.5 (a) – (g)). The increasing lattice strain, therefore, limits the growth of the crystalline structure. Also, the impurities such as  $\text{Na}^+$ ,  $\text{Mg}^{2+}$  ions in cement may disrupt the continuous growth of crystalline region. The formation and propagation of microcracking in the center and edges of the well-grown or adjoined C-S-H precipitates is an indication of the resultant lattice strain after large C-S-H sheets coalesced as

seen in Figure 3.5 (h). Finally, the result is the formation of a relatively large 3D network of C-S-H through connection of the precipitates. Not only the morphology of aggregation of nano C-S-H particles or basic building blocks was observed after opening the chip, but also the C-S-H nucleation happened non-uniformly on the internal surface of the SiN membrane and C-S-H precipitate growth happened, which further confirmed a nuanced realization of both the colloidal and layered structure hypothesis.

Figure 3.6 exhibits a typical image from a well-grown sheet-like C-S-H precipitate formed during in-situ experiment. The diffraction pattern taken in the marked area is presented in the inset. The measured values of the rings from diffraction pattern, which possess d-spacings of 0.3190 nm, 0.2786 nm, 0.1994 nm and 0.1677 nm, are consistent with polycrystalline C-S-H. Generally, the observed d-spacings are very similar to those of poorly crystalline tobermorite and jennite [8]. These phases have a layered sheet-like morphology with layers composed of calcium and oxygen atoms with silica tetrahedra attached, interspersed by water and further calcium ions. Similar results were also obtained from synchrotron X-ray diffraction experiments on dry powder from cement slurry [8]. The structure of C-S-H microcrystals inside C-S-H precipitates was also confirmed by diffraction patterns in the inset of Figure 3.6 (b) with d spacing values of 0.3277 nm, 0.3197 nm, 0.2837 nm. No apparent relationship has been identified between matrix and microcrystals through diffraction pattern, which most likely resulted from special conditions inside liquid cell. Although this main phase from hydrated reactions was considered amorphous in many of X-ray experiments [30, 31], it is certain that some local short order structure was achieved. The contribution of the broad amorphous C-S-H phase in the X-ray diffraction pattern is difficult to discern. Moreover, the presence of hexagonal sheet-like portlandite was also confirmed with SEM and EDS (Figure 3.A4 and Table 3.A2).

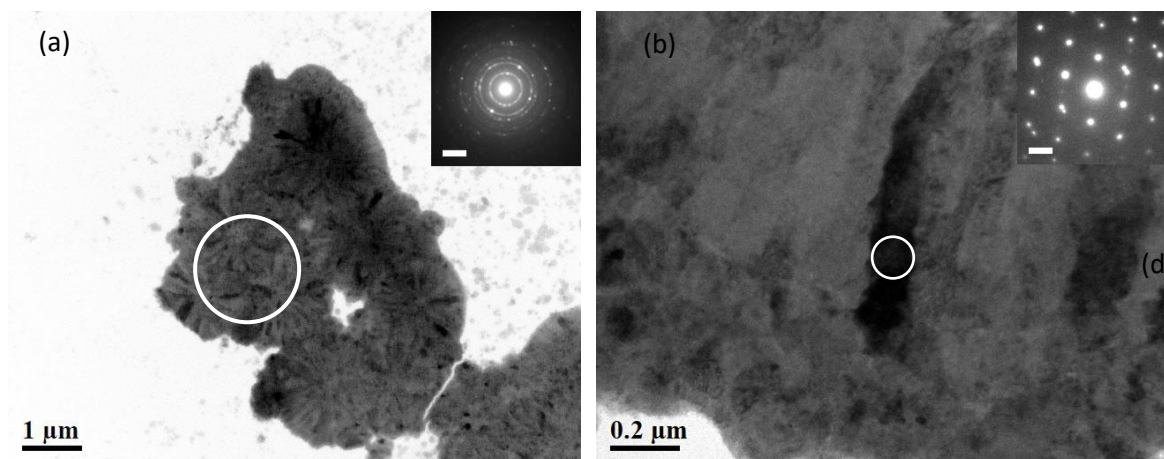


Figure 3.6 Confirmation of C-S-H formed during in-situ reactions s(a) BF image and SAD patterns with d-spacings of 0.3190 nm, 0.2786 nm, 0.1994 nm and 0.1677 nm, indicating a polycrystalline structure similar to tobermorite structure, (b) C-S-H microcrystal inside layered structure with d-spacings of 0.3277 nm, 0.3197 nm and 0.2837 nm structure.

While the advances of liquid cell electron microscopy provide tremendous insights into PC hydration reactions, it is necessary to understand the limitations of this technique regarding electron beam effects, resolution, and reaction time and kinetics. The electron beam has an influence in liquid chemistry, which contributed to the excitation and ionization of liquid molecules, resulting in the formation of hydrated electrons, radicals, ions,  $H_2$  and  $O_2$  [46, 47, 56]. Gas bubbles formed by water electrolysis may cause liquid movement and thickness changes, which limit imaging resolution of small particles by multiple scattering in liquid as well as two layers of SiN membranes [44]. We observed no bubble formation through experiments of hydration reactions of nano PC. The imaged precipitates with defined edges were formed on SiN membranes because heterogeneous nucleation and growth is more energetically favorable than homogeneous nucleation in solution. We further elucidated that the sheet-like C-S-H precipitates were not the effects of confined space and SiN membranes of liquid cell (Figure 3.A3). The planar C-S-H sheets of TEM image (Figure 3.A5) from freeze drying in a falcon tube clearly shows good consistency with in-situ experiments. The results indicate that C-S-H precipitates develop mostly in the form of planar sheets at the beginning of the studied time, namely 24 h. With continued growth, however, they gradually exhibit a 3D

microstructure. Also, the interactions between high-energy electrons and SiN membrane, to some extent, contribute to the crystallinity and chemical information, which makes the identification of main hydrated products much difficult. Besides, the induced electric field on liquid specimen may also be responsible for drifting of cations and anions, resulting in the local composition variation and supersaturation [57]. The second limitation was an inability to observe the very first dissolution and hydration reactions due to time spent on sample preparation and vacuum checking. We deposited the sample on the chips in a static rather than dynamic flowing mode to prevent blockage of the internal channels of the holders with hydrated cement end-products. In this case, imaging dissolving nano particles at the onset of the reaction is difficult. Finally, the reaction kinetics might be affected by the local heating effects [46, 57, 58] and local composition variation [46, 47]. Furthermore, the possible variations in liquid thickness may affect the kinetic of hydration reactions. To avoid beam effects, the electron dose was strictly limited during imaging (i.e. navigating with fiducial marks and only opening the beam to acquire an image). The acquisition time in one AOI was minimized. No apparent microstructural change was observed due to beam effects after 2s ~ 3s of beam exposure.

### **3.4. Conclusions**

We reported the first application of liquid cell electron microscopy technology in hydration reactions of nano PC. With the emerging advancement of in situ characterization, new insights into cement hydration reactions in early stages became possible. It allowed us to obtain detailed, real-time information of nucleation and growth of main hydration products, namely C-S-H. The main by-product of hydration reactions, Portlandite, was also confirmed by ex-situ experiment. In general, the sequence of hydration reactions of nano PC matched that of mortar and concrete samples of practical use. The needle-like ettringite crystals were formed in the reacting medium at the very early stage. It was also observed that ettringite crystals that partly

served as nucleation sites for hydration products remained stable in the timescale of the experiment and even after opening the cell and drying the chips. The findings also provided further direct evidence for both two competing C-S-H growth mechanism that had been debated for decades. The differences between two hypotheses were focused on whether C-S-H grows by aggregation of solid nano particles or by attachment of silicate tetrahedral from solution, as well as the size of precipitates. Our work suggested that development of C-S-H precipitates, like imperfect tobermorite, is through attachment of silicate tetrahedra from solution resulting in the formation of a stack of layered structure made of many C-S-H sheets with limited short order structure. The C-S-H embryos after nucleation evolved through linking of silicate ions to form growing planar silicate sheets, leading to nanocrystalline C-S-H structure of 5 nm to 10 nm in size. Beyond that dimension, defects were built in, which contributed to disordered arrangements of atoms, and thus caused local stress. These internal stresses firstly limit the size of nanocrystals resulting in the formation of an amorphous matrix and finally they cause buckling and cracking, which lead to new C-S-H embryos forming and aggregating together. These evidences shown here is a step forward for cement hydration research. The verified layered structure hypothesis and aggregation of C-S-H nanoparticles for C-S-H growth mechanism is crucial to understand and control the hydration reactions. While our results were not extensive about all early hydration stages due to limitations of the liquid cell technique, they provide new insight into the cement hydration reaction.

### **3.5 Acknowledgements**

The authors thank Madeline Dukes from Protochips, Inc. for the advice regarding liquid holder and chip selection. We would also like to thank Jie Yang and Christopher Butcher for the helpful discussion. We are grateful for the support of Mike Stanzel and Lehigh Cement Company for providing raw materials. LC-TEM work as well as TEM imaging was performed

on FEI Titan and JEOL 2010, separately, in Canadian Centre for Electron Microscopy (CCEM) at McMaster University. The efforts from CCEM staff were highly appreciated.

### 3.6 References

1. Elsen, J., G. Mertens, and R. Snellings, *Portland Cement and other Calcareous Hydraulic Binders*, in *Advances in the characterization of industrial minerals*. 2010. p. 441-479.
2. Mehta, P. and P. Monteiro, *M. Concrete: microstructure, properties, and materials*. 3rd. New York, 2006.
3. Bullard, J.W., et al., *Mechanisms of cement hydration*. *Cement and Concrete Research*, 2011. **41**(12): p. 1208-1223.
4. Pustovgar, E., et al., *Understanding silicate hydration from quantitative analyses of hydrating tricalcium silicates*. *Nat Commun*, 2016. **7**: p. 10952.
5. Richardson, I., *The calcium silicate hydrates*. *Cement and concrete research*, 2008. **38**(2): p. 137-158.
6. Allen, A.J., J.J. Thomas, and H.M. Jennings, *Composition and density of nanoscale calcium-silicate-hydrate in cement*. *Nat Mater*, 2007. **6**(4): p. 311-6.
7. Jennings, H.M., et al., *A multi-technique investigation of the nanoporosity of cement paste*. *Cement and Concrete Research*, 2007. **37**(3): p. 329-336.
8. Garbev, K., et al., *Cell Dimensions and Composition of Nanocrystalline Calcium Silicate Hydrate Solid Solutions. Part 1: Synchrotron-Based X-Ray Diffraction*. *Journal of the American Ceramic Society*, 2008. **91**(9): p. 3005-3014.
9. Jennings, H.M., *A model for the microstructure of calcium silicate hydrate in cement paste*. *Cement and concrete research*, 2000. **30**(1): p. 101-116.
10. Allen, A., et al., *Development of the fine porosity and gel structure of hydrating cement systems*. *Philosophical Magazine B*, 1987. **56**(3): p. 263-288.

11. Papatzani, S., K. Paine, and J. Calabria-Holley, *A comprehensive review of the models on the nanostructure of calcium silicate hydrates*. Construction and Building Materials, 2015. **74**: p. 219-234.
12. Taylor, H.F., *Proposed structure for calcium silicate hydrate gel*. Journal of the American Ceramic Society, 1986. **69**(6): p. 464-467.
13. Taylor, H.F.W., *Nanostructure of CSH: Current status*. Vol. 1. 1993. 38-46.
14. Gartner, E.M., *A proposed mechanism for the growth of CSH during the hydration of tricalcium silicate*. Cement and concrete research, 1997. **27**(5): p. 665-672.
15. Richardson, I. and G. Groves, *Models for the composition and structure of calcium silicate hydrate (CSH) gel in hardened tricalcium silicate pastes*. cement and concrete research, 1992. **22**(6): p. 1001-1010.
16. Richardson, I. and G. Groves, *The incorporation of minor and trace elements into calcium silicate hydrate (CSH) gel in hardened cement pastes*. Cement and Concrete Research, 1993. **23**(1): p. 131-138.
17. Cuesta, A., et al., *Multiscale understanding of tricalcium silicate hydration reactions*. Sci Rep, 2018. **8**(1): p. 8544.
18. Richardson, I. and G. Groves, *Microstructure and microanalysis of hardened ordinary Portland cement pastes*. Journal of Materials Science, 1993. **28**(1): p. 265-277.
19. Plank, J., M. Schönlein, and V. Kanchanason, *Study on the early crystallization of calcium silicate hydrate (C-S-H) in the presence of polycarboxylate superplasticizers*. Journal of Organometallic Chemistry, 2018. **869**: p. 227-232.
20. Li, H., et al., *Crystallization of calcium silicate hydrates on the surface of nanomaterials*. Journal of the American Ceramic Society, 2017. **100**(7): p. 3227-3238.
21. Yu, Z., A. Zhou, and D. Lau, *Mesoscopic packing of disk-like building blocks in calcium silicate hydrate*. Sci Rep, 2016. **6**: p. 36967.
22. Zhang, L., et al., *Hydration for the Alite mineral: Morphology evolution, reaction mechanism and the compositional influences*. Construction and Building Materials, 2017. **155**: p. 413-426.

23. Krautwurst, N., et al., *Two-Step Nucleation Process of Calcium Silicate Hydrate, the Nanobrick of Cement*. Chemistry of Materials, 2018. **30**(9): p. 2895-2904.
24. Kurtis, K., et al., *Imaging of ASR gel by soft X-ray microscopy*. Cement and Concrete Research, 1998. **28**(3): p. 411-421.
25. Gartner, E., K. Kurtis, and P. Monteiro, *Proposed mechanism of CSH growth tested by soft X-ray microscopy*. Cement and Concrete Research, 2000. **30**(5): p. 817-822.
26. Juenger, M.C.G., et al., *A soft X-ray microscope investigation into the effects of calcium chloride on tricalcium silicate hydration*. Cement and Concrete Research, 2005. **35**(1): p. 19-25.
27. Lothenbach, B. and F. Winnefeld, *Thermodynamic modelling of the hydration of Portland cement*. Cement and Concrete Research, 2006. **36**(2): p. 209-226.
28. Thomas, J.J., et al., *Modeling and simulation of cement hydration kinetics and microstructure development*. Cement and Concrete Research, 2011. **41**(12): p. 1257-1278.
29. Bullard, J.W., et al., *Coupling thermodynamics and digital image models to simulate hydration and microstructure development of portland cement pastes*. Journal of Materials Research, 2011. **26**(4): p. 609-622.
30. Merlini, M., et al., *The early hydration and the set of Portland cements: In situ X-ray powder diffraction studies*. Powder Diffraction, 2007. **22**(3): p. 201-208.
31. Hesse, C., et al., *Quantitative in situ X-ray diffraction analysis of early hydration of Portland cement at defined temperatures*. Powder Diffraction, 2009. **24**(2): p. 112-115.
32. Hesse, C., F. Goetz-Neunhoeffler, and J. Neubauer, *A new approach in quantitative in-situ XRD of cement pastes: Correlation of heat flow curves with early hydration reactions*. Cement and Concrete Research, 2011. **41**(1): p. 123-128.
33. Jansen, D., et al., *Does Ordinary Portland Cement contain amorphous phase? A quantitative study using an external standard method*. Powder Diffraction, 2011. **26**(1): p. 31-38.
34. Jansen, D., et al., *The early hydration of Ordinary Portland Cement (OPC): An approach comparing measured heat flow with calculated heat flow from QXRD*. Cement and Concrete Research, 2012. **42**(1): p. 134-138.

35. Ylmén, R., et al., *Early hydration and setting of Portland cement monitored by IR, SEM and Vicat techniques*. Cement and Concrete Research, 2009. **39**(5): p. 433-439.
36. Wu, S., et al., *Quantitative invalidation characterization of Portland cement based on BSE and EDS analysis*. Construction and Building Materials, 2018. **158**: p. 700-706.
37. Ectors, D., et al., *In situ 1 H-TD-NMR: Quantification and microstructure development during the early hydration of alite and OPC*. Cement and Concrete Research, 2016. **79**: p. 366-372.
38. Martínez-Ramírez, S. and M. Frias, *Micro-Raman study of stable and metastable phases in metakaolin/Ca(OH)<sub>2</sub> system cured at 60°C*. Applied Clay Science, 2011. **51**(3): p. 283-286.
39. Hasanzadeh, B., F. Liu, and Z. Sun, *Monitoring hydration of UHPC and conventional paste by quantitative analysis on Raman patterns*. Construction and Building Materials, 2016. **114**: p. 208-214.
40. Ross, F.M., *Electrochemical nucleation, growth and dendrite formation in liquid cell TEM*. Microscopy and Microanalysis, 2010. **16**(S2): p. 326-327.
41. Lee, H.-W., Y. Li, and Y. Cui, *Perspectives in in situ transmission electron microscopy studies on lithium battery electrodes*. Current Opinion in Chemical Engineering, 2016. **12**: p. 37-43.
42. de Jonge, N. and F.M. Ross, *Electron microscopy of specimens in liquid*. Nat Nanotechnol, 2011. **6**(11): p. 695-704.
43. Wu, F. and N. Yao, *Advances in sealed liquid cells for in-situ TEM electrochemical investigation of lithium-ion battery*. Nano Energy, 2015. **11**: p. 196-210.
44. Ross, F.M., *Opportunities and challenges in liquid cell electron microscopy*. Science, 2015. **350**(6267): p. aaa9886.
45. Dukes, M.J., et al., *Three-dimensional locations of gold-labeled proteins in a whole mount eukaryotic cell obtained with 3nm precision using aberration-corrected scanning transmission electron microscopy*. J Struct Biol, 2011. **174**(3): p. 552-62.
46. Grogan, J.M., et al., *Bubble and pattern formation in liquid induced by an electron beam*. Nano Lett, 2014. **14**(1): p. 359-64.

47. Schneider, N.M., et al., *Electron–Water Interactions and Implications for Liquid Cell Electron Microscopy*. The Journal of Physical Chemistry C, 2014. **118**(38): p. 22373-22382.
48. Zhu, G.-Z., et al., *In Situ Liquid Cell TEM Study of Morphological Evolution and Degradation of Pt–Fe Nanocatalysts During Potential Cycling*. The Journal of Physical Chemistry C, 2014. **118**(38): p. 22111-22119.
49. Wu, F. and N. Yao, *Advances in windowed gas cells for in-situ TEM studies*. Nano Energy, 2015. **13**: p. 735-756.
50. De Yoreo, J.J., *In - situ liquid phase TEM observations of nucleation and growth processes*. Progress in Crystal Growth and Characterization of Materials, 2016. **62**(2): p. 69-88.
51. Dong, P., et al., *Application of Liquid Cell-TEM in Hydration Reactions of Nano Portland Cement*. Microscopy and Microanalysis, 2018. **24**(S1): p. 294-295.
52. Noh, K.W., et al., *Challenges associated with in-situ TEM in environmental systems: The case of silver in aqueous solutions*. Ultramicroscopy, 2012. **116**: p. 34-38.
53. Brouwers, H.J.H., *The work of Powers and Brownyard revisited: Part 1*. Cement and Concrete Research, 2004. **34**(9): p. 1697-1716.
54. Brouwers, H.J.H., *The work of Powers and Brownyard revisited: Part 2*. Cement and Concrete Research, 2005. **35**(10): p. 1922-1936.
55. Shi, C., et al., *A review on ultra high performance concrete: Part I. Raw materials and mixture design*. Construction and Building Materials, 2015. **101**: p. 741-751.
56. Sun, L., et al., *In situ transmission electron microscopy observation of silver oxidation in ionized/atomic gas*. Langmuir, 2011. **27**(23): p. 14201-6.
57. Jiang, N., *Note on in situ (scanning) transmission electron microscopy study of liquid samples*. Ultramicroscopy, 2017. **179**: p. 81-83.
58. Jiang, N., *Electron beam damage in oxides: a review*. Rep Prog Phys, 2016. **79**(1): p. 016501.

#### **4. In-situ Observations of Different Cement Hydration Stages Using Liquid-cell Transmission Electron Microscopy**

Peng Dong<sup>1</sup>, Ali Allahverdi<sup>2</sup>, Carmen M. Andrei<sup>3</sup>, and Nabil D. Bassim<sup>1,3</sup>

1. Department of Materials Science and Engineering, McMaster University, 1280 Main St W, Hamilton, ON L8S 4L8, Canada

2. Cement Research Centre, School of Chemical Engineering, Iran University of Science and Technology, Narmak 16846 – 13114, Tehran, Iran

3. Canadian Centre for Electron Microscopy, McMaster University, 1280 Main St W, Hamilton, ON L8S 4L8, Canada

**Author contributions:** In Chapter 4, the original idea of researching cement hydration kinetics was suggested to Mr. Peng Dong by Dr. Ali Allahverdi and Dr. Nabil Bassim. Mr. Peng Dong performed most experiments and data analysis with the help of Dr. Ali Allahverdi. The freeze-drying experiment was conducted in Dr. Todd Hoare's lab with the assistance of Mr. Ali Affar. The manuscript was originally drafted by Mr. Peng Dong, improved by Dr. Ali Allahverdi and Dr. Carmen M. Andrei, and edited to the final version by Dr. Nabil Bassim. This work will be submitted to a journal for publication.

## **Abstract**

Liquid cell transmission electron microscopy (LC-TEM) has the potential to revolutionize the understanding of nanoscale hydration mechanisms in Portland cement. However, the volume of the materials under observation must be confined to an electron-transparent volume in order to make meaningful measurements. This confinement may alter the chemical kinetics because of an increase in surface reactivity of the species under study. To understand the applicability of nanoscale measurements to real-world applications, a study of these effects is necessary. In this case, the hydration reactions of nano Portland cement (PC) were researched using LC-TEM and compared to isothermal calorimetry and quantitative X-ray diffraction (QXRD). Consistent with the authors' previous study, the water to cement (w/c) ratio was adjusted to 15 to achieve proper electron transparency. Freeze drying and QXRD experiments at time points of 0.5 h, 1.5 h, 3 h, 5 h, 14 h, and 24 h were chosen based on hydration peaks from heat flow curves and interesting phenomena from in-situ imaging. The hydrated samples for ex-situ experiments were obtained after freeze drying, which stopped the reaction at the specified time point. In terms of hydration kinetics, the initial period and induction period in nano PC system were 0.5 h and 0.5 h, respectively, much shorter than that of 2 h and 1 h in a typical OPC system. The acceleration stage of the nano PC system contains three peaks, in which a broad silicate peak appears much later than the aluminate peak. During this stage, the retardation effects caused by hydration products were also observed. Phase transformation and microstructure formation are discussed and compared in different hydration stages. We

also reported the real-time dissolution of ettringite crystals and formation of hydration products inside LC-TEM.

**Keywords:** cement hydration, hydration stages, Rietveld refinement, real-time imaging, aluminate and silicate peaks, liquid cell TEM, in situ

## 4.1. Introduction

Hydration reactions of PC in early stage are responsible for the development of the permanent microstructure and mechanical properties. Though PC was first introduced in 19<sup>th</sup> century [1, 2], cement hydration reactions are still not fully understood due to complicated compositions and interaction of simultaneous chemical reactions. The main constituents of PC are alite ( $C_3S$ ), belite ( $C_2S$ ), aluminate ( $C_3A$ ) and aluminoferrite ( $C_4AF$ ), which transform mainly to calcium silicate hydrate (C-S-H), portlandite, ettringite and monosulfate [2, 3]. The two most important categories of cement hydration reactions involve silicate and aluminate reactions [4]. Historically, cement hydration reactions are divided into four main time periods following mixing cement and water. The initial reaction period involves cement wetting and rapid reactions between aluminate and alite with water, followed by a slow reaction period, which is called induction period [5]. During the induction period, the formation rate of C-S-H precipitates are very low. Attribution for the induction period has been debated based on two theories, namely, protective phase theory and delayed nucleation and growth theory [6, 7]. The following acceleration period of higher rates of nucleation and growth, and the subsequent deceleration period are sometimes characterized as main hydration stages.

Many efforts have been devoted to studying alite hydration stages and kinetic studies using calorimetry methods in past years. Juilland et al. [6] studied alite hydration kinetics and ascribed the advent of induction period to the formation of etch pits on surfaces, based on geochemical mechanism. Nicoleau [8] provided a better

understanding of C-S-H precipitation mechanisms by comparing both calculated and experimental heat flow curves of alite in the presence of different accelerators. The kinetic laws that related the dissolution rates of alite and the degree of the undersaturation in the mixture were also obtained [9, 10], and undersaturation with respect to  $C_3S$  was observed to increase during induction period, resulting from precipitation of portlandite and thus the reduction of calcium and hydroxyl ions [11]. It was also reported that the tricalcium silicate hydration process was tracked using calorimetry and synchrotron X-ray diffraction [12]. However, it is rather difficult to research PC hydration due to aluminate phase reactions and their interactions with silicate phase reactions [13-15], which probably change the kinetics of hydration reactions. Heat flow calorimetry is a useful technique to determine different stages of hydration reactions, but it only provides information on kinetics with less details.

The X-ray powder diffraction (XRPD) technique has proven to be applicable in characterizing crystalline phases in cementitious materials [16, 17]. Quantitative XRD analysis of relative phase fractions can be achieved by employing the Rietveld refinement technique, in which a simulated pattern, based on presumed contents and certain lattice parameters of a known phase is compared with an experimental pattern [18]. Therefore, all crystalline phases can be evaluated with a total amount of 100%. Amorphous or unknown phases are determined using several approaches, including the internal standard method [18-20], or the scale factor method [21-23]. The contents of C-S-H, free and bonded water can be calculated via Portlandite content based on an alite hydration model since belite phase does not undergo significant hydration in the

early hydration stage, and all crystalline and amorphous contents are adjusted to a new total sum of 150 wt% [24]. Rietveld analysis is thus applicable in providing phase information in different hydration stages.

Another interest is to study the microstructural evolution of cement at different time scales, which has been limited by the weaknesses of various characterization techniques (including bulk vs. micro-nano, and the requirement of high vacuum to achieve electron probes at nanoscale in the case of electron microscopy). The liquid cell transmission electron microscopy (LC-TEM) technique allows new insights into many liquid reactions, including electrochemistry [25-27], fluid physics [28-30], nano patterning [29, 31] and even inorganic hydration reactions [32-34] in real time and with excellent spatial resolution. This opens the new possibility to research cement hydration mechanisms at the nanoscale. However, it is difficult to achieve in-situ cement hydration reactions because it involves reactions of both solid and liquid confined by a liquid reaction cell that is electron transparent. This requires the reduction of Portland cement particles of microscale size to nanoscale size.

While this experimental methodology is not exactly analogous to typical microscale PC, there is merit in this approach. Nanotechnology has attracted much attention in research and engineering communities for its capability to achieve favorable characteristics of materials. Nano cement with higher surface/volume ratios have been demonstrated to improve strength and durability even with lower cement to aggregate ratios as compared to traditional PC [35]. Roddy et al. [36, 37] devised a treatment for

oil and gas applications to mix well treatment fluids with nano-cements to manufacture cement utilizing nano hydraulic cement and nano clay. Bickbau [38] employed a mechanochemical activation of dispersed grains of Portland cement in the presence of polymeric modifier to produce nano cement, leading to great superiority over Portland cement concrete in all indicators and achieving high economic efficiency. Arulraj [39] researched the replacement of nano cement in Portland cement and associated strength and durability properties and achieved higher compressive strength and better permeability in concrete with nano cement replacement. It is thus critical to understand the size effects of the nanoscale cement to clarify the hydration mechanisms and kinetics for effective materials design.

This work is an attempt to apply nanoscale materials and characterization techniques to facilitate the understanding of cement hydration reactions and kinetics. The applications of nanomaterials potentially enhance unique physical and chemical properties of building materials as well. In this paper, a freeze-drying technique was applied to the same nano PC system as previous LC-TEM experiments. Isothermal calorimetry and quantitative XRD analyses were combined with LC-TEM to provide correlated details of phase transformation and reaction kinetics in different hydration stages. We further reveal that aluminate and silicate reactions were responsible for the peaks in calorimetry data, indicating varied kinetics in different stages.

## **4.2. Materials and Methods**

### **4.2.1 As – received and Nano PC**

The chemical composition of as – received PC were provided in Table 4.A1. The average particle size of OPC was 45  $\mu\text{m}$  measured by the Lehigh Cement Company (Picton plant, Ontario, Canada), which greatly exceeded the size of the liquid reaction cell. To reduce the particle size, a three – step ball milling operation was considered to make it accessible for LC-TEM. The first two steps were conducted using corundum balls (diameter; 10 mm, 14 days) and zirconia balls (diameter; 4 mm, 32 days), separately. Both two steps were in the presence of anhydrous ethanol to disperse particles and enhance the milling efficiency. The nano cement powder underwent a final ball milling stage for 3 days after being dried from cement-ethanol slurry on a hot plate (70  $^{\circ}\text{C}$ ). This was to crush cement lumps formed during drying. The particle size of nano cement (Figure 4.A1) was reduced efficiently, in which 83.0% of cement particles were below 200 nm and 66.3% of those were below 50 nm.

### **4.2.2 Liquid Cell Assembly and In-situ Imaging**

A special liquid cell holder (Protochips, Poseidon Select holder) containing both a small chip (with 150 nm spacers) and a large chip (4 by 8 microwells, no spacers) was applied. This allowed a sealed cell with an approximate 250 nm thickness, where liquid reactants were located. In this work, we considered a dilute nano cement system with water/cement (w/c) ratio of 15, in which liquid sample is relatively transparent for electron beam to go through. The 0.2 g nano cement and 3 ml deionized water were mixed in a glass vial, and sonicated for 5 min, after which a 2  $\mu\text{l}$ -drop was taken from

the top of the suspension using a micropipette. The liquid cell unit was assembled carefully and after vacuum checking was inserted into microscope (ThermoFisher-FEI Titan). The beam energy was 300 keV with screen current of 1.21 nA. The microstructure evolution of main phases was studied through tracking different areas of interests (AOI). The electron beam was left on any AOI only for 2 to 3 seconds for the purpose of minimizing beam effects on the hydration reaction and acquiring images.

#### **4.2.3 Isothermal Calorimetry and Heat Flow**

Heat flow calorimetry was conducted using I-Cal 8000 HPC, 8-channel isothermal high precision calorimeter. A flow of deionized water was kept in a suction cup in the machine at the curing temperature of 25 °C. The w/c ratio was kept consistent with that of LC-TEM experiment, in which 7.000 g nano cement was mixed with 105.000 g water. In this case, a high degree of precision was applied regarding the weight of the reactants.

#### **4.2.4 Lyophilization and Quantitative XRD Analysis**

Nano cement powder was mixed with deionized water at w/c ratio of 15, the same as previous experiments. Six samples that arrested the hydration reaction mid-process were prepared and frozen according to different reaction times, namely, 30 min, 1 h 30 min, 3 h, 5 h, 14 h and 24 h, which corresponded to significant observations both in LC-TEM and isothermal calorimetry experiments. The cement suspensions were then dried below -80 °C in a vacuum dryer for 3 days.

The diffraction patterns of 6 freeze-dried samples were recorded by a D8 diffractometer (Bruker). Co K $\alpha$  radiation was used at a voltage of 35 kV and a current of 45 mA. The measurements were performed ranging from 8° to 90° with a step width of 0.02 and 2500 s per step. The measurement of each diffraction pattern took nearly 3 h 30 min. The quantitative analysis of hydrated products was performed with TOPAS 3.0 (Bruker). Rietveld refinement was applied, in which intensities from a model of assumed crystalline phases were fitted and compared with measured X-ray pattern through a least-square refinement. In this method, all parameters of crystalline phases including structures, space groups and peak profiles must be known, which gave dry phase composition normalized to 100%. However, composition of amorphous phases cannot be determined directly from the software due to their lack of certain structural information. Amorphous phase content was calculated based on Rietveld refinement and simplified early-age hydration reactions models [24]. Therefore, the content of crystalline and amorphous phases that incorporated reaction water were then recalculated.

#### **4.2.5 Scanning Electron Microscopy and Energy Dispersive Spectroscopy**

The structural and compositional information of hydrated products were measured after the in-situ experiments by opening the liquid chips and examining the products using scanning electron microscopy (SEM) and energy dispersive spectroscopy (EDS). The post-situ liquid chips were fully dried, and carbon coated before imaging. The SEM and EDS were performed on a JEOL 7000F with a beam energy of 9 keV and working

distance of 10 mm to acquire images with minimal charging and excite all present elements.

### 4.3. Results and Discussion

We observed the in-situ hydration reactions of a very dilute nano PC slurry inside a liquid cell. The water to cement ratio was controlled at 15 to meet the electron-transparency requirements. The reaction took place the moment cement particles and water were mixed prior to loading the TEM specimen holder. Figure 4.1a shows a bright field (BF) image obtained at 2 h 31 min after mixing. As can be seen, C-S-H precipitates appear to be round in shape. The precipitates with sharp edges nucleated on the SiN membranes since the heterogeneous precipitation on cell membranes requires less surface energy [28]. Figure 4.1b was acquired at the same area with a time interval of 8 min. Comparing the circled areas on two figures, we found that C-S-H precipitates collapsed and formed a network.

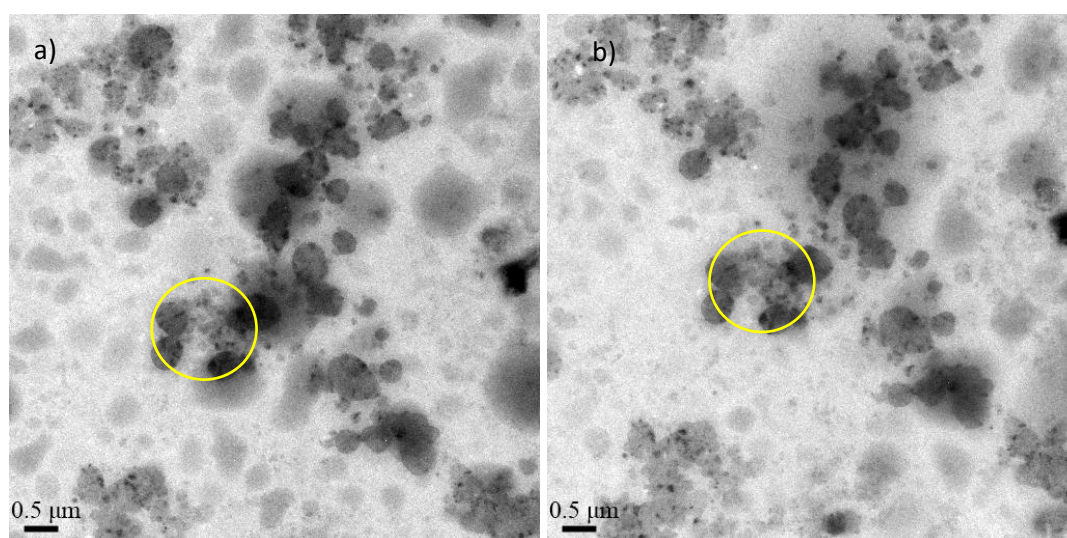


Figure 4.1 BF images showing growth and collapse of C-S-H precipitates with time a) at 2 h 31 min and b) 2 h 39 min

A serial of images from another area were also obtained. The contrast variance in Figure 4.2 reveals important information about mass and thickness of C-S-H precipitates. The circled areas in Figure 4.2a display a few individually grown C-S-H sheets, which were partially connected in Figure 4.2b. With cement particles being dissolved, more C-S-H precipitated from the solution and grew along the edges of the existing sheets. Compared with that in Figure 4.2a and b, C-S-H precipitates collapsed and grew to a network. The formerly individual C-S-H precipitates that were embedded in the network became darker in contrast. It indicated that C-S-H not only grew laterally, but also increased in thickness in a 3D fashion. This shows that the confinement in the liquid reaction cell did not influence C-S-H growth. A video (V. 4.A1) aligned from 10 images in the same area was also attached.

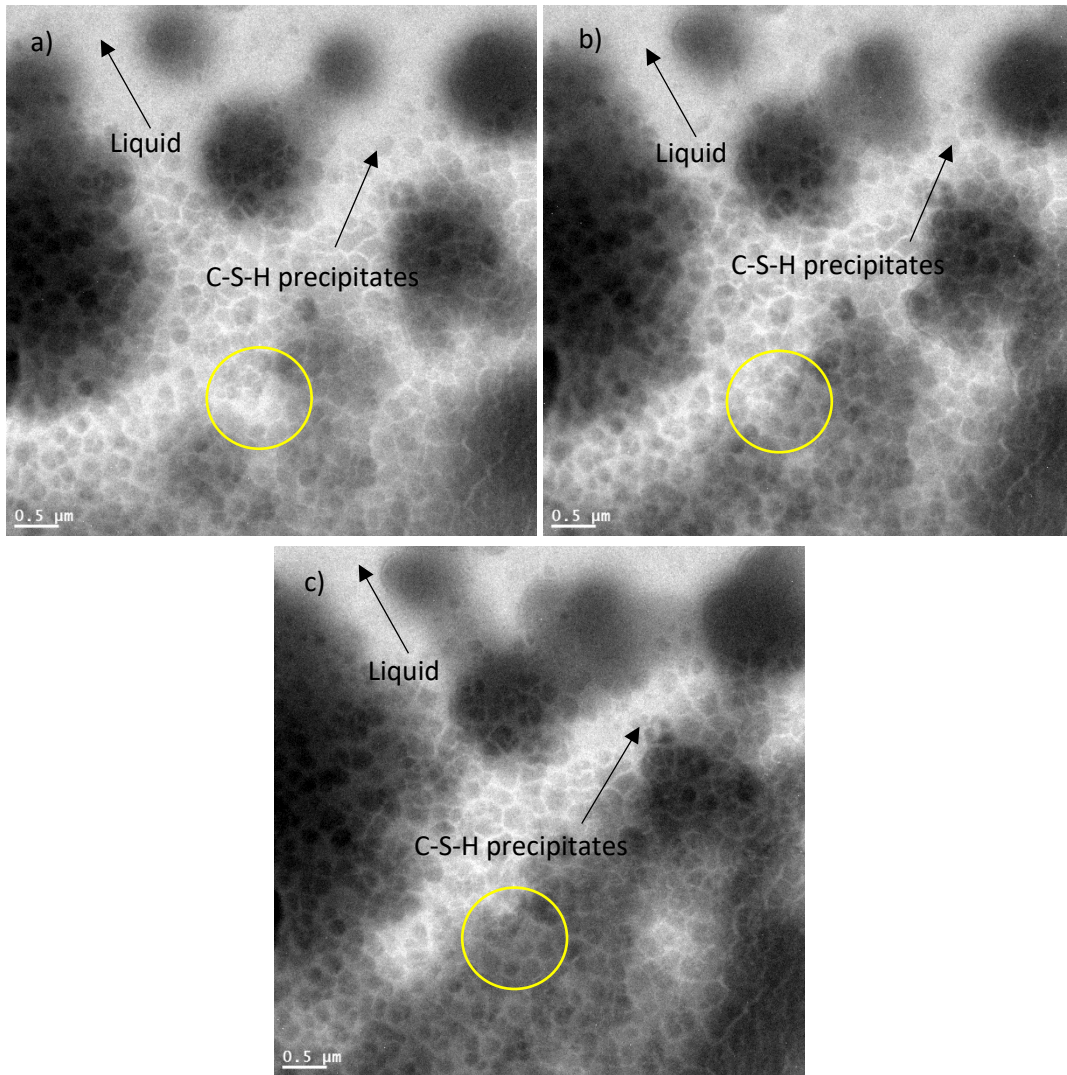
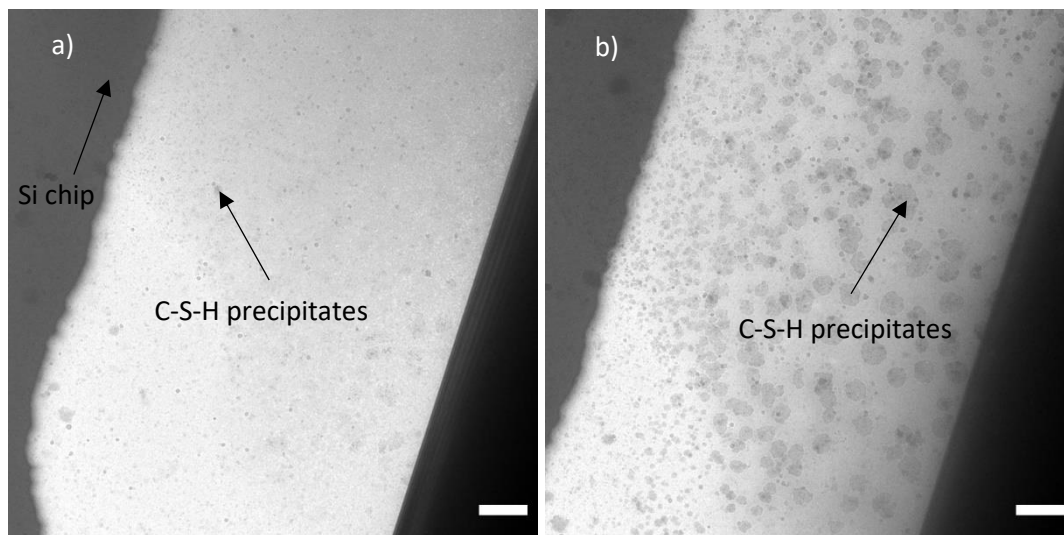


Figure 4.2 Contrast variance of images in the same area showing thickness change and 3D growth of C-S-H precipitates a) 3 h 05 min, b) 3 h 10 min and c) 3 h 23 min

Hydration reactions of a dilute system with w/c of 15 were conducted. In-situ TEM images from the four main hydration stages are shown in Figure 4.3 (b and c are from the same imaging area, and a and d are from different micro-wells), in which survey views of SiN membrane and hydrated products were captured at a relatively low magnification. By careful examination, we were able to evaluate the C-S-H nucleation and growth process. During the induction period, it was observed that C-S-H nucleated and formed leading to small embryos on transparent membranes due to the low surface

energy required for heterogeneous nucleation. These C-S-H embryos developed through precipitation of silicate tetrahedra to the particle margin from the solution, where more defects were built in beyond certain scale of 5 nm to 10 nm [40, 41]. This led to poorly nanocrystalline structure that was tobermorite-like [12, 40, 42]. Later, during the induction period (Figure 4.3b), more C-S-H precipitated, and some grew to intermediate planar sheets. Consequently, C-S-H precipitates grew larger and connected on the membranes in the acceleration stage (Figure 4.3c). However, more C-S-H precipitates were seen to cover most of the membrane surface in deceleration stage (Figure 4.3d). Also, some cracking caused by increasing strain appeared in the sheets leaving some empty areas in between, which further indicated the nature of C-S-H sheets [5, 42].



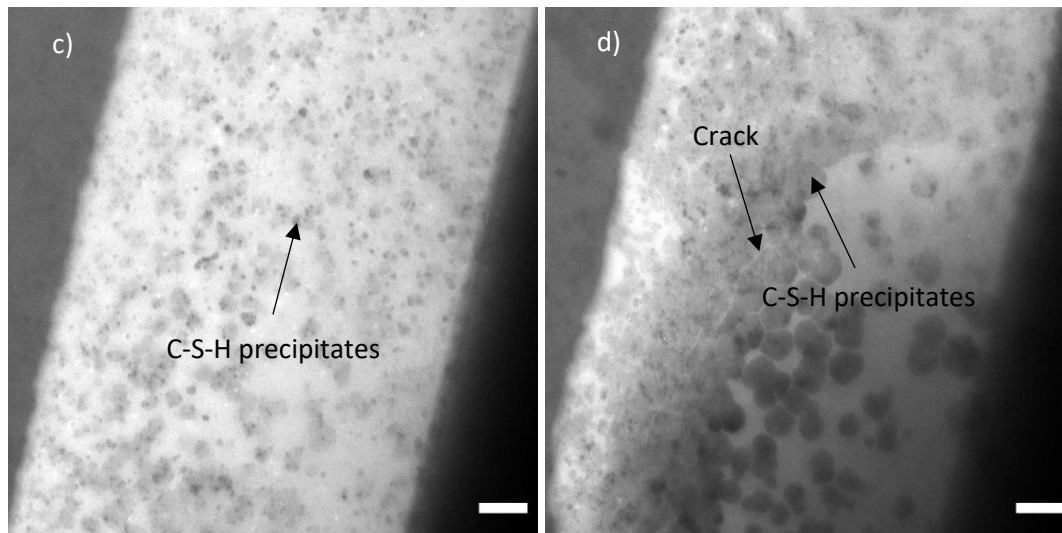


Figure 4.3 C-S-H precipitates from a) acceleration period, at 2 h 10 min, b) acceleration period, at 3 h 30 min, c) acceleration period, at 15 h 53 min and d) deceleration period, at 23 h 48 min. Scale bars, 0.5  $\mu\text{m}$ .

Post-situ TEM experiments were conducted to examine the hydrated products. The BF image (Figure 4.4a) presents the disorganized fibrous C-S-H structure apart from sheet-like C-S-H precipitates, which may be left due to very high relative humidity in the end of induction stage [43, 44]. The dark field (DF) image from the same area is shown in Figure 4.4b. As can be seen, the microstructures with bright contrast alternated with those with dark contrast. In DF image, the bright contrast resulted from the diffracted beam that underwent Bragg diffraction condition with crystalline structure. It revealed that the fibrous C-S-H was nanocrystalline. The selected-area diffraction (SAD) in Figure 4.4c further proved the nanocrystalline nature of C-S-H precipitates since the diffraction pattern consisted of both spot and ring patterns, which correspond to the lattice parameters of C-S-H.

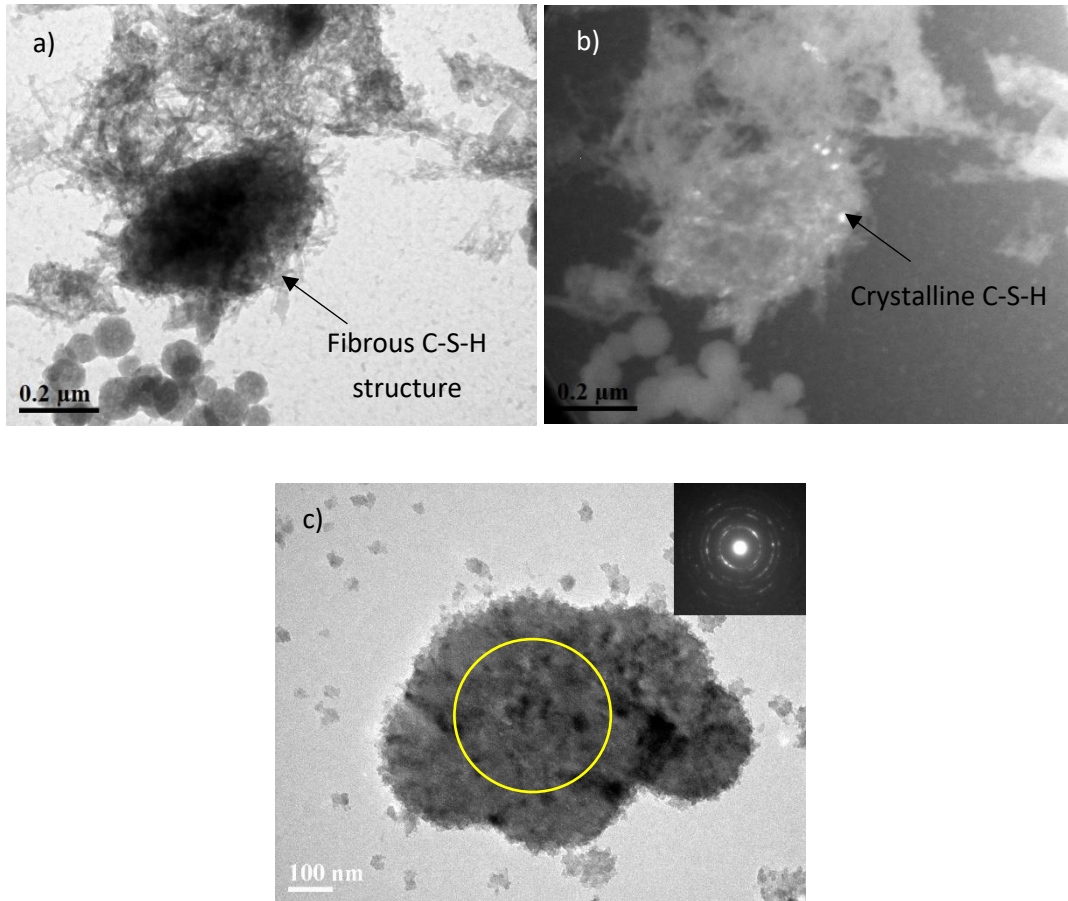


Figure 4.4 Post-situ TEM experiment on C-S-H precipitates a) BF image, b) DF image and c) BF image and diffraction pattern of selected area

Aluminate-based reactions also occurred throughout different hydration stages and had an influence on silicate reactions. Aluminate reactions are responsible for the setting of cement, where sulfates play a role in regulating hydration reactions in the form of anhydrite. This is because  $C_3A$  has close affinity to  $SO_3$  and reacts with it instantly, reducing a large amount of exothermic heat from the reaction between  $C_3A$  and water [14]. In our experiments, anhydrite as a form of sulfates was identified from XRPD and no form of gypsum was detected. The moment water was added to the nano cement system, ettringite was formed. At 0.5 h, 2.3% of ettringite was detected and 12.0% of ettringite was accumulated at 24 h in the deceleration period.

We also report the real-time dissolution of ettringite and the formation of a more hydration product (probably monosulfate, in Figure 4.5). In Figure 4.5, a series of images (see attached video of aligned images, V. 4.A2) were taken at the same position were taken and aligned carefully from LC-TEM experiments. The results indicated that ettringite needles dissolve to form monosulfate. Moreover, it was observed that ettringite crystals were formed and dissolved at different time scales during in-situ hydration reactions (Figure 4.5b and c). On the other hand, the large precipitates around needlelike ettringites with unclear morphologies were most likely to be monosulfates (shown with arrows). It was determined that the structure grew larger in the consumption of dissolved sulfate ions by ettringite crystals. They were later densified and underwent shrinkage (Figure 4.5d), which resembled that of real practice [2]. Quantitative results from Rietveld refinement also showed that anhydrite and  $C_3A$  dissolved at different times. Anhydrite as the sulfate carrier was dissolved completely in the very beginning of hydration reactions, while  $C_3A$  dissolution almost stopped after initial stage. It continued to dissolve slowly after 5 h from induction period to deceleration stage. The behavior that  $C_3A$  does not appear to dissolve with ample anhydrite was also observed by other researchers [23, 24, 45]. The observation of a fast dissolution is attributed to the very high dilution of hydration system and the slow removal of the sulfate due to its adsorption on  $C_3A$  and C-S-H surfaces [46]. However, the quantification of monosulfate was not considered here because of has a composition near or below detection limits for QXRD and for lack of valid structure model [4]. Bergold et al. [46] also observed that ettringite dissolves partially to provide sulfate

ions to form monosulfate. It was also pointed out that the transformation from ettringite to monosulfate should start when excess  $C_3A$  is still present [4].

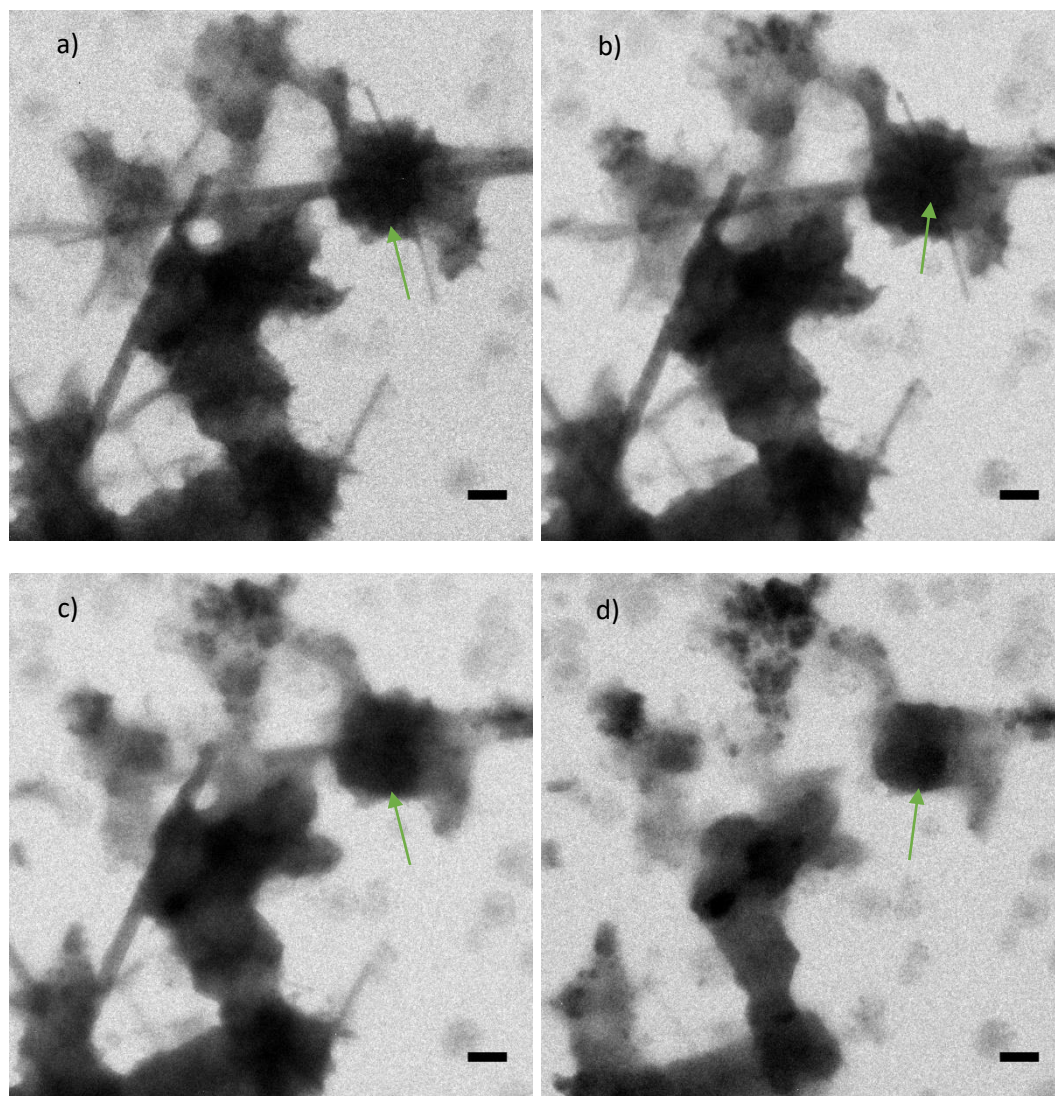


Figure 4.5 The dissolution of ettringite from the same position (a video of aligned images is attached V. 4.A2). a) at 1 h 59 min, b) at 2 h 08 min, c) 2 h 11 min, and d) at 2 h 16 min. Scale bars, 0.5  $\mu\text{m}$

Heat flow calorimetry was conducted at 25 °C, in which the reaction heat was monitored within 24 h (Figure 4.6). As can be seen, there are three hydration peaks (A1, A2 and A3) in dilute nano PC system, indicated by the solid line. The heat flow curve of dilute OPC system used as control, shown in dashed line had a large silicate peak,

which was broadened by the dilution. It was observed that the dissolution (I) rate of cement particles was much faster in nano cement than that in OPC, indicated by the cumulative heat curves in Figure 4.6. Moreover, the induction period (II) of nano PC system was shorter than that of OPC system. This is due to the higher surface area and reactivity of nano PC than that of OPC with normal fineness. The acceleration stage (III) of nano PC appeared much earlier, 1 h after mixing, compared with 2.5 h of OPC. However, cement hydration of nano PC in this stage was soon retarded, which lasted almost 6 h. After peaking at 15 h and 7.5 h, hydration reaction of nano PC and OPC reached deceleration stage (IV), respectively. It is also worth noting that the heat produced by the very early ettringite formation was not detected by calorimeter because of both the very high dilution of the reacting media that significantly reduced the specific heat released and the increase in  $C_3A$  early hydration rate due to highly increased fineness in nano PC. Also, the heat flow curve appears to be negative during the 1<sup>st</sup> hour of the hydration. This is related to the set temperature in calorimetry test, which will be discussed later.

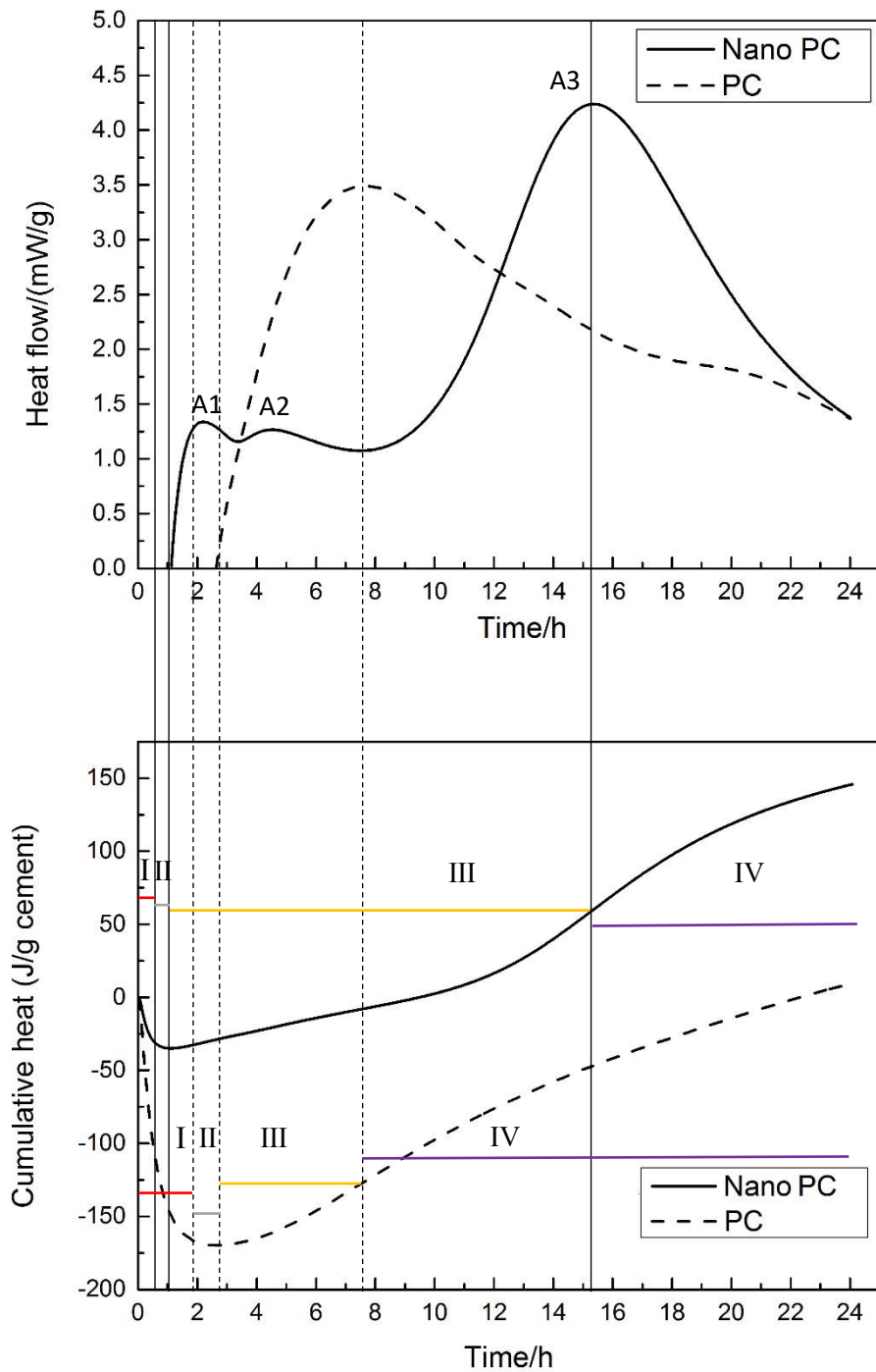


Figure 4.6 Heat flow and cumulative curves of nano PC and OPC hydration within 24 h under the circumstance of 25 °C in solid and dashed lines, respectively. Three peaks of nano PC heat flow curve are A1, A2 and A3. Four different hydration stages: I – initial or dissolution period (red line), containing dissolution of cement particles, II – induction period (green line), involving slow reaction, III – acceleration stage (yellow line), and IV – deceleration stage (blue line).

The phase transformation of the dilute system within 24 h was clarified by X-ray powder diffraction (XRPD) and following Rietveld refinement. Phase composition of as-prepared nano PC is shown in Table 4.1. It was observed that a small amount of Portlandite appeared in nano PC. This is due to minor hydration reactions of nano PC with trace water originating from air humidity and ethanol. The Rietveld analysis leads to quantitative results of crystalline phases, while amorphous phases can be calculated by referencing Portlandite contents [24]. This is based on a simple assumption that C-S-H is only formed from C<sub>3</sub>S hydration reactions, because C<sub>2</sub>S hydration typically starts after the first few days of cement hydration [24]. But free water is not considered, since it does not remain as part of the hydration products after the lyophilization process.

Table 4.1 Phase composition of nano PC (values in wt %) obtained from Rietveld refinement of XRD data

C <sub>3</sub> S	C <sub>2</sub> S	C <sub>3</sub> A	C <sub>4</sub> AF	Anhydrite	Portlandite	Calcite
53.1	23.7	7.0	7.7	1.1	1.0	6.4

Figure 4.7 shows quantitative results of hydrated and anhydrous phases at different time intervals including 0.5 h, 1.5 h, 3 h, 5 h, 14 h, and 24 h. Hydration reactions start the moment that water was added to nano cement. In the first 0.5 h, the contents of portlandite and C-S-H increased quickly, indicating a quick dissolution and nucleation process of C-S-H. Then, the reaction remained at a slow rate between 0.5 to 1 h in induction period with almost no increase in C-S-H content. They increased very slightly between 1.5 h to 3 h while a relatively fast hydration happened between 3 h and 24 h. Regarding aluminate phase hydration, ettringite content exhibited an upward trend, and

the contents of anhydrite and  $C_3A$  went down. The small increase in  $C_3A$  content at 3 h is due to experimental errors. Also, it is clear that anhydrite and  $C_3A$  both played a major role in early ettringite formation.

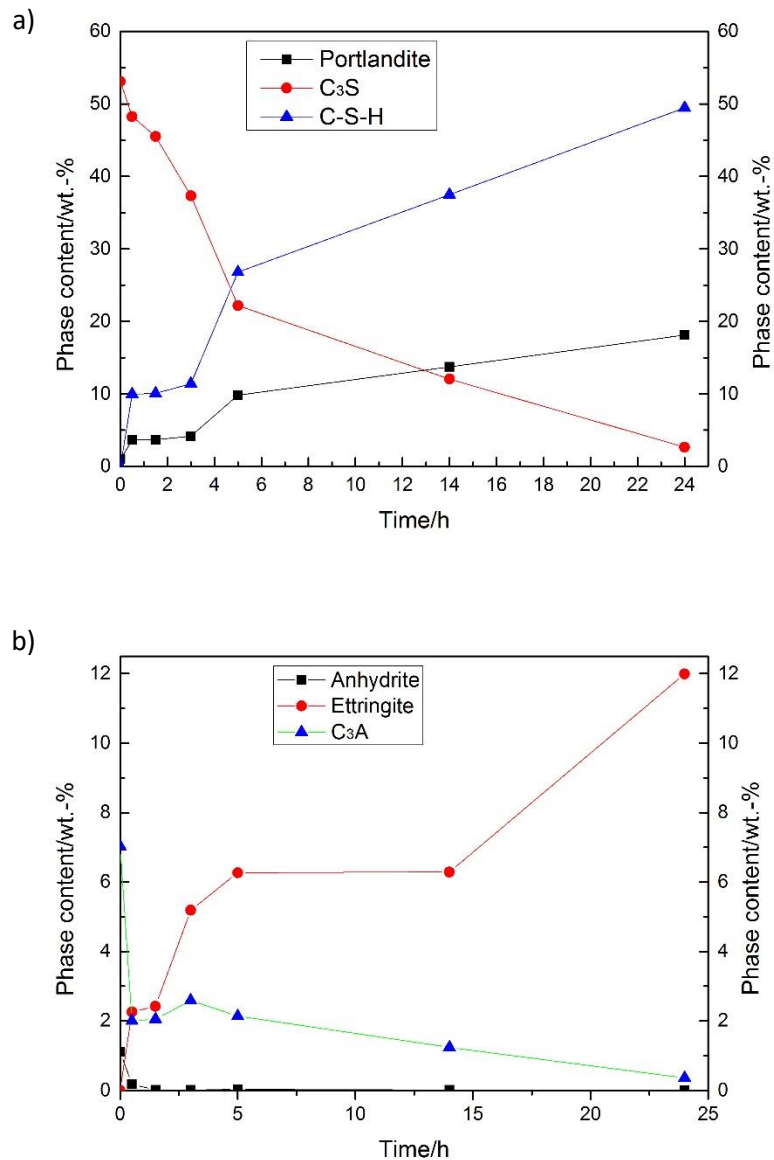


Figure 4.7 Phase contents of main anhydrous and hydrated phases of hydration reactions within 24 h from Rietveld refinement; a)  $C_3S$ , C-S-H, and portlandite, b)  $C_3A$ , ettringite, and anhydrite.

Portland cement hydration is generally characterized by four main stages, i.e. initial period, induction period, acceleration and deceleration stages. It was observed that the

dissolution and initial stage of nano PC was 0.5 h, much shorter than about 2 h of OPC. In the nano PC system, cement particles dissolved after contacting water in this stage, which was accompanied by initial reactions including nucleation of C-S-H and ettringite formation. The induction period lasted about 0.5 h in nano PC system, which was also shorter compared with 1 h in OPC system. It was observed that the content of portlandite went up to 3.7% after 0.5 h and reached 4.2% slowly after 3 h. In the meantime, ettringite accumulated to almost 5.2%, after which the first peak A1 dropped and the heat release rate slowed down.

It was reported that  $C_3S$  dissolution in OPC contributed to a high concentration of calcium and silicate while not necessarily leading to a saturated solution [5]. In a dilute, pure  $C_3S$  suspension, it was likely that portlandite precipitated even though an insufficient supersaturated hydration of  $C_3S$  was achieved [11]. The induction period appeared after 0.5 h and lasted for 0.5 h, during which contents of portlandite, and C-S-H remained almost constant. Similar results were also reported in studies on cement paste with normal fineness [4, 45]. The reason for the existence of an induction period is still under debate with mainly two theories. The metastable barrier hypothesis proposed that newly formed, metastable calcium silicate hydrate prevents underlying alite from further reacting with water [5, 43]. The second theory, slow dissolution step hypothesis implied a steady state balance between the dissolution of  $C_3S$  and the slow growth of C-S-H, where the solution exceeding a C-S-H supersaturation led to C-S-H nucleation, followed by a decrease of silicate concentration in solution [5]. In our conditions, the dissolution rate may not be an issue because of abundant water with

respect to cement. The slowdown effects of alite hydration is likely from Al inhibition [15, 46]. The acceleration stage started around 1.5 h and soon got retarded at 2 h, which lasted until 8 h. This probably resulted from the formation of monosulfates, which covered the surface of newly formed precipitates. This process will also be discussed later.

Figure 4.6 exhibited a large broad  $C_3S$  hydration peak (A3) in the acceleration stage, where contents of portlandite and C-S-H went up with a steady ettringite content. In deceleration stage, the heat release rate went down, resulting in an increased accumulation of large portion of portlandite (18.1%), C-S-H (49.5%) and ettringite (12.0%). The nucleation and growth of C-S-H resulted in a decrease in calcium and silicate concentration, which were necessary for further C-S-H growth. The other reason given for the slowdown of silicate reactions is space limitation [5]. However, this would not account for the slowdown for further  $C_3S$  hydration in our case, because of high dilution.

As can be seen, aluminate peaks develop much earlier than silicate peaks in Figure 4.6 compared with OPC paste. Some studies have been carried out by researchers to figure out the effects of sulfate content on hydration kinetics. On one hand, the accelerating effects of sulfate on silicate hydration is due to seeding effects of ettringite [11, 46]. LC-TEM results of nano cement also show that needle-like ettringites provide nucleation surfaces for C-S-H precipitates from the beginning. On the other hand, Bergold et al. [46] concluded that the precipitation of monosulfates that is not an Al-

inhibition process has a negative effect on silicate reaction rate by reducing the C-S-H<sub>1ro</sub> (metastable kind of C-S-H) surface area available for the precipitation of new precipitates. It is due to the change of surface charge from sulfate adsorption that changes the precipitation of C-S-H.

The LC-TEM work shows that the transformation of ettringite to a much more stable hydrated product, monosulfate, later reduces the surface area for potential precipitates, and thus the rate of silicate reaction. This is the reason that we observe obvious retardation effects of nano PC system soon after the acceleration stage starts. Quennoz and Scrivener [15] designed experiments to study C<sub>3</sub>A hydration behaviors in the presence of gypsum and alite, and observed that alite hydration is slowed and the aluminate peak appears ahead of the silicate peak in undersulfated systems with less than 5% gypsum additions in model cement. However, a silicate peak appears before the aluminate peak in properly sulfated systems, as gypsum contents increase [15]. This may explain why large broad silicate peak occurs later. Furthermore, the shape of the heat flow curve is different from those of cement systems with sulfate, especially in the beginning. This is likely affected by temperature, which seems to impact more on aluminate reactions than silicate reactions, and thus results in different interactions [15].

This work shows that LC-TEM and QXRD are powerful techniques to research nucleation, growth and phase transformation of cementitious materials. It is worth mentioning that there are a few limitations of the LC-TEM technique as well. The system is formed by two closed Si chips, in which liquid sample is placed so that

electron beam can go through to acquire images [32]. Therefore, the liquid sample has to be transparent, which required to be highly diluted. The dissolution process is difficult to track in TEM due to the time required to assemble the liquid cell holder and vacuum check. Then heterogeneous nucleation tends to happen on two SiN membranes because it lowers the activation energy for achieving critical nucleus size [47]. Moreover, electron beam may alter local chemistry, resulting in supersaturation, heating and bubble movement [28-30]. During in-situ imaging, special attention was paid to avoid electron beam effects using less exposure and minimizing time on a certain area. The detailed explanation on electron beam effects was also included in authors' previous study. Regarding QXRD analysis, main hydrated and anhydrous phases are considered using Rietveld refinement. It is to be noted that the sudden increase of  $C_3A$  at 3 h is probably due to the experimental error. As mentioned previously, quantification of monosulfate is not conducted since it has no defined crystal structure and low content.

#### **4.4. Conclusions**

This work is to provide kinetics information on hydration reactions of nano Portland cement. Combining isothermal calorimetry, Rietveld analysis and LC-TEM data including heat curves, quantitative phase transformation results, and structure morphology were used to analyze hydration reactions.

LC-TEM is a powerful tool to observe microstructure evolution of different cement hydration stages. The C-S-H precipitates nucleate on the cell membrane and collapse

to form a network. These C-S-H precipitates grow along the margin of existing sheets, and then also develop in 3D that was proved from the contrast change in LC-TEM experiment. The needlelike ettringites contribute to the formation of precipitates on the surface due to the seeding effects. Some C-S-H precipitates grow to about 300 nm in size. Post-situ TEM experiments indicate the nanocrystalline nature of C-S-H. It also sees an increasing content of C-S-H, which tend to grow together and form a network during the acceleration stage. In deceleration stage, the SiN membrane is fully covered with planar C-S-H sheets with cracks inside. We also report real-time dissolution of needle-like ettringite crystals.

The prepared nano Portland cement reacts in an undersulfated way, in which large broad silicate peak appears later than aluminate peak. The initial reaction period includes the dissolution of  $C_3S$ , nucleation of C-S-H and ettringite formation. The reaction rate of C-S-H formation slows down, and many C-S-H precipitates appear on SiN membrane in the end of this period. Induction period starts at around 3 h with further C-S-H nucleation and partial growth, and formation of ettringite. Although part of ettringite is dissolved releasing sulfate to form monosulfate, it has a net accumulation over time. The main silicate peak in heat flow curve of nano PC appeared much later than that of OPC, which exhibited retardation effects caused by reduction of C-S-H surface area by monosulfates for newly formed precipitates.

The present results relate phase transformation and structure development in different hydration stages. We hope to provide new insights on hydration kinetics, the

interactions of various phases in cement reactions. The methods will be applied to other cementitious systems including OPC with nano-silica in the future.

#### **4.5 Acknowledgements**

We thank staff at Canadian Center for Electron Microscopy (CCEM) for technical support. We also thank Prof. Todd Hoare and Mr. Ali Affar for the assistance on lyophilization facility and Miss Victoria Jarvis for the help and discussion on QXRD.

#### **4.6 References**

1. Pintér, F. and C. Gosselin, *The origin, composition and early age hydration mechanisms of Austrian natural Portland cement*. Cement and Concrete Research, 2018. **110**: p. 1-12.
2. Mehta, P. and P. Monteiro, *M. Concrete: microstructure, properties, and materials*. 3rd. New York, 2006.
3. Elsen, J., G. Mertens, and R. Snellings, *Portland Cement and other Calcareous Hydraulic Binders*, in *Advances in the characterization of industrial minerals*. 2010. p. 441-479.
4. Hesse, C., F. Goetz-Neunhoeffler, and J. Neubauer, *A new approach in quantitative in-situ XRD of cement pastes: Correlation of heat flow curves with early hydration reactions*. Cement and Concrete Research, 2011. **41**(1): p. 123-128.
5. Bullard, J.W., et al., *Mechanisms of cement hydration*. Cement and Concrete Research, 2011. **41**(12): p. 1208-1223.

6. Juilland, P., et al., *Dissolution theory applied to the induction period in alite hydration*. Cement and Concrete Research, 2010. **40**(6): p. 831-844.
7. Jennings, H. and P. Pratt, *An experimental argument for the existence of a protective membrane surrounding Portland cement during the induction period*. Cement and Concrete Research, 1979. **9**(4): p. 501-506.
8. Nicoleau, L., *Accelerated growth of calcium silicate hydrates: Experiments and simulations*. Cement and Concrete Research, 2011. **41**(12): p. 1339-1348.
9. Nicoleau, L., A. Nonat, and D. Perrey, *The di- and tricalcium silicate dissolutions*. Cement and Concrete Research, 2013. **47**: p. 14-30.
10. Nicoleau, L., M.A. Bertolim, and L. Struble, *Analytical Model for the Alite (C3S) Dissolution Topography*. Journal of the American Ceramic Society, 2016. **99**(3): p. 773-786.
11. Nicoleau, L. and A. Nonat, *A new view on the kinetics of tricalcium silicate hydration*. Cement and Concrete Research, 2016. **86**: p. 1-11.
12. Cuesta, A., et al., *Multiscale understanding of tricalcium silicate hydration reactions*. Sci Rep, 2018. **8**(1): p. 8544.
13. Minard, H., et al., *Mechanisms and parameters controlling the tricalcium aluminate reactivity in the presence of gypsum*. Cement and Concrete Research, 2007. **37**(10): p. 1418-1426.
14. Bhanumathidas, N. and N. Kalidas, *Dual role of gypsum: Set retarder and strength accelerator*. Vol. 78. 2004. 170-173.

15. Quennoz, A. and K.L. Scrivener, *Interactions between alite and C3A-gypsum hydrations in model cements*. Cement and Concrete Research, 2013. **44**: p. 46-54.
16. Jansen, D., et al., *Does Ordinary Portland Cement contain amorphous phase? A quantitative study using an external standard method*. Powder Diffraction, 2011. **26**(1): p. 31-38.
17. Kjellsen, K.O. and H. Justnes, *Revisiting the microstructure of hydrated tricalcium silicate—a comparison to Portland cement*. Cement and Concrete Composites, 2004. **26**(8): p. 947-956.
18. Scrivener, K.L., et al., *Quantitative study of Portland cement hydration by X-ray diffraction/Rietveld analysis and independent methods*. Cement and Concrete Research, 2004. **34**(9): p. 1541-1547.
19. Korpa, A., T. Kowald, and R. Trettin, *Phase development in normal and ultra high performance cementitious systems by quantitative X-ray analysis and thermoanalytical methods*. Cement and Concrete Research, 2009. **39**(2): p. 69-76.
20. Walenta, G. and T. Füllmann, *Advances in quantitative XRD analysis for clinker, cements, and cementitious additions*. Powder Diffraction, 2004. **19**(1): p. 40-44.
21. Merlini, M., et al., *The early hydration and the set of Portland cements: in situ X-ray powder diffraction studies*. Powder Diffraction, 2007. **22**(3): p. 201-208.
22. Álvarez-Pinazo, G., et al., *Rietveld quantitative phase analysis of Yeelimite-containing cements*. Cement and Concrete Research, 2012. **42**(7): p. 960-971.

23. Jansen, D., et al., *The early hydration of Ordinary Portland Cement (OPC): An approach comparing measured heat flow with calculated heat flow from QXRD*. Cement and Concrete Research, 2012. **42**(1): p. 134-138.
24. Hesse, C., et al., *Quantitative in situ X-ray diffraction analysis of early hydration of Portland cement at defined temperatures*. Powder Diffraction, 2009. **24**(2): p. 112-115.
25. Ross, F.M., *Electrochemical nucleation, growth and dendrite formation in liquid cell TEM*. Microscopy and Microanalysis, 2010. **16**(S2): p. 326-327.
26. Dukes, M.J., et al., *Three-dimensional locations of gold-labeled proteins in a whole mount eukaryotic cell obtained with 3nm precision using aberration-corrected scanning transmission electron microscopy*. J Struct Biol, 2011. **174**(3): p. 552-62.
27. Zhu, G.-Z., et al., *In Situ Liquid Cell TEM Study of Morphological Evolution and Degradation of Pt–Fe Nanocatalysts During Potential Cycling*. The Journal of Physical Chemistry C, 2014. **118**(38): p. 22111-22119.
28. de Jonge, N. and F.M. Ross, *Electron microscopy of specimens in liquid*. Nat Nanotechnol, 2011. **6**(11): p. 695-704.
29. Grogan, J.M., et al., *Bubble and pattern formation in liquid induced by an electron beam*. Nano Lett, 2014. **14**(1): p. 359-64.
30. Schneider, N.M., et al., *Electron–Water Interactions and Implications for Liquid Cell Electron Microscopy*. The Journal of Physical Chemistry C, 2014. **118**(38): p. 22373-22382.

31. Wang, C.-M., H.-G. Liao, and F.M. Ross, *Observation of materials processes in liquids by electron microscopy*. MRS Bulletin, 2015. **40**(01): p. 46-52.
32. Ross, F.M., *Opportunities and challenges in liquid cell electron microscopy*. Science, 2015. **350**(6267): p. aaa9886.
33. Nielsen, M.H., S. Aloni, and J.J. De Yoreo, *In situ TEM imaging of CaCO<sub>3</sub> nucleation reveals coexistence of direct and indirect pathways*. Science, 2014. **345**(6201): p. 1158-1162.
34. Smeets, P.J., et al., *Calcium carbonate nucleation driven by ion binding in a biomimetic matrix revealed by in situ electron microscopy*. Nat Mater, 2015. **14**(4): p. 394-9.
35. Alyasri, S.A.H., I.S. Alkroosh, and P.K. Sarker, *Feasibility of producing nano cement in a traditional cement factory in Iraq*. Case Studies in Construction Materials, 2017. **7**: p. 91-101.
36. Roddy, C.W., et al., *Cement compositions and methods utilizing nano-clay*. 2013, Google Patents.
37. Roddy, C.W., *Cement compositions and methods utilizing nano-hydraulic cement*. 2016, Google Patents.
38. Bickbau, M.Y., *Method for producing nano-cement, and nano-cement*. 2016, Google Patents.
39. Carmichae, M.J. and G.P. Arulraj, *Strength and permeability studies on concrete with Nano-Cement*. IJCIET, 2017. **8**(1): p. 132-139.

40. Taylor, H.F., *Proposed structure for calcium silicate hydrate gel*. Journal of the American Ceramic Society, 1986. **69**(6): p. 464-467.
41. Gartner, E.M., *A proposed mechanism for the growth of C-S-H during the hydration of tricalcium silicate*. Cement and concrete research, 1997. **27**(5): p. 665-672.
42. Gartner, E., I. Maruyama, and J. Chen, *A new model for the C-S-H phase formed during the hydration of Portland cements*. Cement and Concrete Research, 2017. **97**: p. 95-106.
43. Scrivener, K.L., P. Juilland, and P.J.M. Monteiro, *Advances in understanding hydration of Portland cement*. Cement and Concrete Research, 2015. **78**: p. 38-56.
44. Zhang, L., et al., *Hydration for the Alite mineral: Morphology evolution, reaction mechanism and the compositional influences*. Construction and Building Materials, 2017. **155**: p. 413-426.
45. Jansen, D., et al., *A remastered external standard method applied to the quantification of early OPC hydration*. Cement and Concrete Research, 2011. **41**(6): p. 602-608.
46. Bergold, S.T., F. Goetz-Neunhoeffler, and J. Neubauer, *Interaction of silicate and aluminate reaction in a synthetic cement system: Implications for the process of alite hydration*. Cement and Concrete Research, 2017. **93**: p. 32-44.
47. Jiang, N., *Note on in situ (scanning) transmission electron microscopy study of liquid samples*. Ultramicroscopy, 2017. **179**: p. 81-83.

## **5. The Effects of Nano-silica on Early-age Hydration Reactions of Nano Portland Cement**

Peng Dong<sup>1</sup>, Ali Allahverdi<sup>2</sup>, Carmen M. Andrei<sup>3</sup>, and Nabil D. Bassim<sup>1,3</sup>

1. Department of Materials Science and Engineering, McMaster University, 1280 Main St W, Hamilton, ON L8S 4L8, Canada

2. Cement Research Centre, School of Chemical Engineering, Iran University of Science and Technology, Narmak 16846 – 13114, Tehran, Iran

3. Canadian Centre for Electron Microscopy, McMaster University, 1280 Main St W, Hamilton, ON L8S 4L8, Canada

**Author contributions:** In Chapter 5, the research focus is the effects of nano-silica on early-age hydration reactions of nano cement. Mr. Peng Dong conducted most experiments and data analysis with the help of Dr. Ali Allahverdi and Dr. Carmen Andrei. Dr. Nabil Bassim and Dr. Ali Allahverdi provided very important discussion on this topic. The manuscript was initially drafted by Mr. Peng Dong and edited to the final version by Dr. Ali Allahverdi, Dr. Carmen Andrei and Dr. Nabil Bassim. The manuscript will be submitted to Nanoscale.

## **Abstract**

The use of nano hydraulic cements along with supplementary cementitious nanomaterials to enhance microstructure development and properties has been of great interest for designing better concretes. The introduction of nanoscience and nanotechnology to the cement industry has a huge potential to reduce the carbon footprints of cement productions. The early-age hydration kinetics, microstructural evolution and corresponding phase transformations have long been the subjects of cement and concrete research. To this end, the hydration reactions of nano Portland cement (NPC) with and without NS additives were realized and tracked for the first time in a liquid cell transmission electron microscope (LC-TEM), coupled with isothermal calorimetry and quantitative X-ray diffraction (QXRD). We revealed the different hydration mechanisms in nano PC and OPC in the presence of nano-silica (NS). The results showed that NS shortened the dissolution and induction periods of the hydration reaction significantly in OPC systems. The fact that NS contributed less to hydration reactions in NPC systems resulted from the size effect that nano cement with a much higher surface area and reactivity hydrated much faster to a high degree by itself. The LC-TEM observations found that NS was adsorbed on the surfaces of needle-like ettringite crystals accelerating their conversion into monosulfate, and thus achieving lower contents of ettringite in NPC with NS.

**Key words: nanoscience, LC-TEM, QXRD, heat release, early-age hydration**

## 5.1. Introduction

Cement hydration is a complex process because of the presence of various phases and the interdependence of different chemical reactions. Understanding hydration mechanisms and kinetics will facilitate controlling of the hydration rate and the design of desirable concretes. The early hydration reactions include dissolution and precipitation reactions, which are further divided into mainly four time periods, namely, initial period, induction period, acceleration period and deceleration period [1].

In the first few minutes of mixing Portland Cement (PC) with water, ettringite ( $C_3A \cdot 3\bar{C}\bar{S}_3 \cdot H_{32}$ ,  $C = CaO$ ,  $A = Al_2O_3$ ,  $\bar{S} = SO_3$ ,  $H = H_2O$ ) is precipitated from dissolved calcium aluminate ( $C_3A$ ), calcium sulfate and water [2]. Also, tricalcium silicate ( $C_3S$ ,  $S = SiO_2$ ) starts dissolving during the initial stage [2, 3]. The induction stage is a slow reaction period and various theories have been proposed for the existence of this period. One hypothesis suggests that a thin metastable calcium silicate layer is formed covering the surface of cement particles, and that the continuous layer of calcium silicate hydrate prevents the diffusion of water and ions to the reaction surface and thus inhibits further hydration reactions [1, 4-6]. An alternative hypothesis proposes that the undersaturation of solution with regard to  $C_3S$  leads to slow dissolution and contributes to the decrease in reaction rate based on a balance between precipitate growth and particle dissolution [7]. Juilland et al. [8] further ascribed the slow dissolution process observed during the induction period to the formation of etch pits at dislocations of alite that dropped under a high level of undersaturation. Further evidence on kinetics principles between dissolution rate and undersaturation was obtained by Nicoleau et al [3, 9] and the increase of reactivity by etch pit opening was also discussed [10, 11]. It was also reported that the presence of aluminium ions inhibits alite hydration, while the addition of gypsum ( $CaSO_4 \cdot 2H_2O$ ) leads to the acceleration of reactions in alite and  $C_3A$ -gypsum systems [12]. Some researchers believed that this was due to the absorption of an Al-rich layer or

aluminates on hydroxylated  $C_3S$  by ionic interactions [13, 14]. Bergold et al. [15] pointed out that the precipitation of AFm (monosulfate,  $3CaO \cdot (Al,Fe)_2O_3 \cdot CaSO_4 \cdot nH_2O$ ) phases instead of Al-inhibition process resulted in hindering effects on silicate reactions. Reaching a critical point, the rate of C-S-H formation starts to accelerate [16], which may suggest a nucleation and growth mechanisms [7]. The C-S-H growth mechanisms have been debated for decades, with two main theories of layered structure models [17-19] or colloidal models [20, 21]. Many efforts have been devoted to C-S-H growth mechanisms including simulation [5, 22], X-ray diffraction [2, 23] and electron microscopy [24-26], while it still needs further elucidation. The deceleration stage may result from the lack of small particles, the consumption of water and less space and thus a slower diffusion process [1, 27].

The concepts of nanomaterials and nanotechnology have attracted much attention in recent decades [28]. It is promising to further understand the fundamentals of cement chemistry and clarification of microstructural changes in nanoscale and microscale by applying the tools of nanoscience and cutting-edge characterization techniques to cement and concrete research [29, 30]. Some studies on nano cement [31-33] were reported with an aim to improve the compressive strength and durability and reduce the amount used to make concretes, but none was focused on microstructural evolution and hydrated products. The application of nano-silica (NS) with higher surface area and reactivity in concrete contributes to higher strength and durability [30, 34, 35]. This is mainly due to the seeding effect (nanomaterials provide large surface area for precipitation), pozzolanic reaction (silica-rich precursor reacts with  $Ca(OH)_2$  to form C-S-H) and the filler effect (can fill internal porosity defects) [29, 36]. The conflicting effects of NS on compressive strength have also been reported because of agglomeration and the form of NS and difficulties in achieving an effective dispersion of nanoparticles [37, 38]. In order to clarify these effects, more efforts are needed to clarify the role of NS on hydration kinetics and hydrated products.

In this paper, we make efforts to better comprehend the correlated relationship among hydration chemistry, kinetics and microstructural evolution of nano Portland cement (NPC) in early age up to 24 h using nanoscale experimental techniques. We further clarify the effects of NS on microstructure, heat release and contents of hydrated products in NPC system. The heat flow curves of NPC and OPC systems are compared, and different factors controlling hydration kinetics are discussed as well. Figure 5.1 shows a schematic of different hydration reaction processes in nano and OPC with NS. It is found that NS tends to attach to needle-like ettringite crystals and affects hydration mechanisms by accelerating ettringite conversion to monosulfate. The NPC achieves a larger hydration degree due to higher surface area and reactivity, in which the addition of NS plays a less crucial role. However, the incorporation of NS contributes more to hydration reactions in OPC resulting from seeding effect.

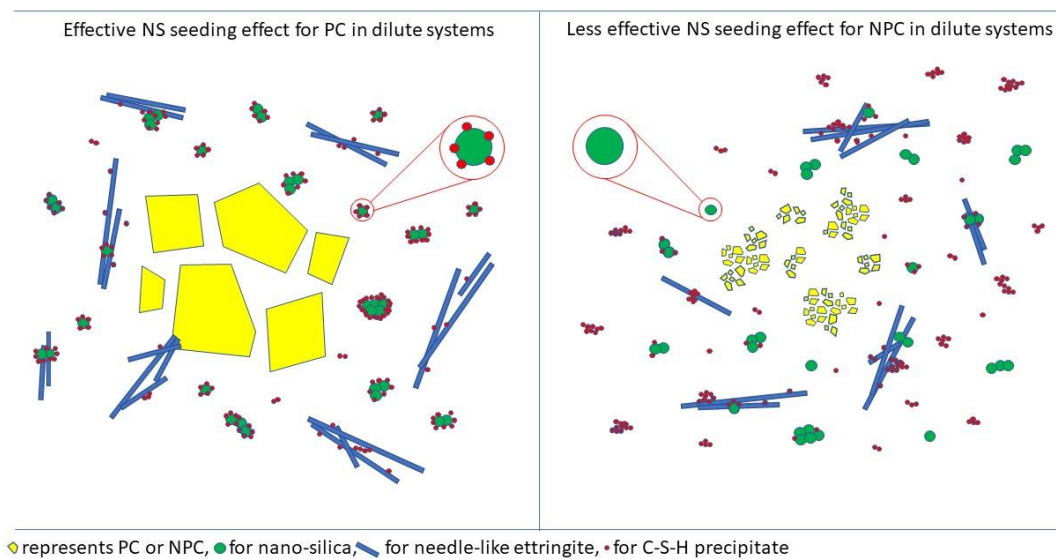


Figure 5.1 Schematic of hydration reactions in NPC and OPC with NS

## 5.2. Experimental

The NPC was prepared from commercial OPC with an average particle size of 45  $\mu\text{m}$ . Commercial OPC is not suitable for LC-TEM experiments due to the limitation of liquid cell geometry. Two-step ball milling was performed in the presence of anhydrous ethanol to reduce

the particle size, while a third-step dry ball milling was conducted to reduce particle agglomeration. The composition of OPC and the results of Rietveld analysis of NPC were given in Table S1. It was achieved that cement particles with size of less than 200 nm accounted for 83.0% in number. NS for research use was obtained from Sigma-Aldrich. The microstructure and morphology of NS were provided in Figure 5.A1.

The structural evolution of hydration products was observed in an in-situ liquid cell holder from Protochips Inc. In order to obtain structural information, the liquid used for transmission electron microscopy (TEM) experiments should be electron transparent which imposes a high dilution of the samples. Dilute suspensions were mixed in glass vials with the water/binder (w/b) ratio of 15, sonicated for 5 min and transferred onto a small chip using a micropipette. After assembly and vacuum checking, the liquid holder was inserted into the microscope (Thermofisher-FEI Titan, 300 keV). The in-situ imaging was performed over a span of 24 h and different areas of interests (AOIs) were tracked with time. To minimize beam effects, the electron beam was kept on any AOI no longer than 2-3 seconds. Scanning electron microscopy (SEM) in conjunction with energy dispersive spectroscopy (EDS) was performed in a JEOL JSM-7000F to obtain structural and elemental information of hydrated products after the in-situ experiments. The chips were coated with a thin layer of carbon (10 nm) to reduce the charging. An electron beam energy of 9 keV and working distance of 10 mm were used during imaging.

The heat flow of both NPC and OPC was obtained on a I-Cal 8000 HPC, 8-channel isothermal high precision calorimeter. The dispersed NS was prepared by mixing 0.02 g NS with 20 ml water, followed by sonication for ten minutes. In the meantime, 0.01g mono (SP, MasterGlenium 7500, as dispersant) was mixed well with 10 ml water. Then a 2 ml sample of dispersed NS and 1 ml SP were taken respectively, and further mixed into a suspension. Dilute suspensions with the same w/b ratio of 15 were mixed in suction cups, where the weights of

binders and water were 7.0 g and 105.0 g, respectively. In both systems, cements were replaced by 1.0 wt% NS, while cements without replacements were taken as control samples. The curing temperature was set to 25 °C and the heat flow was monitored for 24 h.

The ex-situ samples were also prepared for quantitative XRD and Rietveld analysis. Six reaction times were selected combining LC-TEM and calorimetry data, which included 0.5 h, 1.5 h, 3 h, 5 h, 14 h, and 24 h. Two systems of nano cements with and without NS were mixed in falcon tubes at the same w/b ratio. To stop hydration reactions at the end of selected reaction times, the dilute suspensions were immersed in liquid nitrogen, and freeze-drying process was applied under the condition of below -80 °C. Then a D8 diffractometer (Bruker) was used to collect the diffraction patterns of dried samples with a step width of 0.02° and 2500 s per step. The voltage and current were 35 kV and 45 mA, respectively. The 2θ range of diffraction patterns were from 8° to 70°. After phase identification, Rietveld refinement was conducted on TOPAS 3.0 (Bruker). It worked by refining all known parameters of crystalline phases including structures, space groups and peak profiles, in which crystalline phase contents normalized to 100% can be obtained. It is worth noting that C-S-H content cannot be determined directly from refinement due to lack of certain structural information. It was calculated based on Rietveld results and the assumption that Portlandite was merely the by-product of C<sub>3</sub>S [2]. The contents of crystalline and amorphous phases were recalculated and normalized to 100%.

### **5.3. Results and Discussion**

The heat flow curves of NPC and NPC with NS at 25 °C are shown in Figure 5.2 (a) and the corresponding cumulative heat curves are shown in Figure 5.2 (b). Figure 5.3 exhibits heat flow and cumulative heat curves of OPC and OPC with NS. The four main hydration stages of nano systems are to be characterized combining heat flow and cumulative heat curves in Figure 5.2. The heat flow curve shows similar shapes in two systems that are mainly acceleration and

deceleration stages. It seems that the initial stage (dissolution stage) and induction periods of two nano systems are too short to distinguish in comparison to those of OPC systems. The duration of initial and induction periods of NPC with NS lasts a little bit longer than that of NPC system from heat flow curve and the total heat of NPC with NS within 24 h is slightly lower than that of NPC without NS as seen in cumulative heat curve. This is due to the size effect in NPC systems compared to OPC (to be discussed later) and/or probably a slight retardation effect caused by SP [39], which was added to disperse NS in water followed by ultrasonication.

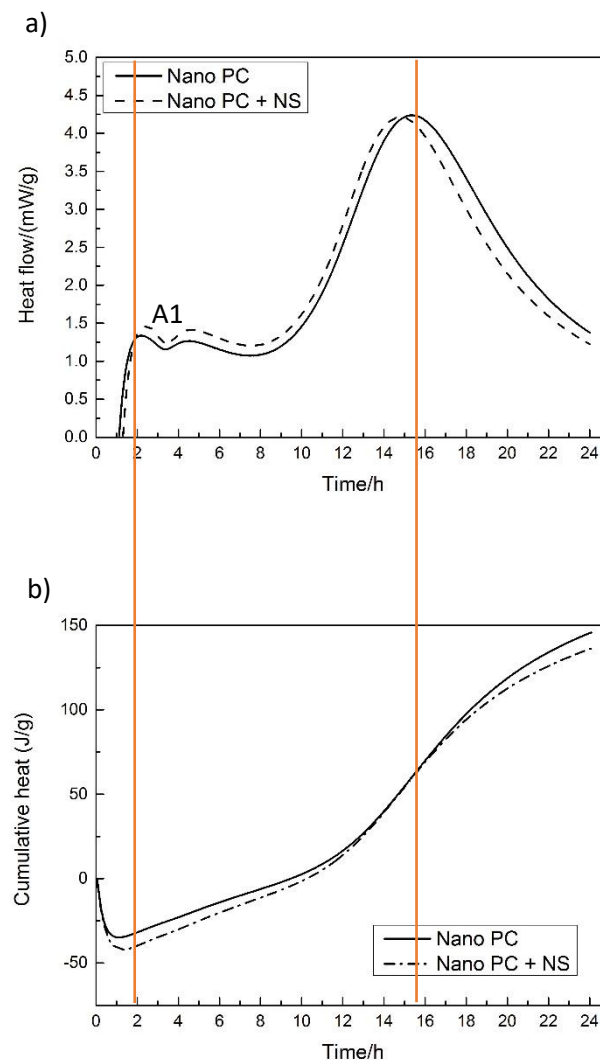


Figure 5.2 Heat flow and cumulative heat curves of nano PC and nano PC with NS (yellow lines indicate the end of induction period and the silicate peak of nano PC with NS, respectively)

Also, another retardation effect in comparison to OPC that is very significant was observed in both systems shortly after the start of acceleration stage (about 2 h). This is attributed to ettringite conversion to monosulfate (peak A1), which covered C-S-H and reduced its surface for further formation and precipitation [12]. The acceleration stage of NPC with NS starts a little later, while the formation rate of hydration products in acceleration stage is higher in NPC with NS than that in NPC. The main C-S-H peak for the NPC with NS shows hydration reactions in following three aspects. First, a small shift of the main silicate peak of NPC with NS was observed. The system with NS attains the maximum heat evolution rate (the peak in the acceleration stage) almost 1 h earlier than the system without NS. Second, the heat flow curves show a slightly narrower peak compared to the system without NS, which is similar to the effect in concentrated (reducing w/c ratio) cement slurry [40]. The systems with lower w/c ratios result in higher concentrations of ions in the solution that may lead to earlier supersaturation and thus accelerated hydration reactions. It is worth noting that NS dissolves in water especially when the pH value rises due to the release of  $\text{Ca(OH)}_2$  [1] and dissolution of NS helps in increasing ion concentration in the solution [1].

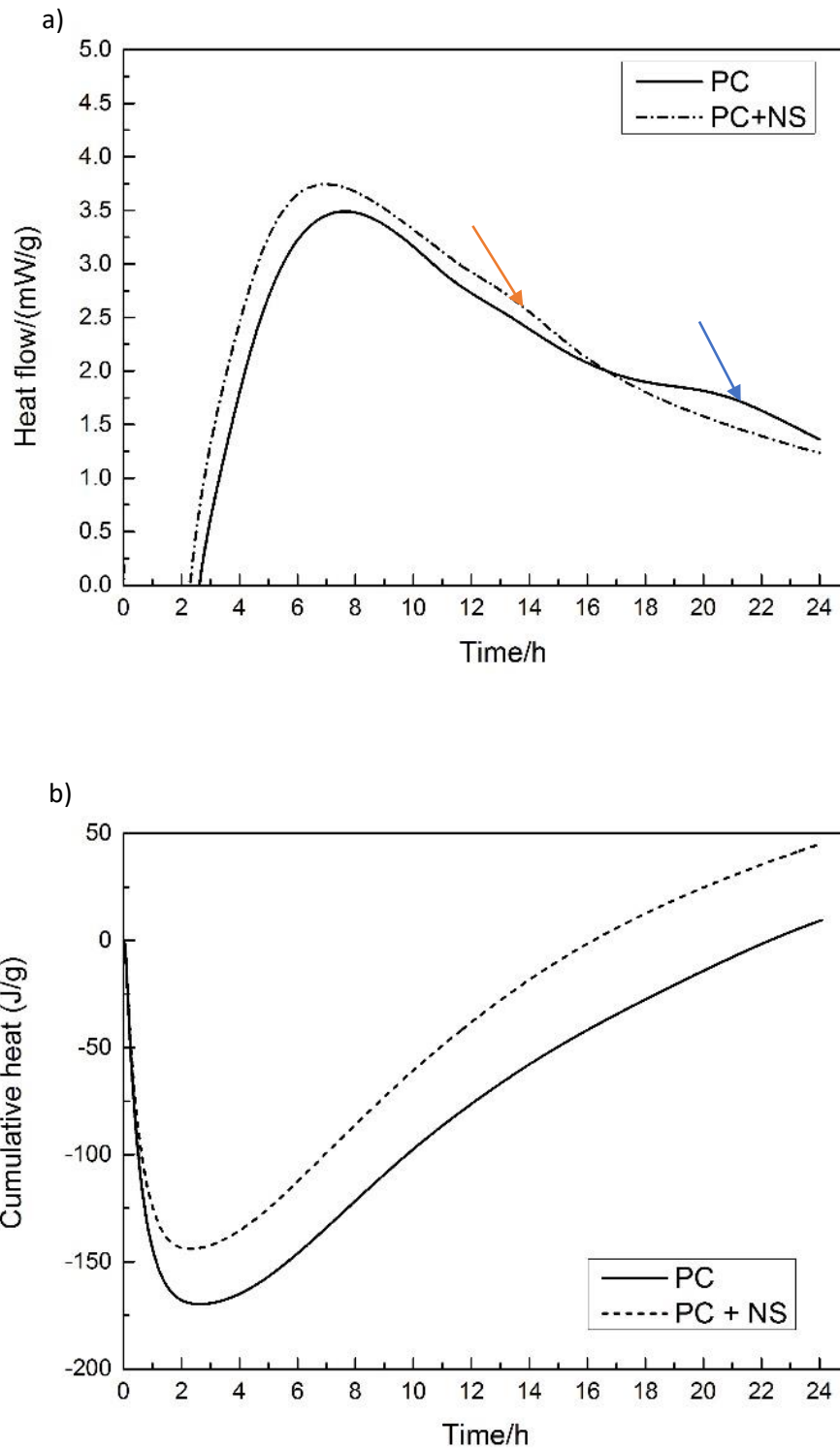


Figure 5.3 Heat flow and cumulative heat curves of OPC and OPC with NS (blue arrow show aluminate peak of PC and yellow arrow show aluminate peak of PC with NS)

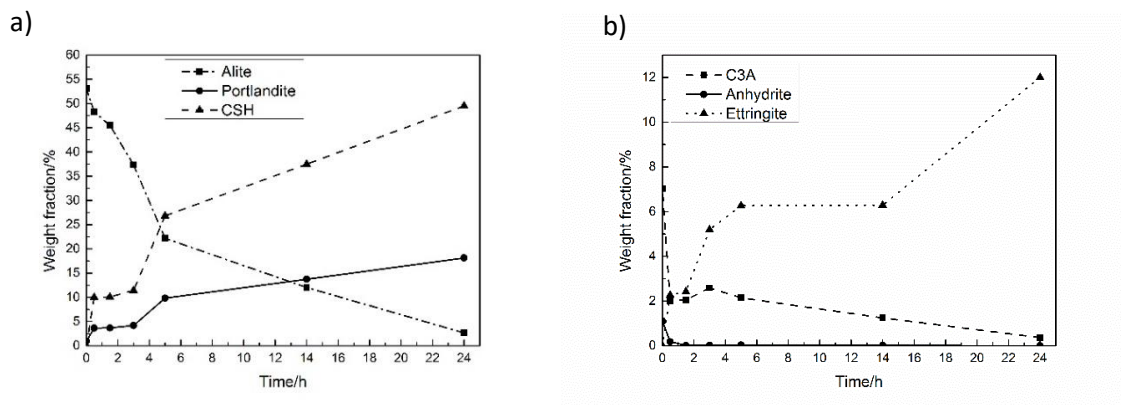
The dissolution and induction periods of OPC with or without NS (Figure 5.3) were longer, compared to those in nano systems. In a dilute system of OPC with NS, the main aluminate

peak appeared early and the formation of ettringite was less compared with that of OPC from heat flow curve [16]. In the case of NPC, addition of NS resulted in faster conversion of ettringite to monosulfate. The decrease in  $C_3A$  showed that formation of ettringite was 1.99% after hydration for 1.5 h, and it was soon converted to monosulfate. The results of OPC with and without NS are consistent with those of NPC with and without NS in terms of the role of NS on aluminate reactions. Clearly, the role of NS on initial and induction stages of nano and normal systems is different. First, the initial induction stage in OPC with NS was shorter than that of PC without NS even in the presence of SP, which was reverse of what observed in NPC systems.

This difference may be attributed to the size effects [8, 39] comparing the two PC and NPC systems with NS. In OPC with NS system, the dissolution rate of cement in the initial stage is comparatively slower due to limited dissolving surface of much larger cement particles with an average size of 45  $\mu\text{m}$ . In such a case, the nucleation seeding effect of NS plays a remarkable role in promoting the rate of cement dissolution which in turn shortens the induction period and result in an earlier acceleration stage, compared to a plain OPC system. In NPC systems, however, a relatively huge dissolving surface is at work leading to much higher rate and degree of dissolution and hydration in a highly dilute suspension even in the absence of NS. Therefore, the seeding effect of NS in highly dilute NPC systems, is insignificant, and the fast dissolving and hydrating nano cement particles with comparatively less reactive NS slightly postpones the start of acceleration stage and reduces the hydration heat slightly.

The phase transformation of NPC with and without NS was evaluated using Rietveld refinement of x-ray diffraction data, shown in Figure 5.4. In both nano systems, C-S-H and portlandite contents increased with time in the consumption of  $C_3S$ . It was observed that C-S-H and portlandite contents went up sharply in first 0.5 h, which indicated a high reaction rate in dissolution stage due to the large surface area of nano cement. The contents remained

relatively consistent between 0.5 h to 3 h during the induction period and subsequent early acceleration stage that retardation effects occurred, and they went up in acceleration and deceleration stages later. Figure 5.4 (e) also compares the C-S-H and ettringite contents of the two systems. As seen, NPC with NS shows a higher content of C-S-H and a lower content of ettringite, compared to plain NPC. In terms of aluminates reactions,  $C_3A$  and anhydrite contents exhibited downward trends in both nano systems, while anhydrite went down sharply in first 0.5 h confirming fast dissolution of anhydrite nano particles in a highly dilute cement suspension. The ettringite content of plain NPC system shows an upward trend (Figure 5.4 (b)), indicating a net accumulation in the first 24 h. On the other hand, the ettringite content in NPC with NS dropped from 1.5 h to 14 h and then increased at 24 h in the end. It is worth noting that a slight increase in  $C_3A$  content at 3 h of hydration is just a measurement error and evidently there should be no increase in the cement phase contents during hydration.



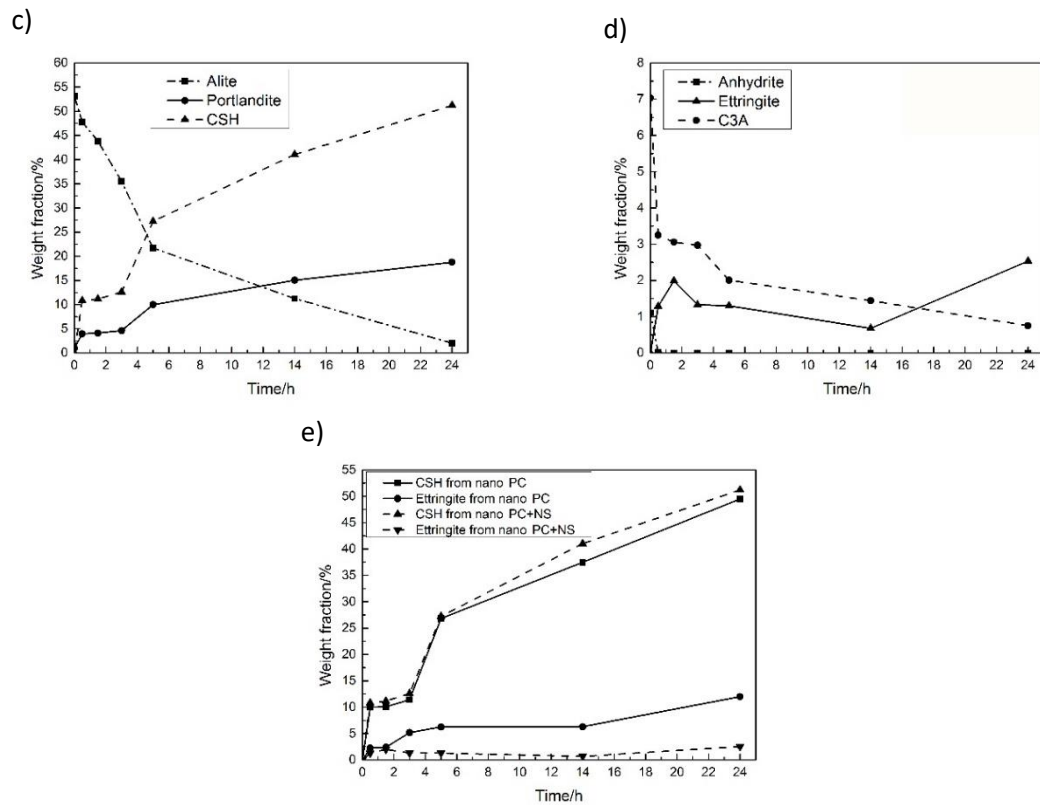


Figure 5.4 Phase evolution of plain NPC (a & b), NPC with nano silica (c & d) and phase contents of C-S-H and ettringite in the two systems (e).

The hydrated products and microstructure evolution were captured in LC-TEM. Nano cement dissolved after mixing with water. The occurrence of needle-like ettringite crystals, a product of aluminate and sulfate with water was observed from the beginning of reactions in LC-TEM. Figure 5.5 (a) shows ettringite crystals that precipitated and provided nucleation sites for other hydrated products. The main hydrated product, C-S-H round precipitates was observed to increase in the amount (number and size) from Figure 5.5 (b) to (c), which was consistent with the peaks in heat flow curve at 3 h and 5 h. The C-S-H precipitates (Figure 5.5 (d)) fully covered the liquid cell during the third peak of heat flow curve. at 15 h. C-S-H precipitates formed a network upon further growth (Figure 5.5 (e)). The morphology of sheet-like C-S-H and embedded portlandite (Figure 5.A2) were further confirmed using SEM.

It was observed that reaction sequences of NPC with NS were similar to those of plain NPC. The ettringite crystals were found since early hydration reactions (Figure 5.6 (a)). Some of

them dissolved with time, releasing sulfate ions, which are shown in Figure 5.6 (b), acquired in the same area of interest (AOI). In terms of the morphology of C-S-H precipitates, the addition of NS led to more dispersed precipitates. (Figure 5.6 (c), (d) and (e)). It is worth mentioning that C-S-H precipitates were less likely to dissolve because the amount of  $\text{Ca}(\text{OH})_2$  from complete hydration of  $\text{C}_3\text{S}$  in 0.2g cement is more than 10 times enough for saturation of 3 ml water, and the pH of the suspension was confirmed to be 12.73 before the holder was inserted into microscope. Moreover, the ettringite crystals were observed to dissolve due to the presence of NS, which was consistent with quantitative XRD results. The SEM results (Figure 5.A3) also confirmed the sheet-like morphology of C-S-H in NPC with NS. Also, needle-like ettringite and hexagonal portlandite crystals were covered with C-S-H precipitates.

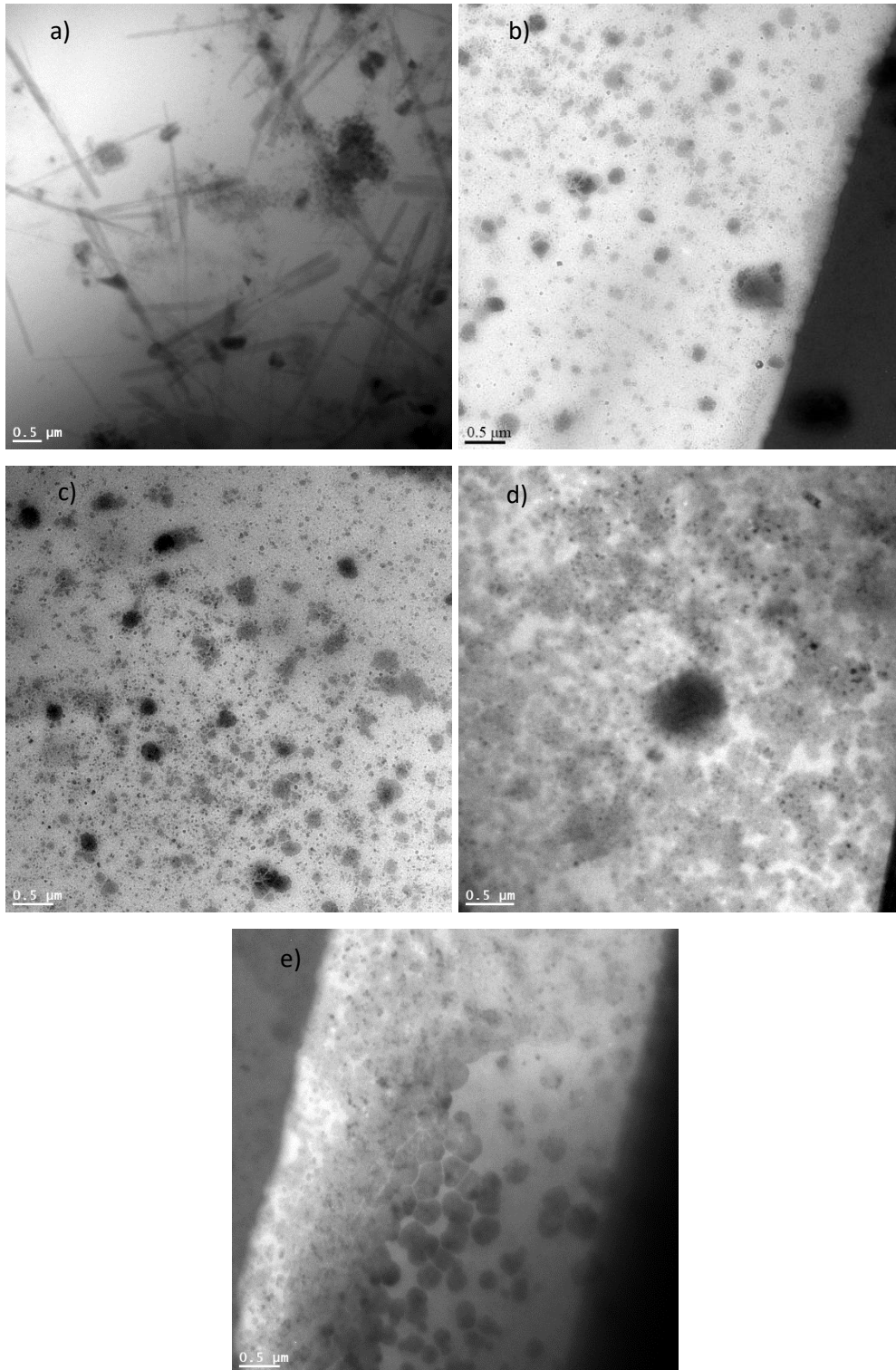


Figure 5.5 LC-TEM images showing microstructure of different areas and time scales in NPC a) 1 h 35 min, b) 3 h 10 min, c) 4 h 52 min, d) 14 h 06 min and e) 24 h 21 min

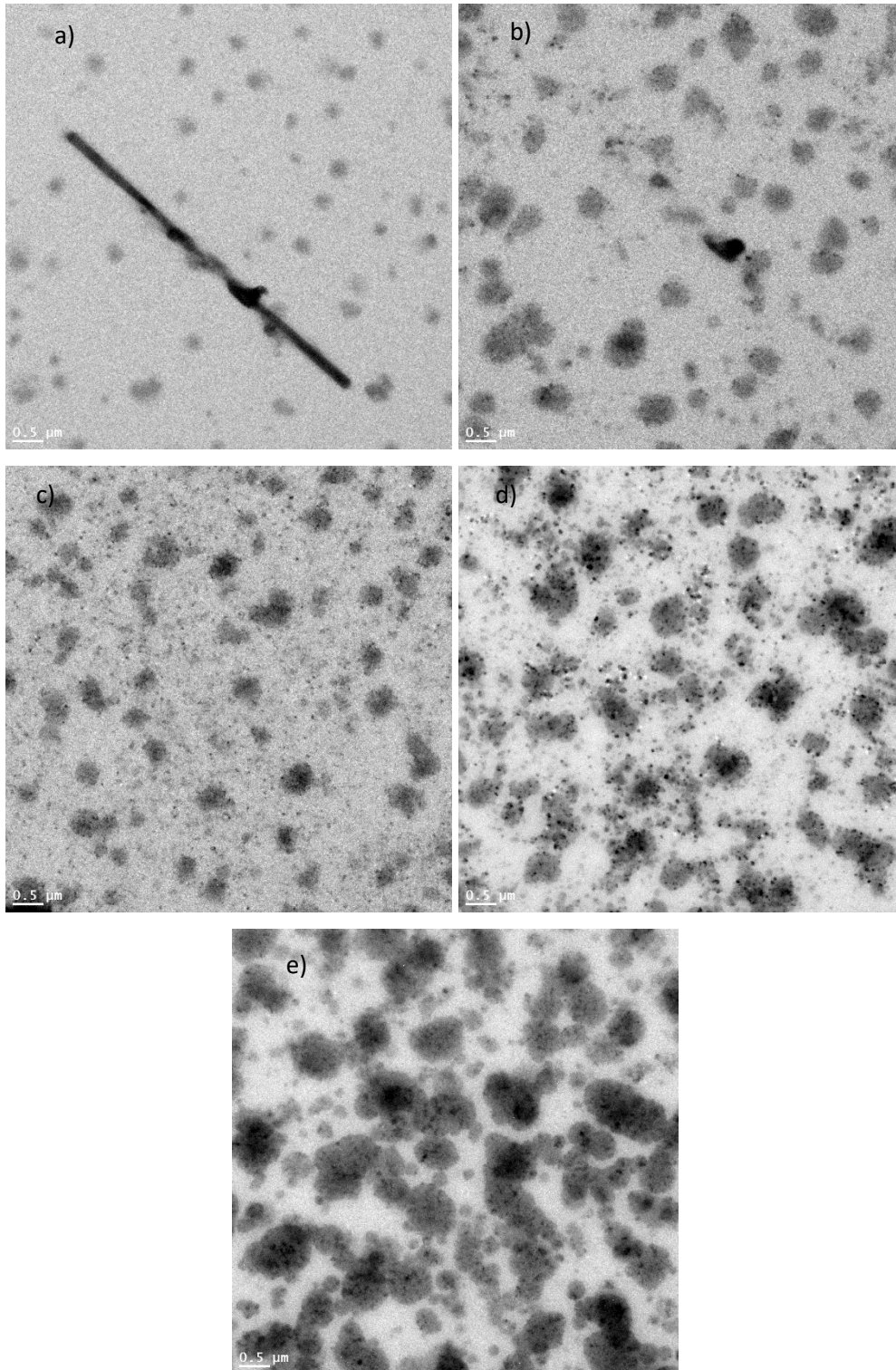


Figure 5.6 LC-TEM images showing microstructure at different time scale in NPC with NS, a) 1 h 48 min, b) 2 h 47 min (same area as first image), c) 4 h 36 min, d) 14 h 16 min and e) 23 h 58 min

Figure 5.7 displays LC-TEM images showing attachment of NS and precipitates to the ettringite crystals. Without plasma cleaning, the surfaces of the  $\text{Si}_3\text{N}_4$  inside liquid cell chips exhibit hydrophobic properties and the tendency of NS to attach to the membranes were

significantly reduced. It was observed that NS tended to adhere to precipitated ettringite crystals, as shown in Figure 5.7 (a). These NS with large surface area provided more nucleation sites for C-S-H precipitates. Afterwards, newly formed C-S-H grew together. This explained the fact that C-S-H precipitates grew along the direction of needles as seen in Figure 5.7 (b). In addition, LC-TEM observations clearly showed that attachment of NS to ettringite crystals resulted in an acceleration in ettringite conversion to monosulfate (V. 5.A1).

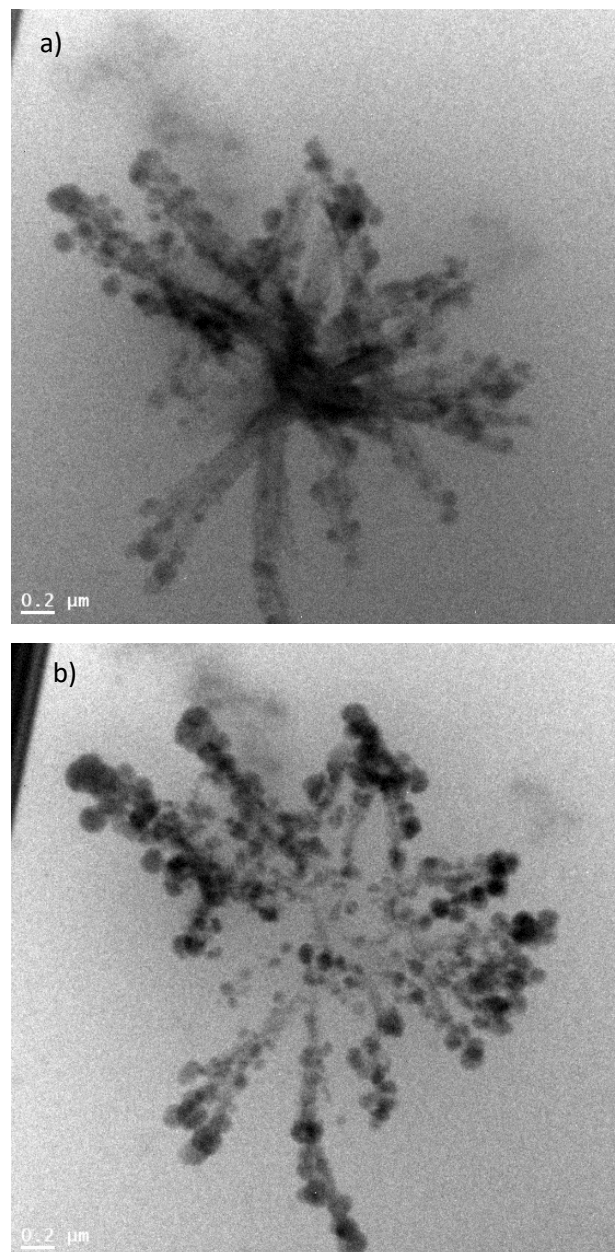


Figure 5.7 a) NS attachment to needle-like ettringite crystals and b) subsequent C-S-H nucleation and growth inside chips without plasma cleaning in advance

In concentrated OPC paste, heat flow curves are relatively sharp [7, 41, 42], while for dilute suspensions they are relatively broad peaks. This is due to both dilution and temperature effects [12]. In concentrated systems, the very high ions concentrations in the cement suspension results in an acceleration in  $C_3S$  hydration [22]. Moreover, the relatively low ions concentrations in dilute suspensions reduces the rate of hydration of  $C_3S$  and results in broader peaks [43, 44]. Also, hydration at relatively low temperatures results in broader heat peaks. The negative heat flow in the induction period as discussed before was caused by temperature setting [12]. The shoulder seen in the heat flow curve of OPC due to the final ettringite formation disappeared in both nano systems. The QXRD results showed that final ettringite formation shifted to earlier times when C-S-H main hydration reaction occurred. This means that final ettringite formation peak is superimposed to the main C-S-H peak due to the fineness effect on hydration reaction kinetics.

The NPC curves in this study are similar to dilute OPC systems except in the following aspects: A very small exothermic peak at time zero was observed, which was due to both fineness (causing fast reaction) and very high dilution (lowering the heat density). The starting time of the acceleration stage was earlier for NPC by almost one hour, resulting from high reaction surface provided by NPC. The plateau in the acceleration stage showed a retardation effect in  $C_3S$  hydration as well. Then, the size of the last big peak (C-S-H and ettringite formation peak) resulted from both the NPC fineness and the pozzolanic reactions that finally overcome the retardation effect. The retardation effect at the beginning of the acceleration stage might be due to traces of ethanol remained in NPC. It is known that poly-alcohols and alcohol amines provide retarding effects at very low concentrations, but unfortunately there are few published results on ethanol or ethyl alcohol [39, 45]. Another probable reason is the ettringite formation that might inhibit  $C_3S$  hydration by reducing the C-S-H precipitating surface [14]. This may result in a retardation effect in the acceleration stage. The phase transformation

indicated that  $C_3S$  decreased with time in plain NPC and NPC with NS. For silicate reactions, fast dissolution of  $C_3S$  and nucleation of C-S-H happen in the first 0.5 h. Then the reaction rate slowed down till 3 h, which was consistent with first peak. Further nucleation and growth of C-S-H around 3 h that also confirmed by LC-TEM contributed to second peak in nano systems. During acceleration and deceleration stages, the C-S-H contents went up due to continued hydration, shown by LC-TEM results. For aluminate reactions, anhydrite serves as a source of sulfate ions, which dissolves in the beginning of the reactions and remains in the solution to form ettringites with gradually dissolved  $C_3A$ . The dissolution behaviors of sulfate and  $C_3A$  were also reported by Bergold et al. [15]. In two nano systems, NS led to faster C-S-H nucleation process and more in phase contents, indicating its role to promote nucleation and growth process. In NPC with NS, ettringite contents appeared to be lower due to its accelerated conversion to monosulfate that further reduced the reaction surface for newly formed precipitates, and thus retarded the reaction [14, 15]. Compared with NPC system, more dissolution of ettringite were observed during LC-TEM imaging. In the experiment without plasma cleaning chips, we observed much more attachment of NS and precipitates to ettringite crystals, resulting in an acceleration in ettringite conversion to monosulfate and providing more nucleation sites for more C-S-H precipitation. This also explained the fact that the reaction rate of NPC with NS was higher than that in plain NPC during early stage of acceleration.

The incorporation of NS accelerates hydration kinetics in both OPC and NPC (more remarkably in OPC) in the following aspects. First, it provides more nucleation sites for C-S-H to precipitate resulting in a relatively higher rate of heat evolution in the acceleration stage [30, 36]. In NPC, this is shown in the first and second peaks, where the one with NS is higher than the one without it confirming a higher hydration degree of  $C_3A$  and  $C_3S$ . Second, the main C-S-H formation peak occurs almost as earlier as one hour in the dilute systems with NS. This is again a consequence of nucleation seeding effect of NS. Third, comparing the amounts of

ettringite formed in plain NPC and NPC with NS, it seems that NS has an impact on reducing the amount of ettringite. As mentioned in LC-TEM observations, NS particles were adsorbed on ettringite crystals as soon as they were formed. This surface adsorption of NS on ettringite crystals seemed to accelerate the conversion of ettringite to monosulfate.

The formation and transformation of monosulfate were confirmed through in-situ imaging and SEM. However, it was not considered in QXRD due to the lack of necessary crystal information as well as being in a minor content [46]. Many factors can affect the shape of heat flow curve, such as temperature setting, particle size effect, nucleation seeding effect, pozzolanic reaction and dilution. Pozzolanic reaction of NS (shown in equation 1) that results in a lower amount of heat evolution compared to C<sub>3</sub>S hydration can also contribute in a higher rate of heat evolution in the acceleration stage if it is incorporated as addition [47]. In this study, we replaced OPC and NPC by just 1 wt.% of NS. Replacement of cement with NS accelerates early hydration and results in a higher rate of heat evolution during acceleration stage, but it reduces the total amount of heat evolution upon almost complete hydration that requires long time calorimetry measurements. In the present work, the study was limited to early hydration (24 h) of PC and NPC. The amount of replacement is also important. NS is usually incorporated in relatively small amounts (less than 3 wt.%) because of difficulties in controlling w/c ratio and achieving a uniform dispersion due to its ultrahigh surface and strong agglomeration tendency. In this work, replacement of OPC and NPC with 1 wt.% NS would contribute to only 0.66% secondary C-S-H, under the assumption that NS fully reacted.



Equation 5.1 – Pozzolanic reaction

The negative parts of heat curves in the beginning is due to the set temperature in software. Some evidence can be found from the literature, where the usual shape of heat flow curve is

obtained at about 23 °C [16]. In this case, the original heat release is considered ‘positive’ by the software, while it is probably treated as negative when the controlling temperature is 25 °C in our case, meaning that the system has to input power to keep the temperature at set temperature. This result is also reported, in which a negative peak appeared at 26 °C and above [12]. Also, traces of residual ethanol in cement may affect the hydration kinetics, which need further clarification. LC-TEM has some limitations. The liquid suspension has to be highly dilute to provide a transparent medium so that electron beam can go through to achieve structural information. It is necessary that cement suspension be prepared in a very high w/c ratio. Furthermore, we miss the dissolution and precipitation within the first 1 h due to necessary preparation time.

#### **5.4. Conclusions**

The nano cements along with supplementary cementitious nanomaterials can lead to significant improvements in strength and durability in concretes. This study on the early-age hydration reactions of nano PC with and without NS shows the correlated relationships among microstructure, heat release and phase transformation, and the role that NS plays in above features.

First, the incorporation of NS shortens the dissolution and induction periods significantly in OPC. The acceleration stage appears 1 h earlier and the main silicate peak shows up to 2 h earlier in OPC with NS compared with that of OPC. Also, the total heat after first day is more in OPC with NS. The initial and induction periods in both nano-systems are very short and difficult to distinguish. In acceleration stage, the rate of heat release of nano PC with NS is slightly higher compared to that in nano PC system. The total heat of NPC with NS within 24 h is slightly lower than that of NPC without NS. This can be explained by size effect, in which OPC with normal fineness shares less surface area and the nucleation sites by NS contribute more to hydration degree.

Second, a strong retardation effect was observed in NPC and NPC with NS in the beginning of the acceleration stage between 1.5 h and 8 h, in which hydration reactions show significantly lower heat rate and cumulative heat. This can be attributed to the conversion of ettringite to monosulfate, which covers the surface of newly formed C-S-H, preventing further precipitation.

Third, the main hydrated product, C-S-H in NPC with and without NS first precipitates on the  $\text{Si}_3\text{N}_4$  membrane surface due to lower surface energy. However, C-S-H precipitates in NPC with NS exhibit well-distributed microstructure compared with that in plain NPC system. This resulted from seeding effect of NS. More ettringite crystals are dissolved in NPC with NS compared to that in plain NPC system. This may suggest that NS accelerates the conversion from ettringite to monosulfate. Our LC-TEM results also indicate that NS tends to be adsorbed to needle-like ettringite leading to needle-like C-S-H precipitates.

This work reveals the structural evolution and hydration kinetics of NPC by applying the nanoscience and nanotechnology. The present results promote the understanding of the role of NS in nano and OPC systems. The work clarifies a critical topic in cement and concrete research and different hydration paths in nano PC and OPC systems with the addition of NS. This provides new insights for designing proper nano cements with supplementary cementitious nanomaterials, which will certainly achieve great economic benefits.

## **5.5 Acknowledgements**

The authors would like to thank Dr. Madeline Dukes from Protochips Inc. and Dr. Jie Yang for the discussion on LC-TEM, and Dr. Samir Chidiac and Dr. Sylvia Mihaljevic for calorimetry test. Thanks to Miss Victoria Jarvis for the assistance in QXRD and Mr. Michael Stanzel from Lehigh Cement Company for providing raw materials. We would also like to acknowledge the help from staff in Canadian Center for Electron Microscopy (CCEM).

## 5.6 References

1. Bullard, J.W., et al., *Mechanisms of cement hydration*. Cement and Concrete Research, 2011. **41**(12): p. 1208-1223.
2. Hesse, C., F. Goetz-Neunhoeffler, and J. Neubauer, *A new approach in quantitative in-situ XRD of cement pastes: Correlation of heat flow curves with early hydration reactions*. Cement and Concrete Research, 2011. **41**(1): p. 123-128.
3. Nicoleau, L., A. Nonat, and D. Perrey, *The di- and tricalcium silicate dissolutions*. Cement and Concrete Research, 2013. **47**: p. 14-30.
4. Bellmann, F., et al., *Improved evidence for the existence of an intermediate phase during hydration of tricalcium silicate*. Cement and Concrete Research, 2010. **40**(6): p. 875-884.
5. Zhang, L., et al., *Hydration for the Alite mineral: Morphology evolution, reaction mechanism and the compositional influences*. Construction and Building Materials, 2017. **155**: p. 413-426.
6. Nicoleau, L., *Accelerated growth of calcium silicate hydrates: Experiments and simulations*. Cement and Concrete Research, 2011. **41**(12): p. 1339-1348.
7. Scrivener, K.L., P. Juilland, and P.J.M. Monteiro, *Advances in understanding hydration of Portland cement*. Cement and Concrete Research, 2015. **78**: p. 38-56.
8. Juilland, P., et al., *Dissolution theory applied to the induction period in alite hydration*. Cement and Concrete Research, 2010. **40**(6): p. 831-844.
9. Nicoleau, L. and A. Nonat, *A new view on the kinetics of tricalcium silicate hydration*. Cement and Concrete Research, 2016. **86**: p. 1-11.
10. Bergold, S.T., F. Goetz-Neunhoeffler, and J. Neubauer, *Influence of the reactivity of the amorphous part of mechanically activated alite on its hydration kinetics*. Cement and Concrete Research, 2016. **88**: p. 73-81.
11. Nicoleau, L., M.A. Bertolim, and L. Struble, *Analytical Model for the Alite (C3S) Dissolution Topography*. Journal of the American Ceramic Society, 2016. **99**(3): p. 773-786.

12. Quennoz, A. and K.L. Scrivener, *Interactions between alite and C3A-gypsum hydrations in model cements*. Cement and Concrete Research, 2013. **44**: p. 46-54.
13. Myers, R.J., et al., *Role of Adsorption Phenomena in Cubic Tricalcium Aluminate Dissolution*. Langmuir, 2017. **33**(1): p. 45-55.
14. Pustovgar, E., et al., *Influence of aluminates on the hydration kinetics of tricalcium silicate*. Cement and Concrete Research, 2017. **100**: p. 245-262.
15. Bergold, S.T., F. Goetz-Neunhoeffler, and J. Neubauer, *Interaction of silicate and aluminate reaction in a synthetic cement system: Implications for the process of alite hydration*. Cement and Concrete Research, 2017. **93**: p. 32-44.
16. Jansen, D., et al., *The early hydration of OPC investigated by in-situ XRD, heat flow calorimetry, pore water analysis and 1 H NMR: Learning about adsorbed ions from a complete mass balance approach*. Cement and Concrete Research, 2018. **109**: p. 230-242.
17. Taylor, H.F., *Proposed structure for calcium silicate hydrate gel*. Journal of the American Ceramic Society, 1986. **69**(6): p. 464-467.
18. Gartner, E.M., *A proposed mechanism for the growth of C-S-H during the hydration of tricalcium silicate*. Cement and concrete research, 1997. **27**(5): p. 665-672.
19. Gartner, E., I. Maruyama, and J. Chen, *A new model for the C-S-H phase formed during the hydration of Portland cements*. Cement and Concrete Research, 2017. **97**: p. 95-106.
20. Jennings, H.M., *A model for the microstructure of calcium silicate hydrate in cement paste*. Cement and concrete research, 2000. **30**(1): p. 101-116.
21. Allen, A.J., J.J. Thomas, and H.M. Jennings, *Composition and density of nanoscale calcium-silicate-hydrate in cement*. Nat Mater, 2007. **6**(4): p. 311-6.
22. Thomas, J.J., et al., *Modeling and simulation of cement hydration kinetics and microstructure development*. Cement and Concrete Research, 2011. **41**(12): p. 1257-1278.
23. Cuesta, A., et al., *Multiscale understanding of tricalcium silicate hydration reactions*. Sci Rep, 2018. **8**(1): p. 8544.

24. Plank, J., M. Schönlein, and V. Kanchanason, *Study on the early crystallization of calcium silicate hydrate (C-S-H) in the presence of polycarboxylate superplasticizers*. Journal of Organometallic Chemistry, 2018. **869**: p. 227-232.
25. Krautwurst, N., et al., *Two-Step Nucleation Process of Calcium Silicate Hydrate, the Nanobrick of Cement*. Chemistry of Materials, 2018. **30**(9): p. 2895-2904.
26. Li, H., et al., *Crystallization of calcium silicate hydrates on the surface of nanomaterials*. Journal of the American Ceramic Society, 2017. **100**(7): p. 3227-3238.
27. Bergold, S.T., F. Goetz-Neunhoeffler, and J. Neubauer, *Mechanically activated alite: New insights into alite hydration*. Cement and Concrete Research, 2015. **76**: p. 202-211.
28. Gann, D., *A review of nanotechnology and its potential applications for construction*. SPRU, University of Sussex, 2002. **28**.
29. Sharma, U., et al., *Effect of Particle Size of Silica Nanoparticles on Hydration Reactivity and Microstructure of C-S-H Gel*. Advances in Civil Engineering Materials, 2019. **8**(3).
30. Rupasinghe, M., et al., *Investigation of strength and hydration characteristics in nano-silica incorporated cement paste*. Cement and Concrete Composites, 2017. **80**: p. 17-30.
31. Carmichael, M.J. and G.P. Arulraj, *Strength and permeability studies on concrete with Nano-Cement*. IJCIET, 2017. **8**(1): p. 132-139.
32. Bickbau, M.Y., *Method for producing nano-cement, and nano-cement*. 2016, Google Patents.
33. Roddy, C.W., *Cement compositions and methods utilizing nano-hydraulic cement*. 2016, Google Patents.
34. Gupta, S., *Application of Silica Fume and Nanosilica in Cement and Concrete – A Review*. Journal on Today's Ideas - Tomorrow's Technologies, 2013. **1**(2): p. 85-98.
35. Flores, Y.C., et al., *Performance of Portland cement pastes containing nano-silica and different types of silica*. Construction and Building Materials, 2017. **146**: p. 524-530.
36. Zhang, X., et al., *Effects of particle size of colloidal nanosilica on hydration of Portland cement at early age*. Advances in Mechanical Engineering, 2019. **11**(2).

37. Senff, L., et al., *Effect of nano-SiO<sub>2</sub> and nano-TiO<sub>2</sub> addition on the rheological behavior and the hardened properties of cement mortars*. *Materials Science and Engineering: A*, 2012. **532**: p. 354-361.
38. Kong, D., et al., *Effect and mechanism of colloidal silica sol on properties and microstructure of the hardened cement-based materials as compared to nano-silica powder with agglomerates in micron-scale*. *Cement and Concrete Composites*, 2019. **98**: p. 137-149.
39. Huang, S.M. and F.L. Zhou, *Retardation effect of different alcohols on the cement coagulation in polycarboxylate- and naphthalene-based cement admixtures*. *IOP Conference Series: Materials Science and Engineering*, 2017. **283**.
40. Lin, R.S., et al., *Hydration and Microstructure of Cement Pastes with Calcined Hwangtoh Clay*. *Materials (Basel)*, 2019. **12**(3).
41. Jansen, D., et al., *The early hydration of Ordinary Portland Cement (OPC): An approach comparing measured heat flow with calculated heat flow from QXRD*. *Cement and Concrete Research*, 2012. **42**(1): p. 134-138.
42. Bergold, S.T., F. Goetz-Neunhoeffler, and J. Neubauer, *Quantitative analysis of C–S–H in hydrating alite pastes by in-situ XRD*. *Cement and Concrete Research*, 2013. **53**: p. 119-126.
43. Klemczak, B. and M. Batog, *Heat of hydration of low-clinker cements*. *Journal of Thermal Analysis and Calorimetry*, 2015. **123**(2): p. 1351-1360.
44. Moghaddam, F., V. Sirivivatnanon, and K. Vessalas, *The effect of fly ash fineness on heat of hydration, microstructure, flow and compressive strength of blended cement pastes*. *Case Studies in Construction Materials*, 2019. **10**.
45. Muhua, T. and D.M. Roy, *An investigation of the effect of organic solvent on the rheological properties and hydration of cement paste*. *Cement and Concrete Research*, 1987. **17**(6): p. 983-994.
46. Hesse, C., et al., *Quantitative in situ X-ray diffraction analysis of early hydration of Portland cement at defined temperatures*. *Powder Diffraction*, 2009. **24**(2): p. 112-115.

## **6. Advanced Characterization of 3D Structure and Porosity of Ordinary Portland Cement (OPC) Mortar Using Plasma Focused Ion Beam Tomography and X-ray Computed Tomography**

Peng Dong<sup>1</sup>, Hui Yuan<sup>2</sup>, Ali Allahverdi<sup>3</sup>, Jatheeshan Raveenthiran<sup>4</sup>, Nicolas Piché<sup>5</sup>, Benjamin Provencher<sup>5</sup>, and Nabil D. Bassim<sup>1,2</sup>

1. Department of Materials Science and Engineering, McMaster University, 1280 Main St W, Hamilton, ON L8S 4L8, Canada

2. Canadian Centre for Electron Microscopy, McMaster University, 1280 Main St W, Hamilton, ON L8S 4M1, Canada

3. Cement Research Centre, School of Chemical Engineering, Iran University of Science and Technology, Narmak 16846 – 13114, Tehran, Iran

4. Department of Electrical and Computer Engineering, McMaster University, 1280 Main St W, Hamilton, ON L8S 4L8, Canada

5. Object Research Systems, 760 St-Paul West, Suite 101, Montreal, Quebec, H3C 1M4, Canada

**Author contributions:** In Chapter 6, Mr. Peng Dong conducted all the experiments and data analysis with the help of Dr. Hui Yuan and Dr. Ali Allahverdi. Nicolas Piché and Benjamin Provencher provided assistance of training a neural network. Dr. Nabil Bassim and Dr. Ali Allahverdi and Mr. Jatheeshan Raveenthiran also provided important discussions. The draft was originally drafted by me and edited to the final version by Dr. Ali Allahverdi and Dr. Nabil Bassim. The manuscript will be submitted to microscopy for publication.

## **Abstract**

The visualization and quantification of pore networks and main phases have been critical research topics in cementitious materials as many critical mechanical and chemical properties and infrastructure reliability rely on these 3-D characteristics. In this study, we realized the mesoscale serial sectioning and analysis up to  $\sim 80\ \mu\text{m}$  by  $\sim 90\ \mu\text{m}$  by  $\sim 60\ \mu\text{m}$  on Portland cement mortar using plasma focused ion beam (PFIB) for the first time. The workflow of working with mortar and PFIB was established applying a prepositioned hard Silicon mask to reduce curtaining. Segmentation with minimal human interference was performed using a trained neural network, which was compared using multiple types of segmentation models. Combining PFIB analysis at the microscale with X-ray micro-computed tomography (micro-CT, sample size of 10 mm by 10 mm by 2 mm) at 10 s of microns scale, the analysis of capillary pores and air voids ranging from hundreds of nanometers to millimeters can be conducted. The volume fraction of large capillary pores and air voids are 11.5% and 12.7%, respectively. Moreover, the skeletonization of connected capillary pores clearly shows fluid transport pathways, which are a key factor determining durability performance of concrete in aggressive environments. Another interesting aspect of the FIB tomography is the reconstruction of anhydrous phases and enables direct study of hydration kinetics of individual cement phases. This work opens the possibility of characterizing porosity in cementitious materials at all critical length scales.

**Keywords:** PFIB, large-scale serial sectioning, 3D reconstruction, pore network, quantification

## **6.1. Introduction**

Portland cement-based concrete is the most widely used construction material worldwide. Its properties, like compressive strength and durability depend strongly on the internal pore system [1, 2]. The pore size distribution spans a wide volume range, with equivalent diameters

ranging from a few nanometers to hundreds of microns, among which the large capillary pores affect largely fluid transport properties, which influences rebar corrosion while air voids influence freeze-thaw properties greatly [3-5]. A traditional technique to analyze the porosity in cementitious materials is mercury intrusion porosimetry (MIP), which usually results in an overestimation of volume fraction for smaller pores due to the ‘ink-bottle’ effect [6, 7]. Also, it cannot provide information on pore type and interconnectivity of porosity that are necessary to understand fluid transport properties [8].

Many characterization techniques have been applied to clarify pore characteristics. The applications of electron microscopy methods, including scanning electron microscopy (SEM) [9-11] and transmission electron microscopy (TEM) [7, 12] allow 2D imaging of pores with nanometer scale. However, 3D parameters and pore structures are inaccessible using above techniques. 3D atom probe tomography and TEM tomography can reconstruct structure with resolution less than 1 nm [13]. Rae et al. [14] investigated the nanostructure and pore network of cement-based systems and obtained a well-defined pore network with diameter of 1.7-2.4 nm by rotating the sample between  $-65^\circ$  to  $+65^\circ$  in TEM tomography. However, it is not technologically relevant to the large-scale and heterogeneous structure of cement. To obtain appropriate statistics, it is necessary that multiple samples with volumes of tens of  $\text{mm}^3$  be prepared to study macroscopic fluid transport property, for aggregate sizes of tens of mm [15]. Nano- and micro- computed x-ray tomography (CT) allows 3D structure visualization up to millimetric scale, with a maximum resolution of 50 nm for nano-CT [16], while other advanced synchrotron-based tools further enhance the capability of understanding cement systems with the ultimate resolutions of 10 nm. Therefore, various imaging methods are required to characterize multiple length scales of porosity because of the complexity and size distribution in cementitious materials.

Dual-beam focused ion beam (FIB) tomography enables 3D reconstruction of structure and pore systems filling in the gap left from other imaging methods [8, 13, 17]. The dual-beam system takes the advantage of materials removal capability of ion beam sputtering, and various contrast mechanisms of electron beam-based imaging leading to sectioning and image acquisition at nanometer-scale resolution [18]. Holzer et al. [19] investigated the volume fraction of porosity in BaTiO<sub>3</sub> with a stack of 105 images and data volume of 6.01 × 6.04 × 1.74 μm and demonstrated the capabilities of FIB tomography to reconstruct 3D structures smaller than 100 nm. He et al. [20] combined FIB/SEM (500 images) with micro-CT (exposure time of 120 s, 1600 slices) to obtain the 3D pore distribution at multiple length scale (mm, μm and nm-scale) in different layers of shale rock, concluding that the connected pores are dominated by millimetric and micrometric pores, and fracturing shale layer provided shale gas migration pathways. Recently, the application of FIB-SEM on cementitious materials have been reported by a few researchers. Holzer et al. [21] presented the first application of cryo-FIB-nanotomography for quantifying particle structure in dense cement suspensions by etching the specimen at -105 °C for 4 min and transferring onto the cold stage (-115 °C), followed by FIB-milling and imaging processes with electron beam voltage and spot size of 3 kV and spot 3, respectively. Brisard et al. [15] promoted the understanding of potential fluid transport and 3D pore network and microstructure (10-20 nm voxel size) combining with small angle X-ray scattering and FIB/SEM experiments, in which four samples (volumes of 61-118 μm<sup>3</sup>) were required on a Ga<sup>+</sup> FIB/SEM system. Lim et al. [22] implemented FIB tomography on cement pastes incorporating nano-silica and silica fume from 1000 images with dimensions of 10 × 10 × 20 μm. By 3D modelling, it was possible to obtain direct measurements of pore structure of cement pastes with voxel dimensions in the range of 10 nm [22]. Song et. al [23] performed serial sectioning and electron imaging with voxel sizes of 5.9 × 7.5 × 10 nm<sup>3</sup> (or 5.9 × 7.5 × 20 nm<sup>3</sup>) on four independent samples (sample volumes of 61-118 μm<sup>3</sup>) of high performance

concrete (HPC) and predicted fluid transport properties from the acquired pore size distribution, which was on the same order of magnitude as experimental permeability, indicating that FIB/SEM had a relevant contribution to study transport properties.

Despite the above progress of FIB-based 3D tomography on cementitious materials, working with Ga<sup>+</sup> liquid metal ion sources (LMIS) to obtain relatively large number of 2D images can be time-consuming with a relatively small imaging volume (about 4000  $\mu\text{m}^3$ ). The advancement of new ion sources enables serial sectioning at faster milling rates [18]. Compared with Ga<sup>+</sup> FIB, a dual-beam system equipped with Xe<sup>+</sup> plasma source can achieve probe currents higher than 2  $\mu\text{A}$  with smaller spot sizes (at high current), resulting in an increase in sputtering and milling of 50 fold [24, 25], which significantly reduce the time for investigating the region of interest (ROI). Some researchers have reported the progress of Xe<sup>+</sup> plasma FIB (PFIB) in machining of metal micropillars [26] and serial sectioning tomography of an organic paint coating [27]. However, the application of PFIB and minimization of curtaining effects at large scale of cementitious materials needs further exploration.

Image processing, especially the image segmentation, is a crucial step to get interpretable result to characterize structures in materials. Segmentation is the assignment of pixel values in a digital image or voxel values in a 3-D dataset via mathematical classification technique into various sub-phases for further quantification. This can often be done using thresholding [28], edge detection [29] followed by watershed [30], and more recently, machine learning techniques [31]. Because of the complexity of a 3-D concrete dataset, the approach chosen here was using a machine learning category, namely a deep learning tool.

The advent of PFIB enhances the capabilities of 3D tomography on cementitious materials. In this paper, we report the application of 3D tomography on ordinary Portland cement (OPC) mortar using PFIB for the first time. It is aimed at providing a standard workflow to study pore

structures related to transport properties. Sample preparation procedures and instrumentation setup are clarified. Moreover, 3D models of pore systems and anhydrous phases are reconstructed using a deep learning toolkit, which allows for improvements in accuracy of pore size identification. By combining the quantification of pore size both from nano-tomography and micro CT-tomography, we can measure porosity in different length scales, thus enabling a more holistic evaluation of materials structure.

## 6.2. Materials and Methods

### 6.2.1. Materials and Sample Preparation

Cement mortars were prepared with CSA-A3001 Type GU Portland cement, sand and deionized water according to ASTM C109 and ASTM C305 protocols. The water-to-cement ratio was 0.485 and sand-to-cement ratio was 2.75. The physical and chemical compositions of as-received Portland cement are shown in Table. 6.1. Mixing was carried out in a laboratory planetary mixer and cement mortars were formed in 5 cm cubic molds, which were covered by plastic bags to prevent water loss. They were demolded after 24 h and cured in almost 100% relative humidity at room temperature. The cured mortar specimens that cured for 6 months were used for experiments.

Table 6.1 Chemical, Bogue’s potential phase compositions and physical properties of the as  
– received OPC

Chemical composition		Bogue’s potential phase compositions	
Oxide	Quantity/wt.%	Phase	Quantity/wt.%
SiO <sub>2</sub>	20.32	C <sub>3</sub> S	46.72
Al <sub>2</sub> O <sub>3</sub>	5.44	C <sub>2</sub> S	24.12
Fe <sub>2</sub> O <sub>3</sub>	2.92	C <sub>3</sub> A	9.71
CaO	63.64	C <sub>4</sub> AF	9.04
MgO	2.30	<b>Physical properties</b>	
SO <sub>3</sub>	3.56	Property	Quantity

Na <sub>2</sub> O/K <sub>2</sub> O	0.15/1.07	Blaine fineness (m <sup>2</sup> /kg)	376
------------------------------------	-----------	--------------------------------------	-----

The mortar specimens were stored in the air and then dried in a furnace at 50 °C for 4 days. Rough cutting was then performed with no lubricant, which and then followed by fine cutting on a diamond blade in the presence of pure ethanol to eliminate damage caused by the previous procedure. Vacuum pressure impregnation of epoxy was applied to mortar samples to preserve the internal porosity, in which the impregnation process was repeated for 3 to 4 times until epoxy fills in plastic molds. This is to protect internal porosity during subsequent sample preparation processes. After demolding, grinding and polishing with isopropylene glycol were conducted so that the surface and adjacent cross section have a surface roughness of about 1.5 μm. The polished surface and cross section were also coated with more than 30 nm thick platinum layer for mitigation of charging during electron beam imaging.

### 6.2.2. Predetermination and Si Mask

The secondary electron image of sample surface was acquired on JEOL 6610 and given in Figure 6.1. As observed in the image, it consisted of air voids, sand particles and matrix. Instead of using a large chemical deposition layer on top of a volume of VOI, a single-crystal Si mask method [32] for curtaining mitigation was implemented for mortar samples in FIB-SEM system. A hard mask blocks the view of further navigation and investigation of sample surface. Therefore, several potential VOIs were predetermined, considering smooth paste areas on both surface and the cross section. The distances between VOIs and adjacent distinguishable features were also recorded. The potential VOIs were then covered with cut pieces of single-crystal Si wafer using TEM epoxy (epoxy: hardener = 10: 1). The Si wafer with a thickness of 10 μm was aligned with the edge of sample under the optical microscope, after which they were heated at 50 °C for 3 h so that TEM epoxy was hardened and attached the mask to the top surface of the specimen.

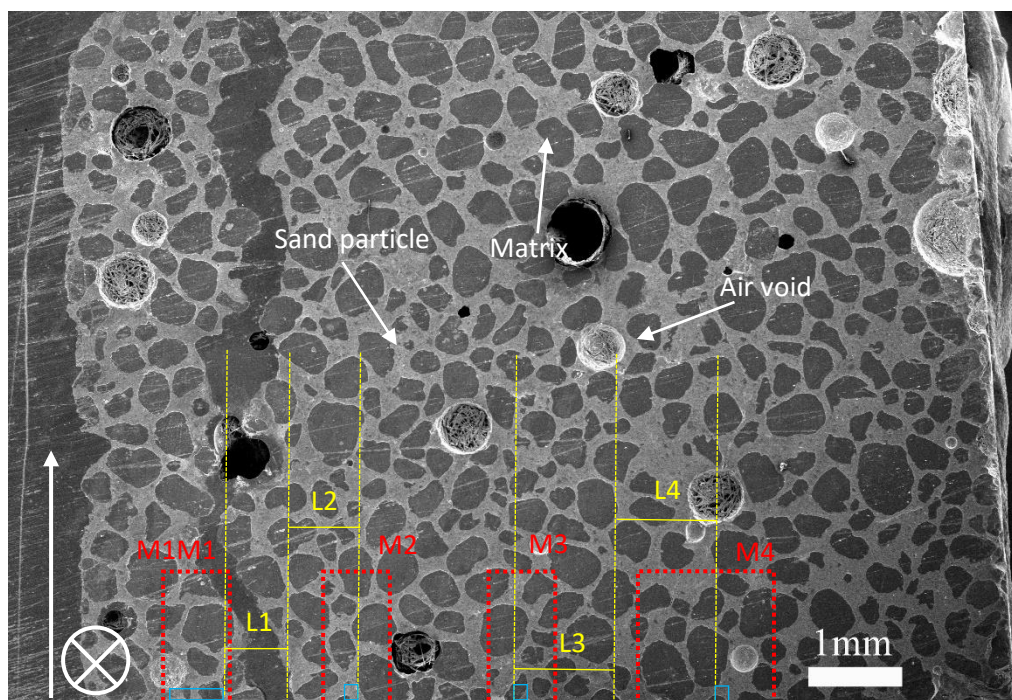


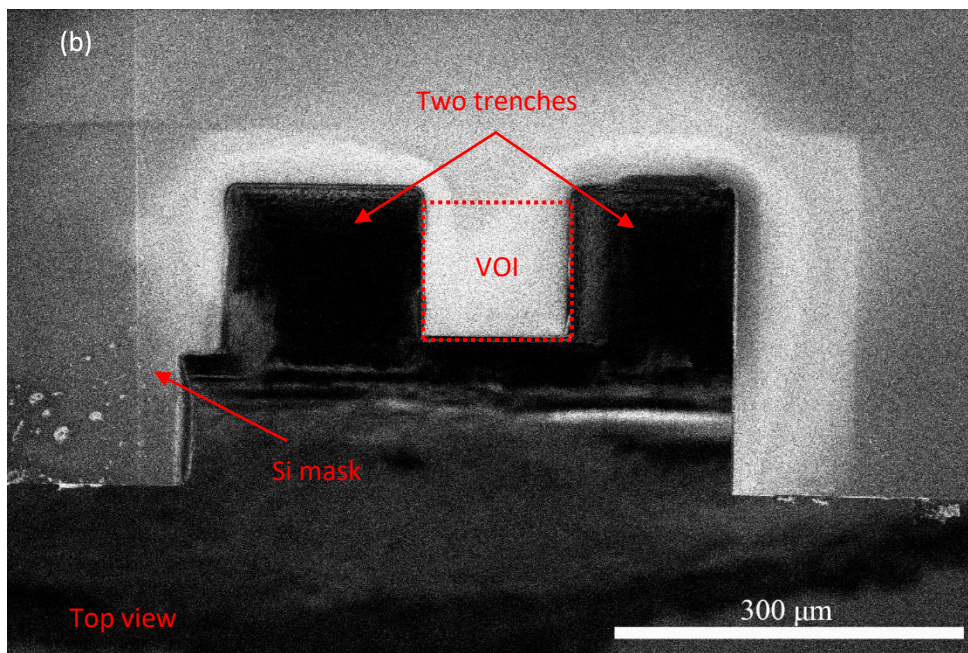
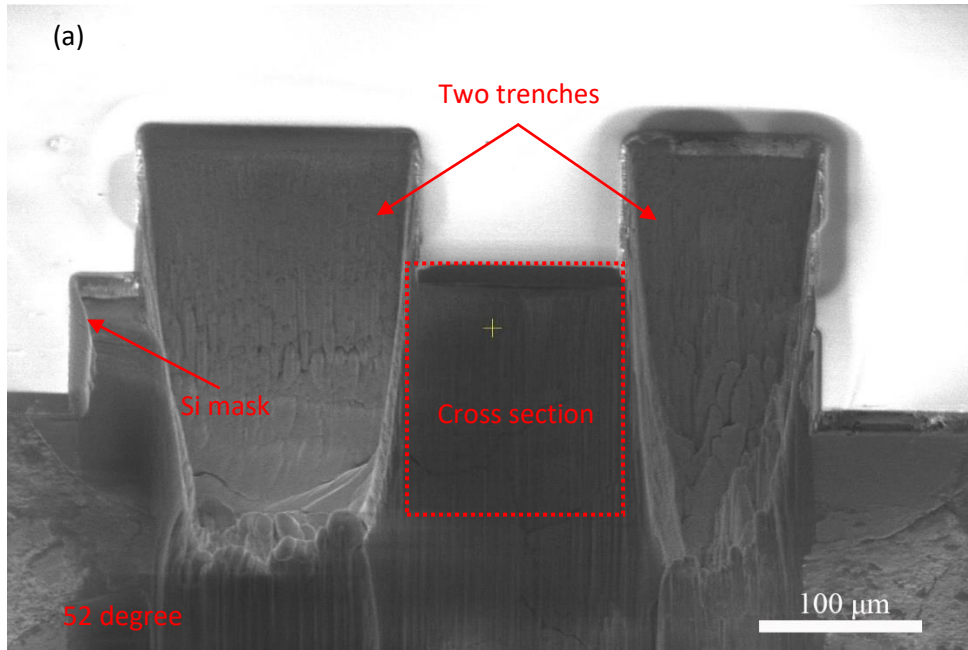
Figure 6.1 The SE image of sample surface by JEOL 6610, and schematic of hard single-crystal Si masks (M1, M2, M3 and M4) on top of possible VOIs, which were indicated in blue rectangles and their distances to selected features were measured to be L1, L2, L3 and L4. Milling front and milling directions are shown by the cross and arrow on left side.

### 6.2.3. Plasma FIB – SEM Setup and Serial Sectioning

A ThermoFisher Helios G4 PFIB dual-beam system was utilized to prepare a VOI for serial sectioning and subsequent milling. The sample was mounted on an aluminum stub with Ni paste and the working distance was set to about 4 mm. A VOI that was free of sand particles was selected under one of the Si masks using chosen features and measured distance as navigation tools. While the desired area was in the view, the electron and ion beams were brought to the coincident point. An area with a dimension of  $150\ \mu\text{m} \times 100\ \mu\text{m}$  was rough milled, after which two trenches with dimension of  $200\ \mu\text{m} \times 120\ \mu\text{m}$  were milled away on both sides (Figure 6.2 a and b) with a milling current of  $2.5\ \mu\text{A}$  at 30 kV. Then tungsten deposition ( $100\ \mu\text{m} \times 100\ \mu\text{m} \times 5\ \mu\text{m}$ ) was carried out on Si mask under 12 keV/60 nA, which was followed by creating a fiducial (Figure 6.2 c) for subsequent rocking milling. A rocking polish by rotating the stage to achieve specific sample geometry with respect to ion beam was performed on the VOI for 4 cycles under the beam condition of 30 keV/15 nA. Finally, the

sample was rotated relatively  $180^\circ$  with respect to  $0^\circ$  rotation and a fiducial was created for SEM alignment using 30 keV/15 nA.

The serial sectioning was conducted using ion beam parameters of 30 kV/15 nA, in which the sample was tilted  $52^\circ$  making it perpendicular to ion beam. The simultaneous electron images from concentric backscatter (CBS) detector and in-chamber electron (ICE – detects secondary electrons and ions) detectors were obtained. The through-the-lens detector (TLD) was used for backscattered electron (BSE) imaging with the electron beam condition of 2 keV/3.2 nA. The Auto Brightness/Contrast algorithm and Y-drift correction were carried out on every image as well. The horizontal field of view was  $153.6\ \mu\text{m}$  and pixel size was 25 nm, which enabled a view of  $153.6\ \mu\text{m} \times 102.4\ \mu\text{m}$ . Also, the slice thickness was 100 nm and 631 slices were obtained in total. The image stack was aligned relative to the fiducial in SEM images using MultiStackReg plugin of ImageJ software. The whole image stack was cropped, which led to a dimension of  $79.8\ \mu\text{m}$  by  $88.3\ \mu\text{m}$ , as indicated in the first slice (Figure 6.2 d).



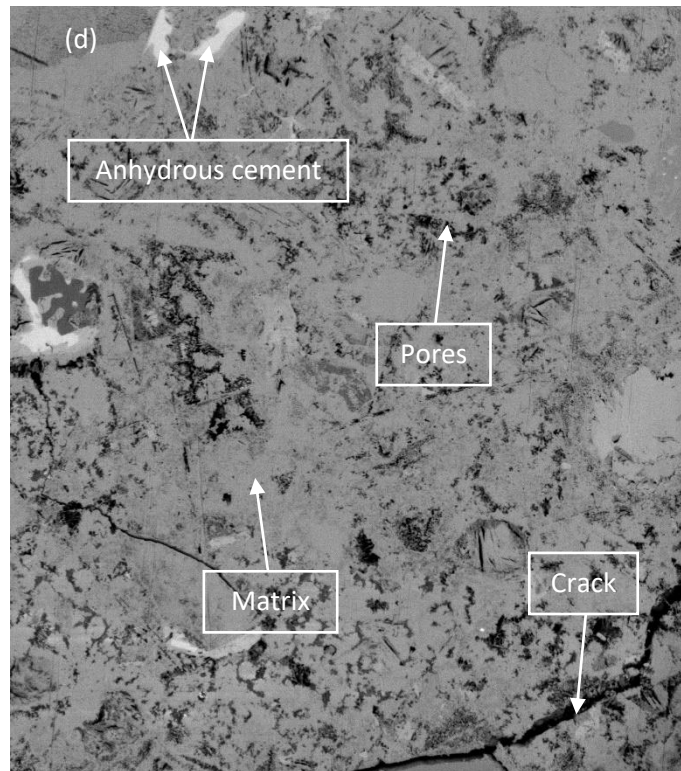
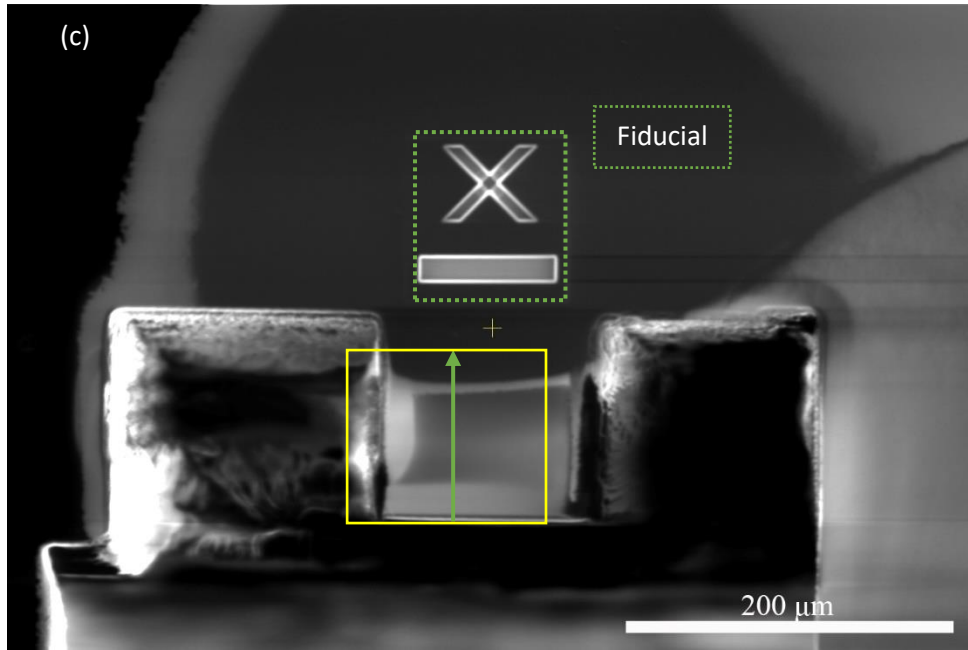


Figure 6.2 Experimental setup of FIB-SEM dual-beam system. a) 52-degree secondary electron image showing a prepared VOI with two trenches on both sides. b) Top-view ion beam image after trench milling. c) Top-view ion beam image showing deposition layer and a fiducial on top for rocking milling as well as sectioning direction. d) Backscattered electron image of the first slice of serial sectioned image stack, 79.8  $\mu\text{m}$  by 88.3  $\mu\text{m}$ , pixel size = 25 nm in both x and y direction.

## 6.2.4 Segmentation and Quantification

Segmentation is the assignment of pixel values in a digital image or voxel values in a 3-D dataset via mathematical classification technique into various sub-phases for further quantification. This can often be done using thresholding [30], edge detection [33] followed by watershed, and more recently, machine learning techniques. Because of the complexity of a 3-D concrete dataset, the approach chosen here was using a machine learning category, namely a deep learning tool.

Segmentation was conducted using the Deep Learning Tool in Dragonfly (Object research systems Inc., Montreal). Only 3 representative images were chosen through the whole dataset and were fully segmented manually by the authors for fodder as training data (Figure 6.3 a). A train, validation, and test masks mosaics of 128x128 square patch were randomly generated consisting of 20348928( $\approx 70\%$ ), 5799936( $\approx 20\%$ ) and 2899968( $\approx 10\%$ ) voxels respectively (Figure 6.3 b).

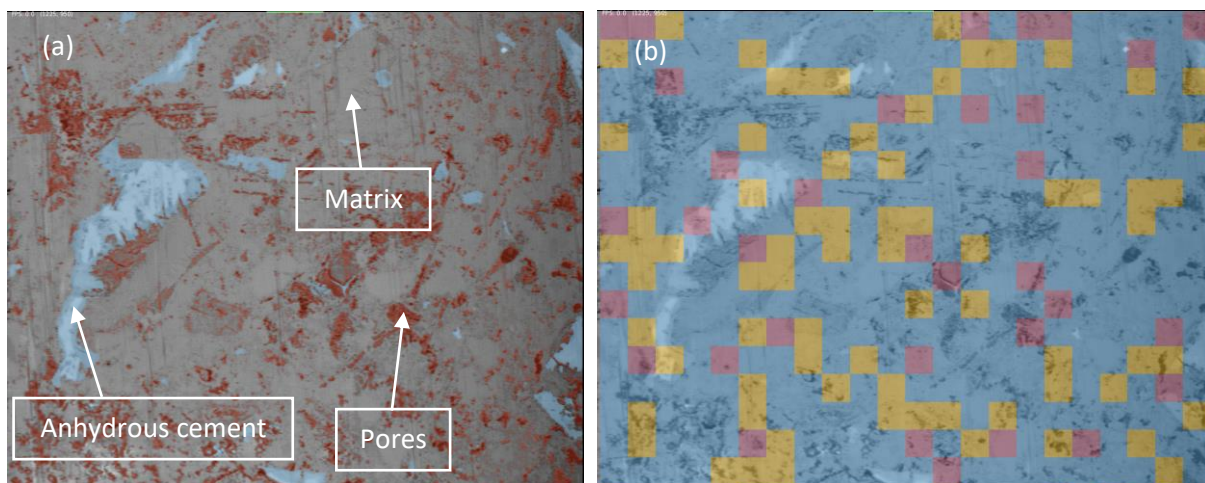


Figure 6.3 Deep learning trainset. a) The manual segmentation consisting of 3 phases, namely, anhydrous phases, pores, and matrix. b) The generated train (blue), validation(yellow) and test(red) masks.

Two segmentation models' architecture available in Dragonfly were tested, U-Net [31] and Sensor3D [34] to segment the dataset. Furthermore, Dragonfly model architectures allow multi-input and multi-slice models, the former meaning that more than one modality can be

given as input, the later meaning that more than one input z slice can be given for each output z slice. In multi-slice models, slice count indicates the number of input slices supplied to the model for each output slice, while slice spacing indicates the distance, or offset, between slices. A slice spacing of '1' means that slices are taken sequentially, '2' means every other slice is taken, and so on.

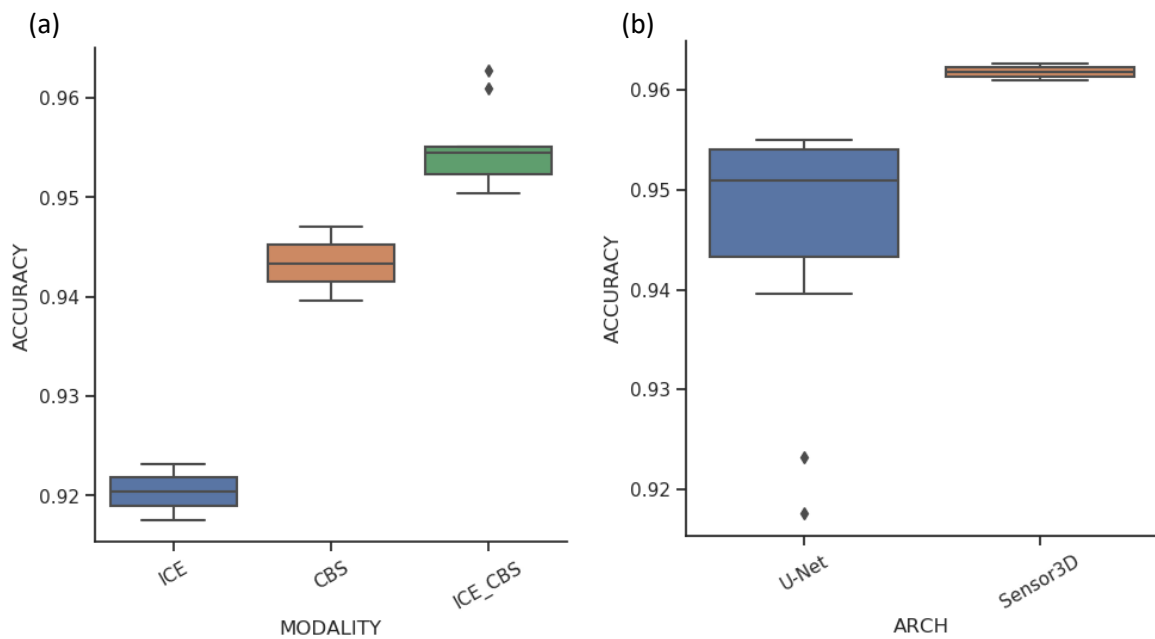
Thirteen models were trained for 100 epochs (Patch Size 64, Batch size 32, Dice loss function). Table 6.2 shows accuracy and DICE score (indicator for similarity of two samples) for models with varying computational Architecture, Modality, Slice count and spacing (CBS: SEM Multi-Detector Image\_CBS\_1, ICE: SEM Multi-Detector Image\_ICE\_3). Training time varies from 1h26 (U-Net\_BASIC\_ICE) to 15h21 (Sensor3D\_MS\_05\_01\_ICE\_CBS). The model with the best accuracy (Sensor3D\_MS\_05\_01\_ICE\_CBS) was applied to the whole dataset for a full segmentation, where a mask excluding the large sand particle was used.

Table 6.2 The results are given in the following table, sorted by accuracy:

Model Name	Architecture	Modality	Slice count	Slice Spacing	Accuracy	DICE
U-Net_BASIC_ICE	U-Net	ICE	1	NA	0.9175	0.8763
U-Net_MS_03_01_ICE	U-Net	ICE	3	2	0.9232	0.8848
U-Net_BASIC_CBS	U-Net	CBS	1	NA	0.9396	0.9094
U-Net_MS_03_01_CBS	U-Net	CBS	3	1	0.9470	0.9206
U-Net_MS_05_02_ICE_CBS	U-Net	ICE_CBS	5	2	0.9504	0.9256
U-Net_MS_05_01_ICE_CBS	U-Net	ICE_CBS	5	1	0.9510	0.9265
U-Net_BASIC_ICE_CBS	U-Net	ICE_CBS	1	NA	0.9523	0.9285
U-Net_MS_03_01_ICE_CBS	U-Net	ICE_CBS	3	1	0.9537	0.93058
U-Net_MS_03_02_ICE_CBS	U-Net	ICE_CBS	3	2	0.9544	0.9317
U-Net_MS_05_03_ICE_CBS	U-Net	ICE_CBS	5	3	0.9546	0.9319
U-Net_MS_03_03_ICE_CBS	U-Net	ICE_CBS	3	3	0.9550	0.9325

Sensor3D_MS_03_01_ICE_CBS	Sensor3D	ICE_CBS	3	1	0.9610	0.9415
Sensor3D_MS_05_01_ICE_CBS	Sensor3D	ICE_CBS	5	1	0.9627	0.9441

Some trends can be extracted from the following results (Figure 6.4). Using both modalities (i.e. both detectors) increases mean accuracy by 1.17% and 3.46% over CBS and ICE alone, shown in Figure 6.4 a. Sensor3D architecture is slower to train but increases mean accuracy by 1.64% over U-Net architecture (Figure 6.4 b). Multi-slice models outperform regular models by giving 3D context. Increasing slice counts increase performance as well. We observe a mean accuracy gain of 0.57% and 1.84% for a 5-slice model over 3 and 1 slice model, respectively (Figure 6.4 c). Furthermore, Figure 4 d shows that the impact of slice spacing is less obvious.



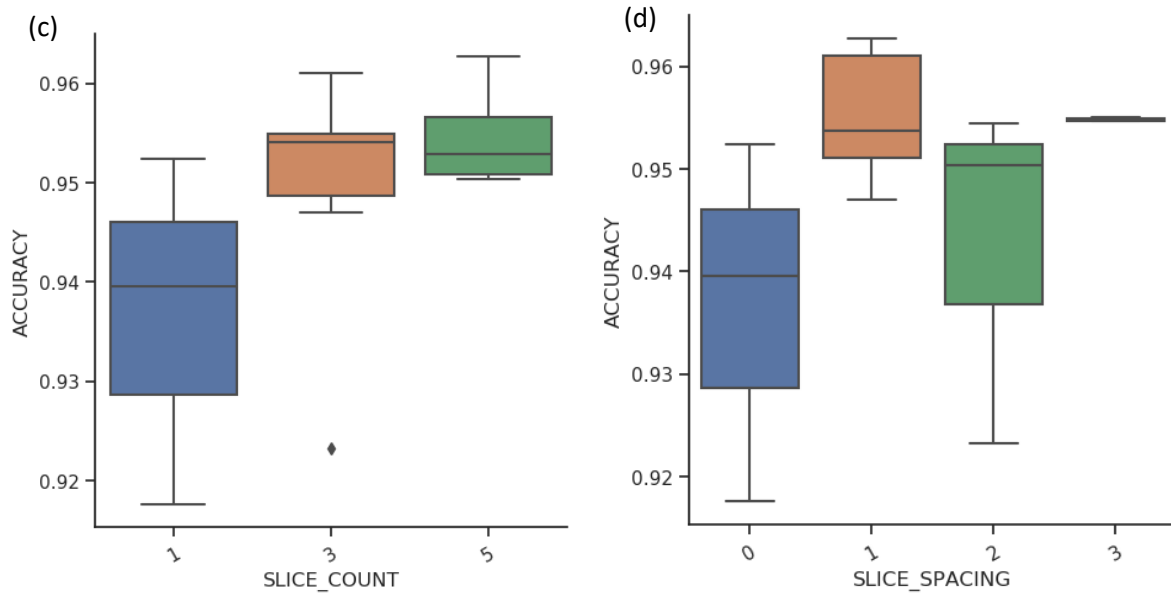


Figure 6.4 The accuracy of segmentation by varying (a) Modality, (b) Architecture, (c) Slice count and (d) spacing.

The 3D skeleton of connected pores was computed from separate layer of segmented results using the function “Get the Skeleton from ROI”. The decimated thickness mesh of anhydrous phases was created by To a Thickness Mesh (Normal). The quantification of pore characteristics was conducted through Multi-ROI Analysis in the software. The pore size was evaluated following the concept of Mean Feret Diameter and the size distribution was conducted, subsequently.

### 6.2.5. Micro – CT and 3D reconstruction on pore system

Micro – CT was able to provide 3D information on the pore system and micro cracks on a larger scale non – destructively. Measurements were conducted on Bruker Skyscan 1172 model. The mortar sample with a dimension of 12 mm × 10 mm × 3 mm was used. Multiple images were formed from transmitted X-rays through the object, which rotated on a high – precision stage. The resolution of image stacks was highly dependent on the size of X – ray source and the magnification. A pixel size of 4.5 μm was achieved while the whole sample was scanned. More than 3000 images were obtained, and the porosity model was constructed in NRecon software. Then segmentation was based on a simple thresholding using Dragonfly

software. The large capillary pores, air voids and crack propagation were analyzed at a micrometric scale.

## 6.3. Results

### 6.3.1. PFIB Results

Figure 6.5 represents a 3D mortar cube in grayscale excluding area with much shading effect, with an effective dimension of 79.8  $\mu\text{m}$  by 88.3  $\mu\text{m}$  by 63.1  $\mu\text{m}$ . This was after cropping from the original setup that was up to 153.6  $\mu\text{m}$  by 102.4  $\mu\text{m}$  by 63.1  $\mu\text{m}$ . A cement mortar sample consists of hydrated products (also known as matrix), anhydrous cement phases, pores, cracks and sand particles, which makes sectioning and imaging rather challenging. This is in part due to the variation of their hardness and thus different milling/sputtering rates [35, 36]. The most common image artefact is curtaining that makes following data analysis quite difficult [37]. The success of pore and structure characterization depends strongly on sample preparation [22, 38]. Instead of using built-in gas deposition layers, we applied a thin Si mask that proved to be effective of reducing curtaining and acquiring good-quality images.

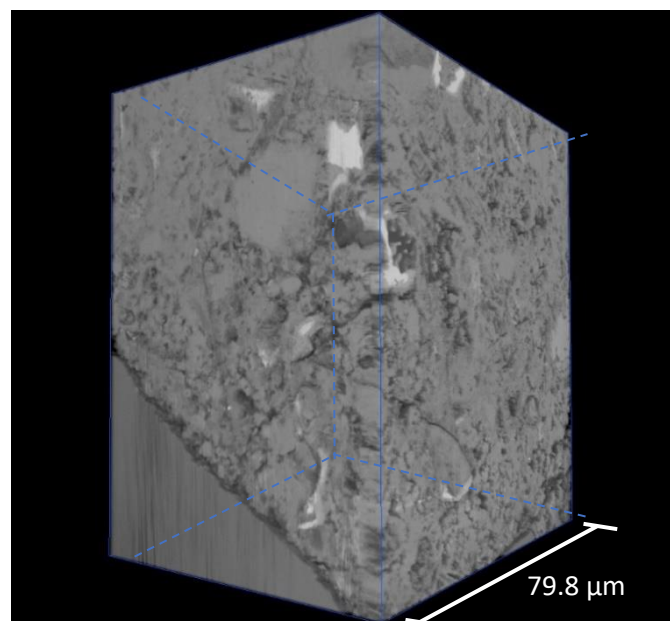


Figure 6.5 3D reconstruction of 631 BSE images after cropping, with the dimension of 79.8  $\mu\text{m}$  by 88.3  $\mu\text{m}$  by 63.1  $\mu\text{m}$

The 3D models of pores and anhydrous phases were reconstructed using the Deep Learning Tool in Dragonfly software. The total porosity is 11.5% and the connected porosity (defined as region of interest segments being connected to the borders of its volume, subvolume, or to the faces of a clipping plane) is 8.4% by volume. The skeleton method was applied to research connectivity by reducing each connected component in a region of interest to a single-voxel wide feature. The skeletonization model of connected pores is presented in Figure 6.6 (a). This clearly shows the water transport pathways inside cement mortar. The anhydrous phases [22] contain four main compounds and a few minor components, which appeared bright in grayscale. In above mature cement mortar, anhydrous phases accounts for 0.8% of total volume. The thickness mesh of 3D reconstruction (Figure 6.6 (b)) displays the spatial distribution of anhydrous cement which were left inside the mortar post hydration reactions. This is due to incomplete contact between water and cement particles and the hydrated layer that prevent complete hydration reactions of cement particles [39]. This could reveal the various hydration rates in different directions of anhydrous cement particle due to when segmented relative to other water diffusion pathways [40]. It is important to realize that the distribution of anhydrous cement could play a critical role in the strength and long-term durability of the material.

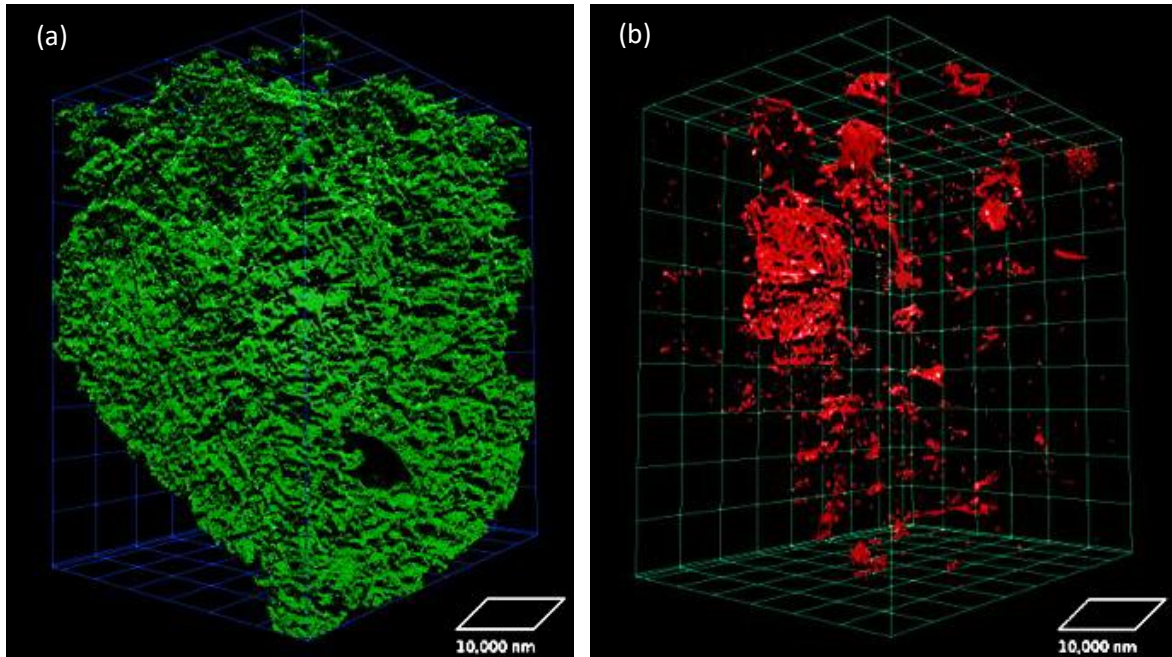


Figure 6.6 3D Segmentation models of cement mortar a) Skeletonization of connected pores, b) thickness mesh of anhydrous phases

### 6.3.2 Micro-CT Analysis of Porosity

The presence of spherical air voids results from the entrapped and entrained air during the mixing process. Compared with capillary pores, air voids are usually much larger, ranging from 50  $\mu\text{m}$  to 200  $\mu\text{m}$  in diameter [3]. They were both evaluated by X-ray micro-CT technique using a large bulk sample. One of the advantages of micro-CT is that analysis can be done within a scale up to tens of millimetres. But the pixel size is limited, namely, 4.21  $\mu\text{m}$  in our case, which will allow an estimation of air voids and large capillary voids in microscale. The image slices from micro-CT were reconstructed in NRecon software, and the pore systems were then segmented in Dragonfly. As observed in Figure 6.7, air voids are spherical and non-connected. On the other hand, capillary pores are irregular, and some are interconnected. Also, the closed porosity of the bulk sample is 12.7%, which does not affect the transport property, but strongly influence the mechanical strength.

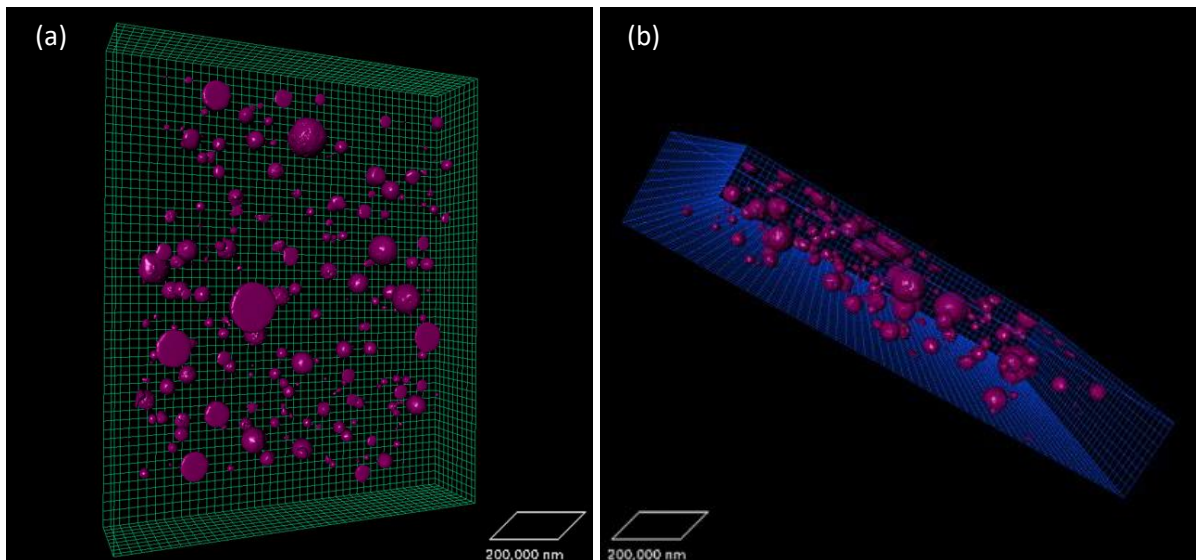


Figure 6.7 X-ray micro-CT and reconstruction models of air voids and large capillary pores of OPC mortar in different viewing directions

### 6.3.3 Pore Size Distribution

The diagrams of pore size distribution (Figure 6.8) were derived using 3D models from PFIB and micro-CT, respectively. The voxel size is 25 nm by 25 nm by 100 nm that will allow analysis into pores of equivalent diameter of hundreds of nanometers and up. It is observed that the pore size maxima determined from PFIB images can be as large as 6700 nm. It is worth noting that pores larger than 4200 nm computed from PFIB reconstruction account for less than 10 in number. The voxel size of micro-CT image is 4.21  $\mu\text{m}$  by 4.21  $\mu\text{m}$  by 4.21  $\mu\text{m}$  and the largest pore detected is 1000  $\mu\text{m}$ . Therefore, the above techniques come to a good agreement and provide the capability to accurately characterize the pores from hundreds of nanometers to millimeters.

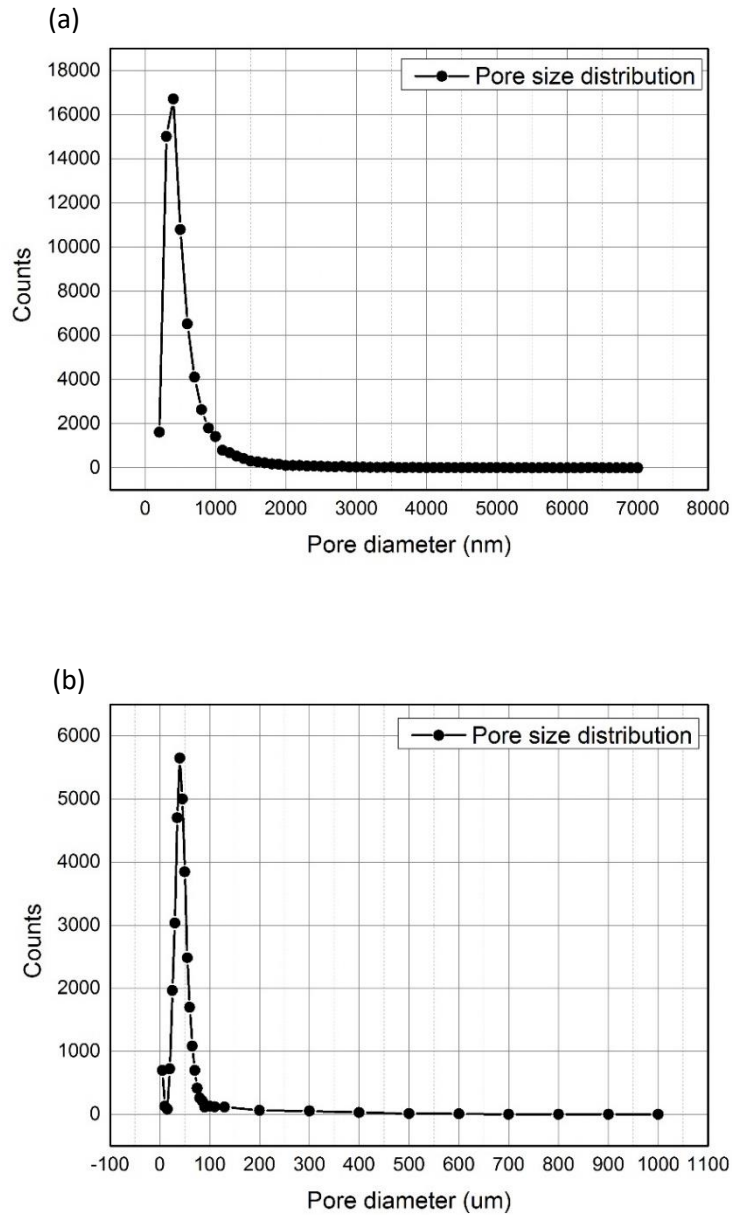


Figure 6.8 Pore size distribution of a) capillary pores from PFIB reconstruction and b) air voids and large capillary pores from micro-CT reconstruction

#### 6.4. Discussion

The visualization and quantification depend greatly on the sample preparation. Instead of using deposition layer on top, we applied a new method [32] that involved a hard Si mask. The idea is to predetermine a few potential VOIs in advance and record the distance between VOI and an identical feature. Also, it is better to use separate pieces of Si wafers rather than a large Si mask, because this allows an observation of more identical feature and a quick navigation

to the area. Sometimes the acquisition and matching of images both from the surface and cross section is also very helpful. The application of sacrificial mask is believed to tailor the beam, minimize milling artefacts and provide protection over high-current beam from over-milling [32]. This method allowed to achieve good image quality even in large dimension, which made subsequent segmentation and quantification much easier.

Cement phases are not usually hydrated to a completion even after long times from mixing with water. The larger the cement particles, the higher the amount of anhydrous phases. One possible explanation is that the surface of the cement particles are soon covered with primary C-S-H reducing further contact between the anhydrous core and the water [41]. The reconstruction of the anhydrous phases at different time intervals provides important data enabling direct study of hydration kinetics of different cement phases individually. Knowing that alite and belite both produce similar hydration products (CSH and calcium hydroxide), direct study of hydration kinetics of individual cement phases has been impossible because the hydration products of the cement phases cannot be measured individually. The remaining anhydrous cement phases inside the matrix can be simply distinguished from their relative contrast. PFIB tomography then enables determination of representative anhydrous cement phase volume at different time intervals, which provides data for direct kinetics study of each phase individually.

Another interesting observation is the shape of the remaining anhydrous phases resembling some hollow geometry (see Figure 6.6 (b)) showing that the dissolution is not homogeneous and indicates preferential dissolution locations, such as etch pits [42]. The formation of etch pits at early hydration stages occurs under high degrees of undersaturation, which provides more available surface and significantly influence the dissolution rate [39, 40, 43].

The pore systems of cementitious materials consist of capillary pores, air voids and gel pores that not only affect mechanical performance but also influence durability. It is generally believed that large capillary pores, especially macropores (0.05 – 10  $\mu\text{m}$ ) drive macroscopic fluid transport [23]. The entrained air voids with  $\mu\text{m}$  to mm scale range are related to the resistance to freeze-thaw property [44-47]. It is crucial that PFIB and micro-CT techniques are combined to analyze pore system due to its wide range. These techniques add subtlety to typical methods, like MIP, that overestimates the small pores [2, 22, 48]. MIP only detects the size of pore entrance that does not exactly reflect the size and shape of a pore leading to the so-called ink-bottle effect [49, 50]. The difference of total porosity can be as high as 40% among cement paste, paste with silica fume and paste with nano-silica using MIP and FIB-SEM techniques [22]. The fact that MIP measures pore entry sizes and closed pores are not detected lead to an order of magnitude smaller than the estimation from BSE and laser scanning confocal microscopy (LSCM) [51]. MIP simulations were also developed to be compared with experimental MIP, which showed a difference of 18 nm between the simulated and experimental peaks due to small sample volume (61-118  $\mu\text{m}^3$ ) and sample heterogeneity in FIB-SEM [23]. The advent of PFIB improves the capability to acquire large-scale serial sectioning in nanometric resolution and benefits simulation work. The technique also provides research capabilities in studying microstructural features of cement mortar including structural defects like cracks, inhomogeneities, and porosity in interfacial transition zone. In previous research, it was also necessary that several serial sectioning have to be conducted so that they can be representative [23, 52, 53]. This is complemented by a large-volume serial sectioning with the assistance of PFIB technique.

## **6.5. Conclusions**

We applied PFIB and micro-CT to cement mortar achieving the multi-scale analysis of pore system and visualization of main structure. The application of PFIB broadens the capability for

potential sectioning of hundreds of nanometers and effective analyzing dimension of 79.8  $\mu\text{m}$  by 88.3  $\mu\text{m}$  by 63.1  $\mu\text{m}$  for the first time. The workflow involving prepositioned hard Si masks on cement mortar was established and proved to be useful in reducing curtaining artifacts. The image stack was then segmented through Neural Network with human interference being kept to a minimum. The reconstruction model reveals that cement particle hydrates in different rates from different directions. The large capillary pores and air voids account for 11.5% and 12.7%, respectively. The quantification of PFIB and CT reconstruction provides insights on pore size distribution that covers the range from hundreds of nanometers to millimeter.

## 6.6 Acknowledgements

The authors would like to thank the staff in Canadian Centre for Electron Microscopy (CCEM) for the assistance of sample preparation. We also acknowledge the help and useful discussion from Dakota Binkley and Joe Deering. Thanks to Professor Kathryn Grandfield for the support in instrumentation.

## 6.7 References

1. Babae, M. and A. Castel, *Chloride-induced corrosion of reinforcement in low-calcium fly ash-based geopolymer concrete*. Cement and Concrete Research, 2016. **88**: p. 96-107.
2. Yu, Z., et al., *Relationship between water permeability and pore structure of Portland cement paste blended with fly ash*. Construction and Building Materials, 2018. **175**: p. 458-466.
3. Mehta, P. and P. Monteiro, *M. Concrete: microstructure, properties, and materials*. 3rd. New York, 2006.
4. Sun, Z. and G.W. Scherer, *Effect of air voids on salt scaling and internal freezing*. Cement and Concrete Research, 2010. **40**(2): p. 260-270.
5. Fonseca, P.C. and G.W. Scherer, *An image analysis procedure to quantify the air void system of mortar and concrete*. Materials and Structures, 2014. **48**(10): p. 3087-3098.

6. Yio, M.H., et al., *3D imaging of cement-based materials at submicron resolution by combining laser scanning confocal microscopy with serial sectioning*. *J Microsc*, 2015. **258**(2): p. 151-69.
7. Shi, M., et al., *Microstructural characterization of pores in marine shales of the Lower Silurian Longmaxi Formation, southeastern Sichuan Basin, China*. *Marine and Petroleum Geology*, 2018. **94**: p. 166-178.
8. Liu, Y., et al., *Nano-Tomography of Porous Geological Materials Using Focused Ion Beam-Scanning Electron Microscopy*. *Minerals*, 2016. **6**(4).
9. Pappalardo, G., et al., *The role of porosity on the engineering geological properties of 1669 lavas from Mount Etna*. *Engineering Geology*, 2017. **221**: p. 16-28.
10. Jiang, J., et al., *Study on the preparation and properties of high-porosity foamed concretes based on ordinary Portland cement*. *Materials & Design*, 2016. **92**: p. 949-959.
11. Kamseu, E., et al., *Influence of fine aggregates on the microstructure, porosity and chemico-mechanical stability of inorganic polymer concretes*. *Construction and Building Materials*, 2015. **96**: p. 473-483.
12. Zhang, L., et al., *Hydration for the Alite mineral: Morphology evolution, reaction mechanism and the compositional influences*. *Construction and Building Materials*, 2017. **155**: p. 413-426.
13. Cantoni, M. and L. Holzer, *Advances in 3D focused ion beam tomography*. *MRS Bulletin*, 2014. **39**(04): p. 354-360.
14. Taylor, R., et al., *Developments in TEM Nanotomography of Calcium Silicate Hydrate*. *Journal of the American Ceramic Society*, 2015. **98**(7): p. 2307-2312.
15. Brisard, S., et al., *Mesoscale pore structure of a high-performance concrete by coupling focused ion beam/scanning electron microscopy and small angle X-ray scattering*. *Journal of the American Ceramic Society*, 2018.
16. Priebe, A., G. Audoit, and J.P. Barnes, *A novel PFIB sample preparation protocol for correlative 3D X-ray CNT and FIB-TOF-SIMS tomography*. *Ultramicroscopy*, 2017. **173**: p. 10-13.

17. Holzer, L. and M. Cantoni, *Review of FIB-tomography*. Nanofabrication Using Focused Ion and Electron Beams: Principles and Applications, 2012. **559201222**: p. 410-435.
18. Bassim, N., K. Scott, and L.A. Giannuzzi, *Recent advances in focused ion beam technology and applications*. MRS Bulletin, 2014. **39**(04): p. 317-325.
19. Holzer, L., et al., *Three-dimensional analysis of porous BaTiO<sub>3</sub> ceramics using FIB nanotomography*. Journal of microscopy, 2004. **216**(1): p. 84-95.
20. He, J., et al., *Pore structure of shale and its effects on gas storage and transmission capacity in well HD-1 eastern Sichuan Basin, China*. Fuel, 2018. **226**: p. 709-720.
21. Holzer, L., et al., *Cryo-FIB-nanotomography for quantitative analysis of particle structures in cement suspensions*. Journal of Microscopy, 2007. **227**(3): p. 216-228.
22. Lim, S., H.-S. Lee, and S. Kawashima, *Pore structure refinement of cement paste incorporating nanosilica: Study with dual beam scanning electron microscopy/focused ion beam (SEM/FIB)*. Materials Characterization, 2018. **145**: p. 323-328.
23. Song, Y., et al., *Pore network of cement hydrates in a High Performance Concrete by 3D FIB/SEM — Implications for macroscopic fluid transport*. Cement and Concrete Research, 2019. **115**: p. 308-326.
24. Jiruse, J., et al., *Combined plasma FIB-SEM*. Microscopy and Microanalysis, 2012. **18**(S2): p. 652-653.
25. Burnett, T.L., et al., *Large volume serial section tomography by Xe Plasma FIB dual beam microscopy*. Ultramicroscopy, 2016. **161**: p. 119-29.
26. Xiao, Y., et al., *Investigation of the deformation behavior of aluminum micropillars produced by focused ion beam machining using Ga and Xe ions*. Scripta Materialia, 2017. **127**: p. 191-194.
27. Zhong, X., et al., *Multi-Modal Plasma Focused Ion Beam Serial Section Tomography of an Organic Paint Coating*. Ultramicroscopy, 2018.
28. Hoang, T.V., et al., *Automatic segmentation of high pressure frozen and freeze-substituted mouse retina nuclei from FIB-SEM tomograms*. J Struct Biol, 2017. **197**(2): p. 123-134.

29. Khalaf, W., et al., *A DC optimization-based clustering technique for edge detection*. Optimization Letters, 2016. **11**(3): p. 627-640.
30. El Aziz, M.A., A.A. Ewees, and A.E. Hassanien, *Whale optimization algorithm and moth-flame optimization for multilevel thresholding image segmentation*. Expert Systems with Applications, 2017. **83**: p. 242-256.
31. Ronneberger, O., P. Fischer, and T. Brox. *U-net: Convolutional networks for biomedical image segmentation*. in *International Conference on Medical image computing and computer-assisted intervention*. 2015. Springer.
32. Subramaniam, S., et al., *A Comprehensive Approach Towards Optimizing the Xenon Plasma Focused Ion Beam Instrument for Semiconductor Failure Analysis Applications*. Microsc Microanal, 2017. **23**(4): p. 769-781.
33. Shan, H., F. Li, and Y. Jinchi, *An Image Edge Detection Algorithm Based on Improved Mathematical Morphology and Wavelet Transform*. DEStech Transactions on Environment, Energy and Earth Sciences, 2019(iccis).
34. Novikov, A.A., et al., *Deep sequential segmentation of organs in volumetric medical scans*. IEEE transactions on medical imaging, 2018. **38**(5): p. 1207-1215.
35. Chalmers, G.R., R.M. Bustin, and I.M. Power, *Characterization of gas shale pore systems by porosimetry, pycnometry, surface area, and field emission scanning electron microscopy/transmission electron microscopy image analyses: Examples from the Barnett, Woodford, Haynesville, Marcellus, and Doig units*. AAPG Bulletin, 2012. **96**(6): p. 1099-1119.
36. Zankel, A., J. Wagner, and P. Poelt, *Serial sectioning methods for 3D investigations in materials science*. Micron, 2014. **62**: p. 66-78.
37. Schankula, C.W., C.K. Anand, and N.D. Bassim, *Multi-Angle Plasma Focused Ion Beam (FIB) Curtaining Artifact Correction Using a Fourier-Based Linear Optimization Model*. Microscopy and Microanalysis, 2018. **24**(6): p. 657-666.
38. Lim, S. and P. Mondal, *Micro-and nano-scale characterization to study the thermal degradation of cement-based materials*. Materials Characterization, 2014. **92**: p. 15-25.

39. Bullard, J.W., et al., *Mechanisms of cement hydration*. Cement and Concrete Research, 2011. **41**(12): p. 1208-1223.
40. Nicoleau, L., M.A. Bertolim, and L. Struble, *Analytical Model for the Alite (C3S) Dissolution Topography*. Journal of the American Ceramic Society, 2016. **99**(3): p. 773-786.
41. Scrivener, K.L., P. Juilland, and P.J.M. Monteiro, *Advances in understanding hydration of Portland cement*. Cement and Concrete Research, 2015. **78**: p. 38-56.
42. Juilland, P. and E. Gallucci, *Morpho-topological investigation of the mechanisms and kinetic regimes of alite dissolution*. Cement and Concrete Research, 2015. **76**: p. 180-191.
43. Bergold, S.T., F. Goetz-Neunhoeffler, and J. Neubauer, *Interaction of silicate and aluminate reaction in a synthetic cement system: Implications for the process of alite hydration*. Cement and Concrete Research, 2017. **93**: p. 32-44.
44. Lu, H., *X-ray Computed Tomography Assessment of Air Void Distribution in Concrete*. 2017.
45. Mayercsik, N.P., M. Vandamme, and K.E. Kurtis, *Assessing the efficiency of entrained air voids for freeze-thaw durability through modeling*. Cement and Concrete Research, 2016. **88**: p. 43-59.
46. Liu, Z. and W. Hansen, *Freezing characteristics of air-entrained concrete in the presence of deicing salt*. Cement and Concrete Research, 2015. **74**: p. 10-18.
47. Jin, S., J. Zhang, and B. Huang, *Fractal analysis of effect of air void on freeze-thaw resistance of concrete*. Construction and Building Materials, 2013. **47**: p. 126-130.
48. Wu, Z., et al., *Effects of different nanomaterials on hardening and performance of ultra-high strength concrete (UHSC)*. Cement and Concrete Composites, 2016. **70**: p. 24-34.
49. Wu, Z., K.H. Khayat, and C. Shi, *Effect of nano-SiO<sub>2</sub> particles and curing time on development of fiber-matrix bond properties and microstructure of ultra-high strength concrete*. Cement and Concrete Research, 2017. **95**: p. 247-256.
50. Elgalhud, A.A., R.K. Dhir, and G. Ghataora, *Limestone addition effects on concrete porosity*. Cement and Concrete Composites, 2016. **72**: p. 222-234.

51. Yio, M.H.N., H.S. Wong, and N.R. Buenfeld, *3D pore structure and mass transport properties of blended cementitious materials*. Cement and Concrete Research, 2019. **117**: p. 23-37.
52. Wang, P., et al., *Pore structure characterization for the Longmaxi and Niutitang shales in the Upper Yangtze Platform, South China: Evidence from focused ion beam–He ion microscopy, nano-computerized tomography and gas adsorption analysis*. Marine and Petroleum Geology, 2016. **77**: p. 1323-1337.
53. Aslannejad, H., et al., *Characterizing the hydraulic properties of paper coating layer using FIB-SEM tomography and 3D pore-scale modeling*. Chemical Engineering Science, 2017. **160**: p. 275-280.

## 7. Conclusions and Outlook

This work is focused on understanding hydration reactions in both early and late stages of cement systems with nano-silica. In early hydration reactions up to 24 h, it is important to clarify microstructural evolution, phase transformation and hydration kinetics, which contribute to early structure and strength development. The effects of nano-silica on cement hydration reactions are also clarified. For these experiments, nano PC was prepared through three-step ball milling process. The in-situ hydration reactions were conducted in LC-TEM and the real-time growth and dissolution were captured. The post-situ experiments including (HR)TEM, SEM and EDS, QXRD and isothermal calorimetry are performed as well, to understand the crystallinity, morphology and composition, and kinetics.

Furthermore, it is also crucial to understand pore systems and the distribution of different phases in mature samples of late hydration stage. This is because porosity and pore characteristics determine the properties of cementitious materials, including compressive strength, fluid transport property and freeze-thaw property. The study into spatial distribution of different phases allows a better understanding of hydration kinetics. A novel characterization tool, PFIB technique was applied to obtain serial sectioning, in which the workflow and method of using a hard Si mask on sample surface were explored. After segmentation and quantitative analysis, the characteristics of pore systems, e.g., porosity, connectivity and pore size distribution were researched, and dissolution rates and hydration kinetics further revealed. The major findings are summarized as follows:

In Chapter 3, the first application of liquid cell electron microscopy in cement hydration reactions was realized. This enables a real-time imaging of main hydrated products, and thus provides new insights into microstructure evolution. In general, the reaction sequences of nano PC were similar to that in practice use. The in-situ hydration reactions reveal direct evidence

of C-S-H growth that has been debated for decades. Combined with post-situ experiments, it is found that C-S-H starts according to the layered structure model. The nucleated C-S-H embryos evolve through attachment of silicate tetrahedra from solution along the margin of precipitates to form planar silicate sheets. An alternation of nanocrystalline structure of 5 nm to 10 nm and amorphous region is achieved. The internal stress is built in between disordered arrangements of atoms and nanocrystalline regions that is the cause of buckling and cracking. These internal stresses and rolling up of the precipitates promote new embryos to form and aggregate together, which also indicate the other growth mechanisms of aggregation of building blocks. It is also observed that needle-like ettringite crystals form in the early hydration reactions. The SEM results further confirm the composition of C-S-H precipitates and 3D microstructure indicating enough room in liquid cell for 3D microstructure development later. The morphology and composition of portlandite and monosulfate are also confirmed by SEM and EDS.

In Chapter 4, different cement hydration stages of nano PC as well as hydration kinetics were studied using LC-TEM, freeze drying, QXRD and isothermal calorimetry. LC-TEM shows that C-S-H precipitates nucleate on the cell membrane with sharp edges and develop in 3D. The needle-like ettringite crystals provide the seeding effects that further promote the C-S-H precipitation on the surface. The initial reaction period consists of the dissolution of C<sub>3</sub>S, nucleation of C-S-H as well as ettringite formation. It is also found that the formation rate of C-S-H precipitates slows down during this period. The induction period involving further C-S-H nucleation and partial growth and continuous formation of ettringite appears around 3 h. A net accumulation of ettringite content is seen, in spite of partial dissolution releasing sulfate to form monosulfate. The real-time dissolution of needle-like ettringite crystals is also reported. During the acceleration stage, the retardation effects occurs due to the reduction of C-S-H surface area by monosulfates for newly formed precipitates, leading to a much later main

silicate peak in heat flow curve of nano PC than that of OPC. C-S-H precipitates continue to develop, form a network, and fully cover the SiN membrane during acceleration and deceleration stages.

Chapter 5 clarifies the effects of nano-silica on the early-age hydration reactions of nano PC, including microstructure, heat release and phase transformations. It is observed that nano-silica plays different roles in nano PC and OPC. In both nano-systems, it is very difficult to distinguish the initial and induction periods since they are very short. Similar to hydration reactions of nano PC, it also exhibits a strong retardation effect in nano PC with NS in the beginning of the acceleration stage between 2 h and 8 h with lower heat rate and cumulative heat, which due to the formation of monosulfates. Compared with nano PC system, the rate of heat release of nano PC with nano-silica is slightly higher, and the total heat within 24 h is slightly lower. However, the initial and induction periods of OPC are significantly shortened by incorporating nano-silica. The appearance of acceleration stage is 1 h earlier, and the main silicate peak 2 h earlier in OPC with NS compared with that of OPC. The total heat after the first day is much more in OPC with nano-silica. The reason is that OPC with normal fineness shares less surface area and nano-silica provides more nucleation sites and contributes to a greater degree of hydration.

Chapter 5 also summarizes the effects of nano-silica on microstructure development. It is observed that more well-distributed microstructure forms in nano PC with NS resulting from seeding effects. LC-TEM results also show that nano-silica has a strong tendency to be absorbed to ettringite crystals. More ettringite are found to be dissolved in nano PC with nano-silica compared to that in plan nano PC system, suggesting that the addition of nano-silica accelerates the conversion of ettringite to monosulfate.

Chapter 6 demonstrates the capability of PFIB on acquiring large-scale 3D dataset and reconstruction models of cementitious materials. A new method of applying a hard Si mask on mortar sample surface was investigated. The results show that the image quality is significantly improved using Si mask with curtaining effects being minimized. After alignment and cropping the whole dataset, the effective volume dimension is 79.8  $\mu\text{m}$  by 88.3  $\mu\text{m}$  by 63.1  $\mu\text{m}$ . A neural network was trained for segmenting the dataset and quantitative analysis conducted afterwards. The 3D reconstruction models from PFIB dataset clearly reveal the fluid transport pathways. The percentages of large capillary pores and air voids are 11.5% and 12.7%, respectively. Combining with X-ray micro-CT technique, the pore systems ranging from hundreds of nanometers to millimeters can be well covered.

In-situ imaging of C-S-H precipitate assembly with atomic resolution requires more studies. This can provide insights into C-S-H nucleation whether it begins from crystalline or amorphous embryos. The effects of dose rate on the pH value of liquid sample and formation rates can be monitored so that the role of electron dose is clarified and mitigated. A simulation can be conducted to further predict the pH value in cement slurry with various dose rates. This will help to better understand the beam conditions and cement hydration reactions quantitatively.

Finally, the application of PFIB into cementitious materials requires more research. First, the PFIB acquisition of serial images needs to be improved. It runs into the problem that large volume of data is cut out under current conditions. This results from the fact that the SEM fiducial for alignment is on the image leading to shading effect later. A new method is worth investigating to keep more effective volume after cropping due to shading effect around SEM fiducial. Second, it is required that gel pores ( $< 10 \text{ nm}$ ) and small capillary pores (10 nm – 50 nm) be studied since gel pores are related to shrinkage and small capillary pores need higher resolution leading to longer data acquisition times. Third, the pore systems and hydration

degree in OPC mortar with nano-silica are worth researching. It is also important to investigate pore characteristics, and distribution of various phases in different cements and concretes. The relationship between porosity and properties including compressive and transport properties can be established in these cementitious materials.

## **Appendix**

### **Note 3.A1. Chemical Compositions of Ettringite and Monosulfate**

The chemical compositions of a needle-like crystal and the adjoining hydration product were examined by SEM and EDS in Figure 3.A2. Both two forms of structure contain featured peaks of Ca, Al, S, and O. The Spectrum 2 exhibits more Al and Ca compared with Spectrum 1. The needle-like crystal is ettringite and the foil-like structure is likely to be monosulfates based on their morphology. The N and Si peaks are attributable to the background of the SiN substrates, and Mg peak is resulted from impurities in Portland cement. The adjoined hydration product (spectrum 2) comprised of mainly Ca, Al, O, and small amounts of S was likely to be calcium monosulfates (AFm) formed from ettringite conversion. It was reported that AFm might form usually after the first 24 hours from the start of hydration time and is difficult to be detected in some calorimetry or in-situ XRD experiments [1-3].

### **Note 3.A2. Chemical Composition of Portlandite Embedded in the Matrix**

The main by – product of hydration reactions of calcium silicate phases is  $\text{Ca(OH)}_2$ , which crystallizes to hexagonal sheet-like Portlandite crystals upon saturation of the reacting medium. Portlandite crystals were also observed in our experiment and confirmed by SEM and EDS. Figure 3.A4 shows a typical SEM image with EDS results of Portlandite in post situ characterization. Table 3.A1 represents the contents of elements averaged with four spectra. As can be seen, the observed hexagonal sheet-like crystals were composed of mainly CaO indicating the existence of Portlandite. The presence of a small amount of Si can be the result of the electron beam interaction with the SiN membrane or the existing C-S-H precipitates.

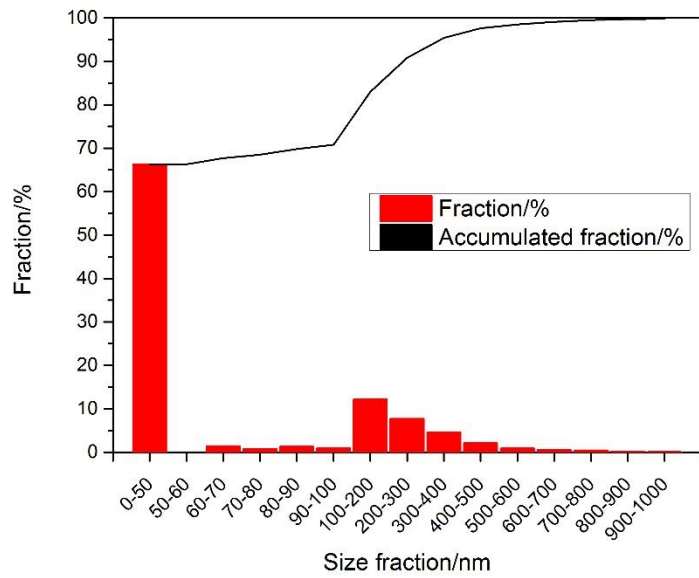
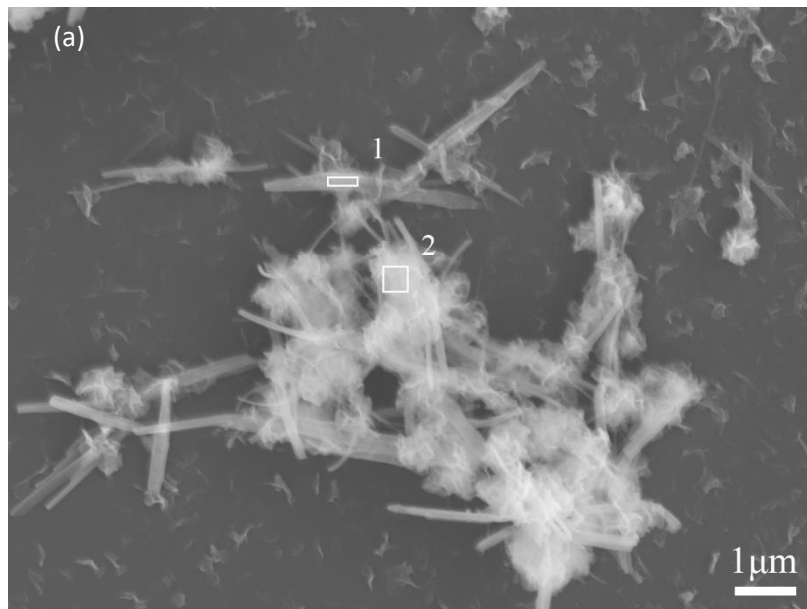


Figure 3.A1. Particle size distribution of nano PC after three-step ball milling



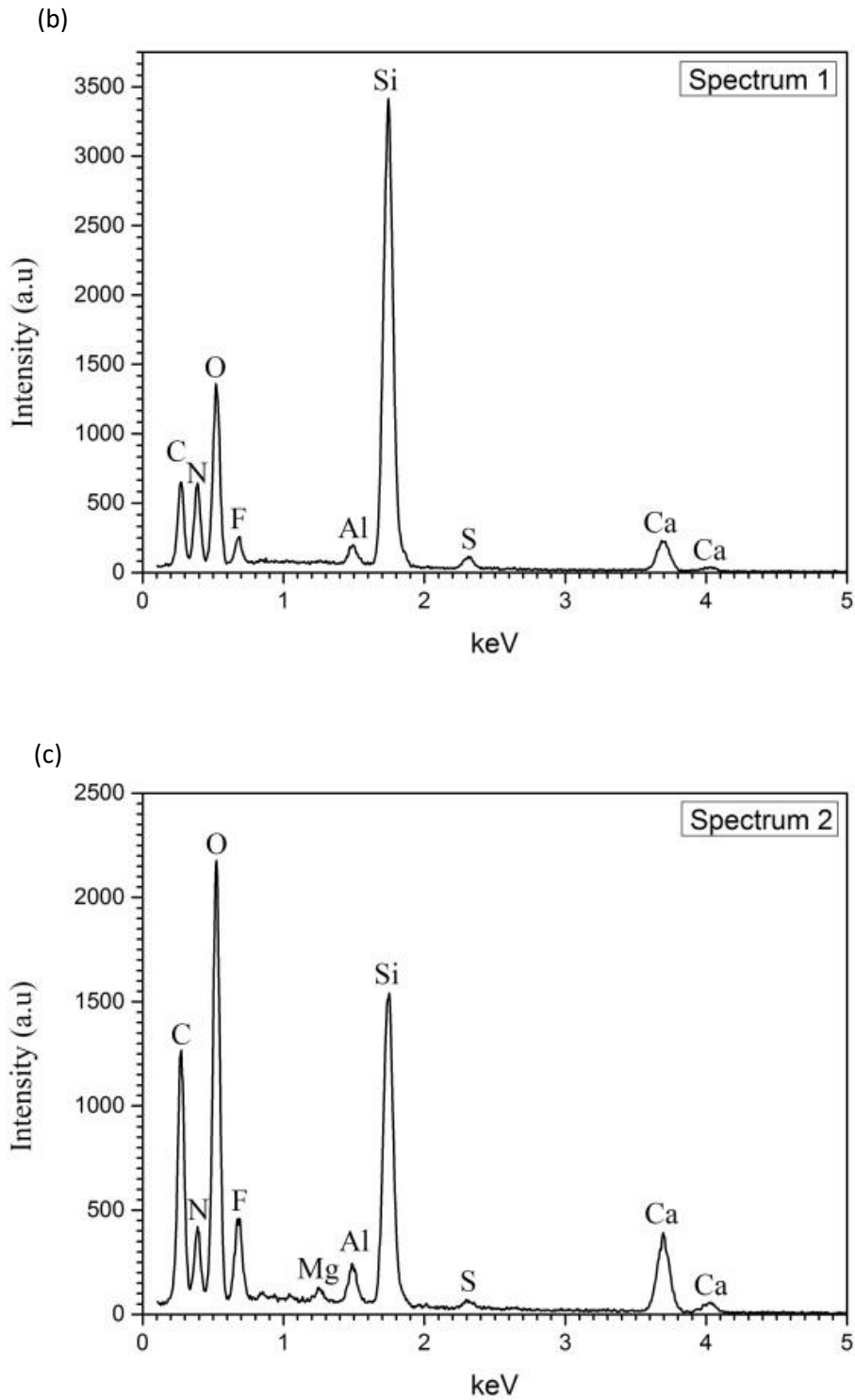


Figure 3.A2. SEM image and EDS spectra showing ettringite (spectrum 1) and calcium monosulfate (spectrum 2)

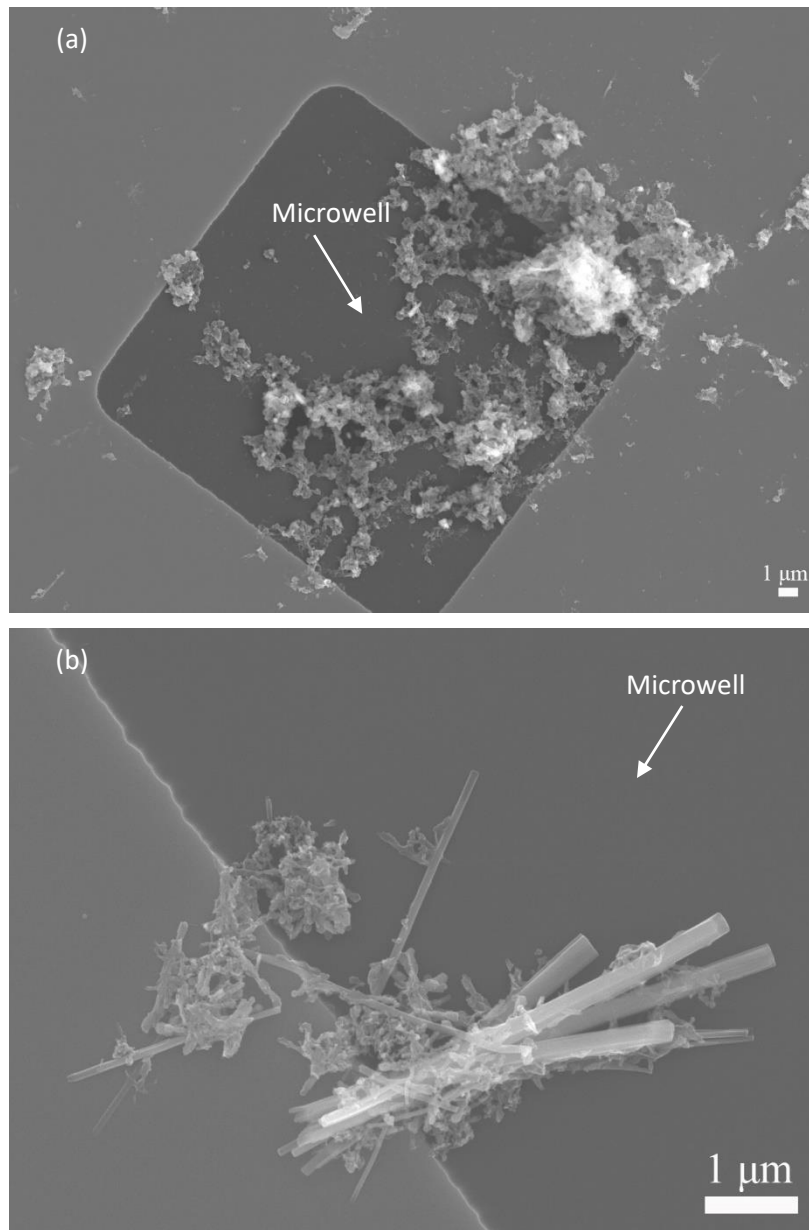


Figure 3.A3 Secondary electron image of (a) C-S-H precipitates and (b) C-S-H precipitates and ettringite crystals inside liquid reaction cell after opening the chips, indicating enough room of liquid cell for 3D structure development

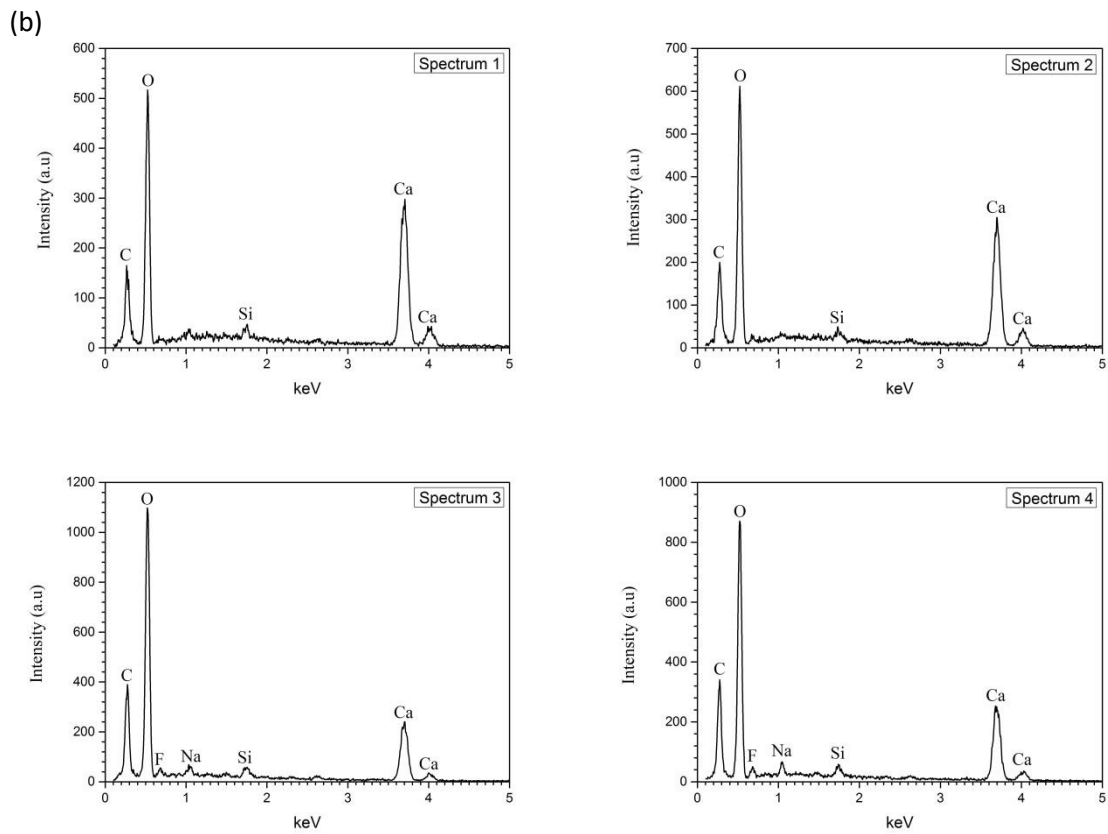
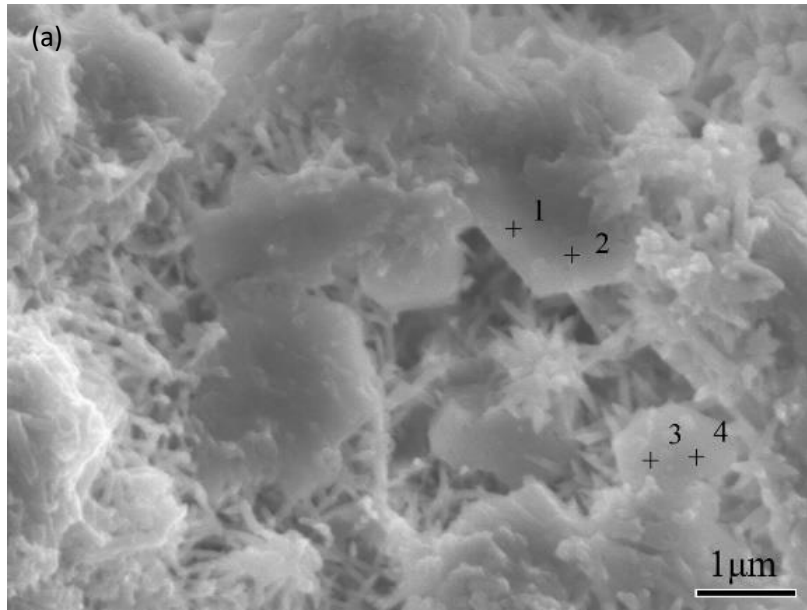


Figure 3.A4 Post-situ characterization of Portlandite (a) SEM and (b) EDS spectra from the positions marked in Figure 3-A3 (a)

Table 3.A1 Chemical, Bogue’s potential phase compositions and physical properties of as –

received OPC

Chemical composition		Bogue's potential phase compositions	
Oxide	Quantity/wt.%	Phase	Quantity/wt.%
SiO <sub>2</sub>	20.32	C <sub>3</sub> S	46.72
Al <sub>2</sub> O <sub>3</sub>	5.44	C <sub>2</sub> S	24.12
Fe <sub>2</sub> O <sub>3</sub>	2.92	C <sub>3</sub> A	9.71
CaO	63.64	C <sub>4</sub> AF	9.04
MgO	2.30	<b>Physical properties</b>	
SO <sub>3</sub>	3.56	Property	Quantity
Na <sub>2</sub> O	0.15	Blaine fineness (m <sup>2</sup> /kg)	376
K <sub>2</sub> O	1.07	% Retained on 45 μm (No. 325) sieve	97.50
LOI	2.05		

Table 3.A2 Elemental analysis of Portlandite by EDS

	Ca/%	O/%	Si/%	C/%	Na/%	F/%
Spectrum 1	61.4	33.0	0.9	4.6	—	—
Spectrum 2	58.1	35.7	0.7	5.5	—	—
Spectrum 3	40.1	46.0	1.3	10.2	0.9	1.5
Spectrum 4	45.4	41.2	1.2	9.3	1.2	1.8
Average/%	51.25	38.98	1.03	7.40	0.53	0.83

#### References

1. Scrivener, K.L., P. Juilland, and P.J.M. Monteiro, *Advances in understanding hydration of Portland cement*. Cement and Concrete Research, 2015. **78**: p. 38-56.
2. Bhanumathidas, N. and N. Kalidas, *Dual role of gypsum: Set retarder and strength accelerator*. Vol. 78. 2004. 170-173.
3. Jansen, D., et al., *Does Ordinary Portland Cement contain amorphous phase? A quantitative study using an external standard method*. Powder Diffraction, 2011. **26**(1): p. 31-38.
4. 50, <[David\_R.\_Gaskell]\_INTRODUCTION\_TO\_THE\_THERMODYNAM(b-ok.org).pdf>.

Table 4.A1 Chemical, Bogue’s potential phase compositions and physical properties of as –  
received OPC

<b>Chemical composition</b>			
Oxide	Quantity/wt.%	Oxide	Quantity/wt.%
SiO <sub>2</sub>	20.32	MgO	2.30
Al <sub>2</sub> O <sub>3</sub>	5.44	SO <sub>3</sub>	3.56
Fe <sub>2</sub> O <sub>3</sub>	2.92	Na <sub>2</sub> O	0.15
CaO	63.64	K <sub>2</sub> O	1.07
<b>Physical properties</b>			
Property	Quantity	Property	Quantity
Blaine fineness (m <sup>2</sup> /kg)	376	% Retained on 45 μm (No. 325) sieve	97.50

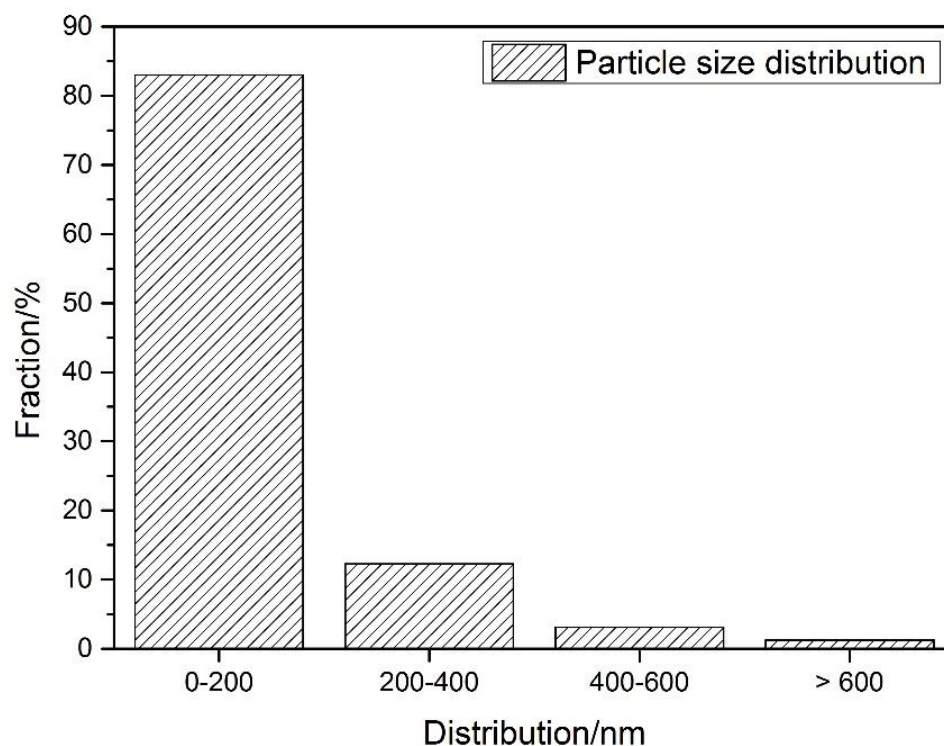


Figure 4.A1 Particle size distribution of nano OPC

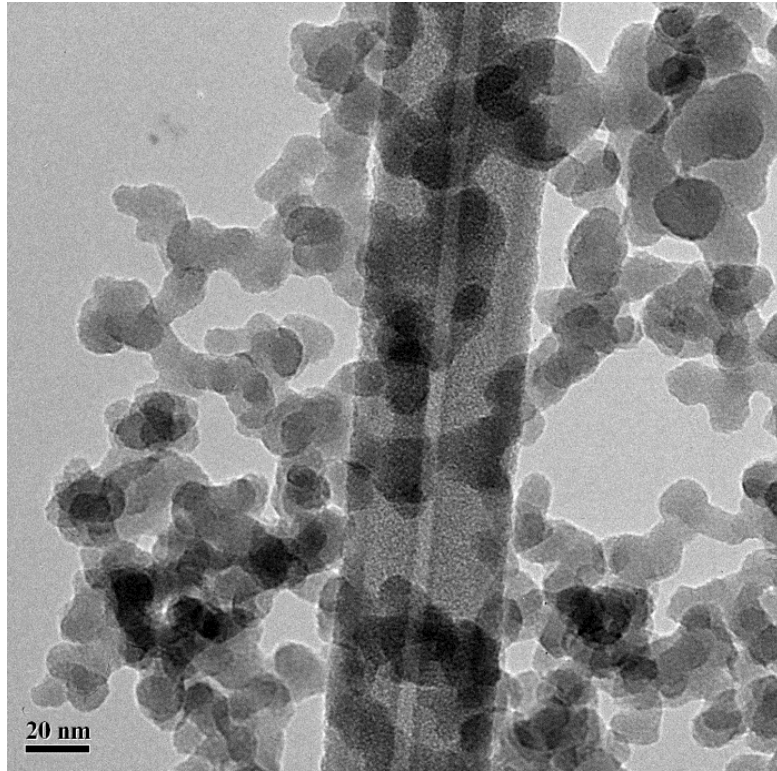


Figure 5.A1 Microstructure and morphology of nano-silica

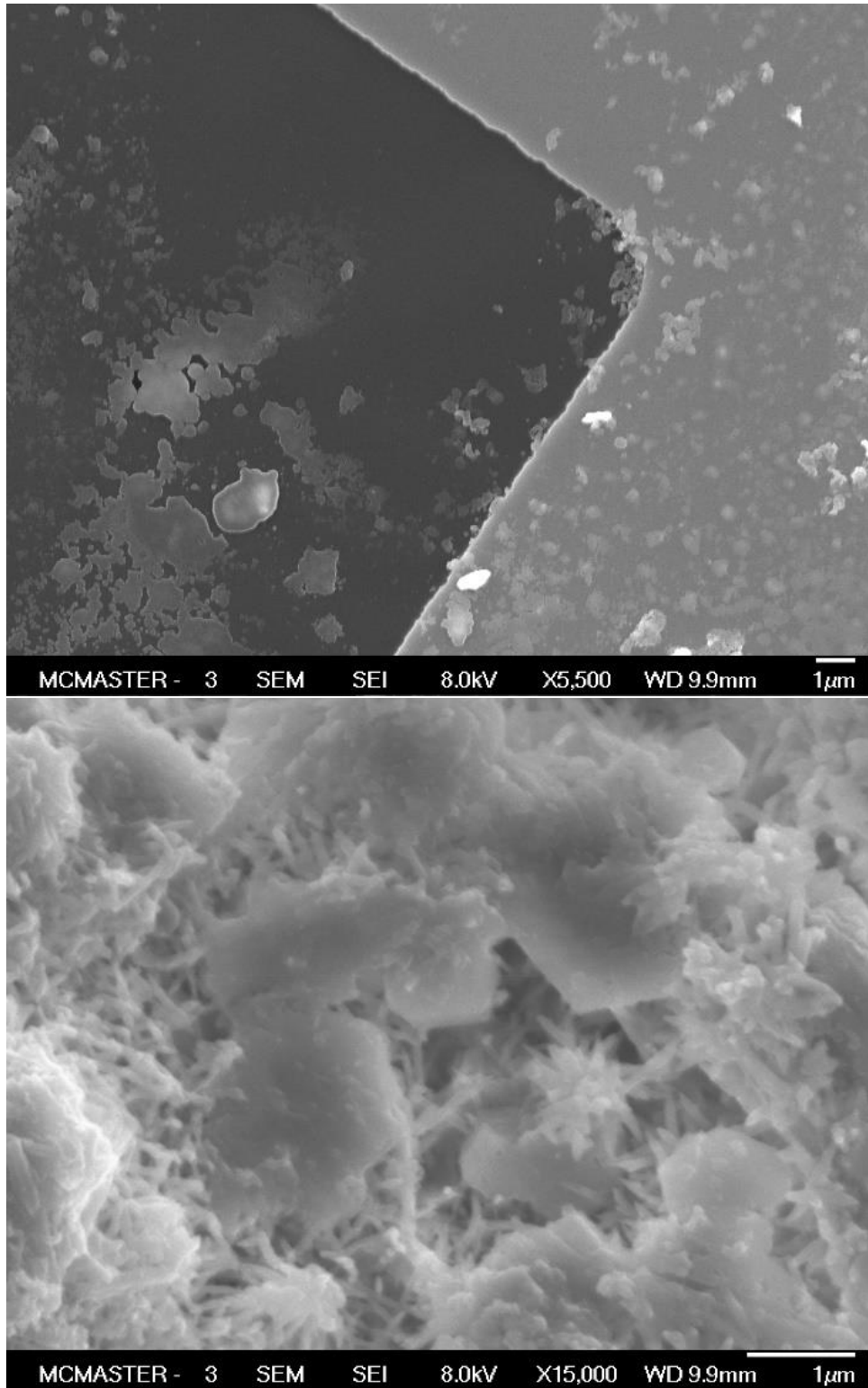


Figure 5.A2 SEM showing morphology of hydrated products in nano PC, a) sheet-like C-S-H and b) embedded portlandite in C-S-H precipitates

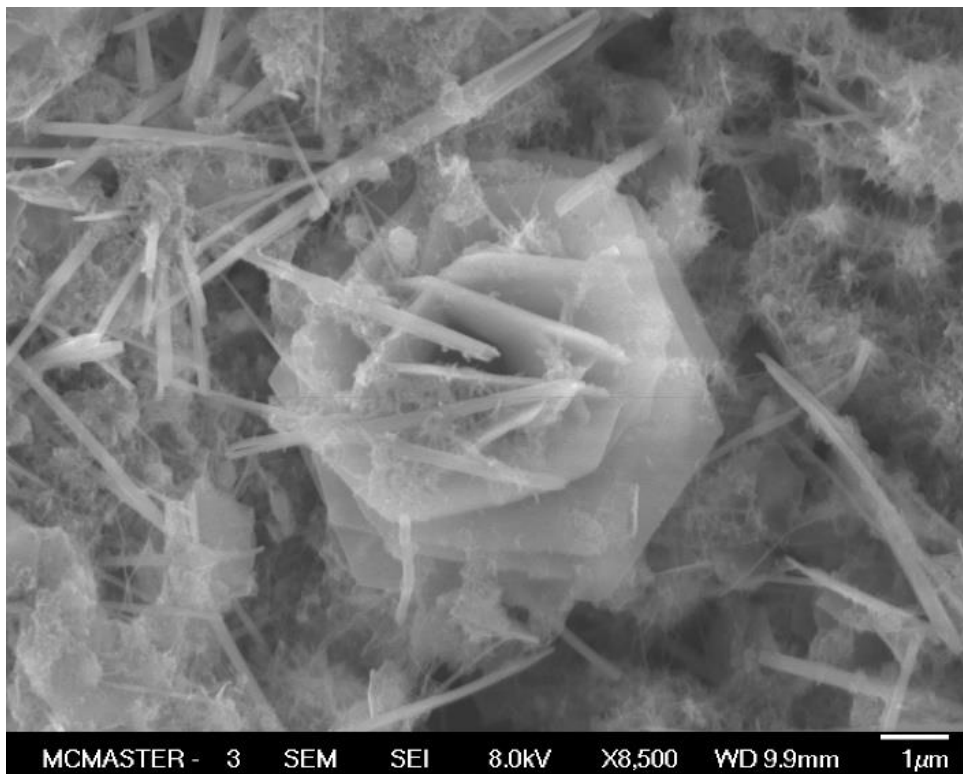
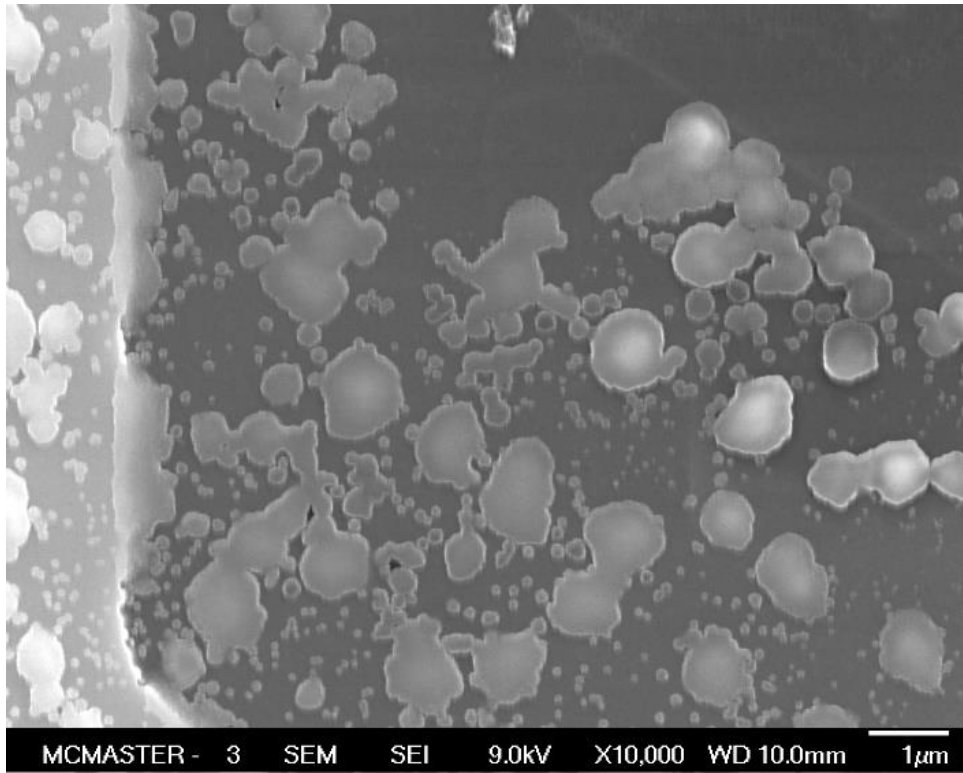
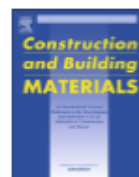


Figure 5.A3 SEM images showing morphology of hydrated products in nano PC with nano-silica, a) more distributed sheet-like C-S-H and b) embedded portlandite



## Acid attack on geopolymer cement mortar based on waste-glass powder and calcium aluminate cement at mild concentration



Mostafa Vafaei<sup>a</sup>, Ali Allahverdi<sup>b,\*</sup>, Peng Dong<sup>c</sup>, Nabil Bassim<sup>c</sup>

<sup>a</sup>Research Laboratory of Inorganic Chemical Process Technologies, School of Chemical Engineering, Iran University of Science and Technology, Narmak 1684613114, Tehran, Iran

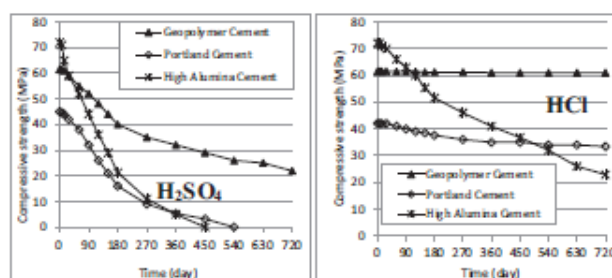
<sup>b</sup>Cement Research Center, Iran University of Science and Technology, Narmak 1684613114, Tehran, Iran

<sup>c</sup>Department of Materials Science and Engineering, McMaster University, Hamilton, Ontario L8S 3Z9, Canada

### HIGHLIGHTS

- Durability of geopolymer based on waste glass/CAC in mild acid solutions was studied.
- Geopolymer showed superior durability in both acid solutions compared to PC and HAC.
- $H_2SO_4$  attack promoted more rapid and greater deterioration than HCl attack.
- The sodium content of the material displayed a two-stage leaching process.

### GRAPHICAL ABSTRACT



### ARTICLE INFO

#### Article history:

Received 24 July 2018

Received in revised form 12 September 2018

2018

Accepted 25 October 2018

#### Keywords:

Geopolymer  
Waste glass powder  
Acid resistance  
Mild concentration  
HCl  
 $H_2SO_4$

### ABSTRACT

The performance of geopolymer cement based on blend of waste-glass powder and calcium aluminate cement in pH = 3 of HCl and  $H_2SO_4$  solutions for 24 months were investigated and compared to Portland cement and high alumina cement mortars as reference. The residual compressive strength and mass loss were monitored at different time intervals, and the reaction products were characterized by XRD, FTIR spectroscopy and SE microscopy to quantify the compositional and microstructural changes. The findings revealed that geopolymer cement possessed superior acid resistance compared to references.  $H_2SO_4$  attack caused more deterioration than HCl attack due to the accelerating effect of gypsum formation.

© 2018 Elsevier Ltd. All rights reserved.

### 1. Introduction

Durability is a most important criteria for the design of concrete structures. A durable concrete helps the environment by conserving natural resources, minimizing wastes and reducing the

environmental impacts of repair and maintenance. The service life of cementitious materials may be threatened and lost by interaction with aggressive environments. One critical damage mechanism is acid attack [1]. During the contact of concrete with acidic media, calcium ions are leached from calcium-containing phases present in the hardened cement paste i.e. Portlandite and calcium silicate hydrated to form calcium salt (decalcification), leading to an increased total porosity of the concrete and subsequently resulting in a significant decrease in mechanical strength and durability performance [2]. The rate and mechanism of acid attack

\* Corresponding author.

E-mail addresses: [m\\_vafaei@alumini.iust.ac.ir](mailto:m_vafaei@alumini.iust.ac.ir) (M. Vafaei), [ali.allahverdi@iust.ac.ir](mailto:ali.allahverdi@iust.ac.ir) (A. Allahverdi), [dongp1@mcmaster.ca](mailto:dongp1@mcmaster.ca) (P. Dong), [bassim@mcmaster.ca](mailto:bassim@mcmaster.ca) (N. Bassim).

<https://doi.org/10.1016/j.conbuildmat.2018.10.203>

0950-0618/© 2018 Elsevier Ltd. All rights reserved.

on concrete depend on different factors, including type of cement based materials, water-to-binder ratio, type and pH of the acid solution, temperature etc. [3,4]. Therefore, thorough investigation of the effect of acid exposure conditions on the mechanical and microstructural changes of the cement-based materials is key.

Since their development in the last few decades, geopolymer cements (GCs) have emerged as one of the possible alternative to Portland Cement (PC) due to their advantages including relatively high mechanical strength and excellent durability in addition to its environmental friendliness [5]. Geopolymers are a group of inorganic polymeric binders, manufactured by chemical activation of aluminosilicate source materials with strong alkali solutions at slightly elevated or ambient temperatures to form a mainly amorphous structure that perform a similar function compared to PC [6]. The most readily available used materials for the synthesis of GCs are fly ash, metakaolin and natural aluminosilicate minerals. However, the use of aluminosilicate solid waste materials as geopolymer precursor have attracted attention in recent years due to economic and environmental benefits of geopolymer technology in aiding waste management [7]. Based upon that, numerous waste materials were proposed and waste-glass powder is one of these materials [8]. In a comprehensive study by Vafaei et al [8], the potential of waste-glass powder for geopolymerization was investigated. They concluded that waste-glass powder alone is not enough reactive in geopolymerization reactions due to its deficiency in reactive-Al and addition of reactive-Al by incorporating materials rich in reactive-Al like calcium aluminate cements can result in the formation of a more cross-linked aluminosilicate (N-A-S-H) network that exhibits significantly higher compressive strengths.

Excellent acid resistance properties of GCs in comparison with PC were reported by various researchers [7,9]. Ariffin et al. [10] subjected geopolymer concrete developed from a blend of pulverized fuel ash and palm oil fuel ash to 2% sulfuric acid solution for 18 months, and concluded that this geopolymer exhibited superior resistance to acid attack as compared to PC. Fernando et al [11] studied the effect of 5% sulfuric, hydrochloric and nitric acid immersion on the performance of mine waste-based geopolymer up to 56 days, and reported that this geopolymer possessed higher acid resistance than PC based concrete mixtures. Alahverdi et al [12–15] compared the acid resistance of several binders; fly ash/ Blast furnace slag-based GC, PC, gypsum-free Portland cement/slag binder and high alumina cement, when immersed in nitric (pH = 1, 2 & 3) and sulfuric (pH = 1, 2 & 3) acid solutions. They found that GC presented higher stability in these aggressive environments compared to other binders.

The effect of highly concentrated acid solutions, i.e. HCl and H<sub>2</sub>SO<sub>4</sub> at pH = 1, on the durability performance of GC mortar based on waste-glass powder was investigated in details in author's previous study [16]. Inasmuch as different conditioned acid solutions have different effects on durability properties, prepared GC also requires evaluation of acid resistance at moderate concentration acid solutions. Attack by highly concentrated acid media occurs mainly in industrial environments due to random spill and leakage varying from a long-term trickle to a sudden drenching, whereas attack by moderate acid media is much more likely to occur. It occurs not only in industrial environments, but also in concrete structures exposed to acidic ground-waters with pH values ranging from 5.0 to as low as 3.0 [17] and acid precipitations with a pH value down to 3.5 [18]. The work reported herein, therefore, aimed to study the effect of exposure to relatively moderate concentration (pH = 3) of HCl and H<sub>2</sub>SO<sub>4</sub> on GC based on blend of waste-glass powder and calcium aluminate cement by using physical and mechanical properties evolution and by the visual, mineralogical and chemical information provided by scanning electron

microscopy (SEM), X-ray diffractometry (XRD) and Fourier transform infrared spectroscopy (FTIR) over a period of 24 months.

## 2. Experimental program

### 2.1. Materials

Waste-glass powder (WGP) was used as source aluminosilicate precursor for making GC mortars. The WGP was prepared by milling the glass cullet with a laboratory ball-milling machine and then sieving the powder to a desired particle size (70 µm). Calcium aluminate cement (CAC, Fondu from Kemeos, France) was used as an additive to modify the chemical composition of WGP. Type II Portland cement (PC) and high alumina cement (HAC, Secar 80 from Kerneos, France) mortars were also fabricated and used as the control specimens. Table 1 shows the properties of these materials including the physical properties and the chemical composition, obtained by wet chemical analysis. The fine aggregate used in the manufacture of mortars was standard sand with the requirement of DIN-EN 196-1 standard. Sodium silicate (Na<sub>2</sub>SiO<sub>3</sub>·nH<sub>2</sub>O) composed of 28.5 wt% SiO<sub>2</sub>, 8.5 wt% Na<sub>2</sub>O and 63 wt% H<sub>2</sub>O and sodium hydroxide (NaOH, 98% purity), supplied by Merck International Ltd., Darmstadt, Germany, were used as chemical activator. The acid solutions of pH = 3 ± 0.05 were also prepared by diluting concentrated commercial H<sub>2</sub>SO<sub>4</sub> and HCl acids with distilled tap water.

### 2.2. Specimens preparation

The GC mortar was prepared with a binary mixture of WGP (76 wt%) and CAC (24 wt%), activated by an activator solution containing 10 wt% Na<sub>2</sub>O (by weight of dry binder) and having a silica modulus (SiO<sub>2</sub>/Na<sub>2</sub>O mass ratio) of 1.5. Water-to-binder ratio was fixed at 0.50. These ratios were selected based on the author's previous study [16], where the decision criteria was the compressive strength. To fabricate GC mortar specimens, the WGP/CAC blend and standard quartz sand were first dry mixed for 2 min and then the activator solution was added, followed by remixing for 3 more minutes to obtain a uniform fresh mortar. After casting into 50 mm cubic steel molds, the fresh GC mortars were stored at room temperature (23.0 ± 2.0 °C) and at a relative humidity more than 95% for 24 h and then were demolded and subjected to hydrothermal curing conditions at 95 °C for 20 h [16]. Besides, a group of PC and HAC control mortar specimens of the same size were prepared and cured in standard water curing condition for 28 days and used for comparison purpose. Water-to-binder ratios for PC and HAC mortars were fixed at 0.485 and 0.550, respectively to adopt a flow of 110 ± 5% in flow table test in accordance with ASTM C 109 [19] and ASTM C 1437 [20]. The aggregate to binder ratio for all mortar samples was controlled at 2.75 in accordance with ASTM C109 [19].

### 2.3. Testing procedure

Acid resistance tests were carried out according to ASTM C 267 standard [21]. As prepared mortar specimens were exposed to H<sub>2</sub>SO<sub>4</sub> and HCl solutions of pH = 3 at a room temperature for time frames of up to 24 months. The ratio of acid volume (cm<sup>3</sup>) to specimen's surface area (cm<sup>2</sup>) was kept as near as possible to 10 for both batches. Concentrated acid was periodically added to each samples container to achieve a final pH level within an acceptable range of 5%. At designed intervals, the post-exposed specimens were taken out of the solutions, brushed under tap water with a soft plastic brush to remove detachable particles and wiped with a dry cloth. The acid resistance of different cement mortars was determined by monitoring the weight and compressive strength changes of the soaked specimens before and after acid attack.

**Table 1**  
Chemical and physical properties of the materials.

	WGP	CAC	PC	HAC
<i>Chemical composition (%)</i>				
SiO <sub>2</sub>	72.10	3.75	21.90	0.40
Al <sub>2</sub> O <sub>3</sub>	0.50	39.90	4.62	80.50
Fe <sub>2</sub> O <sub>3</sub>	0.20	16.15	3.40	0.20
CaO	10.20	38.20	64.50	17.50
MgO	3.00	1.50	1.52	0.50
SO <sub>3</sub>	–	–	1.15	0.10
K <sub>2</sub> O + Na <sub>2</sub> O	13.90	0.40	0.25	0.70
<i>Physical properties</i>				
Specific gravity (g/cm <sup>3</sup> )	2.90	3.20	3.15	3.25
Blaine specific surface area (m <sup>2</sup> /kg)	450	315	320	1000

#### 2.4. Instrumental techniques

The compressive strength tests on mortar cubes were performed using a digital hydraulic compression testing machine of 300 kN-capacity with  $\pm 1\%$  accuracy and a loading rate of 75 KN/min, in accordance with ASTM C 109 standard. The compressive strength value was obtained from an average of three measurements, with standard deviation less than 4% ( $\pm 3$  MPa).

The microstructure and element compositions of the pre- and post-exposed mortar samples were studied using scanning electron microscopy (TESCAN Vega II and JEOL 6610 equipped with an energy dispersive spectrometer (EDS) at accelerating voltages of 20 kV and 10 kV, respectively). To prepare SEM samples, a number of 24-month exposed GC mortar cubes were broken into pieces and suitable samples from the fracture surface encompassing both deteriorating and intact areas were prepared. For microstructural investigations, SEM samples taken from the fractured surface were dried at 70 °C for 24 h and sputter-coated with gold prior to imaging with TESCAN Vega II SEM. For the purpose of elemental composition investigations using JEOL 6610 (coupled with EDS), SEM samples were dried at 70 °C for 24 h and carbon coated after impregnating with epoxy resin and polishing. An accurate calibration of EDS was done using the copper K $\alpha$  peak, under the beam energy of 12 keV before each elemental analysis for the results to be comparable. The X-ray elemental analyses (EDS) were performed on selected rectangular areas as well as on line-scans extending from the exposed surface across the corroding area towards the internal intact area.

X-ray diffraction (XRD) patterns and FTIR spectra were acquired to study the mineralogical phase changes and bond characteristics of the unexposed and exposed samples during the course of acid attack. XRD patterns were recorded with a Philips PW 1800 X-ray diffractometer in the 5–80 °2 $\theta$  range, with a step size of 0.02 $\theta$  and scanning speed of 0.5 s. The FTIR spectra were obtained using KBr pellet method (0.5 mg sample per 250 mg KBr) on a PerkinElmer FTIR spectrometer, in the range of 4000 to 400  $\text{cm}^{-1}$  with a 4  $\text{cm}^{-1}$  resolution. The mortar samples after compression tests were ground to particle size less than 45  $\mu\text{m}$  and used for FTIR spectroscopy and XRD analyses.

### 3. Results and discussion

#### 3.1. Visual observations

Fig. 1 shows the appearances of PC, HAC and GC mortar specimens before and after 24 months of immersion in HCl and H<sub>2</sub>SO<sub>4</sub> solutions. Both control specimens i.e. PC and HAC mortars exhibited an evident apparent physical degradation after exposure to HCl solution. The most severe apparent deterioration, however, was visually observed on mortar specimens immersed in H<sub>2</sub>SO<sub>4</sub> solution. However, the apparent physical changes were found



conditions. On the other hand, visual inspection of the exposed specimens confirmed minimum apparent physical changes in GC mortars as compared to control mortars. The appearance of the immersed GC specimens did not exhibit any significant apparent physical damage, and was seemed to remain structurally intact; only slight erosions on the corners and regions close to the edges were noticed. However, in the case of  $H_2SO_4$ -exposed GC specimens, a higher apparent surface deterioration was observed and showed deposition of some very tiny white flaky substance on the specimen's surface, which were practically difficult to collect for the identification purposes. The key to this differentiated behavior of  $H_2SO_4$ -exposed and of HCl-exposed specimens is related to the formation of gypsum crystals which induce higher volumetric expansions and lead to spalling of surface layers. It should be noted that apparent physical damages do not necessarily reflect the real order of the acid resistance of the mortars.

### 3.2. Mass loss

The mass loss evolution of mortar specimens in acid solutions is plotted versus the immersion time, as shown in Fig. 2. After exposure to HCl solution for 24 months, the mass changes of PC, HAC and GC

exposure to  $H_2SO_4$  solution were about 57%, 70% and 29%, respectively. The mass loss of control mortar specimens exposed to the same conditions of acid attack was considerably higher than that of GC mortar, as can be seen in Fig. 2. This is due to the relative stability of GC structure in acid media and also to their high calcium contents [22]. Calcium compounds in these systems react with the acid solutions, resulting in the decomposition of hydration products and increasing the total porosity, subsequently accelerating the acid attack [23]. Moreover, the higher rate of mass loss of  $H_2SO_4$ -exposed specimens as compared to specimens that were immersed in HCl solution could be related to the chemical reaction of attacking sulfate with calcium compounds of cement to form gypsum which lead to induce internal disintegrating stresses and spalling of surface layers [24]. This implies that in addition to the type of salts formed by acid solution, the acid resistance of mortar specimens depends on the type of oxide composition ( $CaO$ ,  $SiO_2$  and  $Al_2O_3$ ) and chemically stability of tested materials.

### 3.3. Residual compressive strength

The results of the compressive strength measurement of mortar cubes subjected to acid solutions are shown in Fig. 3. The

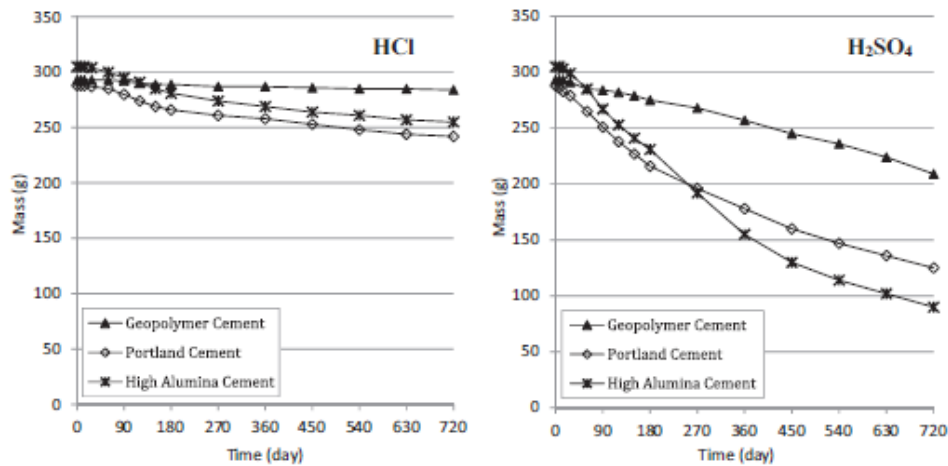


Fig. 2. Mass loss versus exposure time for mortar specimens immersed in  $H_2SO_4$  and HCl solutions of pH = 3 for 24 months.

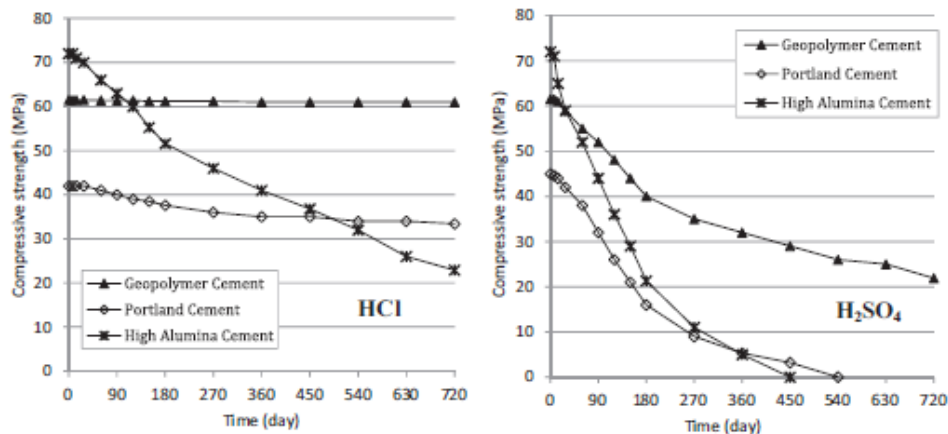


Fig. 3. Compressive strength versus exposure time for mortar specimens immersed in  $H_2SO_4$  and HCl solutions of pH = 3 for 24 months.

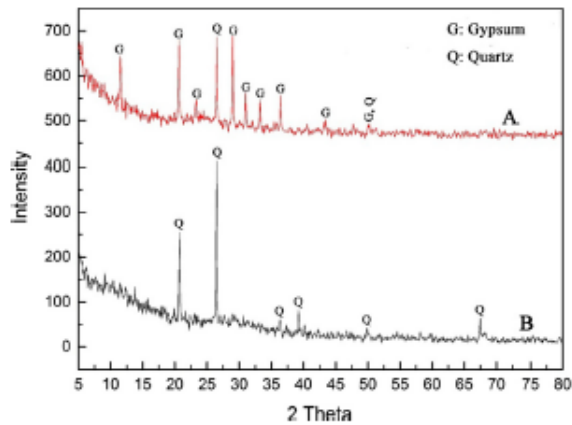


Fig. 4. X-ray diffractograms of geopolymer cement samples (A: geopolymer cement after 24 months of  $H_2SO_4$  exposure; B: geopolymer cement before acid exposure).

maximum strength loss was observed in the case of HAC control specimens immersed in  $H_2SO_4$  solution, whereas minimum loss experienced in HCl-exposed GC specimens. The GC mortars had the best performance with a 1% and 64% strength decline in HCl and  $H_2SO_4$  solutions after 24 months exposure. For the same conditions, the PC and HAC control specimens suffered strength loss of 100% and completely deteriorated after only 540 and 450 days

of  $H_2SO_4$  ( $_{(aq)}$ ) immersion, respectively. Meanwhile, the PC and HAC control specimens exhibited 20% and 68% strength loss after HCl ( $_{(aq)}$ ) exposure, respectively. The aforementioned findings for the GC are in agreement with the mass loss trends observed in the exposed specimens. The lower rate of strength loss for GC compared to control specimens is mainly attributed to the existence of a more stable binding compound N(C)-A-S-H [8] with a lower calcium contents in GC paste matrix that present less susceptibility to acid attack when compared to PC and HAC hydration products [24].

When comparing the results of residual compressive strength with mass loss, an inconsistency can be observed in the case of HAC control specimens exposed to HCl solution. Residual compressive strength shows a significant decline of about 68% during the course of acid attack, whereas mass loss data display limited changes. It should be noted that both residual compressive strength and mass loss data are not very accurate. The amount of mass loss depends greatly on the type of brush used (plastic or steel), the mechanical stability of the deteriorated layer and also the amount of force applied when brushing the specimens. In case of continuous and complete removal of deteriorated layer, there is a direct relationship between residual compressive strength and mass loss so that the higher the mass loss, the lower the residual compressive strength. For the other cases, however, there is no unique relationship between residual compressive strength and mass loss and stability of the deteriorated layer must also be taken into account. On the other hand, residual compressive strength of the mortar specimens at any time during acid exposure is dependent on the initial strength of the specimens and also the

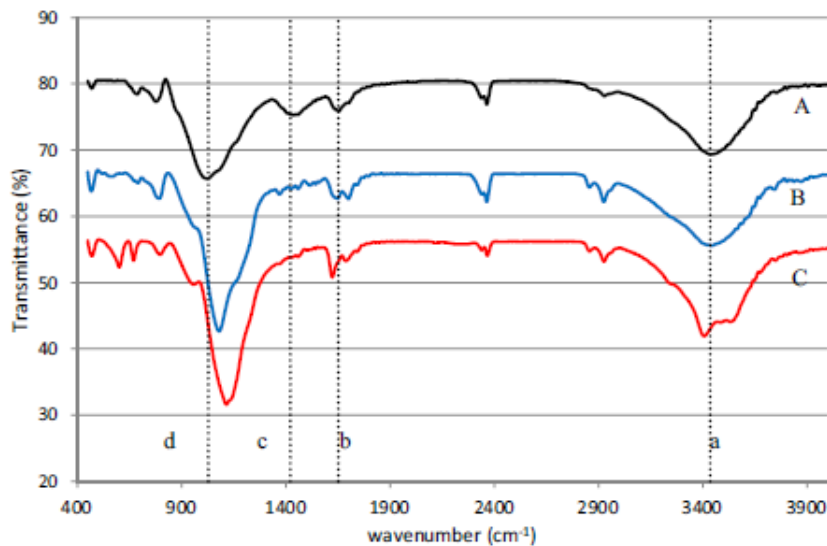


Fig. 5. FTIR spectra of the geopolymer cement samples (A: geopolymer cement before acid exposure; B: geopolymer cement after 24 months of HCl exposure; C: geopolymer cement sample after 24 months of  $H_2SO_4$  exposure).

Table 2  
FTIR characteristic bands in the spectra of samples shown in Fig. 5.

Symbol	Sample type	a	b	c	d
		Band (Wavenumber - $cm^{-1}$ )			
A	Before acid exposure	3444	1654	1414	1030
B	After HCl exposure	3448	1638	-	1076
C	After $H_2SO_4$ exposure	3400-3532	1622-1688	-	1116
	Characteristic bands	O-H stretching	H-O-H bending	O-C-O stretching	Si-O-Si and Si-O-Al stretching
	References	[10,30]	[10,30]	[29]	[29,31,32]

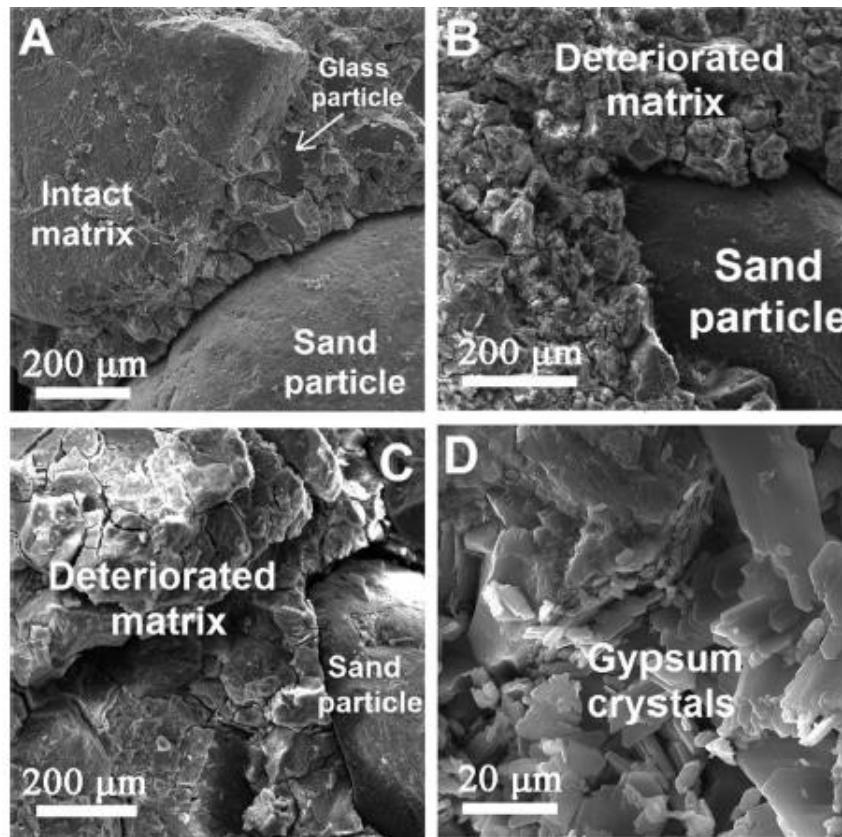


Fig. 6. SEM micrographs of geopolymer cement mortars (A) before acid attack, (B) after 24 months of HCl exposure, (c) after 24 months of H<sub>2</sub>SO<sub>4</sub> exposure, (d) gypsum crystals formed in geopolymer cement matrix after H<sub>2</sub>SO<sub>4</sub> exposure.

proportion of the total cross sectional area that has been damaged by acid attack. The gradual non-uniform changes in the cubic shape of the specimens during the course of acid attack also result in significant errors in compression strength tests. This means that neither the mass loss nor the compressive strength change alone are an accurate measures for evaluating the extent of deterioration and all the property changes must be considered together and carefully compared. The residual compressive strength results, however, are usually considered as relatively more reliable than mass loss data and even visual observation of the appearance of specimens. The observed inconsistency, therefore, should be due to inaccuracy in the mass loss data of HAC control specimens. The remarkable deterioration of HAC control specimens in HCl solution based on residual compressive strength data can be attributed not only to the type of binding compounds in hydrated HAC, but also to the relatively high water-to-binder ratio considered for HAC mortar. According to the product data sheet of the Kerneos Inc. [25], Secar 80 has a very high Blaine specific surface area in the range 800 to 1200 m<sup>2</sup>/kg (in accordance with EN 196-6). Such a relatively high Blaine specific area requires a relatively high amount of water to prepare a workable mortar. The increase in the amount of water in fresh mortar increases the mortar vulnerability against acid attack due to increased penetrability. Here, as mentioned in Section 2.2 and based on flow table tests, we considered a water-to-binder ratio of 0.550 for HAC control mortar compared to values of 0.485 and 0.500 considered for PC and GC mortars.

### 3.4. Changes in the geopolymer composition and microstructure

Mineralogical and microstructural changes in the GC mortars due to the effect of HCl and H<sub>2</sub>SO<sub>4</sub> solutions were studied using X-ray diffractometry (XRD), Fourier transform infrared spectroscopy (FTIR) and scanning electron microscopy (SEM) to obtain complementary information about the deterioration mechanism in GC mortar.

#### 3.4.1. X-ray diffraction

Fig. 4 exhibits the XRD patterns for the GC sample before (4A) and after 24 months of H<sub>2</sub>SO<sub>4</sub> exposure (4B). The diffraction pattern of the HCl-exposed sample was very similar to that of intact sample and therefore is not presented. The intact sample diffractogram revealed crystalline phase of quartz corresponding to standard sand (quartz, PDF#00-046-1045) as well as amorphous feature, i.e. the broad hump appeared approximately between theta of 20 to 30°. On the other hand, gypsum (CaSO<sub>4</sub>, PDF#00-033-0311) was detected in the H<sub>2</sub>SO<sub>4</sub>-exposed GC sample, resulting from reactions of calcium compounds with sulfate ions. These observations for gypsum deposition in the GC after H<sub>2</sub>SO<sub>4</sub> exposure were similar to previous observations reported by other researchers [10,14,26,27].

As can be seen in Fig. 4, the geopolymer cement before exposure to acid attack (pattern B) does not contain any calcium aluminate hydrate phases as high-alumina cement hydration products that have potential for ettringite formation in the presence of gypsum.

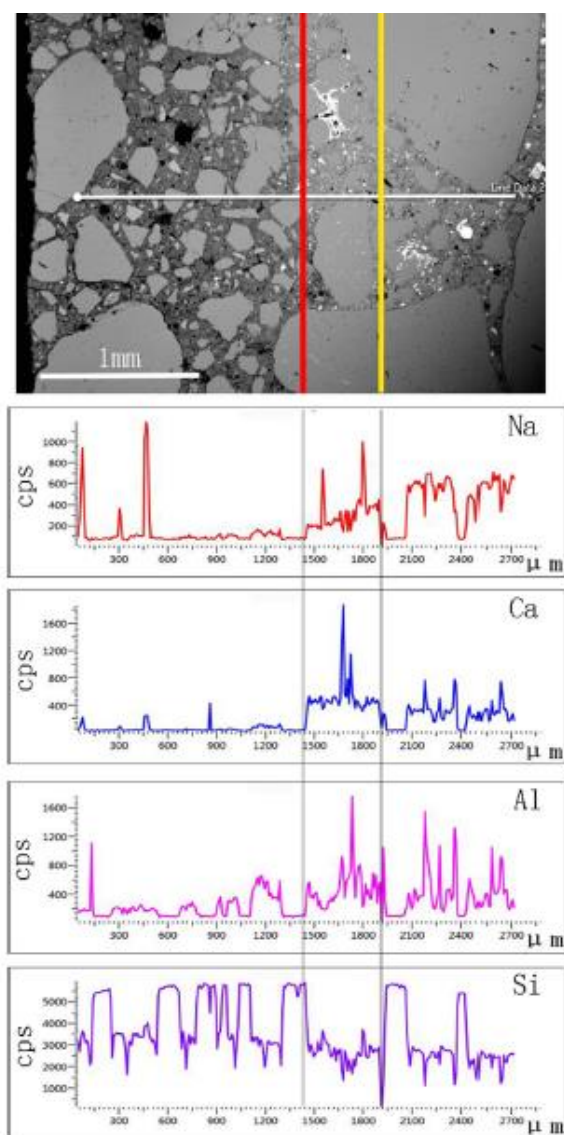


Fig. 7. SEM micrograph of geopolymer cement mortar after 24 months of exposure to pH = 3 HCl and EDS elemental line analyses profiles.

This means that almost all calcium aluminate cement took part in geopolymerization reactions forming the geopolymer aluminosilicate (N-A-S-H) network.

### 3.4.2. Fourier transform infrared spectroscopy

Fig. 5 shows the FTIR spectra of the exposed and unexposed GC sample to  $H_2SO_4$  and HCl solutions. The identified IR characteristic bands and their assignments are summarized in Table 2. From FTIR spectra, the asymmetric stretching of Si-O-T (T = Al or Si) shifted from  $1030\text{ cm}^{-1}$  toward higher wavenumbers and located at  $1116\text{ cm}^{-1}$  and  $1076\text{ cm}^{-1}$  upon its exposure to  $H_2SO_4$  and HCl solutions, relatively, indicating that weaker Al-O bonds were substituted with the stronger Si-O bonds during the course of acid attack due to the dealumination of the aluminosilicate framework [28,29]. This upward shift was more pronounced for  $H_2SO_4$ -exposed sample compared to HCl, implying that  $H_2SO_4$  exposure

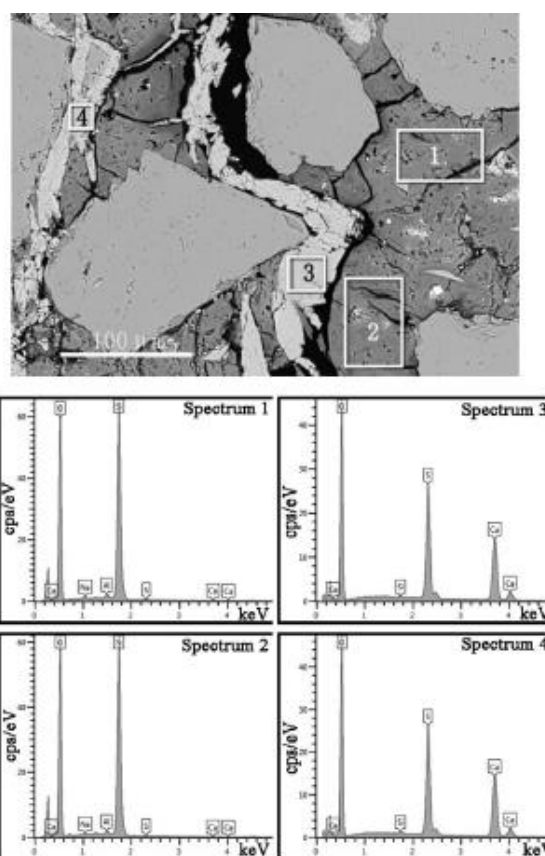


Fig. 8. SEM micrograph of deteriorated layer of geopolymer cement mortar after 24 months of exposure to pH = 3  $H_2SO_4$  and EDS elemental analyses results.

led more leaching of Al from this sample. Upon immersion in the acid solutions, the carbonate compounds formed due to geopolymerization were also dissolved in the solutions, leading to the disappearance of stretching vibrations of O-C-O band around  $1414\text{ cm}^{-1}$  [29]. Beside, FTIR spectra further showed that the O-H stretching band was displaced from  $3444\text{ cm}^{-1}$  to  $3400\text{--}3532\text{ cm}^{-1}$  and the position of chemically bonded H-O-H band also changed from  $1654\text{ cm}^{-1}$  to  $1622\text{--}1688\text{ cm}^{-1}$  by the exposure to  $H_2SO_4$  solution as a consequence of formation and precipitation of gypsum [10].

### 3.4.3. Scanning electron microscopy

Scanning electron microscopy (SEM) was also carried out to investigate the microstructural changes that occurred in GC mortars during the acid exposure. The results are exhibited in Fig. 6. In the pre-exposure mortar, a dense and homogeneous structure was observed in the GC matrix, where some non-reacted and/or partially reacted glass gains were embedded, as shown in Fig. 6 (a). A few micro-cracks were also detected mainly due to the moisture loss from the structure during prolonged high temperature curing and/or preparing of SEM samples that induces excessive shrinkage and subsequently destroy the structure [33]. On the other hand, upon exposure to both acid solutions the well-packed structure of the pre-exposure sample was changed to a very porous structure with higher micro-cracks as a consequence of GC network breakdown by acid attack [34,35]. Moreover, by

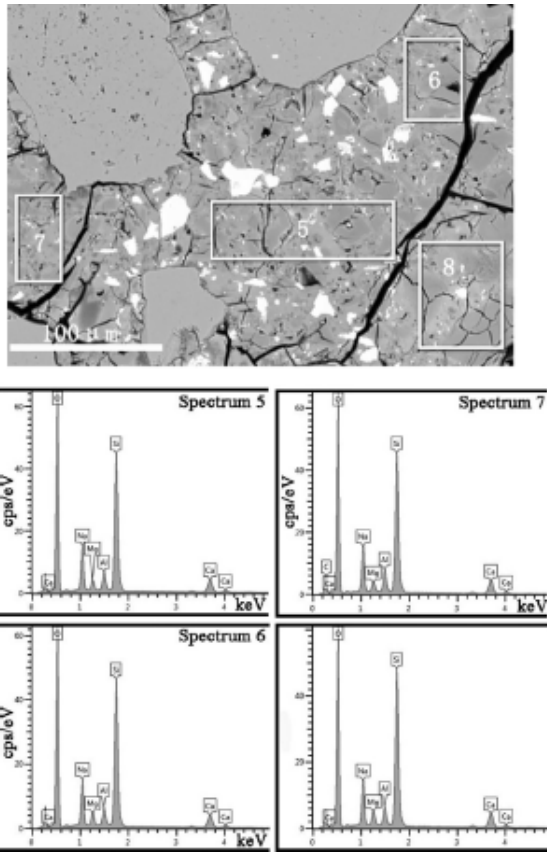


Fig. 9. SEM micrograph of intact area of geopolymer cement mortar and EDS elemental analyses results.

SEM observation at relatively high magnifications of the  $H_2SO_4$ -exposed GC structure, as per Fig. 6(d) a large number of rod-like gypsum crystals ( $CaSO_4 \cdot H_2O$ ) could be seen in the morphological features, confirming the XRD and FTIR results.

Fig. 7 displays a typical SEM micrograph prepared from GC mortar sample after 24 months of exposure to pH = 3 HCl and EDS elemental profiles for Na, Ca, Al and Si along the horizontal line shown in micrograph. It is necessary to remind that the presence of sand particles in the GC mortar resulted in disturbances in elemental profiles. The location of the sand particles can be easily distinguished from Si-, Na-, Ca-, and Al-profiles where Si has a much higher concentration with almost no Na, Ca and Al. The changes

the presence of three different regions including a completely deteriorated surface layer with a depth of about 1.6 mm on left side of the micrograph, an intact area on the right side of the micrograph, and a partially deteriorated intermediate region of thickness about 0.5 mm shown by vertical lines on the micrograph. The complete and partial depletion of sodium in the completely- and partially deteriorated regions, respectively, indicate a two-stage sodium-leaching process depending on sodium bonding type and strength in molecular structure of GC matrix and non-reacted WG precursor particles embedded in the geopolymer matrix. Based on the proposed charge-balancing models for alkali cations in geopolymers [36], the weakly bound Na cations in the form of  $Na(H_2O)_6^+$  in the structure of the N-A-S-H gel is easily leachable even in deionized water. This alkali is therefore easily and completely leached in the first stage when exposed to acid solutions. The Na present in the non-reacted WG particles remaining in the geopolymer matrix, however, is relatively strongly bound to the glass molecular structure and is leached only in acid solution and not in deionized water [36,37]. This relatively strongly bound alkali in the non-reacted glass particles is leached in the second stage forming the partially deteriorating region adjacent to the completely deteriorated surface layer. This two-stage sodium-leaching process was not observed in author's previous study [16] on acid deterioration of the same material at highly concentrated (pH 1) HCl solution. Calcium can be present either in the form of C-S-H or C-A-S-H [38] in alkali-activated materials and geopolymers. In either case, it is easily leached in acid solutions [39] and as seen in Fig. 7, calcium was totally leached in the completely deteriorated region. It is a little bit enriched in the partially deteriorated region due to the leaching of sodium. Aluminum is partially leached in the completely deteriorated surface layer confirming the dealumination process observed in FTIR spectroscopy results discussed in Section 3.4.2. Gradual complete leaching of Na and Ca and partial leaching of Al into the acid solution enriches the GC matrix in silica, as Si-profile displays (Fig. 7), and causes significant shrinkage which in turn results in the formation of a highly microcracked deteriorated surface layer, as can be seen in SEM micrograph of Fig. 7.

Figs. 8 and 9 display SEM micrographs from deteriorated layer of GC mortar after 24 months of exposure to pH = 3  $H_2SO_4$  and intact area of GC mortar for comparison purposes, respectively, with EDS elemental analyses spectra. Table 3 summarizes EDS elemental analyses results from rectangular regions shown in SEM micrographs represented in Figs. 8 and 9. Noticeable microstructural and chemical compositional changes were observed in the deteriorated surface layer compared to intact area, though changes due to leaching of Na, Ca and dealumination between mortar specimens exposed to HCl and  $H_2SO_4$  solutions are very similar, except for the formation and deposition of gypsum crystals in the case of exposure to  $H_2SO_4$ . As seen in

Table 3

EDS elemental analyses (mass%) results from regions shown in SEM micrographs represented in Figs. 8 and 9.

	O	Si	Al	Na	Ca	Mg	S
Spectrum 1	53.8	44.8	0.7	0.4	0.1	-	0.2
Spectrum 2	54.4	44.5	0.7	0.2	0.1	-	0.1
Deteriorated Matrix (Average)	<b>54.1</b>	<b>44.6</b>	<b>0.7</b>	<b>0.3</b>	<b>0.1</b>	-	<b>0.1</b>
Spectrum 3	54.1	0.1	-	-	25.1	-	20.6
Spectrum 4	54.5	0.2	-	-	25.0	-	20.2
Gypsum (Average)	<b>54.3</b>	<b>0.1</b>	-	-	<b>25.0</b>	-	<b>20.4</b>
Spectrum 5	52.2	27.9	3.5	8.7	7.7	-	-
Spectrum 6	51.6	28.9	3.3	8.8	7.4	-	-
Spectrum 7	50.9	27.6	3.9	8.4	7.6	1.7	-
Spectrum 8	49.6	29.4	3.0	7.9	7.8	2.3	-
Intact matrix (Average)	<b>51.1</b>	<b>28.4</b>	<b>3.4</b>	<b>8.4</b>	<b>7.6</b>	<b>2.0</b>	-

Fig. 9, the intact area of GC mortar exhibits a microcracked matrix due to chemical shrinkage during geopolymerization reactions and/or drying shrinkages during hydrothermal curing and/or drying of SEM samples [16,33]. Non-reacted glass particles embedded in the geopolymer matrix, observed on fractured surface (Fig. 6(a)), cannot be simply distinguished here on polished surfaces. As can be seen in Fig. 8, after 24 months of exposure to pH 3 H<sub>2</sub>SO<sub>4</sub>, microstructural deteriorations appeared in the form of a more permeable microstructure due to higher number of newly formed microcracks with some enlarged microcracks partially filled with gypsum crystals. SEM observations with EDS elemental analysis confirmed the formation and deposition of gypsum crystals in some of the enlarged microcracks as a result of reactions between sulfate ions of acid and calcium compounds of geopolymer matrix. As can be seen in Fig. 8 and in Table 3, the EDS spectra 3 and 4 revealed major elements of calcium (Ca), sulfur (S), and oxygen (O), confirming the presence of gypsum, as previously confirmed by XRD results in Section 3.4.1. In addition, Table 3 displays the quantitative chemical compositional changes happening in the geopolymer matrix during acid attack. The obtained results show that almost 96% of Na and about 98% of Ca were leached into acid solution. The breakdown of the geopolymer molecular structure, Si–O–Al bonds as confirmed in Section 3.4.2, also resulted in about 79% loss of Al. These leaching of alkali and alkali earth metals (Na and Ca) accompanied with extensive dealumination of the molecular structure causes the formation of shrinkage microcracks, as discussed before for the case of exposure to pH 3 HCl. In addition as claimed by researchers [15,24], gypsum deposition in the GC matrix and subsequent internal disintegrating stresses caused by gypsum crystal growth results in the formation of some expansive microcracks. Enlargement of expansive microcracks due to continued growth of gypsum crystals finally results in spalling of deteriorated surface layers and this accelerates the rate of deterioration compared to pH 3 HCl. The deterioration mechanism in pH 3 H<sub>2</sub>SO<sub>4</sub>, therefore, consists of simultaneous shrinkage- and expansion-based microcracking due to leaching of alkali and alkali earth metals from geopolymer matrix together with dealumination of matrix molecular structure and gypsum deposition within the matrix, respectively, compared to pH 3 HCl. The more aggressive nature of H<sub>2</sub>SO<sub>4</sub> and the higher rate of deterioration of mortar specimens in which compared to HCl at the same pH value of 3 can be linked to expansion caused by gypsum formation and deposition.

Now comparing the results of this study to author's previous study [16], it seems that the only differences between mild (pH 3) and high (pH 1) concentrations of HCl and H<sub>2</sub>SO<sub>4</sub> attacks on geopolymer cement mortar developed from waste-glass powder and calcium aluminate cement lies in deterioration kinetics and two-stage sodium-leaching at mild concentrations.

#### 4. Conclusions

The durability performance of geopolymer cement mortar developed from blend of waste-glass powder and calcium aluminate cement (Ciment Fondu) and exposed to pH=3 of HCl and H<sub>2</sub>SO<sub>4</sub> attacks up to 24 months were studied using Portland cement (type II in accordance with ASTM) and high alumina cement (Secar 80) mortars as control and the following conclusions have been made:

- 1- The geopolymer mortar presented superior durability in both acid solutions compared to control mortars, with minimal mass losses of 3% and 29% and compressive strength losses of 1% and 64% in HCl and H<sub>2</sub>SO<sub>4</sub> solutions, respectively, compared to mass losses of 16% and 57% for Portland

cement and 16% and 70% for high alumina cement mortars and compressive strength losses of 24% and 100% for Portland cement and 68% and 100% for high alumina cement mortars in the same acid solutions.

- 2- The superior durability of geopolymer cement could be attributed to higher stability of its aluminosilicate structure and also to its relatively low calcium content that causes this binder to be more resistant toward acid attack.
- 3- At mild concentrations ( $\approx$  pH 3) of acids, sodium content of the material with a main source of N-A-S-H gel and a minor source of non-reacted waste-glass particles embedded in the matrix displays a two-stage leaching process depending on its bonding type and strength. The weakly bound sodium cations in the N-A-S-H gel is easily leached in the first stage and the relatively strongly bound sodium in non-reacted waste-glass particles is leached in the second stage.
- 4- H<sub>2</sub>SO<sub>4</sub> attack promoted more rapid and greater deterioration than that resulting from HCl exposure due to the formation of gypsum crystals within the geopolymer matrix that imposed internal disintegrating stresses, thus leading to cracking, spalling and accelerated deterioration. This is in addition to the deterioration caused by leaching of both alkali and alkali earth metals from geopolymer matrix and dealumination of the geopolymer matrix as observed in the case of HCl.

#### Conflict of interest

None.

#### References

- [1] C.L. Page, M.M. Page, *Durability of Concrete and Cement Composites*, Elsevier, 2007.
- [2] K. Scrivener, J.F. Young, *Mechanisms of Chemical Degradation of Cement-based Systems*, CRC Press, 1997.
- [3] V.R. Živica, A. Bajza, Acidic attack of cement based materials- a review: Part 1. Principle of acidic attack, *Constr. Build. Mater.* 15 (8) (2001) 331–340.
- [4] V.R. Živica, A. Bajza, Acidic attack of cement-based materials- a review: Part 2. Factors of rate of acidic attack and protective measures, *Constr. Build. Mater.* 16 (4) (2002) 215–222.
- [5] M. Albitara, M.S. Mohamed Ali, P. Visintin, M. Drechsler, Durability evaluation of geopolymer and conventional concretes, *Constr. Build. Mater.* 136 (1) (2017) 374–385.
- [6] J. Davidovits, *Geopolymer Chemistry and Applications*, Geopolymer Institute, 2008.
- [7] J.L. Provis, J.S.J. Van Deventer, *Geopolymers: Structures, Processing, Properties and Industrial Applications*, Woodhead Publishing Limited, 2009.
- [8] M. Vafaei, A. Allahverdi, High strength geopolymer binder based on waste-glass powder, *Adv. Powder Technol.* 28 (1) (2017) 215–222.
- [9] P. Duxson, A. Fernández-Jiménez, J.L. Provis, G.C. Lukey, A. Palomo, J.S.J. van Deventer, Geopolymer technology: the current state of the art, *J. Mater. Sci.* 42 (9) (2007) 2917–2933.
- [10] M.A.M. Ariffin, M.A.R. Bhutta, M.W. Hussin, M. Mohd, T.N. Aziah, Sulfuric acid resistance of blended ash geopolymer concrete, *Constr. Build. Mater.* 43 (2013) 80–86.
- [11] P.T. Fernando, J. Said, Resistance to acid attack, abrasion and leaching behavior of alkali-activated mine waste binders, *Mater. Struct.* 44 (2) (2011) 487–498.
- [12] A. Allahverdi, F. Skvara, Nitric acid attack on hardened paste of geopolymeric cements: part 1, *Ceram.-Silik.* 45 (3) (2001) 81–88.
- [13] A. Allahverdi, F. Skvara, Nitric acid attack on hardened paste of geopolymeric cements: part 2, *Ceram.-Silik.* 45 (4) (2001) 143–149.
- [14] A. Allahverdi, F. Skvara, Sulfuric acid attack on hardened paste of geopolymer cements: Part 1. Mechanism of corrosion at relatively high concentrations, *Ceram.-Silik.* 49 (4) (2005) 225–229.
- [15] A. Allahverdi, F. Skvara, Sulfuric acid attack on hardened paste of geopolymer cements: Part 2. Corrosion mechanism at mild and relatively low concentrations, *Ceram.-Silik.* 50 (1) (2006) 1–4.
- [16] M. Vafaei, A. Allahverdi, Durability of geopolymer mortar based on waste-glass powder and calcium aluminate cement in acid solutions, *J. Mater. Civ. Eng.* 29 (10) (2017) 04017196.
- [17] E.P.M.J. Fest, E.J.M. Temminghoff, J. Griffioen, B. Van Der Grift, W.H. Van Riemsdijk, Groundwater chemistry of Al under Dutch sandy soils: effects of land use and depth, *Appl. Geochem.* 22 (2007) 1427–1438.
- [18] National Trends Network Annual Maps, NADP Program Office, Illinois State Water Survey, Champaign, IL (2014), <http://nadp.sws.uiuc.edu/ntn/maps.aspx> (accessed 17.08.16).

- [19] ASTM C109/C 109M-02, Standard test method for compressive strength of hydraulic cement mortars (using 2-in. or [50-mm] cube specimens), American Society of Testing Materials, 2002.
- [20] ASTM C1437, Standard test method for flow of hydraulic cement mortar, American Society of Testing Materials, 2001.
- [21] ASTM C267, Standard test methods for chemical resistance of mortars, grouts, and monolithic surfacings and polymer concretes American Society of Testing Materials 2001.
- [22] J.N.Y. Djobo, A. Elimbi, H.K. Tchakouté, S. Kumar, Mechanical properties and durability of volcanic ash based geopolymer mortars, *Constr. Build. Mater.* 124 (2016) 606–614.
- [23] P. Duan, Ch. Yan, W. Zhou, W. Luo, Ch. Shen, An investigation of the microstructure and durability of a fluidized bed fly ash-metakaolin geopolymer after heat and acid exposure, *Mater. Des.* 74 (5) (2015) 125–137.
- [24] V. Sata, A. Sathonsaowaphak, P. Chindaprasit, Resistance of lignite bottom ash geopolymer mortar to sulfate and sulfuric acid attack, *Cem. Concr. Compos.* 34 (5) (2012) 700–708.
- [25] <http://www.kemeosinc.com/secar80.php>.
- [26] S. Thokchom, Fly ash geopolymer pastes in sulphuric acid, *Int. J. Eng. Innov. Res.* 3 (6) (2014) 943–947.
- [27] X.J. Song, M. Marosszeky, M. Brungs, R. Munna, Durability of fly ash based geopolymer concrete against sulphuric acid attack, Proceedings of 10DBMC International Conference on Durability of Building Materials and Components, 17-20 April, 2005, Lyon, France, 2005.
- [28] Z. Baščarević, M. Komljenović, Z. Miladinović, V. Nikolić, N. Marjanović, Z. Žujović, R. Petrović, Effects of the concentrated NH<sub>4</sub>NO<sub>3</sub> solution on mechanical properties and structure of the fly ash based geopolymers, *Constr. Build. Mater.* 41 (2013) 570–579.
- [29] S. Ahmari, L. Zhang, Durability and leaching behavior of mine tailings-based geopolymer bricks, *Constr. Build. Mater.* 44 (2013) 743–750.
- [30] N.V. Chukanov, A.D. Chervonnyi, *Infrared Spectroscopy of Minerals and Related Compounds*, Springer International Publishing, 2016.
- [31] M. Zhang, M. Zhao, G. Zhang, D. Mann, K. Lumsden, M. Tao, Durability of red mud-fly ash based geopolymer and leaching behavior of heavy metals in sulfuric acid solutions and deionized water, *Constr. Build. Mater.* 124 (2016) 373–382.
- [32] W.K. Part, M. Ramli, C.B. Cheah, An overview on the influence of various factors on the properties of geopolymer concrete derived from industrial by-products, *Constr. Build. Mater.* 77 (2015) 370–395.
- [33] D.S. Perera, O. Uchida, E.R. Vance, K.S. Finnie, Influence of curing schedule on the integrity of geopolymers, *J. Mater. Sci.* 42 (9) (2007) 3099–3106.
- [34] T. Bakharev, Resistance of geopolymer materials to acid attack, *Cem. Concr. Res.* 35 (4) (2005) 658–670.
- [35] F. Slaty, H. Khoury, H. Rahier, J. Wastiels, Durability of alkali activated cement produced from kaolinitic clay, *Appl. Clay Sci.* 104 (2015) 229–237.
- [36] F. Škvára, V. Šmilauer, P. Hlaváček, L. Kopecky, Z. Gllová, A weak alkali bond in (N, K)-A-S-H gels: evidence from leaching and modeling, *Ceramics-Silikáty* 56 (4) (2012) 374–382.
- [37] T. Akai, K. Kuraoka, D. Chen, Y. Yamamoto, T. Shirakami, K. Urabe, T. Yazawa, Leaching behavior of sodium from fine particles of soda-lime-silicate glass in acid solution, *J. Am. Ceram. Soc.* 88 (10) (2005) 2962–2965.
- [38] F. Puertas, M. Palacios, H. Manzano, J.S. Dolado, A. Rico, J. Rodríguez, A model for the C-A-S-H gel formed in alkali-activated slag cements, *J. Eur. Ceram. Soc.* 31 (2011) 2043–2056.
- [39] T. Bakharev, J.G. Sanjayan, Y.B. Cheng, Resistance of alkali-activated slag concrete to acid attack, *Cem. Concr. Res.* 33 (10) (2003) 1607–1611.

## Durability performance of geopolymer cement based on fly ash and calcium aluminate cement in mild concentration acid solutions

Mostafa Vafaei<sup>a</sup>, Ali Allahverdi<sup>a,b,\*</sup>, Peng Dong<sup>c</sup> and Nabil Bassim<sup>c</sup>

<sup>a</sup>Research Laboratory of Inorganic Chemical Process Technologies, School of Chemical Engineering, Iran University of Science and Technology, Tehran, Iran; <sup>b</sup>Cement Research Center, Iran University of Science and Technology, Tehran, Iran; <sup>c</sup>Department of Materials Science and Engineering, McMaster University, Hamilton, ON, Canada

The present work evaluates 2-year durability performance of geopolymer cement (GC) mortar derived from a blend of low calcium fly ash and calcium aluminate cement in hydrochloric and sulfuric acid solutions of mild concentration (pH 3). The dry binary blend was activated by a solution of sodium hydroxide and liquid sodium silicate and the GC mortar specimens were cured hydrothermally. At different time intervals of acid attack, the compressive strength and mass loss of specimens were measured and complementary studies on compositional and microstructural changes were performed using X-ray diffractometry, Fourier transform infrared spectroscopy, and scanning electron microscopy with energy dispersive X-ray spectroscopy. The results revealed a superior durability performance for GC mortar especially in hydrochloric acid, compared to Portland and high alumina cement mortars used as reference. In addition, all the three cements showed a considerably higher degree of deterioration in exposure to sulfuric acid than in hydrochloric acid.

**Keywords:** Geopolymer; fly ash; durability; sulfuric acid; hydrochloric acid

### 1. Introduction

The lifespan of concrete structures strongly depends on durability of cementitious materials that may be affected and lost by attacking aggressive environments. Chemical attack by acid media is known to be very aggressive and deteriorating due to the alkaline nature of concrete [1–4]. Portland cement (PC) based concretes are highly vulnerable to acid media due to chemical instability of calcium silicate hydrate and portlandite. These two constituents of hardened PC paste react with acid molecules to form either soluble or insoluble calcium salts resulting in loss of

properties and durability [1, 2]. The mechanism and kinetics of concrete deterioration depends on type of cement, concrete permeability, type and concentration of the attacking acid, temperature, etc. [1–4]. Therefore, many research attempts have been devoted to acid attack on property and microstructural changes of cement-based materials. Some of the researchers investigated the possibility of imparting acid resistant property to concrete by either using acid resistant supplementary cementing materials or replacing PC with non-Portland cements such as geopolymer cements (GCs).

---

\*Corresponding author. Email: [ali.allahverdi@iust.ac.ir](mailto:ali.allahverdi@iust.ac.ir)

The research activities on GCs in the few last decades have been considerably increased due to their significant potentials for CO<sub>2</sub> emission reduction and energy saving [5]. Unlike PC that is based on calcium silicate hydrates, GCs are mainly based on amorphous sodium aluminosilicate hydrates [6, 7] that are claimed to be more durable than calcium silicate hydrates even in acid media [8–11].

Allahverdi et al. [10–13] reported a superior durability performance for a GC based on a blend of fly ash (50%) and Blast-furnace slag (50%) in both nitric and sulfuric acid solutions compared to PC, high alumina cement, and Blast-furnace slag blended gypsum-free PC. Femando et al. [14] claimed a higher acid resistance for GC concrete based on calcined mine waste mud in 5% hydrochloric, sulfuric, and nitric acid solutions than PC concretes. Ariffin et al. [15] concluded that GC based on binary blend of fuel ash and palm oil ash exhibits a superior resistance to 2% sulfuric acid solution compared to PC. Recently, Vafaei et al. [16, 17] investigated the durability performance of GC mortars based on binary blends of waste-glass powder/calcium aluminate cement and low calcium fly ash/calcium aluminate cement in pH 1 of both sulfuric and hydrochloric acid solutions. They claimed that GC mortars exhibited minimal loss of mass and mechanical strength compared to PC and high alumina cement mortars. In overall, compared to PC, GCs are claimed to exhibit superior durability performance in acidic media especially if they are derived from low calcium aluminosilicate precursor materials such as low calcium fly ash and waste glass powder [10–17].

Many of the studies on acid resistance of GCs were performed in acid solutions of relatively high concentrations to limit the study time by accelerating the deterioration process. Since the pH or the concentration of the acidic media is a key factor in determining the kinetics and probably the

mechanism of the phenomenon, it is necessary to extend the research activities to mild concentrations of acid solutions. In addition, it should be noted that mild acidic media are more likely to occur than highly concentrated acidic media. Examples of acidic media of mild concentration include acid ground-waters and acid precipitations with pH values ranging from about 5.0 down to as low as 3.0 [18, 19].

The aim of the present work, therefore, is to evaluate the durability performance of GC mortar based on binary blend of low calcium fly ash/calcium aluminate cement in mild concentration (pH 3) of hydrochloric and sulfuric acid solutions over a relatively long exposure time of 24 months and to compare the mechanism of deterioration to attack by pH 1 of the same acids [17]. In addition to visual observations for qualitative comparison purposes, the gradual deterioration of the mortar specimens was compared quantitatively by measuring their physical and mechanical properties at different time intervals during exposure time. Complementary information were also acquired by X-ray diffractometry (XRD), Fourier transform infrared (FTIR) spectroscopy, and scanning electron microscopy with energy dispersive X-ray spectroscopy (SEM + EDS) to realize the mineralogical, compositional and microstructural changes happening during the acid attack.

## 2. Materials and methods

### 2.1. Materials

Class F fly ash (FA) from a French power plant and calcium aluminate cement (CAC, FONDU, Kemeos, France) were used to prepare the binary blend used as an aluminosilicate precursor. The FA was firstly ground to a desired fineness (410 m<sup>2</sup>/kg) using a laboratory ball-mill of the size 38 cm in length and 11 cm in diameter partially filled with 20 kg steel balls of different sizes ranging from 2 to 4 cm in

Table 1. Chemical composition and physical properties of materials.

	Fly ash	Calcium aluminate cement	Portland cement	High alumina cement
Chemical composition (%)				
SiO <sub>2</sub>	47.10	3.75	21.90	0.40
Al <sub>2</sub> O <sub>3</sub>	29.05	39.90	4.62	80.50
Fe <sub>2</sub> O <sub>3</sub>	8.51	16.15	3.40	0.20
CaO	3.20	38.20	64.50	17.50
MgO	3.02	1.50	1.52	0.50
SO <sub>3</sub>	—	—	1.15	0.10
K <sub>2</sub> O + Na <sub>2</sub> O	5.20	0.40	0.25	0.70
Physical properties				
Specific gravity (g/cm <sup>3</sup> )	2.26	3.20	3.15	3.25
Blaine specific surface area (m <sup>2</sup> /kg)	410	315	320	1000

diameter and rotated at the speed of 89 rpm. For comparison purposes, PC (type II in accordance with ASTM C150 [20]) of strength grade 42.5 MPa and high alumina cement (HAC, Secar 80 from Kemeos, France) mortar specimens were also prepared and used as reference. Chemical composition prepared by standard wet analytical procedures (ASTM C311 [21] and C114 [22]) and physical properties (fineness and density) measured by standard test procedures (ASTM C204 [23] and ASTM C188 [24]) of the materials are given in Table 1. Mortar specimens were prepared using standard quartz sand (CEN-Normsand EN 196-1) in accordance with DIN-EN 196-1 [25]. Analytical grade liquid sodium silicate (H<sub>2</sub>O; 63 wt.%, SiO<sub>2</sub>; 28.5 wt.%, and Na<sub>2</sub>O; 8.5 wt.%) and sodium hydroxide (98% purity), supplied by Merck International Ltd., Darmstadt, Germany, were also used to prepare alkali-activator solution. Commercial hydrochloric and sulfuric acids were diluted with distilled tap water to prepare pH 3 acid solutions.

## 2.2. Methods

### 2.2.1. Specimens preparation

CAC was used as an additive rich in reactive alumina to improve the reactivity of FA

and to enhance the compressive strength of GC mortar. Based on authors' previous study [17], a binary blend of FA (76 mass%) and CAC (24 mass%) was activated with a proportioned combination of NaOH and Na<sub>2</sub>SiO<sub>3</sub> with silica modulus (SiO<sub>2</sub>/Na<sub>2</sub>O mass ratio) adjusted at 1.5. The concentration of Na<sub>2</sub>O in GC was adjusted at 12% by mass of dry binary binder by controlling the amount of alkali-activator in the geopolymer mixture. The mass ratio of water-to-dry binary binder (W/B) was fixed at 0.50. All these values are optimum based on the highest achievable compressive strength criterion [17]. The fresh GC mortar was prepared by manual dry blending of FA/CAC and standard quartz sand for 2 min and then adding the proportioned alkali-activator and remixing for 3 more minutes in a laboratory planetary mortar mixer. The fresh GC mortar was then cast into 50 mm cubic steel molds and stored in a curing chamber held at 23.0 ± 2.0 °C and a relative humidity more than 95% for the first 24 h. After the first 24-h pre-curing regime, the GC mortar specimens were subjected to a 20-h hydrothermal curing regime at 95 °C in a sealed chamber containing water at its bottom. Enough reference mortar specimens of the same size from PC and HAC were also

prepared and cured in water-submerged condition at  $23.0 \pm 2.0^\circ\text{C}$  for 28 days. The W/B ratio for PC and HAC reference mortars were controlled at 0.485 and 0.550 in accordance with ASTM C 109 [26] and ASTM C 1437 [27], respectively, to control a spread diameter of  $110 \pm 5\%$  in flow table test. The sand-to-dry binder ratio was adjusted at 2.75 for all mortars in accordance with ASTM C109 [26].

### 2.2.2. Testing procedure

The durability performance tests were carried out in accordance with ASTM C267 standard [28]. The cured mortar specimens were divided into two equal batches and submerged in pH 3 solutions of hydrochloric and sulfuric acids kept at ambient temperature (between  $24 \pm 1^\circ\text{C}$ ) for a time period of 24 months. The ratio of the acid solution volume ( $\text{cm}^3$ ) to the total specimens' exposed surface area ( $\text{cm}^2$ ) was kept constant at 10 for both acid solutions for accurate comparison purposes and also for providing sufficient acid for a continued and relatively stable acid attack. The pH of the solutions was also controlled in the range  $3 \pm 0.05$  by frequently adding concentrated acids. This was done more frequently at the beginning (once per day) and less frequently at the end (once per week). During addition of concentrated acid, the acid solutions were thoroughly and continuously mixed with an acid-resistant-blade mixer to avoid any concentration gradient. The durability performance of the cements was evaluated by regularly measuring and comparing the mass changes and the compressive strength loss of mortar specimens. Before any measurement, the specimens removed from acid solutions were lightly brushed under tap water using a soft plastic brush to remove loose surface particles and then wiped with a dry towel to remove free surface water.

### 2.2.3. Instrumental techniques

A 300 kN compression testing machine with an accuracy of  $\pm 1\%$  was used to measure compressive strength. The loading rate was controlled at about 75 kN/min that is in the range specified by ASTM C109 standard [26]. The average of three measurements with a maximum standard deviation less than 4% (about  $\pm 3$  MPa) was reported as the compressive strength value. TESCAN Vega II scanning electron microscope (SEM) and JEOL 6610 coupled with an energy dispersive spectrometer (SEM + EDS) operating at accelerating voltages of 20 and 10 kV, respectively, were used for microstructural and compositional changes happened in the acid exposed mortar specimens. Microstructural studies were performed on fractured surfaces sputter-coated with gold after being dried at  $70^\circ\text{C}$  for 24 h and compositional studies were carried out on fractured surfaces impregnated with epoxy resin, polished and coated with carbon after being dried at  $70^\circ\text{C}$  for 24 h. Before each elemental analysis, EDS was accurately calibrated using the copper K $\alpha$  peak, under the beam energy of 12 keV. For samples to be representative for elemental analysis, care was taken to prepare samples from the middle of the top surface of acid-exposed mortar cubes and not from the side surfaces or areas close to the edges. In addition, we performed 3–4 elemental analyses on each sample to achieve typical results from areas of lower sand accumulation. All the results were similar and consistent and those from areas of relatively lower sand accumulation were selected for presentation in this paper.

A Philips PW 1800 X-ray diffractometer was used for investigating the mineralogical phase changes happening during the course of acid attack. The X-ray diffraction (XRD) patterns were acquired in the  $5\text{--}80^\circ$   $2\theta$  range, with a step size of 0.02 degree at scanning speed of 0.5 s. A PerkinElmer Fourier-transform infrared (FTIR) spectrometer was used to compare the chemical

bond characteristics of intact and deteriorated matrixes. The FTIR spectra were obtained using KBr pellet method (0.5 mg sample per 250 mg KBr), in the range of 4000 to 400  $\text{cm}^{-1}$  with a 4  $\text{cm}^{-1}$  resolution.

### 3. Results and discussion

#### 3.1. Visual observations

Apparent damage of different mortar specimens after 24 months of exposure to acid solutions were photographed for comparison purposes. Figure 1 represents the captured photographs before and after acid exposure. As seen, exposure to sulfuric acid seemed to be more aggressive than

hydrochloric acid. All the mortars exposed to sulfuric acid including GC exhibited noticeably higher degrees of apparent damage compared to those exposed to hydrochloric acid. The greatest apparent damage, however, was seen on PC and especially on HAC mortar specimens exposed to sulfuric acid attack. On the other hand, GC mortar exhibited the minimum apparent damage especially in hydrochloric acid solution. As seen in Figure 1, a typical GC mortar specimen exposed to hydrochloric acid attack showed very limited surface damage at the corners and edges. In the case of sulfuric acid attack, however, a noticeably higher extent of damage was observed. It must be taken into account that

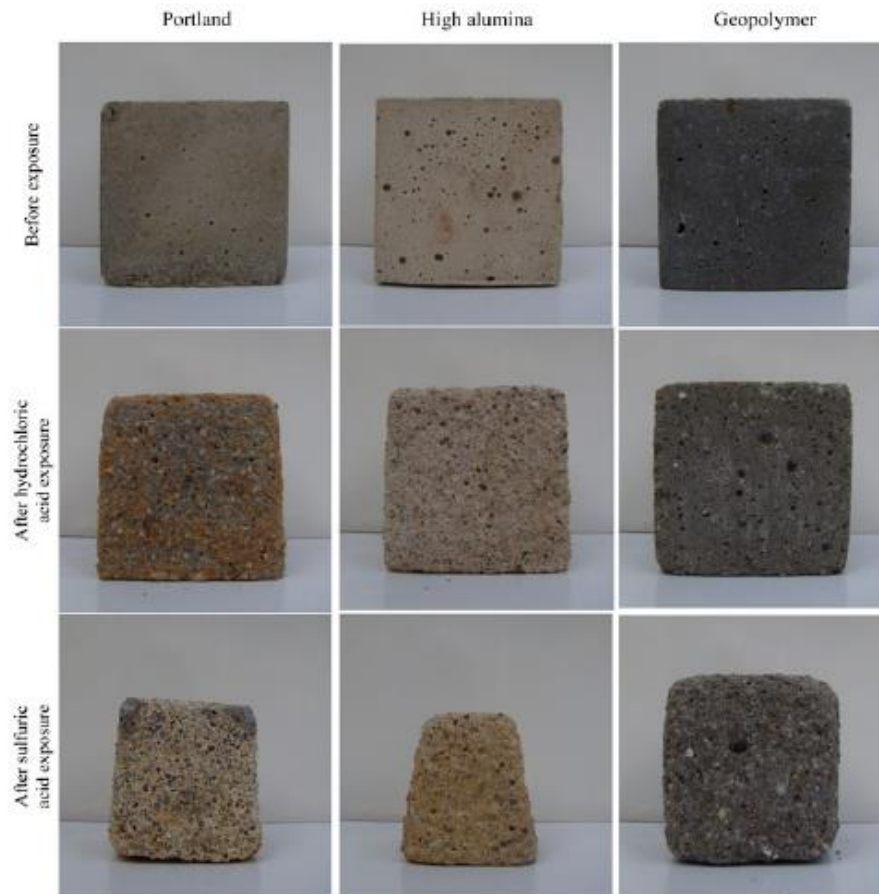


Figure 1. Different cement mortar specimens before and after 24 months of acid exposure at pH 3.

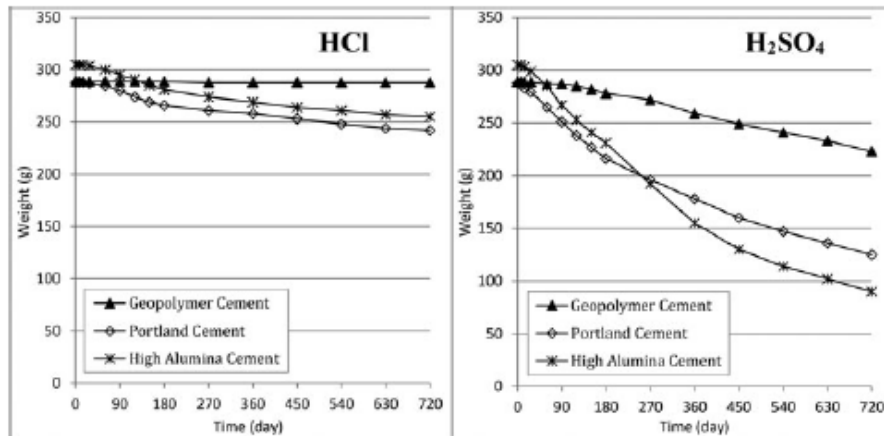


Figure 2. Mass changes of mortar specimens during 24 months of acid exposure at pH 3.

visual observations of apparent physical damage do not necessarily reflect the real order of the acid resistance of the studied mortars.

### 3.2. Mass loss

Mass loss of different mortar specimens due to acid attack was monitored during the course of acid exposure. Figure 2 shows the mass loss results versus exposure time. As seen, exposure to sulfuric acid resulted in much higher mass losses than exposure to hydrochloric acid. In the case of sulfuric acid attack, HAC, PC, and GC mortar specimens exhibited mass losses by about 70%, 56%, and 23%, at the end of exposure time, whereas the corresponding mass losses for exposure to hydrochloric acid solution were about 26%, 16%, and less than 1%, respectively. These mass loss results are in confirmation with visual observations. Compared to reference mortars, GC mortar exhibited a considerably lower mass loss, especially in hydrochloric acid. The dramatic mass losses in PC and HAC reference mortars are due to the fact that they are based on calcium silicate and calcium aluminate hydrates (C-S-H and C-A-H), respectively, that are not chemically stable in acid media. As confirmed in previous studies [1–4], these calcium-based binding compounds are easily decomposed

in acid media resulting in gradual complete deterioration of the cement matrix. The significantly higher mass losses in sulfuric acid compared to hydrochloric acid can be related to gypsum formation due to the chemical reaction between calcium compounds of hydrated cement phases and sulfate anion of sulfuric acid. The internal disintegrating stresses caused by growth of gypsum crystal deposited inside the deteriorating matrix can result in cracking and spalling of surface layers that accelerates the total rate of deterioration compared to hydrochloric acid attack at the same pH [16, 17]. On the other hand, the significantly lower mass losses of GC mortar in both sulfuric and hydrochloric acid solutions indicate a comparatively higher acid resistance, as confirmed in other studies for pH 1 acid media [10–13]. It must be considered that durability indicators, including mass loss, do not necessarily correlate with each other and each of these indicators alone does not necessarily justify the real durability of the material. For a sound conclusion, therefore, different indicators must be considered together.

### 3.3. Residual compressive strength

Compressive strength of mortar specimens exposed to acid solutions were measured at different time intervals to monitor the

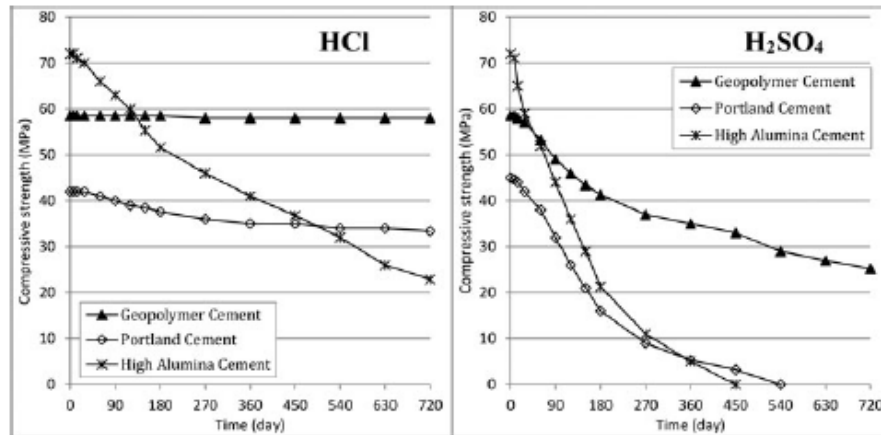


Figure 3. Compressive strength changes of mortar specimens during 24 months of acid exposure at pH 3.

amount of strength loss due to acid attack. Figure 3 displays the changes in compressive strength during the course of acid exposure. As seen, HAC and PC reference mortars exhibited 100% loss of compressive strength after 450 and 540 days of exposure to sulfuric acid, respectively. These reference mortars were suffered from compressive strength losses of about 68% and 20% at the end of exposure time to hydrochloric acid. In comparison, however, the GC mortar showed a significantly better performance with about 57% and almost no (less than 1%) strength losses at the end of exposure time in sulfuric and hydrochloric acid solutions, respectively. These findings that confirm the superior durability performance of GC mortar at pH 3 of sulfuric and hydrochloric acid solutions are in agreement with visual observations of apparent physical damage and mass loss results. The exceptional durability performance of GC mortar, especially in hydrochloric acid, can be attributed to the relative chemical stability of its main binding compound, i.e. sodium aluminosilicate hydrate (N-A-S-H) in acid media. This binding compound represents a considerably lower vulnerability to chemical attack by acidic media compared to the main calcium-based binding compounds of the

reference mortars [16, 17, 29]. The relatively weaker durability performance of GC mortar in exposure to sulfuric acid compared to hydrochloric acid can be attributed to the effect of gypsum formation and deposition in the deteriorating matrix on the mechanism and rate of deterioration, as observed in reference mortars also. The presence of calcium-based compounds in GC, such as C-A-S-H and N-(C)-A-S-H [30–32], due to the use of CAC as an additive rich in reactive alumina to improve the reactivity of FA can result in the formation of gypsum in the deteriorating areas that accelerates the rate of deterioration through expansion and cracking of the surface layers [16, 17].

The residual compressive strength data are consistent with mass loss data, except for the case of HAC exposed to hydrochloric acid that shows a relatively large compressive strength loss versus a relatively small mass loss. The durability performance of calcium aluminate cements in acid media has been studied by a number of researchers [33, 34]. It is well known that HAC exhibits a good acid resistance down to a pH of about 4, due to the relative chemical stability of alumina hydrate, i.e.  $\text{Al}(\text{OH})_3$ , that is often poorly crystalline in hydrated HAC paste. This is because

dissolution of calcium aluminate hydrates (C-A-H) results in the formation of additional quantities of alumina hydrate, which provides a protective effect by precipitating in the deteriorating matrix and infilling the pores. At pH values lower than 3.5, however, the alumina hydrate is not stable and does not provide any protective effect. HAC mortar specimens, therefore, are expected to exhibit a relatively high loss in compressive strength, as confirmed by other researchers [33, 34]. The obtained mass loss data, which are dependent greatly on the type of brush (steel or plastic) and the force applied, are not enough accurate. The vulnerability of HAC mortar specimens to acid attack can also be related to the relatively high water demand of the utilized HAC product (with the trade name of Secar 80). The very high Blaine specific surface area of this product (1000 m<sup>2</sup>/kg, as reported in Table 1) required a relatively high W/B-ratio (0.550 as reported in Section 2.2). The use of such a high amount of water increases the vulnerability of HAC mortar specimens against acid attack due to increased porosity and penetrability.

### 3.4. Compositional and microstructural changes in geopolymer

The mechanism of deterioration in GC mortar due to 24 months of acid exposure at pH 3 acid solutions was studied by investigating the changes in mineralogy and microstructure using XRD, Fourier transform infrared spectroscopy (FTIR), and scanning electron microscopy (SEM) techniques.

#### 3.4.1. X-ray diffraction

X-ray diffraction patterns of GC samples taken from mortar specimens before acid exposure (A) and after 24 months of exposure to hydrochloric and sulfuric acid solutions (B, C) are represented in Figure 4. As seen in Figure 4A, before exposure the

diffraction pattern displays the presence of a very small amount of anorthite (PDF#04-011-1371 [35]) originating from FA and a relatively high amount of quartz (PDF#04-008-4821 [35]) originating from standard sand. The geopolymerization reaction products were all amorphous in character. The small broad hump between  $2\theta$  degrees of 25 to 35 can be attributed to the presence of amorphous phase. The diffraction pattern of the GC mortar sample after exposure to hydrochloric acid solution (Figure 4B) is very similar to the diffraction pattern of intact GC (Figure 4A), confirming the amorphous character of the acid attack products in the deteriorated layer.

The peak positions in the diffraction pattern of hydrochloric acid-exposed GC sample do not match with similar phases present in the other two patterns. This is because the pattern of the hydrochloric acid-exposed GC sample was prepared with cobalt anode tube rather than copper anode tube. All the d-spacings, however, are correct.

The diffraction pattern of the GC mortar sample after exposure to sulfuric acid solution (diffraction pattern 4C) confirmed the formation and deposition of gypsum (PDF# 04-010-9409 [35]) as the only crystalline compound resulting from the reaction between calcium compounds of GC and sulfate ions. Identification of gypsum in different GC samples exposed to sulfuric acid attack has been reported by other researchers [13, 15–17, 29]. The intensity of gypsum deposition and its mechanistic role in sulfuric acid attack, however, greatly depends on the calcium content of the GC. It is believed that limited gypsum deposition in the exposed surface layer may provide some protective effect by infilling the porosity [12, 13].

The minor crystalline phase of anorthite originating from FA, which was depleted in the hydrochloric acid-exposed sample (Figure 4B), is still present in the diffraction pattern of sulfuric acid-exposed

sample (Figure 4C). Anorthite is a member of the plagioclase feldspar mineral series, which are acid soluble at pH 3 [36, 37]. The presence of this minor phase in the sulfuric acid-exposed sample shows that the prepared sample included materials from the deteriorating or even intact parts, in addition to the fully deteriorated part.

As can be seen, both diffraction patterns of acid-exposed samples display the formation of a very small amount of calcite (PDF#00-047-1743 [35]) in the deteriorated surface layer. Formation of calcite in the deteriorated surface layers of acid-

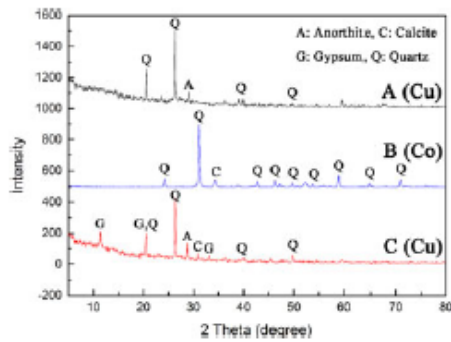


Figure 4. X-ray diffraction patterns: (A) intact geopolymer and (B, C) geopolymer exposed to hydrochloric and sulfuric acid solutions for 24 months, respectively.

exposed samples is due to the carbonation of CaO with atmospheric carbon dioxide after removing the mortar specimens from acid solutions.

### 3.4.2. Fourier transform infrared spectroscopy

The FTIR spectra obtained from GC samples taken from mortar specimens before acid exposure (A), after 24 months of exposure to hydrochloric acid solution (B), and after 24 months of exposure to sulfuric acid solution (C) are represented in Figure 5. The characteristic bands appeared in these FTIR spectra are represented in Table 2. The most important band corresponds to the asymmetric stretching of Si-O-T (T = Al or Si) that confirms the presence of N-A-S-H in the aluminosilicate framework of GC [38–44]. This band appeared at  $1024\text{ cm}^{-1}$  in the intact sample. A comparison of the spectra shows that this band shifted slightly towards higher wavenumbers at about  $1080$  and  $1114\text{ cm}^{-1}$  after exposure to hydrochloric and sulfuric acid solutions, respectively. This shifting is an indication of some depolymerization in the molecular structure of the GC due to some tetrahedral aluminum ejection during acid

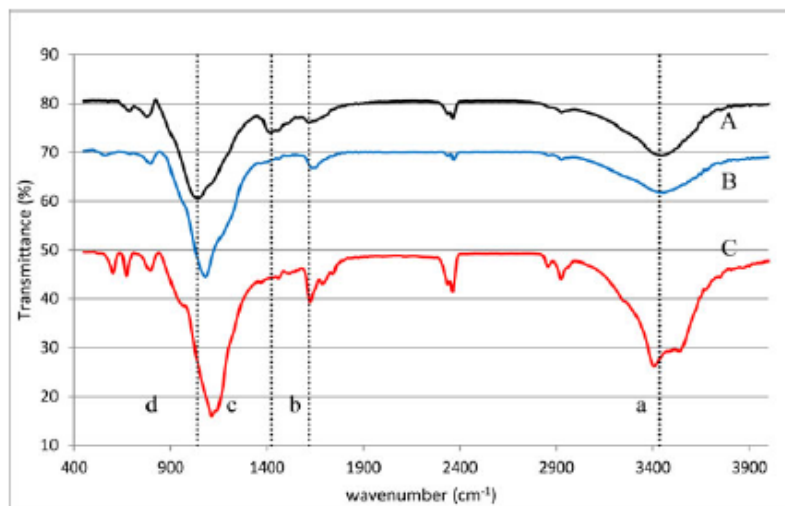


Figure 5. FTIR spectra; (A) intact geopolymer, (B) geopolymer exposed to hydrochloric acid solution for 24 months, and (C) geopolymer exposed to sulfuric acid solution for 24 months.

Table 2. Characteristic bands of FTIR spectra of geopolymer cement samples before and after acid exposure (shown in Figure 5).

Symbol	Sample type	Characteristic band (Wavenumber - $\text{cm}^{-1}$ )			
		a	b	c	d
A	Before acid exposure	3442	1644	1414	1024
B	After exposure to HCl	3455	1659	-	1080
C	After exposure to $\text{H}_2\text{SO}_4$	3408-3542	1624-1686	-	1114
	Characteristic bands	O-H stretching	H-O-H bending	O-C-O stretching	Si-O-Si and Si-O-Al stretching
	References	[12,34]	[12,34]	[32]	[32, 35, 36]

exposure [10–13]. As seen, this shifting is a little bit more in GC sample exposed to sulfuric acid solution, which implies a higher degree of depolymerization in sulfuric acid compared to hydrochloric acid at the same pH of 3. The band at  $1414\text{ cm}^{-1}$  in the intact sample belongs to vibrations of O-C-O in carbonate compounds resulting from carbonation of unreacted alkalis with atmospheric carbon dioxide [38]. The disappearance of this band in the exposed samples is an indication of complete dissolution of carbonates during acid attack. In addition, the absorption bands at  $3400\text{--}3550\text{ cm}^{-1}$  and at  $1620\text{--}1690\text{ cm}^{-1}$  due to O-H group stretching and bending vibration of chemically bonded water molecules [15, 39, 40] are noticeably enlarged in the acid-exposed samples especially in sulfuric acid exposed one. This confirms the effect of acid attack in increasing the concentration of Si-O-H terminals in GC due to depolymerization caused by partial ejection of tetrahedral aluminum [39, 40] and formation and deposition of gypsum in the case of exposure to sulfuric acid.

### 3.4.3. Scanning electron microscopy

The effects of 24 months of exposure to acid solutions on microstructure and chemical composition of GC mortar were investigated using fractured and polished surfaces. Figure 6 displays typical micrographs prepared from fractured surfaces. As seen in Figure 6(A), the GC mortar microstructure before acid attack consists of a relatively dense and homogeneous matrix with embedded sand particles and partially or non-reacted FA spheres. Observations on acid exposed-samples at relatively higher magnifications, as seen in Figures 6(B) and (C), revealed the deteriorating effects of acid attack in the form of increased porosity and breakdown of aluminosilicate network in the form of microcracks caused by depolymerization due to partial ejection of tetrahedral aluminum. The mechanism for these microstructural

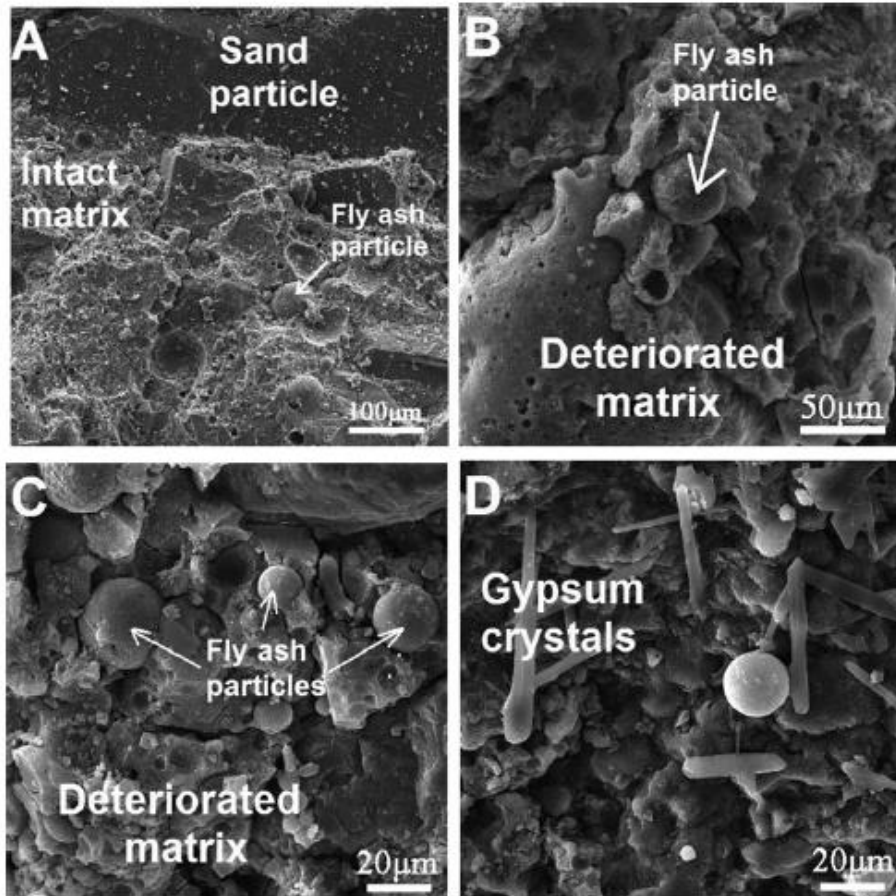


Figure 6. SEM micrographs prepared from fractured surface of geopolymer mortars; (A) intact geopolymer, (B) geopolymer exposed to hydrochloric acid solution after 24 months, (C) geopolymer exposed to sulfuric acid solution after 24 months, and (D) gypsum crystals deposited due to sulfuric acid attack.

changes that were also reported in other studies [16, 17, 43], will be discussed later. For sulfuric acid-exposed samples, in addition to porosity increase and microcracking, gypsum deposition in the form of fine rod-like crystals was also revealed as displayed in Figure 6(D) and previously confirmed in XRD and FTIR results (Sections 3.4.1 and 3.4.2).

A typical SEM micrograph prepared from fractured surface of GC mortar exposed to pH 3 HCl for 24 months along with EDS line concentration profiles for all the four main elements along the line shown in micrograph are displayed in

Figure 7. It must be noted that quartz aggregates caused strong variations in concentration profiles. Knowing that quartz is composed of mainly Si with almost no Al, Ca, and Na, these disturbances, however, can be simply realized. As seen, Na was leached partially (by about 50 to 75%) from the deteriorated surface layer. The total Na content of the GC can be divided into different parts. The main part is the charge balancing Na in the GC aluminosilicate gel (N-A-S-H). The other minor parts include some unreacted Na, which is converted to carbonate due to carbonation with atmospheric carbon dioxide and a small

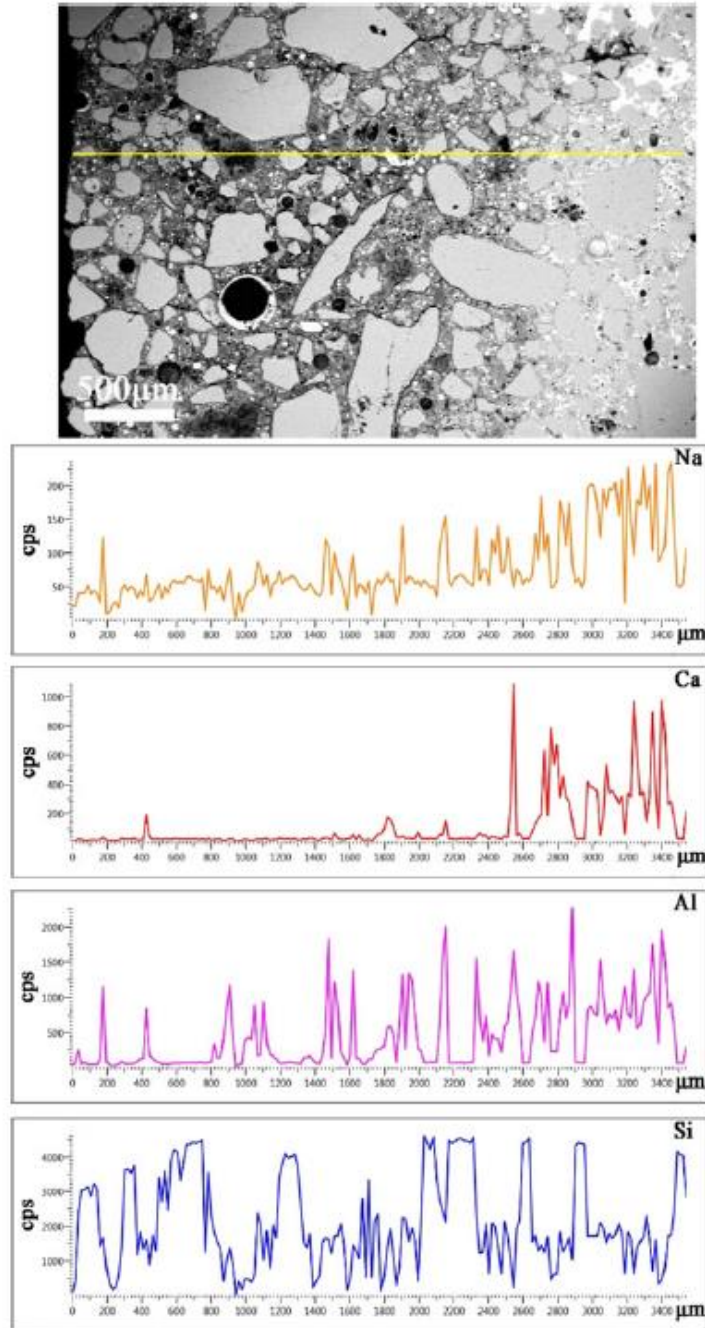


Figure 7. SEM micrograph and EDS elemental line concentration profiles prepared from polished fractured surface of geopolymer mortar exposed to hydrochloric acid solution after 24 months.

part of Na that might be present in anorthite that was originally present in the starting FA. In addition to these, some Na must

also be present in a stable and acid resistant phase. This is the Na that remained in the deteriorated surface layer of GC even after

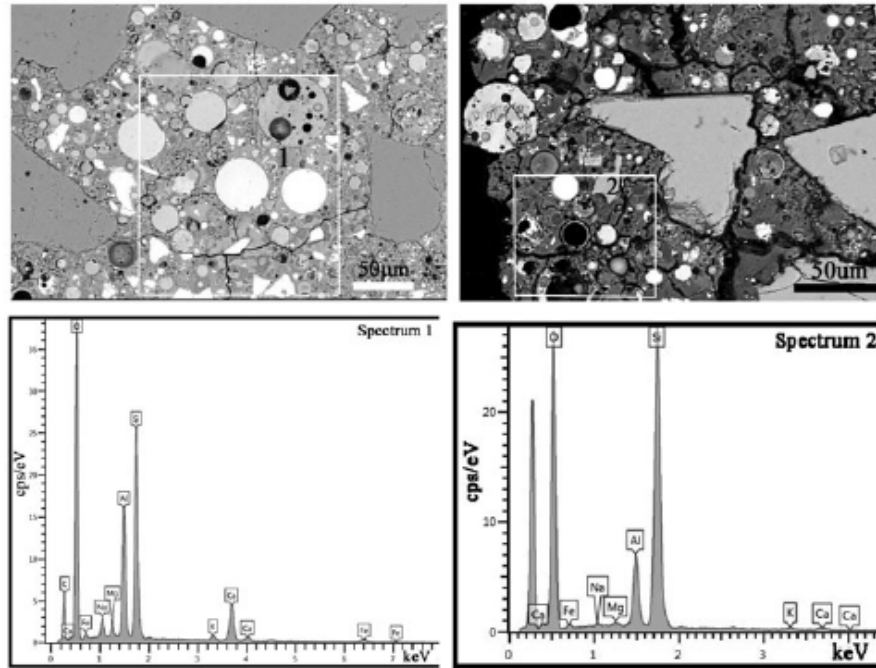


Figure 8. SEM micrographs and EDS elemental spectra prepared from polished fracture surface of geopolymer mortars; (Left) intact geopolymer, (Right) geopolymer exposed to hydrochloric acid solution after 24 months.

Table 3. EDS elemental composition (mass%) of the regions shown in SEM micrographs represented in Figure 8.

Spectrum	O	Si	Al	Ca	Fe	Na	K	Mg
1	45.8	21.8	11.7	11.2	5.6	1.9	1.2	0.9
2	46.9	37.4	7.9	1.0	4.4	0.3	0.7	0.3

24 months of exposure to pH 3 hydrochloric acid solution. The charge balancing Na present in N-A-S-H gel is weakly bound and, therefore, is easily leached out in acid solutions [45]. Since carbonates are easily dissolved in acid solutions, confirmed by FTIR spectroscopy results also (see Figure 5 and Table 2 in Section 3.4.2), the unreacted Na in the form of carbonate is also easily leached out in acid solutions. As mentioned before, it is also known that the Na and Ca contents of plagioclase feldspar including anorthite are easily released in acid media [36, 37]. The small remaining part of Na which is strongly bound in

an acid resistant phase can be present in a stable glass phase probably formed during to the high temperature coal combustion process. As seen in Ca concentration profile, calcium was almost completely leached from the deteriorated surface layer of GC. The Ca which was originally present in calcium aluminate phases in CAC is usually converted to C-S-H and/or C-A-S-H during the course of alkali activation [46]. Both of these gels are highly vulnerable to acid attack [1, 47] and therefore Ca is easily and almost completely leached into acid solutions. The total Al in GC is mainly present in the form of N-A-S-H and

C-A-S-H gels and partially in form of anorthite and glass phase as non-reactive phases during the course of alkali activation. As seen in Al concentration profile, Al is partially leached out from the deteriorated surface layer showing a dealumination of GC during acid attack, as previously confirmed by FTIR spectroscopy results (see Figure 5 and Table 2 in Section 3.4.2). As seen in Figure 7, 24 months of leaching of Ca, Al, and Na from acid exposed surface of the GC mortar left a silica enriched and highly porous (see Si concentration profile in Figure 7)

deteriorated surface layer of approximate thickness of 3 mm.

Figure 8 and Table 3 represent typical micrographs along with EDS elemental spectra and the corresponding elemental compositions prepared from polished fracture surface of intact GC matrix (Left), and GC matrix exposed to hydrochloric acid solution after 24 months (Right). As EDS elemental compositions show, the 24-month chemical attack by pH 3 hydrochloric acid resulted in the leaching of Al, Ca, Na and K from the acid exposed surface by about 32%, 91%, 84%, and 42%,

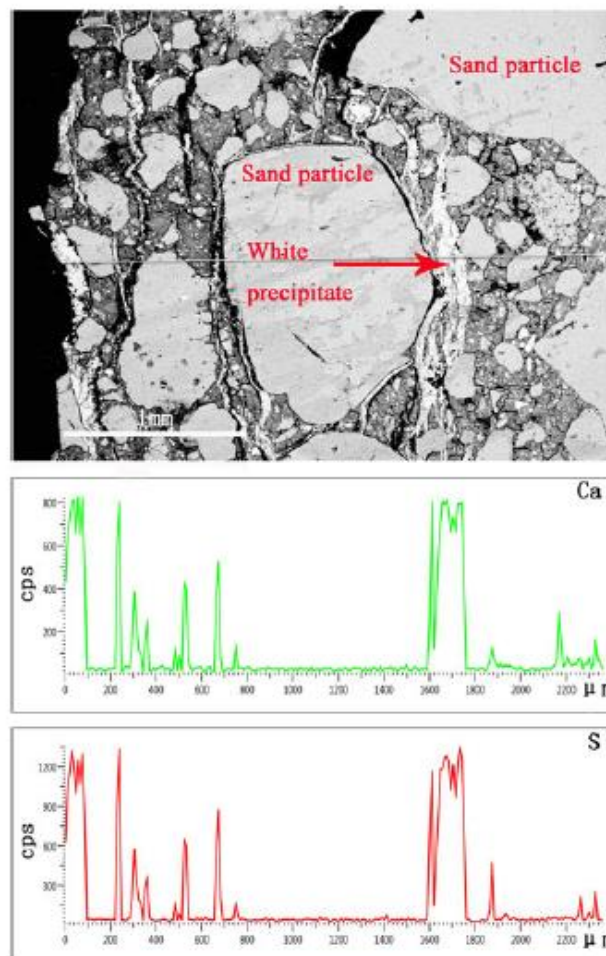


Figure 9. SEM micrograph and EDS line concentration profiles for Ca and S prepared from polished fractured surface of geopolymer mortar exposed to sulfuric acid solution after 24 months.

respectively. The high shrinkage caused by such an intensive leaching process resulted in the formation of a highly porous and microcracked surface layer as seen in Figure 8.

Figure 9 displays a SEM micrograph along with EDS line concentration profiles for Ca and S prepared from polished fractured surface of GC mortar exposed to sulfuric acid solution after 24 months. As can be seen, the 24-month acid attack by pH 3 sulfuric acid solution has resulted in the formation of many relatively large microcracks that are parallel to the acid exposed surface. Many of these microcracks are either completely or partially filled with a white precipitate. A careful comparison of the Ca and S concentration profiles to each other and to SEM micrograph clearly confirms that the two profile are very similar with almost all the peaks coinciding on

each other and on the white precipitate inside the microcracks. This white precipitate that is rich in Ca and S in its elemental composition is gypsum, as confirmed by XRD and SEM results as well as reported by other researchers [12, 16, 17, 29].

Figure 10 displays a typical SEM micrograph and two EDS elemental spectra, one from white precipitate inside a microcrack (spectrum 3) and the other from deteriorated matrix (spectrum 4), prepared from polished fracture surface of geopolymer mortar after 24 months of exposure to sulfuric acid solution. The corresponding elemental compositions are represented in Table 4. As seen, in addition to the microstructural changes in the form of increased porosity and formation of relatively large microcracks parallel to the acid exposed surface, noticeable compositional changes were also happened during the

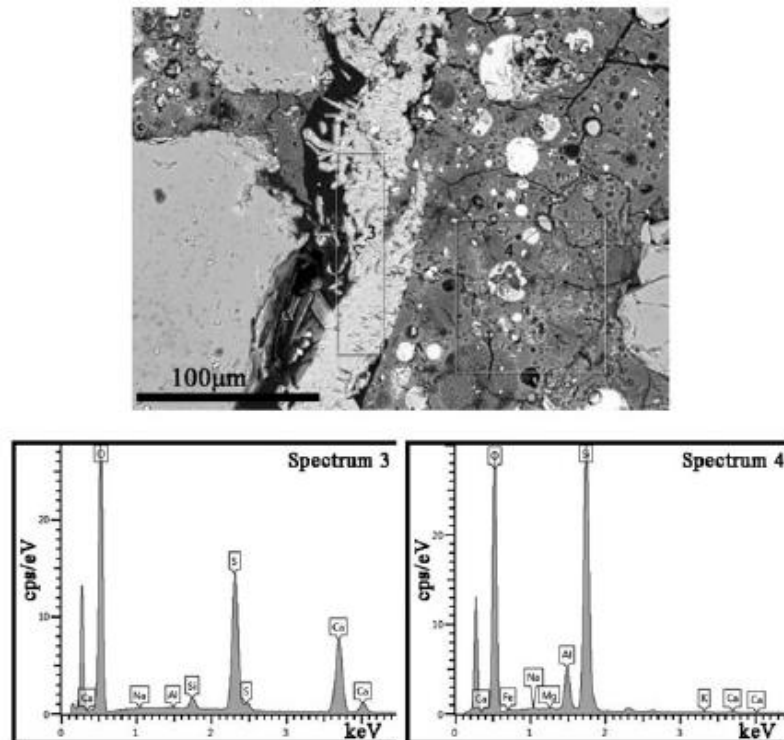


Figure 10. SEM micrograph and EDS elemental spectra prepared from polished fracture surface of geopolymer mortars exposed to sulfuric acid solution after 24 months.

Table 4. EDS elemental composition (mass%) of the regions shown in SEM micrographs represented in Figure 10.

Spectrum	O	Si	Al	Ca	Fe	Na	K	Mg	S
3	55.4	1.0	0.1	23.8	–	0.1	–	–	19.7
4	50.4	41.0	5.6	0.7	1.6	0.2	0.5	0.1	–

course of acid attack compared to intact matrix (see Figure 8). The 24-month chemical attack by pH 3 sulfuric acid resulted in the leaching of Al, Ca, Na and K from the deteriorated layer by about 52%, 94%, 89%, and 58%, respectively, which are almost similar to leaching values determined for hydrochloric acid attack. Similarly, such an intensive leaching process can cause significant shrinkage increasing the porosity and resulting in the formation of shrinkage microcracks in the GC matrix as what observed in the case of pH 3 hydrochloric acid. As seen in Table 4, the EDS spectra 3 shows an elemental composition consisting of major elements of oxygen (O), calcium (Ca), and sulfur (S), confirming the precipitation of gypsum crystals inside relatively large microcracks, as previously confirmed by XRD and SEM results (see Sections 3.4.1 and 3.4.3). In addition, deposition and subsequent growth of gypsum crystals cause disintegrating expansive stresses inside the GC matrix resulting in the formation of expansive microcracks [12, 13, 29] (the relatively large microcracks parallel to the acid exposed surface observed in Figure 9). Upon increased expansion, these relatively large expansive microcracks result in scaling of surface layers and debris from the acid exposed surface. This scaling of surface layers and debris from acid exposed surface increases the amount of mass loss and accelerates the rate of deterioration compared to pH 3 HCl, as considered previously in Sections 3.1–3.3. The deterioration mechanism of GC at pH 3 sulfuric acid, therefore, is based on a combination of both shrinkage and expansion together caused by simultaneous leaching of alkali

and alkali earth metals and gypsum crystals deposition and growth, unlike the deterioration mechanism of GC at pH 3 hydrochloric acid that is based only on shrinkage caused by leaching. The leaching mechanism alone does not effectively result in scaling of surface layers and debris and the remaining deteriorated layer on the acid exposed surface provide a protective effect that decelerates the total rate of deterioration.

#### 4. Conclusion

The following conclusions can be drawn from the present study that evaluates the 2-year durability performance of GC mortar derived from the blend of low calcium fly ash (76 wt.%) and calcium aluminate cement (24 wt.%) in mild concentration (pH 3) of hydrochloric and sulfuric acid solutions considering PC and high alumina cement (Secar 80) mortars as reference:

1. Compared to reference cements and based on mass and compressive strength losses data, the GC exhibited a significantly superior acid resistance especially in pH 3 hydrochloric acid.
2. The GC matrix does not decompose completely upon acid attack, but undergoes significant leaching of alkali and alkali earth metals leaving a highly porous and microcracked deteriorated layer on the acid exposed surface that provides some protective effects decelerating the total rate of deterioration. The deterioration mechanism at pH 3

hydrochloric acid is therefore based on leaching and shrinkage.

3. In pH 3 sulfuric acid, the deterioration mechanism is based on both shrinkage and expansion together caused by simultaneous leaching of alkali and alkali earth metals and gypsum crystals deposition and growth. The shrinkage results in porosity increase and microcracking, whereas expansion causes scaling of surface layers and debris, which in turn accelerates to total rate of deterioration compared to pH 3 hydrochloric acid.

#### Disclosure statement

The authors declare that there is no conflict of interest.

#### References

- [1] Allahverdi A, Škvára F. Acidic corrosion of hydrated cement-based materials, Part 1; Mechanisms of the phenomenon. *Ceram-Silik*. 2000;3; 114–120.
- [2] Zivica VR, Bajza A. Acidic attack of cement-based materials – a review: Part 1. Principle of acidic attack. *Constr Build Mater*. 2001;15(8);331–340.
- [3] Allahverdi A, Škvára F. Acidic corrosion of hydrated cement-based materials, Part 2; Kinetics of the phenomenon and mathematical models. *Ceram-Silik*. 2000;44(4);152–160.
- [4] Zivica VR, Bajza A. Acidic attack of cement-based materials – a review: Part 2. Factors of rate of acidic attack and protective measures. *Constr Build Mater*. 2002;16(4);215–222.
- [5] Duxson P, Provis JL, Lukey GC, et al. The role of inorganic polymer technology in the development of green concrete. *Cem Concr Res*. 2007;7(12); 1590–1597.
- [6] Nadzirri N, Ismail I, Hamdan S. Binding gel characterization of alkali-activated binders based on palm oil fuel ash (POFA) and fly ash. *J Sustain Cem-Based Mater*. 2018;7(1);1–14.
- [7] El-Hassan H, Ismail N. Effect of process parameters on the performance of fly ash/GGBS blended geopolymer composites. *J Sustain Cem-Based Mater*. 2018;7(2);122–140.
- [8] Albitara M, Mohamed Ali MS, Visintin P, et al. Durability evaluation of geopolymer and conventional concretes. *Constr Build Mater*. 2017;136(1); 374–385.
- [9] Shi C, Krivenko PV, Roy D. Alkali-activated cements and concretes. 1st ed. [place unknown]: Taylor & Francis; 2006.
- [10] Allahverdi A, Škvára F. Nitric acid attack on hardened paste of geopolymeric cements: Part 1. *Ceram-Silik*. 2001;45(3);81–88.
- [11] Allahverdi A, Škvára F. Nitric acid attack on hardened paste of geopolymeric cements: Part 2. *Ceram-Silik*. 2001;45(4);143–149.
- [12] Allahverdi A, Škvára F. Sulfuric acid attack on hardened paste of geopolymer cements: Part 1. Mechanism of corrosion at relatively high concentrations. *Ceram-Silik*. 2005;49(4);225–229.
- [13] Allahverdi A, Škvára F. Sulfuric acid attack on hardened paste of geopolymer cements: Part 2. Corrosion mechanism at mild and relatively low concentrations. *Ceram-Silik*. 2006;50(1);1–4.
- [14] Fernando PT, Said J. Resistance to acid attack, abrasion and leaching behavior of alkali-activated mine waste binders. *Mater Struct*. 2011;4(2);487–498.
- [15] Ariffin MAM, Bhutta MAR, Hussin MW, et al. Sulfuric acid resistance of blended ash geopolymer concrete. *Constr Build Mater*. 2013;43;80–86.
- [16] Vafaei M, Allahverdi A. Durability of geopolymer mortar based on waste-glass powder and calcium aluminate cement in acid solutions. *J Mater Civ Eng*. 2017;29(10);04017196.
- [17] Vafaei M, Allahverdi A. Acid-resistant geopolymer based on fly ash–calcium aluminate cement. *J Mater Civ Eng*. 2018;30(7);04018143.
- [18] Fest EPMJ, Temminghoff EJM, Griffioen J, et al. Groundwater chemistry of Al under Dutch sandy soils: effects of land use and depth. *Appl Geochem*. 2007;22;1427–1438.
- [19] National Trends Network (NTN) Maps, Illinois State: NADP Program Office, Illinois State Water Survey; 2014 [cited

- 2017 Aug 16]. Available from: <http://nadp.sws.uiuc.edu/ntn/maps.aspx>.
- [20] American Society for Testing and Materials. Standard specification for Portland cement. United States: ASTM C150/C150M:2018.
- [21] American Society for Testing and Materials. Standard test methods for sampling and testing fly ash or natural pozzolans for use in Portland-cement concrete. United States: ASTM C311/C311M:2017.
- [22] American Society for Testing and Materials. Standard test methods for chemical analysis of hydraulic cement. United States: ASTM C114:2015.
- [23] American Society for Testing and Materials. Standard test methods for fineness of hydraulic cement by air-permeability apparatus. United States: ASTM C204:2017.
- [24] American Society for Testing and Materials. Standard test method for density of hydraulic cement. United States: ASTM C188:2017.
- [25] German Institute for Standardization (DIN) Standards. Methods of testing cement- Part 1: Determination of strength. Germany: DIN-EN-196-1:2016.
- [26] American Society for Testing and Materials. Standard test method for compressive strength of hydraulic cement mortars (using 2-in. or [50-mm] cube specimens). United States: ASTM C109/C109M:2016.
- [27] American Society for Testing and Materials. Standard test method for flow of hydraulic cement mortar. United States: ASTM C1437:2015.
- [28] American Society for Testing and Materials. Standard test methods for chemical resistance of mortars, grouts, and monolithic surfacings and polymer concretes. United States: ASTM C267:2012.
- [29] Sata V, Sathonsaowaphak A, Chindaprasit P. Resistance of lignite bottom ash geopolymer mortar to sulfate and sulfuric acid attack. *Cem Concr Compos.* 2012;34(5):700–708.
- [30] Yan Sh, Sagoe-Crentsil K. Evaluation of fly ash geopolymer mortar incorporating calcined wastepaper sludge. *J Sustain Cem-Based Mater.* 2016;5(6):370–380.
- [31] Chen X, Sutrisno A, Struble LJ. Effects of calcium on setting mechanism of metakaolin-based geopolymer. *J Am Ceram Soc.* 2018;101(2):957–968.
- [32] Adesanya E, Ohenoja K, Luukkonen T, et al. One-part geopolymer cement from slag and pretreated paper sludge. *J Clean Prod.* 2018;185(1):168–175.
- [33] Scrivener KL, Cabiron JL, Letourneux R. High-performance concretes from calcium aluminate cements. *Cem Concr Res.* 1999;29:1215–1223.
- [34] Shi C, Stegemann JA. Acid corrosion resistance of different cementing materials. *Cem Concr Res.* 2000;30(5):803–808.
- [35] International Centre for Diffraction Data, Pennsylvania State: Newtown Square, PA, U.S.A. 19073-3273; [cited 2019 Jan 17]. Available from: <http://www.icdd.com/index.php/pdfsearch/>.
- [36] Welch SA, Ullman WJ. Feldspar dissolution in acidic and organic solutions: Compositional and pH dependence of dissolution rate. *Geochim Cosmochim Acta.* 1996;60(16):2939–2948.
- [37] Lutge A, Bolton EW, Lasaga AC. An interferometric study of the dissolution kinetics of anorthite: the role of reactive surface area. *Am J Sci.* 1999;299:652–678.
- [38] Ahmari S, Zhang L. Durability and leaching behavior of mine tailings-based geopolymer bricks. *Constr Build Mater.* 2013;44:743–750.
- [39] Duxson P, Provis JL, van Deventer JSJ. *Geopolymers: Structures, processing, properties and industrial applications.* Abingdon (United Kingdom): Woodhead Publishing; 2009.
- [40] Chukanov NV, Chervonnyi AD. *Infrared spectroscopy of minerals and related compounds.* 1st ed. [place unknown]: Springer International Publishing; 2016.
- [41] Zhang M, Zhao M, Zhang G, et al. Durability of red mud-fly ash based geopolymer and leaching behavior of heavy metals in sulfuric acid solutions and deionized water. *Constr Build Mater.* 2016;124:373–382.
- [42] Part WK, Ramli M, Cheah CB. An overview on the influence of various factors on the properties of geopolymer concrete derived from industrial by-products. *Constr Build Mater.* 2015;77:370–395.
- [43] Yunsheng Z, Wei S, Zongjin L. Composition design and microstructural characterization of calcined kaolin-based

- geopolymer cement. *Appl Clay Sci.* 2010;47:271–275.
- [44] Bakharev T. Resistance of geopolymer materials to acid attack. *Cem Concr Res.* 2005;35(4): 658–670.
- [45] Škvára F, Šmilauer V, Hlaváček P, et al. A weak alkali bond in (N, K)-A-S-H gels: evidence from leaching and modeling. *Ceram-Silik.* 2012;56(4);374–382.
- [46] Puertas F, Palacios M, Manzano H, et al. A model for the C-A-S-H gel formed in alkali-activated slag cements. *J Eur Ceram Soc.* 2011;31; 2043–2056.
- [47] Bakharev T, Sanjayan JG, Cheng YB. Resistance of alkali-activated slag concrete to acid attack. *Cem Concr Res.* 2003;33(10);1607–1611.



## Green template-free synthesis and characterization of mesoporous alumina as a high value-added product in aluminum black dross recycling strategy



Mostafa Mahinroosta<sup>a</sup>, Ali Allahverdi<sup>a, \*</sup>, Peng Dong<sup>b</sup>, Nabil Bassim<sup>b</sup>

<sup>a</sup> Research Laboratory of Inorganic Chemical Process Technologies, School of Chemical Engineering, Iran University of Science and Technology, Narmak, 1684613114, Tehran, Iran

<sup>b</sup> Department of Materials Science and Engineering, McMaster University, Hamilton, Ontario, L8S 3Z9, Canada

### ARTICLE INFO

#### Article history:

Received 24 November 2018

Received in revised form

28 March 2019

Accepted 1 April 2019

Available online 4 April 2019

#### Keywords:

Inorganic materials  
Nanostuctured materials  
Oxide materials  
Precipitation  
Chemical synthesis

### ABSTRACT

Aluminum black dross (ABD) is a solid waste of aluminum smelting process that causes serious environmental and public health problems. In addition, it imposes significant disposal costs to the aluminum industry. In this study, synthesis and characterization of mesoporous alumina (MA) from the ABD using a novel recycling procedure consisting of leaching at low temperature (85 °C) and atmospheric pressure, co-precipitation, separation through selective dissolution, re-precipitation, aging and finally calcination at 600 °C for 2 h. No hard or soft template was used during the formation of the gel. The as-synthesized MA had a specific surface area, total pore volume and average pore diameter of 123–162 m<sup>2</sup>/g, 0.37 cm<sup>3</sup>/g and 10.6 nm, respectively which were obtained by nitrogen sorption analysis. The as-synthesized MA possessed more than 98% purity. Its XRD pattern exhibited the characteristic peaks of gamma, eta, theta, and delta phase alumina. FESEM and TEM analyses revealed nanoscale morphology of the as-synthesized MA; having crystal size of ~11 nm. The TGA analysis showed that the as-synthesized MA is thermally stable and exhibits only ~5 wt% mass loss for heating from 30 to 800 °C. The characterization of solid residue at the end of the proposed process proved that it contains mainly silica phase which can alternatively be reused as filling agent or aggregate in concrete materials applications. It is quite clear that the process of production of MA from the ABD is feasible and practical and provides a novel mitigation to the environmental problems of the ABD.

© 2019 Elsevier B.V. All rights reserved.

### 1. Introduction

Mesoporous alumina (MA) has received considerable attention from the industrial and academic communities due to its great applicability in the preparation of catalyst/catalyst support, adsorption of various pollutants from wastewater (e.g. fluoride, dyes, heavy metals, organic compounds, etc.) [1–5], chemical and biochemical separation, and sensors [6,7]. This great deal of interest is due to special characteristics of the MA such as porosity, high surface area and chemical activity [8–11].

The MA is prevalently fabricated through one of the following three pathways: 1) hard templating method (e.g. using carbon template) [12,13]; 2) solvent-free synthesis without the use of

structure directing agents [14]; and (3) soft templating process with the contribution of ionic and nonionic surfactant [15,16], organic molecules [9,17], and ionic liquids [18]. The synthesis of the MA has also been reported by a combustion synthesis without template [19].

At present, there are many salts utilized as sources of aluminum for the synthesis of alumina, such as Al(NO<sub>3</sub>)<sub>3</sub>·9H<sub>2</sub>O [20], AlCl<sub>3</sub> and NaAlO<sub>2</sub> [21], aluminum isopropoxide [22], aluminum ammonium carbonate hydroxide [23], and so on. These aluminum sources are expensive, making industrialization of alumina production is very challenging. Recently, the synthesis of alumina from industrial solid waste as secondary sources of aluminum has attracted the attention of researchers. For the synthesis, the researchers have proposed some processes for production of alumina from solid wastes such as the acid-base leaching [24,25], limestone sintering method [26], and lime-soda sinter method [27]. In addition to gaining economic benefits from material production, retrieving/recycling

\* Corresponding author.

E-mail addresses: [ali.allahverdi@iust.ac.ir](mailto:ali.allahverdi@iust.ac.ir), [aliallahverdi@iust.ac.ir](mailto:aliallahverdi@iust.ac.ir) (A. Allahverdi).

<https://doi.org/10.1016/j.jalcom.2019.04.009>

0925-8388/© 2019 Elsevier B.V. All rights reserved.

the wastes is a desirable solution for both industries and the environment to overcome disposal costs and environmental pollution [28].

Aluminum black dross (ABD) is the major aluminum production waste. Unfortunately, reliable statistics are not available on the utilization rate of the ABD, but as a rough estimation, the global ABD generation is more than one million tons per annum, of which around 95% is dumped in the vicinity of factories. In other words, this means a very low recycling rate [29]. The ABD is mostly discarded in landfills and thus imposes a severe menace to the environment [29–31]. The ABD is a compound inorganic waste consisting majorly of nonmetallic materials (oxides and salts) which is formed during the Al melting [32,33]. If an appropriate approach could be found to use and manage the waste, it will provide a three-fold advantage to both environment and industries. Firstly, the volume of the waste and consequently the corresponding disposal costs could be partly diminished. Secondly a cleaner environment can be achieved, and thirdly if possible, production and development of advanced materials from the waste at reasonable cost can lead to the increased economic benefit as well as the conservation of natural resources.

The aim of this work is to prepare MA with a relatively narrow pore size distribution using ABD as a cheap, alumina-rich inorganic material without using a template for the first time. The production process here includes a low-temperature and atmospheric pressure extraction process. The residual solids from the extraction process do not inflict environmental contamination and can be stacked at a much lower risk or alternatively reused as filling agent or aggregate in concrete applications. All these together evince the eco-friendliness of the proposed process within the framework of the principles of green chemistry [34].

## 2. Experimental procedure

### 2.1. Chemicals and materials

The ABD was provided by a national aluminum manufacturer. Sieve analysis disclosed that the  $D_{10}$ ,  $D_{50}$ , and  $D_{90}$  values of the as-received ABD were 46.6, 313.8, and 2111.4  $\mu\text{m}$ , respectively. The oxide composition of the ABD, analyzed by X-ray fluorescence (XRF) technique (according to ISO/IEC 17025:2005 standard), is given in Table 1, which shows that it consists mainly of alumina (about 60%) and silica (about 15%) along with other oxides. The loss on ignition (LOI) of around 9.0% was achieved by heating the sample at 950 °C for 1 h.

The X-ray diffractogram of the as-received ABD is represented in Fig. S1 (refer to online supplementary figure). Analysis of the diffraction pattern of the ABD powder sample revealed the presence of aluminum oxide, spinel, defect spinel ( $\text{Al}_{183}\text{Mg}_{0.87}\text{O}_{3.61}$ ),

quartz, diaoyudaoite ( $\text{NaAl}_{11}\text{O}_{17}$ ), williumite ( $\text{NaF}$ ), cryolite ( $\text{Na}_3\text{AlF}_6$ ), silicon (Si), aluminum nitride and ferric oxide. Minor traces of halite, graphite (C), and fluorite ( $\text{CaF}_2$ ) were also found. The origin of the existence of halite (NaCl), williumite, and fluorite ( $\text{CaF}_2$ ) is the molten salt flux, which is consumed as a melting aid and a protection layer against oxidation of aluminum. Cryolite is used as an electrolyte during the melting process of alumina.

Sodium hydroxide pellets (99% purity), ammonia 25%, and hydrochloric acid 37% were all procured from Merck Company and ethanol absolute ( $\geq 99\%$  purity) was supplied from Riedel-de Haën (Hanover, Germany). Deionized water was utilized throughout the experiments.

### 2.2. Mesoporous alumina synthesis

Fig. S2 (refer to online supplementary figure) depicts the flow chart of the novel process used in synthesizing MA from ABD. The ABD was initially leached by 5 M hydrochloric acid solution in a Pyrex three-neck round-bottom reactor equipped with a Graham reflux condenser and a temperature controller. Since acid leaching is an essential step in the process shown in Fig. S2, the study of dissolution and leaching mechanism and kinetics is of great importance. Such a study was carried out in the previous work [35], and the results showed that the apparent activation energy was about 10.5 kJ/mol and the dissolution of the waste in HCl was an internal diffusion-controlled process. Therefore, to reduce the diffusion resistance, an agitator is used in the leaching step. The leaching temperature and the reaction time were set at 85 °C and 120 min, respectively. The extraction process was performed with solid-to-liquid ratio of 1:20 g/ml under constant agitation speed of 600 rpm. The aforementioned parameters were selected according to the previous study including the study of the effects of acid concentration, time, solid-to-liquid ratio, temperature, and particle size on the alumina extraction efficiency. The results revealed that the extraction efficiency of alumina was about 83% [36]. After the elapsed leaching time, the slurry was filtered to separate insoluble residue. The filtrate was transferred into the co-precipitation stage. In this stage, ammonia was added to the filtrate until the pH reached a value of 5.5–6.0. Following the addition of ammonia, a milky white hydroxide precipitate was readily formed. After filtration of the precipitate, to remove metal cationic impurities from aluminum hydroxide gel, 3 N NaOH was added to the hydroxide precipitate to generate an alkaline sodium aluminate solution. The addition of NaOH was continued until the pH value of 12–13. Then, in the next stage, hydrochloric acid solution was added to the aluminate-rich liquor until a pure white precipitate was formed. In this stage the pH reached 11. The obtained gel was aged for two different times of 1 and 48 h. The new white precipitate was filtered and washed with a mixture of deionized water and ethanol several times until the pH value reached 7. The washed precipitate was then dried in an oven at 110 °C. The oven-dried aluminum hydroxide was finally calcined at 600 °C for 2 h. To ensure the effective removal of metal cationic impurities from aluminum cations, the chemical compositions of chloride leachate and aluminate-rich filtrate were determined by inductively coupled

**Table 1**  
Chemical composition of ABD.

Oxide	(wt%)
$\text{Al}_2\text{O}_3$	64.8
$\text{SiO}_2$	16.5
$\text{Fe}_2\text{O}_3$	6.8
CaO	3.8
MgO	2.9
$\text{Na}_2\text{O}$	2.8
$\text{K}_2\text{O}$	1.0
$\text{TiO}_2$	0.4
MnO	0.4
$\text{SO}_3$	0.3
CuO	0.2
SiO	0.1

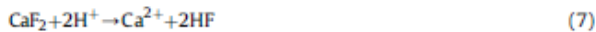
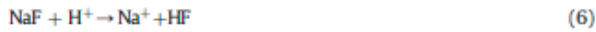
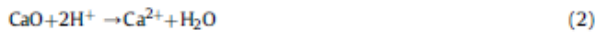
**Table 2**  
Chemical composition of chloride leachate and aluminate-rich liquor.

Sample	Concentration (mg/l)					
	$\text{Al}^{3+}$	$\text{Ca}^{2+}$	$\text{Fe}^{3+}$	$\text{Mg}^{2+}$	$\text{Na}^+$	Si
Chloride leachate	6868.30	1372.80	379.58	250.01	3814.80	35.74
Aluminate-rich filtrate	6804.60	1.85	0.49	ND	30575.00	44.36

ND: Not detected.

plasma atomic emission spectroscopy (ICP-AES). The output of ICP analyses are presented in Table 2. As can be seen, metal cations have effectively been separated from aluminum cations. The high concentration of sodium ion in the aluminate-rich solution is due to the addition of sodium hydroxide solution at the selective dissolution stage, which is later removed easily by washing. In this novel process, alumina is extracted at atmospheric pressure and low temperature, which implies that the extraction process is relatively safe. The separation of aluminum hydroxide from other metal hydroxides is performed without the use of any specific and complex technique, and only with the use of amphoteric property of the aluminum hydroxide. Finally, by adjusting the aging time, mesoporous alumina is obtained without the use of any hard or soft template from a secondary inorganic material. By-products of the proposed process including residual hydroxides and insoluble residues have a potential re-usability. However, they require further study and characterization. The overall process accrues recyclability and recoverability of the ABD adhering to sustainability principles.

All possible reactions in the leaching stage are as follows:



The representative dissolution of silica species under acidic condition is given by Ref. [37]:



The possible interactions of  $\text{Al}_2\text{O}_3$  and acid medium cause the formation of various ions based on the following reactions [38]:



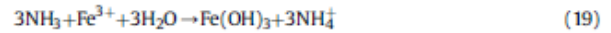
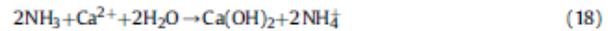
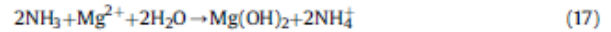
$\text{Al}_2\text{O}_3$  particles have a positive charge at  $\text{pH} < \text{pH}_{\text{ZCP}}$  ( $=8.0-8.5$ ) and a negative charge at  $\text{pH} > \text{pH}_{\text{ZCP}}$  because of the absorption of  $\text{OH}^-$  groups. Since, the pH value at the leaching stage is controlled in the range of 5.5–6, the probability of reactions (9)–(12) is higher.

At the precipitation or base hydrolysis stage,  $\text{Al}^{3+}$  cations in acidic solution initially form a milky gel and then the gel is transmuted into different crystalline hydroxides [39].

The overall reaction at the precipitation stage is as follows [40]:



The other metal cations precipitate through the following reactions by addition of ammonia:



The silanol groups generated at the leaching stage can be dissociated through the following reactions under basic pH [41]:



To remove any impurity from aluminum hydroxide for the production of high purity alumina, 3 N NaOH is added to the precipitated hydroxide product to convert  $\text{Al}(\text{OH})_3$  species into aluminate ions according to its amphoteric characteristic:



Finally, at the re-precipitation stage,  $\text{Al}(\text{OH})_3$  is formed again by adding HCl:



### 2.3. Methods of characterization

To identify crystalline phases, an X-ray diffractometer (Philips Expert System) was utilized at 40 kV and 30 mA. The X-ray diffractograms were recorded at 2 $\theta$  range of 10–90° (scanning rate = 2°/min, anti-scatter = 1°; receiving slit 0.01 mm). Three kinds of microscopes were employed to survey the morphologies of the raw material and products. FESEM (SIGMA VP-500, ZEISS, Germany) was used to study the morphology of the as-prepared aluminum hydroxide and alumina at 15 kV. Energy Dispersive X-ray Spectroscopy (EDX) technique (Oxford Instrument, England) was utilized for elemental analysis. SEM device (TESCAN VEGA II, Czech Republic) was employed to prepare micrographs of the raw ABD and residual solids at 30 kV. The secondary electron (SE) mode of the SEM device was selected for this purpose. A 120 kV TEM (PHILIPS CM12, Netherland) was used to observe the features of the as-prepared aluminum hydroxide and alumina particles. The oxide composition of the as-fabricated alumina was obtained employing an X-ray fluorescence device (ED2000, Oxford). To identify chemical bonds formed in the structure of the products, a Fourier transform infrared (FTIR) spectrometer (SHIMADZU 8400s) was utilized in absorbance mode. The spectra were recorded with a sensitivity of 4  $\text{cm}^{-1}$  and 64 scans per spectrum taken.

The porous nature of the as-synthesized alumina was probed by adsorption-desorption of nitrogen at 77 K with a Microtrac Bel Corp instrument (BEISORP Mini). The dry samples were previously degassed at 300 °C for 5 h, in order to eliminate moisture and any impurities from the material. The chemical analysis of leachates was performed by inductively coupled plasma atomic emission spectroscopy (ICP-AES) using PerkinElmer equipment (USA, Optima 7300D). The thermogravimetric analysis (TGA) of the product was carried out using STA 1500 Rheometric Scientific thermoanalyzer with a heating rate of 10 °C/min in nitrogen atmosphere. The particle size distribution was estimated with the help of a microscopic image processing software, ImageJ as a free and versatile

program package. For more exactness in estimating the size of distinguishable particles, an outline conforming to the TEM image scale bar is drawn. By doing so, the pixel unit is set to nanometer.

### 3. Results and discussion

#### 3.1. Morphological studies

Fig. 1a–d illustrate FESEM micrographs and corresponding EDX analyses of the as-synthesized aluminum hydroxide and alumina samples aged for 1 and 48 h at the last re-precipitating stage. As seen, the morphology of all materials appeared lumpy, consisting of dense agglomerates. In fact, aluminum hydroxide and alumina samples seem to consist of rounded-corner shaped particles. According to Fig. 1a–d, by increasing the aging time, the particle sizes of both aluminum hydroxide and alumina experience an increasing trend, confirming that a prolonged aging time allowed the formation of aluminum hydroxide and alumina samples with larger nanostructures. The results of EDX analyses disclosed a major chemistry of Al and O as the main elements of both  $\text{Al}(\text{OH})_3$  and  $\text{Al}_2\text{O}_3$ . Also, Na was present in accordance with reaction (22).

The bright field TEM images of the as-prepared aluminum hydroxide and alumina samples at different aging times are shown in Fig. 2a–d. With aging time increasing from 1 to 48 h, the particle size becomes larger in both aluminum hydroxide and alumina products. As can be seen from Fig. 2a–c, the aluminum hydroxide and alumina samples display overlapping agglomerates of nanoflakes. For alumina samples, when the aging time increases to 48 h, the morphology changes to enlarged nanoflakes with rounded corners. From inset Fig. 2d, it seems that the alumina nanoparticles obtained at the aging time of 48 h, have spherical morphology, but

Fig. 2d at higher magnification reveals that these nanoparticles are dense overlapped aggregates of round corner-shaped nanoflakes. All TEM images confirm that the obtained products are in the nanoscale. According to the size distribution histograms shown in Fig. 2a–b, both aluminum hydroxide samples exhibit particle size distribution range of 10–50 nm with the difference that about 86% of aluminum hydroxide nanoflakes prepared at aging time of 1 h are smaller than 30 nm, whereas about 80% of aluminum hydroxide nanoflakes prepared at aging time of 48 h are smaller than 30 nm. The size distribution histograms of the alumina samples reveal that ~74% of alumina nanoflakes prepared at aging time of 1 h are smaller than 30 nm, whereas alumina nanoflakes prepared at aging time of 48 h are all larger than 70 nm.

The alumina sample prepared after calcination of 1-h aged aluminum hydroxide was thought to exhibit a large specific surface area (SSA) and total porosity because of its smaller particles, and consequently it is selected for further characterizations including nitrogen sorption, XRD, FTIR, XRF, and TGA analyses.

#### 3.2. Specific surface area and porosity

Fig. 3 illustrates the  $\text{N}_2$  sorption isotherms and respective meso/micropore size distributions of the as-prepared alumina sample after calcination of 1-h aged aluminum hydroxide at  $600^\circ\text{C}$  for 2 h. In accordance with the IUPAC sorption isotherms, the materials exhibiting the typical type IV curve with hysteresis loop of type H2 comprise inter-connected pores. The Type IV isotherm reflects the mesoporosity nature of materials. The hysteresis loop of type H2 indicates capillary condensation phenomenon occurring in mesopores [42]. Also, the emergence of this type of the hysteresis loop reminds ink bottle-shaped pores [43] in the alumina. Fig. 3b reveals

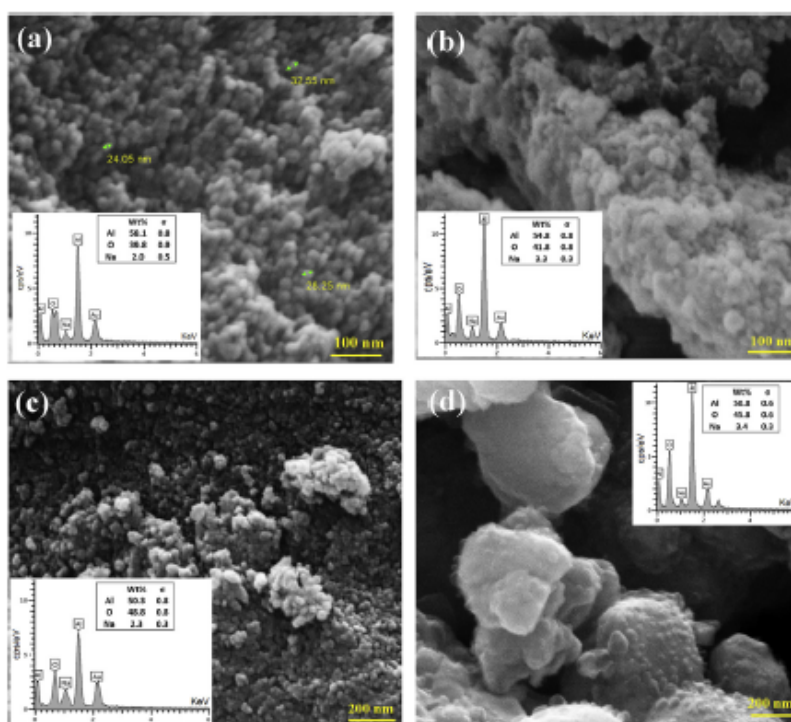
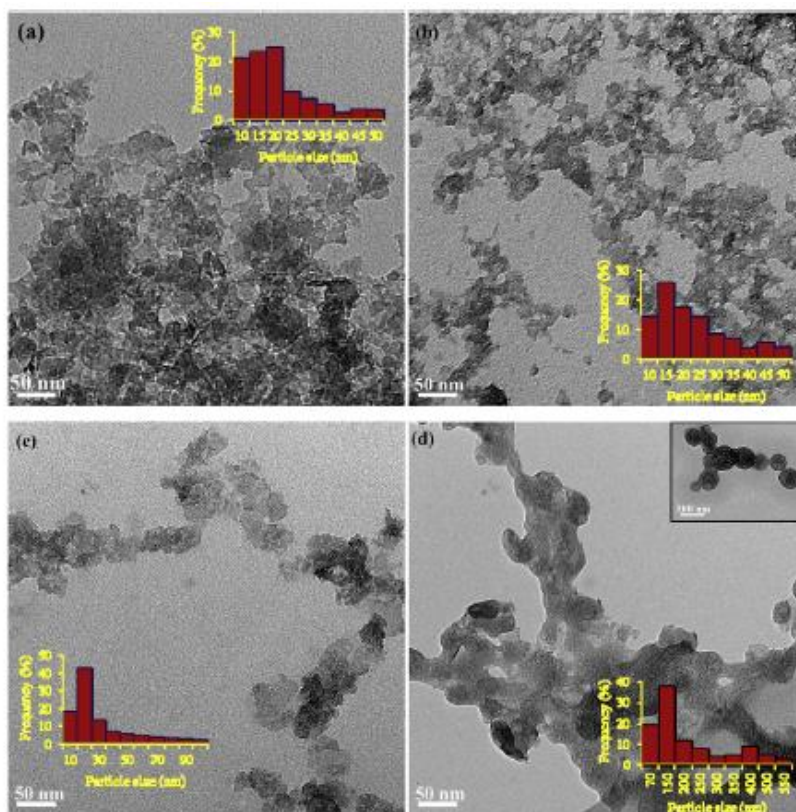


Fig. 1. FESEM images and corresponding EDX analyses of the as-synthesized (a) aluminum hydroxide aged for 1 h, (b) aluminum hydroxide aged for 48 h, (c) alumina obtained after calcination of 1-h aged aluminum hydroxide, and (d) alumina obtained after calcination of 48-h aged aluminum hydroxide.



**Fig. 2.** Typical TEM micrographs and respective particle size distribution of the as-synthesized aluminum hydroxides aged for (a) 1 h, (b) 48 h; and alumina samples prepared after calcination of (c) 1-h aged aluminum hydroxide, and (d) 48-h aged aluminum hydroxide. (Magnification: 35 kX).

a relatively narrow pore size distribution (PSD). To investigate the dependable SSA and PSD, both adsorption and desorption branches of the plot in Fig. 3a were applied in commonly-used methods including BET, BJH (desorption branch), Dollimore-Heal (DH) (desorption branch), Langmuir, t-plot (adsorption branch), MP-plot, and Cranston-Inkley (CI) (desorption branch). The results are presented in Table S1 (refer to online supplementary Table). The data in Table S1 clearly show that the as-prepared alumina exhibits a pore volume of about  $0.37 \text{ cm}^3/\text{g}$ . The average radius of pores is 10.6 nm, confirming the mesoporous nature of the as-prepared alumina. This is confirmed by IUPAC which says a mesopore has a diameter of 2–50 nm. By using MP method (inset Fig. 3b), the averaged diameter of micropores included in the as-prepared alumina is 1.6 nm. Based on the data in Table S1, the as-synthesized alumina in this study has a SSA of  $123\text{--}162 \text{ m}^2/\text{g}$ .

### 3.3. Determination of crystalline phases

The XRD patterns of the as-prepared aluminum hydroxide (aged for 1 h) and the as-synthesized MA are shown in Fig. 4a and b, respectively. As can be observed, aluminum hydroxide has precipitated in the forms of bayerite and gibbsite. The precipitation of gibbsite and a few amount of bayerite at basic pH is expected in accordance with literature [44]. The gibbsite and bayerite have been identified by comparing the peaks with ICDD standard cards of 00-007-0324 and 00-001-0287, respectively. The low crystallinity of the XRD pattern shown in Fig. 4a is attributed to the low aging time (1 h aging). Because there is not enough time to let the

cations and anions arrange in the crystalline network. On the other hand, a short aging time is necessary to reach smaller nanoparticles and higher surface area. Low crystallinity can be compensated by later calcination, as shown in Fig. 4b. When the aluminum hydroxide is calcined at  $600 \text{ }^\circ\text{C}$  for 2 h, the product begins to dehydrate and convert to alumina and the XRD pattern (Fig. 4b) exhibits diffraction peaks corresponding to the reflections of plane of  $\eta$ -alumina (PDF 01-073-6579),  $\gamma$ -alumina (PDF 04-007-2283),  $\delta$ -alumina (PDF 04-008-4096), and  $\theta$ -alumina (PDF 00-035-0121). There were no other distinct peaks, which showed that the resulting aluminum hydroxide and MA products are highly pure.

It is obvious that the XRD patterns in Fig. 4 exhibit the line broadening. A line broadening may be resulted from the contribution of crystallite size (L) and microstrain. The contribution of the former is calculated using Debye-Scherrer equation [45,46]:

$$L = k\lambda/\beta_L \cos\theta \quad (23)$$

where  $k = 0.9$ ,  $\lambda$  the wavelength of incident X-rays ( $1.541874 \text{ \AA}$ ),  $\theta$  is Bragg's angle (in degree), and  $\beta_L$  is the full width at half maximum (FWHM) associated with instrumental broadening.

And the microstrain contribution is calculated by the following equation:

$$\beta_{MS} = 4\epsilon \tan\theta \quad (24)$$

where  $\beta_{MS}$  is the FWHM allocated to the microstrain broadening and  $\epsilon$  reminds the microstrain, which supposed to be identical in all

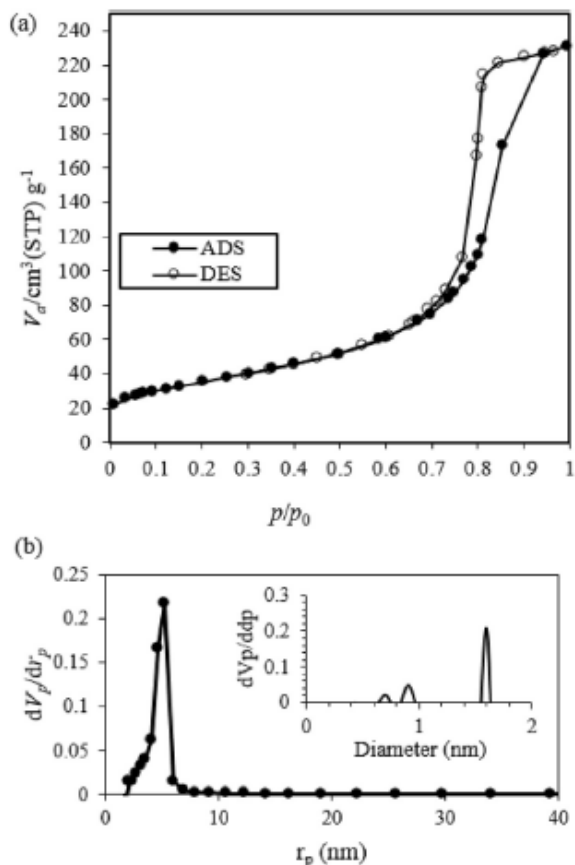


Fig. 3. (a) Adsorption/desorption isotherms of  $N_2$  gas and (b) respective pore size distributions of the as-prepared alumina.

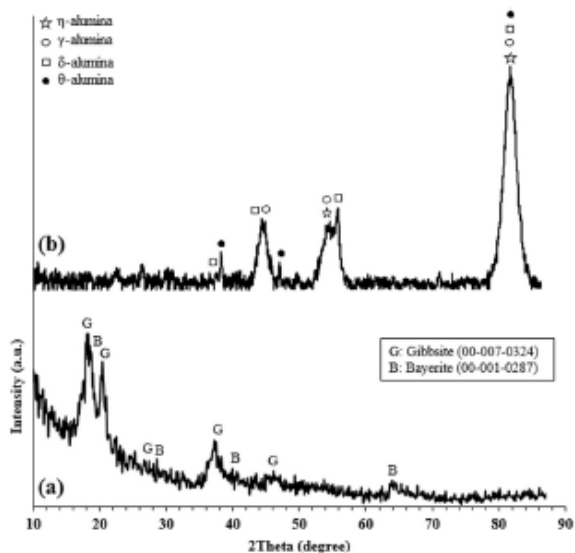


Fig. 4. XRD pattern of the as-fabricated (a) 1-h aged  $Al(OH)_3$  and (b) the as-synthesized mesoporous alumina.

crystallographic orientations.

Supposing the independence of the two main contributions mentioned above for the line broadening, thus the sum of them is [45]:

$$\beta_{hd} = \beta_L + \beta_{MS} \quad (25)$$

By replacing  $\beta_L$  and  $\beta_{MS}$  from equations (23) and (24) in the above summation, followed by a rearrangement, the Williamson-Hall equation is eventually derived [47]:

$$\beta_{hd} \cos \theta = 0.9\lambda/L + 4\epsilon \sin \theta \quad (26)$$

The Y-intercept of the  $\beta_{hd} \cos \theta - 4\epsilon \sin \theta$  plot as presented in Fig. 5 comprises the average crystal size. According to Fig. 5, the average crystal size of about 11.19 nm was obtained from the vertical intercept.

### 3.4. Identification of chemical bonds

Fig. 6 depicts the FTIR spectrum of the as-synthesized MA. The peak at  $596 \text{ cm}^{-1}$  is due to Al–O–Al symmetric bending [48]. The emergence of a weak peak at  $1137 \text{ cm}^{-1}$  is attributed to the existence of cluster of  $O^{2-}$  and  $Al^{3+}$  ions on the of Al–O plane. The peak appeared at  $1656 \text{ cm}^{-1}$  corresponds to the H–O–H bending vibration in the structure of water. The peaks at  $4354$  and  $3754 \text{ cm}^{-1}$  belong to the stretching vibration of hydroxyl group which is most likely due to the adsorption of water molecules by the material [49].

### 3.5. Purity determination

Table 3 presents the results of XRF chemical analysis of the as-prepared MA. It could be observed that the material contains more than 98 wt% of  $Al_2O_3$ . The alumina with more than 90 wt% purity has commercial applications [50]. The impurities present in the material were MgO, CaO,  $Fe_2O_3$ ,  $SiO_2$ , and  $K_2O$  with a total weight percentage of less than 1.3%. Also, a purity of around 98.6% was achieved using Zn-EDTA back titration.

As definitely seen in Table 3, the main impurity is  $SiO_2$ . The presence of  $SiO_2$  confirms the presence of traces of  $Si(OH)_4$  in the aluminum hydroxide precipitate. During calcination and at temperatures about  $200^\circ\text{C}$ , the physisorbed water of  $Si(OH)_4$  species is removed and the remaining silanol groups undergo condensation by releasing water at higher temperatures as shown by the following reaction [51]:

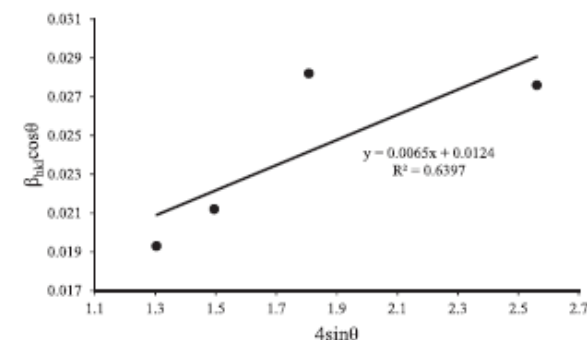


Fig. 5. Williamson-Hall plot for the as-synthesized MA.

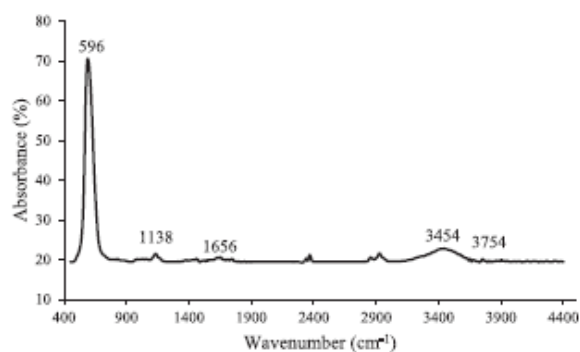


Fig. 6. FTIR spectrum for the as-synthesized mesoporous alumina.

Table 3  
Chemical analysis of the as-prepared mesoporous alumina.

Oxide	Al <sub>2</sub> O <sub>3</sub>	SiO <sub>2</sub>	CaO	Fe <sub>2</sub> O <sub>3</sub>	MgO	K <sub>2</sub> O	SO <sub>3</sub>
wt.%	98.25	0.68	0.28	0.09	0.04	0.06	0.08

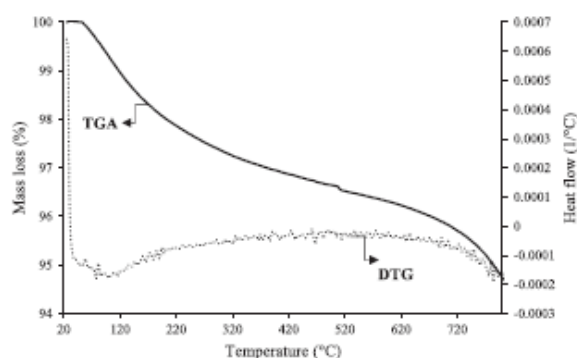


Fig. 7. TGA and DTG profiles of the as-prepared mesoporous alumina.

### 3.6. TGA analysis

Fig. 7 shows the TGA and derivative thermogravimetric analysis (DTG) profiles of the as-synthesized MA.

The material possesses an appropriate thermal stability. The TGA data of the as-fabricated MA presents a total mass loss of around 5.32% over the temperature range of 30–800 °C. The endothermic peak appeared at 40–140 °C in the DTG curve discloses a mass loss due to the dehydration of adsorbed moisture [52]. As can be seen, no mass depletion related to decomposition has been taken place for the MA throughout the studied temperature range, implying that the prepared material is thermally stable.

### 3.7. Characterization of extraction residues

The XRD pattern of solid residue after extraction process is depicted in Fig. 8, showing the peaks of SiO<sub>2</sub>, C, Al<sub>2</sub>O<sub>3</sub>, and NaAl<sub>11</sub>O<sub>17</sub>. The predominant mineral phase is SiO<sub>2</sub> which remains undissolved during acid leaching stage. In comparison with the XRD pattern of the raw ABD, Al and AlN have been removed by the acid leaching of the ABD. The Al and AlN are considered as detrimental components with the potential to result in the generation of harmful gasses including hydrogen and ammonia. The major portion of Al-containing components such as aluminum oxide, spinel, and diaoyudaoite has been leached from the ABD, which is eligible for the extraction of alumina, however, a few amounts of Al<sub>2</sub>O<sub>3</sub> and diaoyudaoite is present as minor phases in the XRD pattern of the solid residue. The XRD phase analysis implies the solid residue of the ABD is less hazardous to the environment when discarded in landfills. In addition, as an alternative, these solid residues may potentially be used in construction applications.

The microstructure of the as-received ABD and the residual solid are shown in Fig. 9. As can be seen, the dense structure of the raw ABD has been destroyed after the leaching reactions. After the reactions, the ABD is split into small particles, forming a loose and porous microstructure.

## 4. Conclusions and future outlook

In this study, a novel eco-friendly procedure was developed for

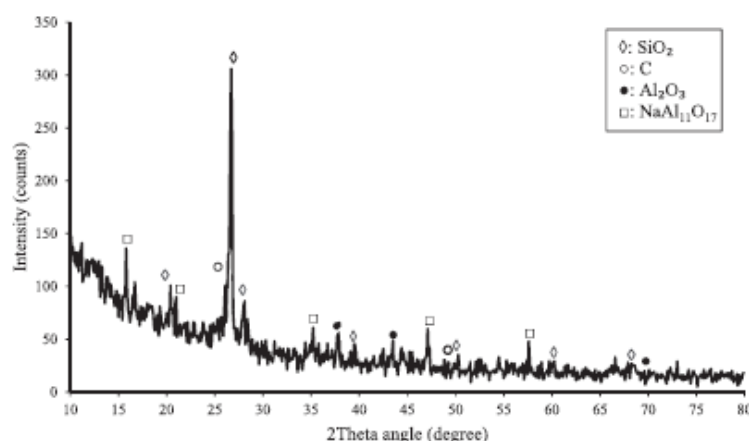


Fig. 8. XRD pattern of solid residue at the end of extraction process.

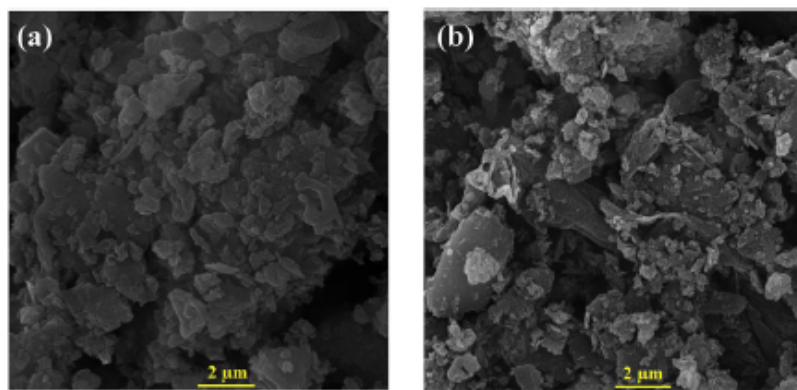


Fig. 9. SEM images of (a) as-received ABD, and (b) add-insoluble residue after leaching.

successful synthesis of mesoporous alumina using aluminum black dross as an alumina-rich waste. The eco-friendliness of a process is determined by the twelve principles of green chemistry. The process developed in this work satisfies the first (prevention), third (less dangerous chemicals), sixth (energy-efficient process), and twelfth (minimized chemical events).

The determination of the chemical composition by XRF and back-titration techniques showed that the aluminum oxide content of the as-synthesized mesoporous alumina was more than 98 wt%. The as-synthesized mesoporous alumina had a specific surface area of 123–162 m<sup>2</sup>/g, a relatively narrow pore size distribution with a peak at a radius of 5.3 nm, and total porosity of 0.37 cm<sup>3</sup>/g. The morphological investigations revealed that the material had a nanometer size, having crystal size of ~11 nm. The as-fabricated material is anticipated to be an excellent candidate as a catalyst, catalyst support, or adsorbent. Overall, the proposed procedure provides a very cost efficient method for mesoporous alumina production. In addition, it leads to a promising solution to the environmental problems of aluminum black dross.

The followings can be considered as the study's future outlooks:

- 1) Investigating the influences of pH, aging time, and aging temperature on the composition and structure of aluminum hydroxide gel. The study of the aforementioned parameters for the preparation of tunable mesoporous alumina can be very important; and 2) the reusability of hydroxide byproducts and insoluble residue as adsorbent and filler/aggregate, respectively.

#### Appendix A. Supplementary data

Supplementary data to this article can be found online at <https://doi.org/10.1016/j.jalcom.2019.04.009>.

#### References

- [1] F. Thomas, E. Schouller, J.Y. Bottero, Adsorption of salicylate and polyacrylate on mesoporous aluminas, *Colloid. Surf. Physicochem. Eng. Asp.* 95 (2–3) (1995) 271–279. [https://doi.org/10.1016/0927-7757\(94\)03022-R](https://doi.org/10.1016/0927-7757(94)03022-R).
- [2] B. Yahyaei, S. Azizian, Rapid adsorption of binary dye pollutants onto the nanostructured mesoporous alumina, *J. Mol. Liq.* 199 (2014) 88–95. <https://doi.org/10.1016/j.molliq.2014.08.023>.
- [3] C. Han, H. Pu, H. Li, L. Deng, S. Huang, S. He, Y. Luo, The optimization of As(V) removal over mesoporous alumina by using response surface methodology and adsorption mechanism, *J. Hazard Mater.* 254–255 (2013) 301–309. <https://doi.org/10.1016/j.jhazmat.2013.04.008>.
- [4] B. Yahyaei, S. Azizian, Rapid adsorption of anionic dyes by ordered nanoporous alumina, *Chem. Eng. J.* 209 (2012) 589–596. <https://doi.org/10.1016/j.cej.2012.08.055>.
- [5] C. Yang, L. Gao, Y. Wang, X. Tian, S. Komarneni, Fluoride removal by ordered and disordered mesoporous aluminas, *Microporous Mesoporous Mater.* 197 (2014) 156–163. <https://doi.org/10.1016/j.micromeso.2014.06.010>.
- [6] R. Chakravarty, R. Ram, R. Mishra, D. Sen, S. Mazumder, M.R.A. Pillai, A. Dash, Mesoporous alumina (MA) based double column approach for development of a clinical scale <sup>99m</sup>Tc generator using (n,γ)<sup>99</sup>Mo: an enticing application of nanomaterial, *Ind. Eng. Chem. Res.* 52 (33) (2013) 11673–11684. <https://doi.org/10.1021/ie401042n>.
- [7] T. Hyodo, T. Hashimoto, T. Ueda, O. Nakagoe, K. Kamada, T. Sasahara, S. Tanabe, Y. Shimizu, Adsorption/combustion-type VOC sensors employing mesoporous γ-alumina co-loaded with noble-metal and oxide, *Sensor. Actuator. B Chem.* 220 (2015) 1091–1104. <https://doi.org/10.1016/j.snb.2015.06.065>.
- [8] J.P. Dacquin, J. Dhainaut, D. Duprez, S. Royer, A.F. Lee, K. Wilson, An efficient route to highly organized, tunable Macroporous–Mesoporous alumina, *J. Am. Chem. Soc.* 131 (36) (2009) 12896–12897. <https://doi.org/10.1021/ja9056486>.
- [9] Q. Wu, F. Zhang, J. Yang, Q. Li, B. Tu, D. Zhao, Synthesis of ordered mesoporous alumina with large pore sizes and hierarchical structure, *Microporous Mesoporous Mater.* 143 (2011) 406–412. <https://doi.org/10.1016/j.micromeso.2011.03.033>.
- [10] C. Otonari, V.F. Rivera, M. Fontana, K. Bejtka, B. Onida, Ultralong and mesoporous ZnO and γ-Al<sub>2</sub>O<sub>3</sub> oriented nanowires obtained by template-assisted hydrothermal approach, *J. Mater. Sci. Technol.* 30 (2014) 1167–1173. <https://doi.org/10.1016/j.jmst.2014.11.005>.
- [11] I. Iatsunskyi, M. Kempinski, M. Jancelewicz, K. Zaleski, S. Jurga, Structural and XPS characterization of ALD Al<sub>2</sub>O<sub>3</sub> coated porous silicon, *Vacuum* 113 (2015) 52–58. <https://doi.org/10.1016/j.vacuum.2014.12.015>.
- [12] Z. Wu, Q. Li, D. Feng, P.A. Webley, D. Zhao, Ordered mesoporous crystalline gamma-Al<sub>2</sub>O<sub>3</sub> with variable architecture and porosity from a single hard template, *J. Am. Chem. Soc.* 132 (34) (2010) 12042–12050. <https://doi.org/10.1021/ja104379a>.
- [13] B. Xu, J. Long, H. Tian, Y. Zhu, X. Sun, Synthesis and characterization of mesoporous γ-alumina template by saccharide molecules, *Catal. Today* 147 (2009) S46–S50. <https://doi.org/10.1016/j.cattod.2009.07.059>.
- [14] B. Huang, C.H. Bartholomew, S.J. Smith, B.F. Woodfield, Facile solvent-deficient synthesis of mesoporous γ-alumina with controlled pore structures, *Microporous Mesoporous Mater.* 165 (2013) 70–78. <https://doi.org/10.1016/j.micromeso.2012.07.052>.
- [15] H.J. Kim, H.C. Lee, D.H. Choo, H.C. Lee, S.H. Chung, J.S. Lee, Synthesis and characterization of mesoporous alumina molecular sieves using cationic surfactants, *Stud. Surf. Catal.* 146 (2003) 213–216. [https://doi.org/10.1016/S0167-2991\(03\)80365-8](https://doi.org/10.1016/S0167-2991(03)80365-8).
- [16] J.C. Ray, K.S. You, J.W. Ahn, W.S. Ahn, Mesoporous alumina (I): comparison of synthesis schemes using anionic, cationic, and non-ionic surfactants, *Microporous Mesoporous Mater.* 100 (1–3) (2007) 183–190. <https://doi.org/10.1016/j.micromeso.2006.10.036>.
- [17] W. Wu, Z. Wan, M. Zhu, D. Zhang, A facile route to aqueous phase synthesis of mesoporous alumina with controllable structural properties, *Microporous Mesoporous Mater.* 223 (2016) 203–212. <https://doi.org/10.1016/j.micromeso.2015.11.004>.
- [18] S.H. Yang, Y.S. Jun, W.H. Hong, J.K. Kang, Facile route to synthesize large-mesoporous γ-alumina by room temperature ionic liquids, *Chem. Mater.* 19 (3) (2007) 535–542. <https://doi.org/10.1021/cm0620887>.
- [19] M. Pavese, S. Biamino, Mesoporous alumina obtained by combustion synthesis without template, *J. Porous Mater.* 16 (2009) 59–64.
- [20] J.H. Kim, K.Y. Jung, K.Y. Park, Characterization of mesoporous alumina particles prepared by spray pyrolysis of Al(NO<sub>3</sub>)<sub>3</sub>·9H<sub>2</sub>O precursor: effect of CTAB and urea, *Microporous Mesoporous Mater.* 128 (2010) 85–90. <https://doi.org/10.1007/s10934-007-9168-5>.
- [21] L. Zhong, Y.F. Zheng, F.F. Chen, Y. Zhang, Synthesis of mesoporous alumina using a recyclable methylcellulose template, *Microporous Mesoporous Mater.*

- 142 (2011) 740–744. <https://doi.org/10.1016/j.micromeso.2010.12.041>.
- [22] K.M.S. Khalil, Formation of mesoporous alumina via hydrolysis of modified aluminum isopropoxide in presence of CTAB cationic surfactant, *Appl. Surf. Sci.* 255 (5) (2008) 2874–2878. <https://doi.org/10.1016/j.apsusc.2008.08.091>.
- [23] X. Shi, C. Yang, L. Zhang, Z. Lu, Y. Zhu, D. Tang, C. Cui, H. Zeng, Mesoporous alumina microfibers in situ transformation from AACH fibers and the adsorption performance, *J. Nanomater.* (2014) 1–6. <https://doi.org/10.1155/2014/381235>.
- [24] Y. Zhou, L. Wu, J. Wang, H. Wang, Y. Dong, Alumina extraction from high-alumina ladle furnace refining slag, *Hydrometallurgy* 140 (2013) 14–19. <https://doi.org/10.1016/j.hydromet.2013.08.007>.
- [25] L. Huiquan, H. Junbo, W. Chenye, B. Weijun, S. Zhenhua, Extraction of alumina from coal fly ash by mixed-alkaline hydrothermal method, *Hydrometallurgy* 147–148 (2014) 183–187. <https://doi.org/10.1016/j.hydromet.2014.05.012>.
- [26] A.A. Abdul Wahab, Z.A. Suhair, A.M. Wasan, Q.A. Malath, K.H. Mohammed, A.J. Falah, Extraction of alumina from Iraqi colored kaolin by lime-sinter process, *Iraqi Bull. Geol. Min.* 10 (3) (2014) 109–117.
- [27] H. Pedersen, Process of manufacturing aluminum hydroxide, US Patent 1,618,105, 15-02-(1927).
- [28] M.S.M. Yusoff, M. Muslim, W. Paulus, A waste to wealth study on converting aluminium dross schedule waste into  $\gamma$  and  $\alpha$  alumina, in: Proceedings of the 7th WSEAS International Conference on ENVIRONMENT, ECOSYSTEMS and DEVELOPMENT (EED '09), Tenerife, Canary Islands, Spain, 2009.
- [29] S.O. Adeosun, O.I. Sekunowo, Q.O. Taiwo, W.A. Ayoola, A. Machado, Physical and mechanical properties of aluminum dross, *Adv. Mater.* 3 (2014) 6–10. <https://doi.org/10.11648/j.am.20140302.11>.
- [30] A. Binnaz, Y. Hazar, M.N. Sarikdede, M. Cigdem, A study on the structural analysis of aluminum drosses and processing of industrial aluminum salty slags, *Scand. J. Metall.* 34 (2005) 213–216. <https://doi.org/10.1111/j.1600-0692.2005.00732>.
- [31] N.W. Liu, M.S. Chou, Reduction of secondary aluminum dross by a waste pickling liquor containing ferrous chloride, *Sustain. Environ. Res.* 23 (2013) 61–67.
- [32] Y. Xiao, M. Reuter, Aluminum recycling and environmental issues of salt slag treatment, *J. Environ. Sci. Health* 40 (2005) 1861–1875. <https://doi.org/10.1080/10934520500183824>.
- [33] B. Dash, B.R. Das, B.C. Tripathy, I.N. Bhattacharya, S.C. Das, Acid dissolution of alumina from waste aluminium dross, *Hydrometallurgy* 92 (2008) 48–53. <https://doi.org/10.1016/j.hydromet.2008.01.006>.
- [34] P.T. Anastas, J.C. Warner, *Green Chemistry: Theory and Practice*, Oxford University Press, New York, 1998.
- [35] M. Mahinroosta, A. Allahverdi, Enhanced alumina recovery from secondary aluminum dross for high purity nanostructured  $\gamma$ -alumina powder production: kinetic study, *J. Environ. Manag.* 212 (2018) 278–291. <https://doi.org/10.1016/j.jenvman.2018.02.009>.
- [36] M. Mahinroosta, A. Allahverdi, A promising green process for synthesis of high purity activated-alumina nanopowder from secondary aluminum dross, *J. Clean. Prod.* 179 (2018) 93–102. <https://doi.org/10.1016/j.jclepro.2018.01.079>.
- [37] A.L.T. Pham, D.L. Sedlak, F.M. Doyle, Dissolution of mesoporous silica supports in aqueous solutions: implications for mesoporous silica-based water treatment processes, *Appl. Catal. B Environ.* 126 (2012) 258–264. <https://doi.org/10.1016/j.apcatb.2012.07.018>.
- [38] Y.A. Lainer, I.G. Gorichev, S.A. Todorov, Aluminum hydroxide nucleation kinetics and mechanism during the electroanalysis decomposition of aluminate solutions, *Russ. Metall. (Metally)* 4 (2008) 301–305. <https://doi.org/10.1134/S0036029508040058>.
- [39] H. Ederfeld, J.D. Hem, The development of crystalline structure in aluminium hydroxide polymorphs on ageing, *Mineral. Mag.* 39 (1973) 89–96.
- [40] C.J. Serna, J.L. White, S.L. Hem, Factors affecting homogeneous precipitation of aluminum hydroxide gel, *J. Pharm. Sci.* 67 (8) (1978) 1179–1181. <https://doi.org/10.1002/jps.2600670845>.
- [41] J.A.A. Júnior, J.B. Baldo, The behavior of zeta potential of silica suspensions, *New J. Glass Ceram.* 4 (2014) 29–37. <https://doi.org/10.4236/njgc.2014.42004>.
- [42] J. Čejka, N. Žilková, J. Rathouskja, A. Zula, Nitrogen adsorption study of organised mesoporous alumina, *Phys. Chem. Chem. Phys.* 3 (2001) 5076–5081. <https://doi.org/10.1039/B105603B>.
- [43] K.S.W. Sing, Reporting physisorption data for gas/solid systems, *Pure Appl. Chem.* 54 (11) (1982) 2201–2218. <https://doi.org/10.1351/pac198254112201>.
- [44] J.O.A. Yvan, R.S.K. Maria, Synthesis of high-surface area  $\gamma$ - $\text{Al}_2\text{O}_3$  from aluminum scrap and its use for the adsorption of metals: Pb(II), Cd(II), and Zn(II), *Appl. Surf. Sci.* 258 (2012) 10002–10011. <https://doi.org/10.1016/j.apsusc.2012.06.063>.
- [45] A.R. Stokes, A.J.C. Wilson, The diffraction of X rays by distorted crystal aggregates - I, *Proc. Phys. Soc.* 56 (1944) 174–181. <https://doi.org/10.1088/0959-5309/56/3/303>.
- [46] A. Khorsand Zak, W.H.A. Majid, M. Ebrahimzadeh Abrishami, R. Yousefi, R. Parvizi, Synthesis, magnetic properties and X-ray analysis of  $\text{Zn}_{0.9}\text{X}_{0.09}\text{O}$  nanoparticles (X = Mn, Ni, and Co) using Scherrer and size-strain plot methods, *Solid State Sci.* 14 (2012) 488–494. <https://doi.org/10.1016/j.solidstatesci.2012.01.019>.
- [47] G.K. Williamson, W.H. Hall, Discussion of the theories of line broadening, *Acta Metall.* 1 (1953) 22. [https://doi.org/10.1016/0001-6160\(53\)90006-6](https://doi.org/10.1016/0001-6160(53)90006-6).
- [48] S. Blonski, S.H. Garofalini, Molecular dynamics simulations of  $\gamma$ -alumina surface stabilization by deposited silicon ions, *Chem. Phys. Lett.* 211 (1993) 575–579. [https://doi.org/10.1016/0009-2614\(93\)80146-G](https://doi.org/10.1016/0009-2614(93)80146-G).
- [49] J.S. Lee, H.S. Kim, N.K. Park, T.J. Lee, M. Kang, Low temperature synthesis of  $\gamma$ -alumina from aluminum hydroxide hydrothermally synthesized using  $[\text{Al}(\text{C}_2\text{O}_4)_2(\text{OH})_2]^-$  complexes, *Chem. Eng. J.* 230 (2013) 351–360. <https://doi.org/10.1016/j.cej.2013.06.099>.
- [50] N. Salahudeen, A.S. Ahmed, A.H. Al-Muhtaseb, M. Dauda, S.M. Waziri, B.Y. Jibril, J. Al-Sabahi, Synthesis, characterization and adsorption study of nanosized activated alumina synthesized from kaolin using novel method, *Powder Technol.* 280 (2015) 266–272. <https://doi.org/10.1016/j.powtec.2015.04.024>.
- [51] A. Lazaro, H.J.H. Brouwers, G. Quercia, J.W. Geus, The properties of amorphous nano-silica synthesized by the dissolution of olivine, *Chem. Eng. J.* 211–212 (2012) 112–121. <https://doi.org/10.1016/j.cej.2012.09.042>.
- [52] X. Liu, R.E. Truitt, DRIFT-IR studies of the surface of  $\gamma$ -alumina, *J. Am. Chem. Soc.* 119 (41) (1997) 9856–9860. <https://doi.org/10.1021/ja971214k>.

## Resistance of red clay brick waste/phosphorus slag-based geopolymer mortar to acid solutions of mild concentration

Mostafa Vafaei<sup>1</sup>, Ali Allahverdi<sup>1,2</sup>, Peng Dong<sup>3</sup>, Nabil Bassim<sup>3</sup>, Mostafa Mahinroosta<sup>1</sup>

<sup>1</sup>Research Laboratory of Inorganic Chemical Process Technologies,  
School of Chemical Engineering, Iran University of Science and Technology,  
Narmak 1684613114, Tehran, Iran

<sup>2</sup>Cement Research Center,  
Iran University of Science and Technology, Narmak 1684613114, Tehran, Iran

<sup>3</sup>Department of Materials Science and Engineering, McMaster University,  
Hamilton, Ontario, Canada, L8S 3Z9

### Abstract

This work is devoted to the investigation of the resistance of geopolymer cement (GC) mortar based on mixture of red clay brick waste (RCBW) and phosphorus slag (PHS) in exposure to HCl and H<sub>2</sub>SO<sub>4</sub> solutions of mild concentration. For this purpose, the GC mortar specimens were exposed to pH=3 of each acid solution for 24 months. To prepare GC mortar, blend of RCBW and PHS was activated by water glass and NaOH and then hydrothermally

---

<sup>1</sup>Corresponding author details:  
Tel.: (0098) 21 7724-0475  
Fax: (0098) 21 7724-0397  
E-mail address: [ali.allahverdi@iust.ac.ir](mailto:ali.allahverdi@iust.ac.ir)

cured. For comparison purpose, reference specimens were also prepared using high alumina and Portland cements. The durability of mortar specimens was evaluated by measuring the changes in compressive strength and mass as key parameters at predetermined time intervals. The structural and compositional changes of the reaction products were studied using appropriate characterization techniques. The obtained results disclosed that GC mortar exhibited an excellent acid resistance compared to reference mortars exhibiting significantly lower durability properties. The exposure to  $H_2SO_4$  caused more deterioration in all specimens than the exposure to HCl owing to the adverse effect of gypsum formation, which results in the expansion and cracking of the paste matrix.

**Keywords:** Geopolymer, Phosphorus slag, Acid resistance, Clay brick waste

## 1. Introduction

Durability is one of the most critical features for the construction of concrete structures. An appropriate durability feature preserves the natural resources and lessens the accumulation of waste, thereby it helps to protect the environment. The service life of concrete structures may be menaced by exposure to aggressive media. One of such important threats for concrete is acid attack [1]. During exposure of a concrete structure to an acidic environment, calcium cations are leached from the calcium-containing constituents (such as calcium silicate hydrate and Portlandite) into the acidic environment. This leads to the deposition of calcium salts within the concrete matrix and increase the total porosity, resulting in a dramatic drop in the durability performance and mechanical strength [2].

Acid attack on concrete occurs with different rate and mechanisms that depends on many factors, including the composition of concrete materials, temperature, pH and type of the acid medium, water-to-binder ratio, etc. [3, 4]. Therefore, a comprehensive study on the effect of acidic attack conditions on changes in the physico-mechanical properties and microstructure of the cementitious materials is of a crucial importance. In the past decades, due to their high

early mechanical strength, superior durability, and environmental friendliness, geopolymer cements (GCs) seriously compete with Portland cement (PC) [4].

For the production of geopolymers, aluminosilicate materials (such as natural aluminosilicate minerals and metakaolin) are alkali-activated at ambient temperature or at elevated temperatures to form a semi-crystalline or amorphous structure [4]. Recently, on account of environmental and economic advantages, the utilization of aluminosilicate waste materials such as fly ash in GCs production has attracted great interest [6].

Kwasny et al. [7] reported that GCs prepared from lithomarge (low-grade kaolin) showed better durability performance in  $H_2SO_4$  and HCl solution than PC. Okoye et al. [8] concluded that the resistance of fly ash-based GC incorporating silica fume against 2%  $H_2SO_4$  solution was considerably higher than that of PC. Jin et al. [9] prepared metakaolin/tannery sludge-based GCs and investigated their durability performance in various aggressive environments. The results showed that the GCs containing 20% tannery sludge exhibited high acid resistant against pH=1, 3, 5 of  $H_2SO_4$  solution. Allahverdi et al. [10-13] investigated the durability performance of different cement binders including PC, high alumina cement, gypsum-free PC/slag binder, and fly ash-based GC, in exposure to different pHs of  $H_2SO_4$  and  $HNO_3$  solutions. The results disclosed that GC exhibited a better resistance against these acid solutions than other cement binders.

In the previous study, the acid resistance of GC mortar based on blend of red clay brick waste (RCBW) and phosphorus slag (PHS) against HCl (pH=1) and  $H_2SO_4$  (pH=1) solutions was comprehensively studied [14].

Since the prepared GC may exhibit different durability characteristics due to exposure to different acidic environments, acid resistance studies at moderate acidic concentration conditions are necessary. Acid attack on concrete structures in industrial environments happens mostly due to leakage and random spillage varying from a steady prolonged drip to a gradual

and brief dousing. Such acid attack may also occur in concrete structures subjected to moderate pH (3.0-5.0) ground waters [15] and acidic depositions with a low pH value [16]. The present study is devoted to investigating the resistance of RCBW/PHS-based GC after immersion in pH=3 of H<sub>2</sub>SO<sub>4</sub> and HCl solutions. The acid resistance of the GC mortars was examined by investigating the changes in physico-mechanical and visual properties. Also, chemical, mineralogical and structural changes were studied by employing appropriate characterization techniques.

## 2. Experimentation

### 2.1. Materials

To prepare RCBW powder, the red clay bricks was first crushed and ground and then sieved to the appropriate particle size of  $\leq 70 \mu\text{m}$ . The PHS was procured from a domestic phosphoric acid production plant in Tehran. High alumina cement (HAC) (Secar 80, Kerneos, France) and Type II Portland cement (PC) were also used to prepare the control mortar specimens. The physico-chemical properties of starting materials are presented in Table 1. DIN-EN 196-1 standard sand was consumed as the fine aggregate in preparing mortar specimens. The chemical activator was prepared from pellet sodium hydroxide (NaOH, 98%) and water glass (Na<sub>2</sub>SiO<sub>3</sub>·nH<sub>2</sub>O, 8.5 wt.% Na<sub>2</sub>O, 28.5 wt.% SiO<sub>2</sub>, 63 wt.% H<sub>2</sub>O) (Merck KGaA, Darmstadt, Germany). To prepare the targeted acid solutions with pH value of  $3 \pm 0.05$ , concentrated HCl and H<sub>2</sub>SO<sub>4</sub> were diluted with distilled water

Table 1. Physico-chemical properties of materials

Chemical composition (wt.%)*				
Oxide	RCBW	PHS	PC	HAC
SiO <sub>2</sub>	51.10	38.42	21.90	0.40
Al <sub>2</sub> O <sub>3</sub>	16.25	7.65	4.62	80.50
Fe <sub>2</sub> O <sub>3</sub>	6.45	0.90	3.40	0.20

CaO	9.90	45.14	64.50	17.50
MgO	5.60	2.60	1.52	0.50
SO <sub>3</sub>	3.35	Trace	1.15	0.10
K <sub>2</sub> O+ Na <sub>2</sub> O	5.05	0.99	0.25	0.70
P <sub>2</sub> O <sub>5</sub>	-	1.50	-	-
<b>Physical properties</b>				
Specific gravity (g/cm <sup>3</sup> )	2.22	3.25	3.15	3.25
Blaine specific surface area (m <sup>2</sup> /kg)	380	315	320	1000

\* Wet chemical analysis in accordance with ASTM C114-04

## 2.2. Preparation of Specimens

The GC mortars were prepared based on the formulation which was optimized in the previous study [17]. The decision criteria on the optimization was the compressive strength. According to the optimum formulation, the GC mortar was prepared by blending RCBW (76 wt. %) and PHS (24 wt.%) [17]. The reason for the incorporation of the PHS is that plain RCBW is not very reactive precursor and gives relatively low compressive strengths [18]. A mixture of NaOH/water glass with silica modulus adjusted at 1.5 was then used to activate the prepared GC mortars. The amount of alkali-activator was controlled to adjust the Na<sub>2</sub>O concentration of the material at 12% by mass of dry binder. To prepare fresh GC mortar, the dry binder was first prepared by dry mixing the standard quartz sand and RCBW/PHS mixture for about 4 min. Then, the prepared dry binder was mixed with the pre-prepared alkali activator solution under 3-min agitation condition. A constant water-to-binder value of 0.50 was considered for the preparation of GC fresh mortar. Molding the fresh mortar was carried out using 5 cm cubic steel molds. The molds were then kept in a humid chamber with RH $\geq$ 95% at 23.0 $\pm$ 2.0 °C for 24 h. Thereafter, the cubic GC mortar specimens were de-molded and exposed to hydrothermal curing at 95 °C for 20 h. For comparison purpose, a series of 5 cm cubic HAC and PC control mortar specimens were subjected to 28-day standard water curing. To prepare

control mortars, water-to-binder ratios were obtained 0.550 and 0.485 for HAC and PC mortars, respectively based on ASTM standards C109 [19] and C1437 [20]. A sand-to-binder ratio of 2.75 was considered for the preparation of all mortar specimens based on ASTM C109 [19].

### **2.3. Acid Resistance Tests**

Acid resistance experiments were performed based on the instruction described in ASTM C267 standard [21]. The as-prepared mortar specimens were subjected to pH=3 of aqueous HCl and H<sub>2</sub>SO<sub>4</sub> for exposure times of up to 24 months. The temperature of the acidic solutions was room temperature. The acid volume-to-surface area ratio of specimens was maintained close to 10 cm<sup>3</sup>/cm<sup>2</sup>. The periodical addition of concentrated acid to each batch performed to keep the pH level at 3 with a standard deviation of 5%. After the predesigned time frames were elapsed, the specimens were removed from the exposure test containers. Immediately the surface of the specimens was smoothed with a plastic brush and then cleaned with a dry towel. The acid resistance evaluation was performed by measuring pre- and post-exposure values of compressive strength and mass of the immersed specimens.

### **2.4. Characterization and Measurement Techniques**

The compressive strength value of the cube specimens was measured employing a 300 kN digital hydraulic compression testing machine with  $\pm 1\%$  accuracy and a loading rate of 0.5 MPa/s, based on ASTM C109 standard. Three measurements were performed for each mortar specimens and the average (standard deviation  $\leq 4\%$ ) of the obtained values were recorded as the final result.

To study the microstructure of the pre- and post-subjected mortar samples, TESCAN VEGA II scanning electron microscope (Czech Republic) was employed at accelerating voltage of 30 kV. For the purpose of microscopy investigations, a number of 24-month subjected GC mortar cubes were smashed into pieces. Then, suitable fractured pieces containing both intact and deteriorated areas were selected. Prior to imaging with microscope, extremely gold layer was

sputtered on the selected pieces at 70 °C for 24 h. The elemental analyses were determined using energy dispersive X-ray spectroscopy (EDS) using Oxford Instrument probe (England). The EDS results were obtained under beam energy of 12 keV.

The mineralogical phase changes in intact and post-exposed samples were investigated by a Philips (PW 1800) X-ray diffractometer at  $2\theta^\circ$  of 5-80° (Cu K $\alpha$  radiation, step size=0.02°, time per step= 0.5 s). The chemical bonding of the intact and post-exposed samples was determined by Fourier transform infrared (FTIR) spectroscopy using PerkinElmer FTIR spectrophotometer. The FTIR data were recorded over the wavenumber range of 400 to 4000  $\text{cm}^{-1}$  (scan resolution=4  $\text{cm}^{-1}$ ). To prepare FTIR spectroscopy samples, the broken mortar pieces were first ground and then sieved to particle size less than 45  $\mu\text{m}$ , and then mixed with pellet KBr. For 0.5 mg sample, 250 mg pellet KBr was used.

### **3. Results and Discussion**

#### **3.1. Appearance Changes**

Photographing intact and acid-exposed specimens was performed to visualize the appearance changes caused by acid attack. Fig. 1 depicts the photos of intact and 24-month acid-exposed mortar specimens of HAC, GC, and OPC.

As clearly seen, both HAC and PC reference mortar specimens experienced a noticeable apparent degradation after immersing in HCl and H<sub>2</sub>SO<sub>4</sub>. The exposure to H<sub>2</sub>SO<sub>4</sub> solution resulted in the greatest damage. However, under the same conditions, the HAC mortar specimens experienced more remarkable appearance changes than OPC. Visual observations confirmed superior resistance of the GC mortar as compared to the reference ones. The HCl-submerged GC specimens did not exhibit any apparent degradation and had a sound appearance; only minor damage on the edges and corners happened. However, more intense surface damage and deterioration occurred in the H<sub>2</sub>SO<sub>4</sub>-submerged GC specimens. Such a

different behavior of HCl-subjected and H<sub>2</sub>SO<sub>4</sub>-subjected specimens is attributed to the induction of volumetric expansions and surface spalling due to deposition of gypsum crystals.

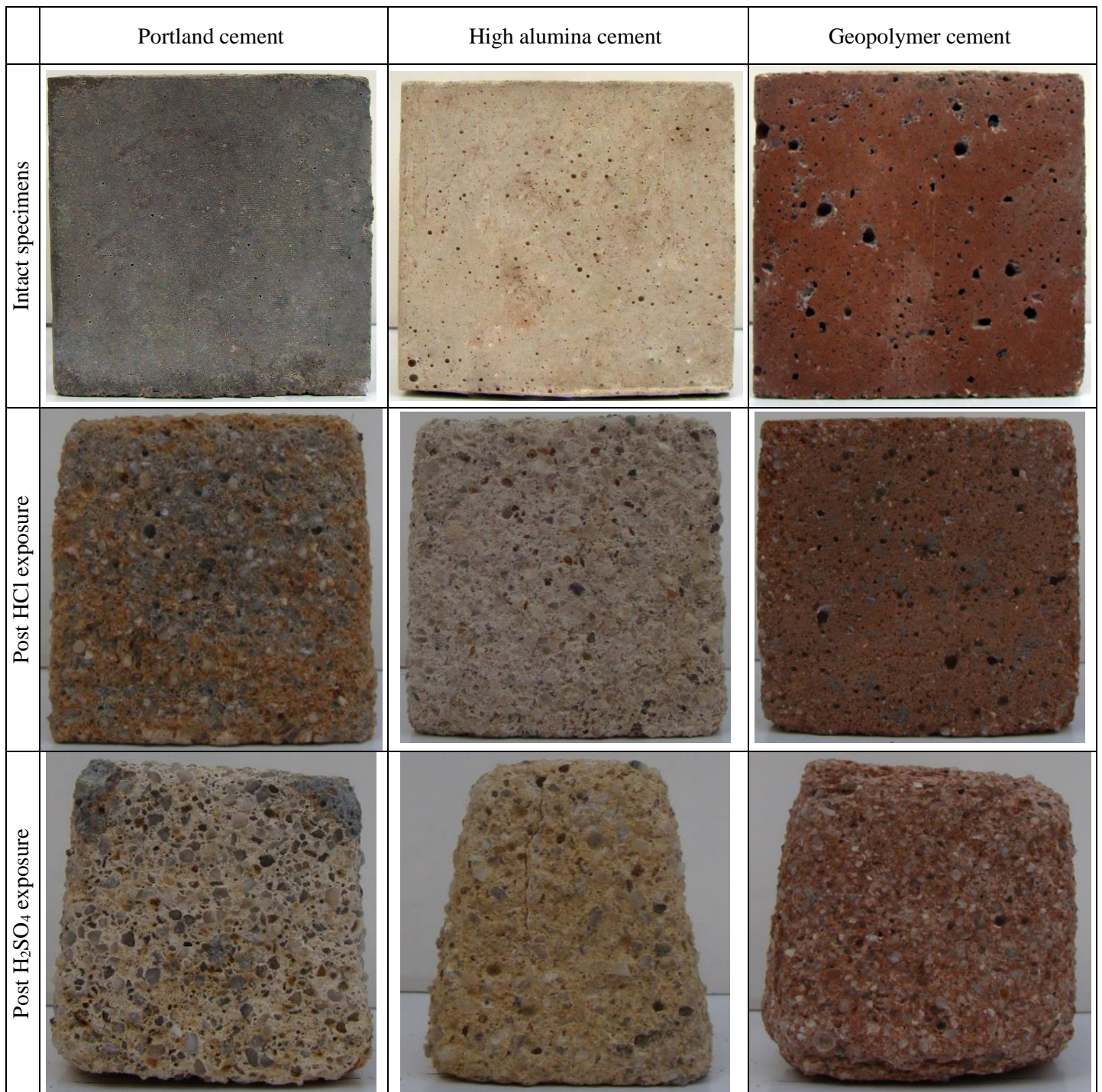


Fig. 1. Appearance of different mortar cubes before and after exposure to pH=3 HCl and H<sub>2</sub>SO<sub>4</sub> for 24 months (Permission has been adopted for the photos of post HCl- and H<sub>2</sub>SO<sub>4</sub>-exposed specimens of Portland and high alumina cements from Elsevier)

### 3.2. Variation of Mass

Fig. 2 depicts the mass changes of mortar specimens as a function of the acid exposure time. The 24-month HCl exposed specimens of OPC, HAC and GC experienced a mass change of about 16%, 16.4% and 4.5%, respectively while the sulfuric acid-exposed specimens experienced a mass change of about 56.6%, 70.4% and 43.4%, respectively. As can be clearly seen in Fig. 2, control mortar specimens exhibited mass losses significantly higher than those of GC mortar. Such a dramatic difference is related to the relative stability of the GC aluminosilicate structure against acid environment and also to high calcium contents of OPC and HAC systems [22]. The hydration products formed in the cement matrix are decomposed due to the reaction of calcium with acidic anions, resulting in an increase in total porosity and an accelerated acid attack [23]. If the acidic anion is sulfate, it results in the formation gypsum and consequently the induction of internal disintegrating stresses and surface spalling. Therefore, the H<sub>2</sub>SO<sub>4</sub>-exposed mortar specimens experienced the higher rate of mass change in comparison with the HCl-exposed ones [24]. This indicates that besides the type of salt deposited during the acid attack, the type of oxide composition (Al<sub>2</sub>O<sub>3</sub>, SiO<sub>2</sub>, CaO) of the starting materials also influences the acid resistance of the mortar specimens.

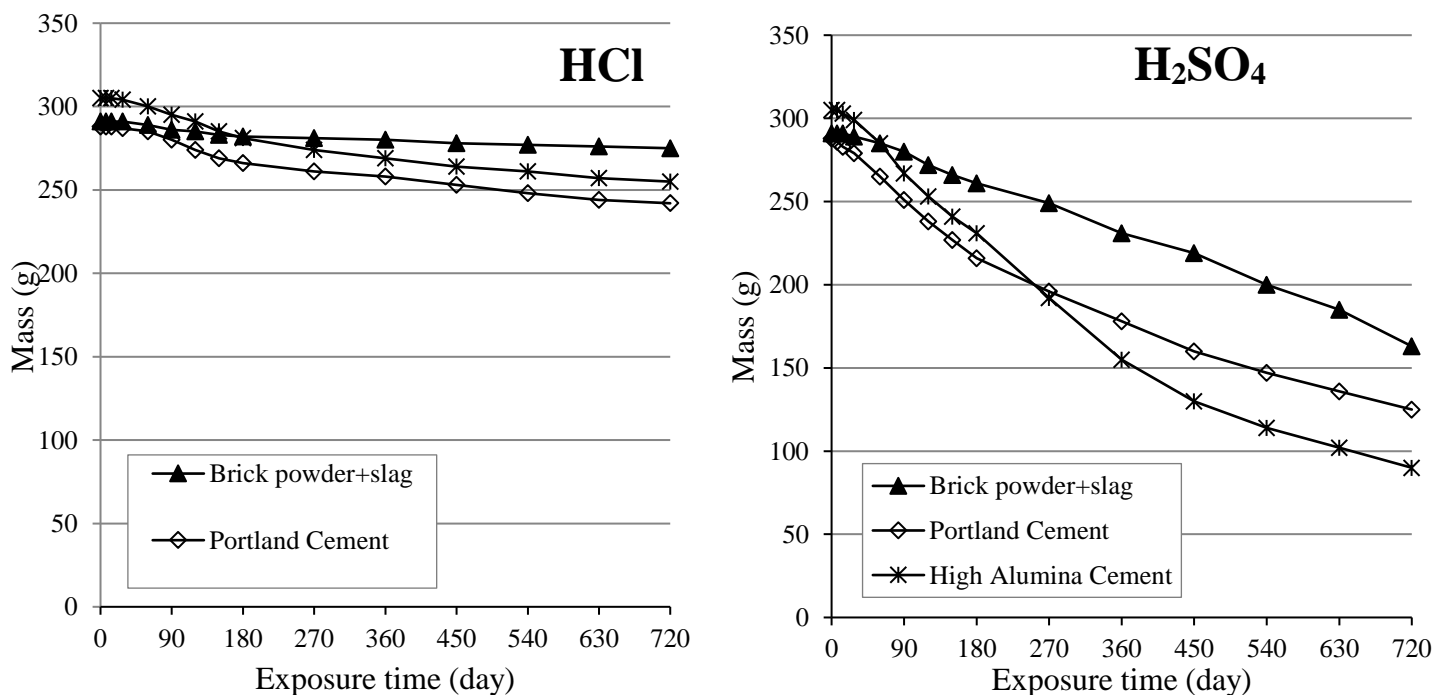


Fig. 2. Mass changes of different mortar exposed to pH=3 HCl and H<sub>2</sub>SO<sub>4</sub> for 24 months

### 3.3. Compressive Strength Loss

Fig. 3 displays changes in compressive strength of different mortar specimens over the 24-month acid exposure test. As seen, GC mortar exposed to pH=3 HCl showed minimal strength loss, whereas HAC control mortar exposed to pH=3 H<sub>2</sub>SO<sub>4</sub> experienced maximal strength loss. All mortar exposed to pH=3 H<sub>2</sub>SO<sub>4</sub> underwent comparatively much higher degrees of deterioration compared to those exposed to pH=3 HCl confirming the more deteriorative nature of pH=3 H<sub>2</sub>SO<sub>4</sub> acid. At the end of exposure time, GC mortar with 2.6% and 83.1% strength losses in HCl and H<sub>2</sub>SO<sub>4</sub>, displayed the best durability performance, whereas HAC and OPC control mortars underwent strength losses of 20.5% and 68.2% in HCl and complete deteriorated after only 540 and 450 days in H<sub>2</sub>SO<sub>4</sub>, respectively. These observations for strength loss that are mostly in coincidence with mass change trends depicted in Fig. 2, confirm a comparatively excellent durability performance for GC mortar in mild concentration acid media. This superior durability performance in acid media for GC mortar compared to HAC and OPC control mortars is related to the relatively higher chemical stability of geopolymer aluminosilicate molecular structure compared to calcium-based hydration products of HAC and OPC [24].

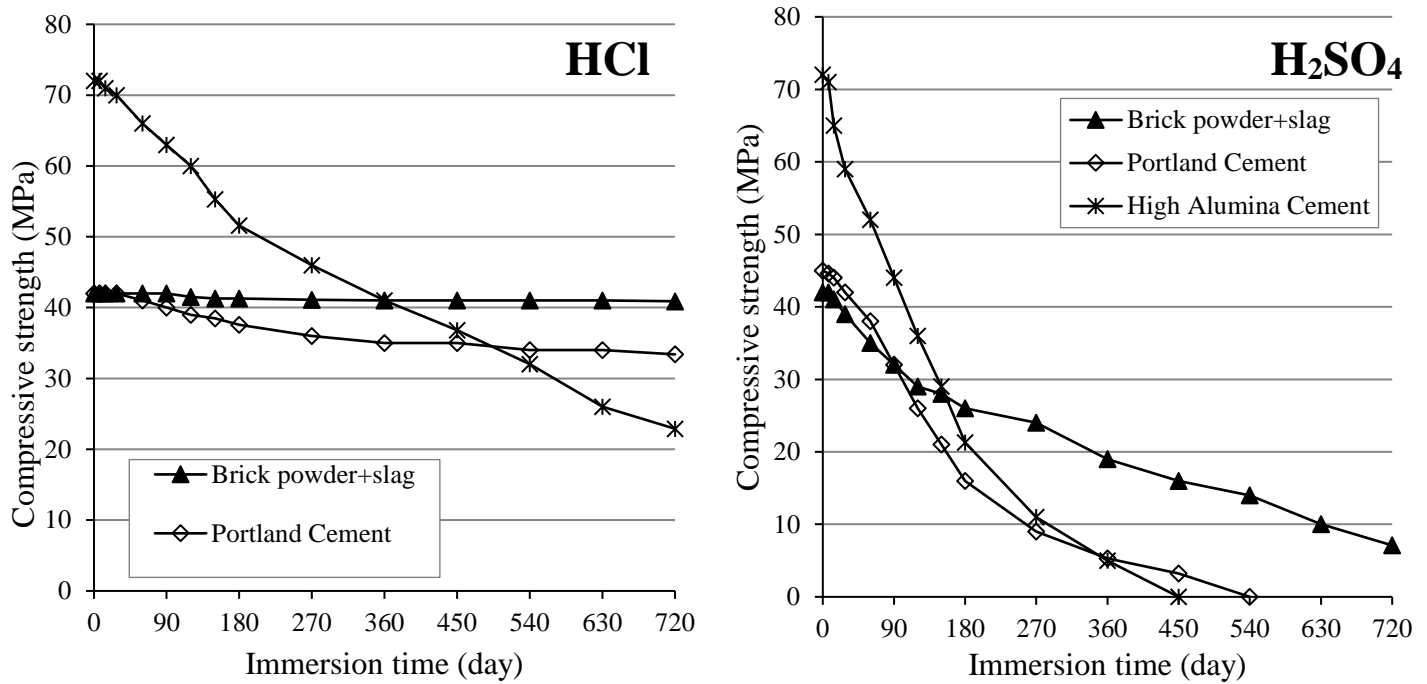


Fig. 3. Compressive strength changes of different mortars exposed to pH=3 HCl and H<sub>2</sub>SO<sub>4</sub> for 24 months

The mass and compressive losses observed for HAC mortar in HCl are not in agreement with each other. As can be seen in Fig. 2 and Fig. 3, HAC shows a limited amount of mass loss at the end of the exposure time, whereas it also displays a relatively high compressive strength loss of about 68% at the same time. Quantitative evaluation of durability performance of mortars in acid media is difficult since it is based on not very accurate measurements. Mass loss values depends not only on the brush type (steel or plastic) used, but also greatly on the amount of force applied for brushing. Compressive strength measurement also is not very accurate since irregular shape of deteriorated mortar specimens result in significant errors. However, results of strength loss measurements are often regarded more reliable than results of mass loss measurements. The exceptionally low resistance of HAC mortar to pH=3 of both HCl and H<sub>2</sub>SO<sub>4</sub> solutions is not only due to instability of its hydration products in acid media, but also due to the high w/c ratio applied in HAC mortar. According to EN 196-6, Secar 80 is produced with a relatively high Blaine specific area [25], which needs a relatively high w/c ratio. The higher the w/c ratio, the higher the penetrability of the mortar.

### 3.4. Complementary Studies on Deteriorated Geopolymer Mortars

For complementary studies on GC deterioration in acid media, samples from GC mortars deteriorated in pH=3 HCl and pH=3 H<sub>2</sub>SO<sub>4</sub> were prepared and analyzed with XRD, FTIR spectroscopy, and SEM/EDS to investigate changes in the structure and chemical composition of the acid exposed samples.

### 3.4.1. X-ray Diffraction

X-ray diffractograms of intact GC mortar (A) and GC mortars exposed to pH=3 H<sub>2</sub>SO<sub>4</sub> (B) and pH=3 HCl for 24 months are displayed in Fig. 4. As seen, the diffractogram of intact GC mortar (A) shows quartz peaks (PDF#00-046-1045) originating from standard sand as well as a small broad hump between 20 to 30 degrees confirming the amorphous nature of the GC hydration products. The diffractogram of GC mortar exposed to H<sub>2</sub>SO<sub>4</sub>, however, confirms the presence of significant amount of gypsum (PDF#00-033-0311) in addition to quartz. Formation and deposition of gypsum crystals in the structure of the H<sub>2</sub>SO<sub>4</sub>-exposed GC is a result of the reaction between calcium-containing compounds of GC and sulfate ions of acid and is also reported by other researchers [26-28]. The amount of gypsum formation and deposition is important since it can strongly affect the mechanism and the kinetics of the deterioration. Very limited amount of gypsum formation and deposition can result in some protective effect, whereas significant amount of which accelerates the deterioration rate through expansion cracking [29, 30]. As seen, the diffractogram of pH=3 HCl exposed GC mortar shows the existence of a few quantity of calcite as another crystalline compound in addition to quartz, confirming the amorphous nature of the degradation products of GC mortar due to pH=3 HCl attack. Calcite is not a direct product of HCl attack, but a secondary product due to gradual carbonation by atmospheric carbon dioxide. In fact, the calcium oxide as a degradation product of calcium-containing compounds undergoes gradual carbonation under the influence of dissolved atmospheric carbon dioxide.

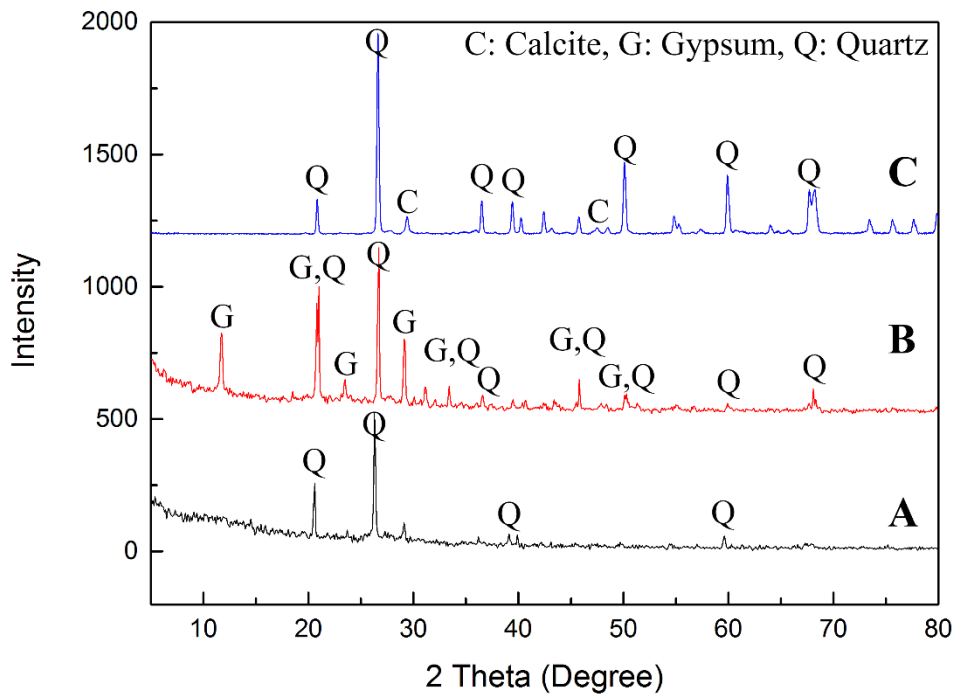


Fig. 4. X-ray diffractograms of intact geopolymer mortar (A) and geopolymer mortars after 24 months of exposure to pH=3 H<sub>2</sub>SO<sub>4</sub> (B) and pH=3 HCl (C)

### 3.4.2. Identification of Chemical Bonds

Studying the nature of chemical bonds by FTIR spectroscopy allows better realizing the chemical changes in the structure of the intact and acid-exposed GC mortars. The FTIR spectra of the intact and acid-exposed GC mortars are shown in Fig. 5. Table 2 presents the recognized absorption bands and their corresponding assignments. As can be seen from the spectra in Fig. 5, the exposure to sulfuric and hydrochloric acid solutions caused the Si-O-X (X= Si or Al) asymmetric stretching to shift from 1028 cm<sup>-1</sup> toward higher absorption wavenumbers of 1120 and 1084 cm<sup>-1</sup>, respectively. This is because weaker Al-O bonds in the aluminosilicate framework were replaced with Si-O bonds during the acid exposure [31, 32]. This shifting was more noticeable for H<sub>2</sub>SO<sub>4</sub>-subjected specimens than that of HCl-exposed ones. In other words, H<sub>2</sub>SO<sub>4</sub> attack resulted in more dealumination in GC mortar specimens. As can be seen in the FTIR spectrum of intact GC mortar (spectrum (1) in Fig. 5), the absorption band at 1422 cm<sup>-1</sup>

corresponds to the stretching vibration of O-C-O bond. The appearance of this band was due to the formation of carbonate compounds during the geopolymerization. However, this band disappeared in acid-exposed specimens (spectra (2) and (3) in Fig. 5), which was due to the dissolution of the carbonate compounds upon the course of acid attack [32]. Moreover, the shift of O-H stretching band from 3435  $\text{cm}^{-1}$  to 3404-3546  $\text{cm}^{-1}$  and also the displacement of H-O-H band from 1652  $\text{cm}^{-1}$  to 1622-1688  $\text{cm}^{-1}$  were due to formation of gypsum crystals in the matrix of sulfuric acid-exposed mortar specimens [28].

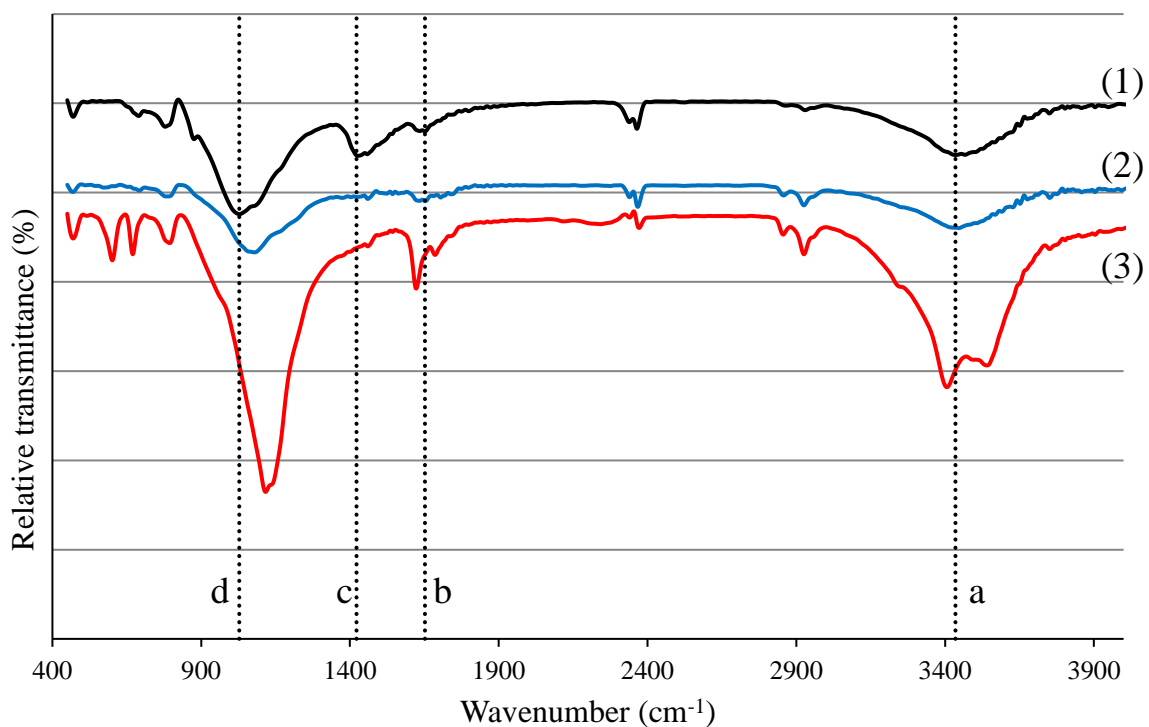


Fig. 5. Absorption bands appeared in the FTIR spectra of the geopolymer mortars: (1) intact geopolymer mortar; (2) 24-month HCl (pH=3) exposed geopolymer mortar; (3) 24-month H<sub>2</sub>SO<sub>4</sub> (pH=3) exposed geopolymer mortar

**Table 2.** Chemical bonds recognized in geopolymer mortars based on FTIR spectroscopy data (see Fig. 5)

Sample No. and type	a	b	c	d
(1) Intact GC sample	3435	1652	1422	1028

(2) HCl-exposed GC sample	3436	1636	-	1084
(3) H <sub>2</sub> SO <sub>4</sub> -exposed GC sample	3404-3546	1622-1688	-	1120
Chemical bonds	Stretching vibration of O-H	Bending vibration of H-O-H	Stretching vibration of O-C-O	Stretching vibration of Si-O-X (X=Al or Si)
Refs.	[28, 33]	[28, 33]	[32]	[32, 34, 35]

### 3.4.3. Microstructural Investigation

The changes in the microstructure of GC mortars exposed to acid attack were studied using SEM/EDS. SEM images displayed in Fig. 6 represent the general appearance of the intact GC mortar (image A) and those exposed to pH=3 HCl acid (image B) and pH=3 H<sub>2</sub>SO<sub>4</sub> acid (images C&D). As seen in Fig. 6(a), a relatively homogeneous and dense microstructure was observed in the intact GC mortar matrix with no clear grain boundary. A few small microcracks were also detected. These microcracks could be drying shrinkage crack formed either during high temperature curing and/or drying SEM samples. Impact stresses applied when breaking mortar cubes for separating SEM samples can also result in some cracking [36]. As can be seen in images B and C, the relatively dense microstructure of intact GC mortar changed to a highly microcracked microstructure upon acid exposure confirming the breakdown of geopolymer network due to acid attack causing [37, 38]. Imaging GC mortar exposed to pH=3 H<sub>2</sub>SO<sub>4</sub> at a relatively higher magnification enabled us to detect fine gypsum (CaSO<sub>4</sub>·H<sub>2</sub>O) crystals deposited inside the GC matrix (image D) confirming the same results achieved by XRD and FTIR spectroscopy.

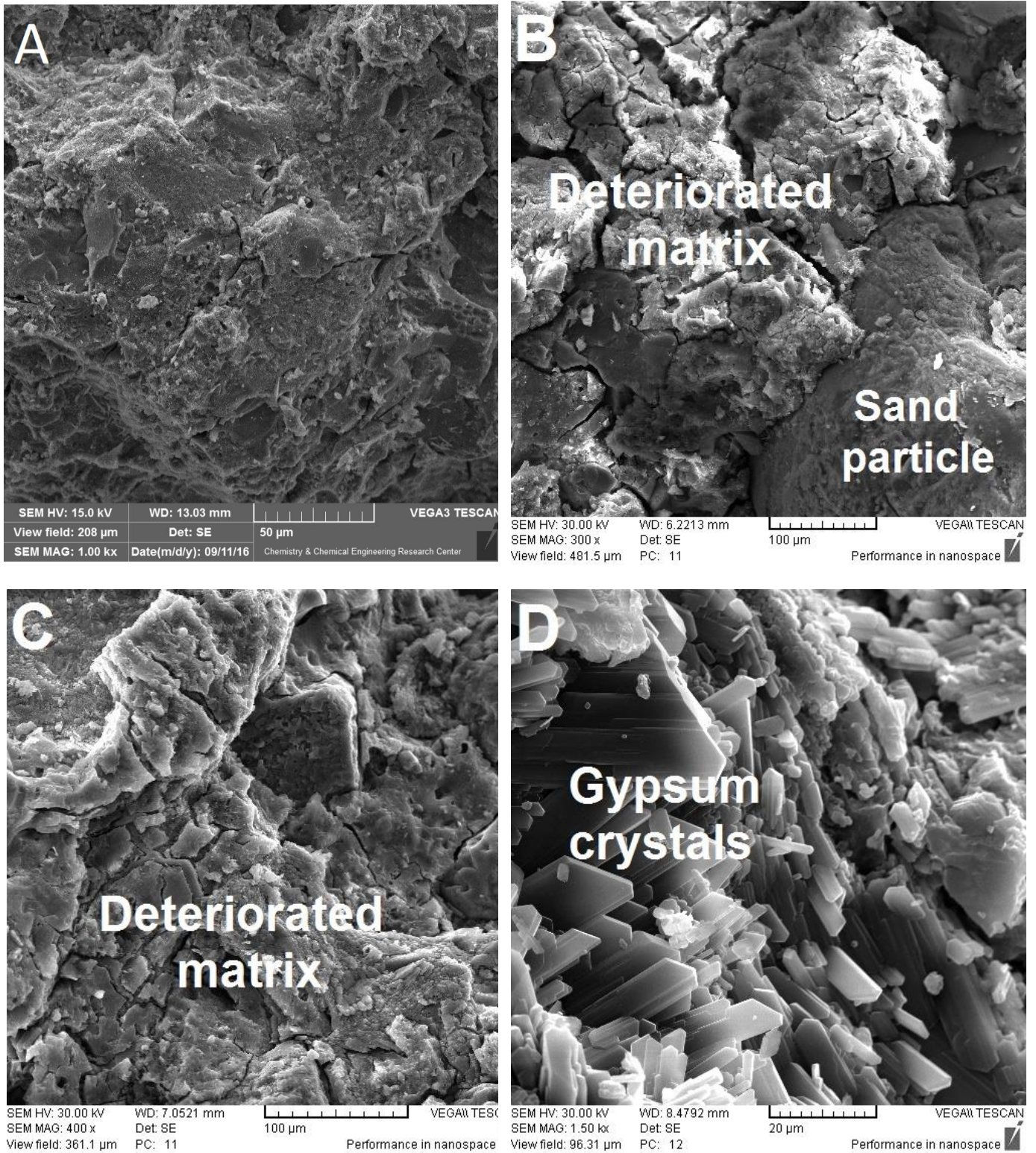


Fig. 6. SEM images representing the general appearance of the microstructure of: (A) intact GC mortar, (B) pH=3 HCl exposed GC mortar, (C) pH=3 H<sub>2</sub>SO<sub>4</sub> exposed GC, (D) gypsum crystals deposited in pH=3 H<sub>2</sub>SO<sub>4</sub> exposed GC mortar

The microstructure and chemical composition of the deteriorated surface layer of 24-month HCl (pH=3) exposed GC mortar was studied using SEM+EDS. A typical SEM image from polished fracture surface of this area with three EDS profiles of elemental analyses for Si, Ca, Al, Na, and Cl performed on deteriorated paste are displayed in Fig.7. For comparison purposes, the same information was obtained from intact GC mortar. Fig. 8 shows a typical SEM image from GC intact area with three EDS profiles of elemental analyses for Si, Ca, Al, Na, and Cl performed on intact hardened GC paste. The oxygen-free elemental composition obtained from EDS analyses on the selected deteriorated and intact areas (see Fig. 7 & Fig. 8) are represented in Table 3. The intact GC paste matrix exhibited a relatively dense and uniform microstructure with few fine microcracks due to shrinkage either during geopolymerization reactions or drying [39, 40] (see Fig. 8). Attack by pH=3 HCl, however, converted this relatively dense and uniform matrix into a highly porous and microcracked one that still exhibits some binding properties enabling it to retain its basic structure (see Fig. 7). A comparison of the oxygen-free elemental compositions of intact and deteriorated GC pastes (see Table 3) clearly confirms remarkable changes upon pH=3 HCl attack.

pH=3 HCl attack resulted in severe leaching of Ca (by about 92%), significant leaching of Na (by almost 62%), partial leaching of Al (by about 9%) from GC paste of the deteriorated surface layer compared to the intact GC paste. Knowing that leaching of these elements is due to the degradation of hydration products containing these elements, it can be claimed that almost all Ca-containing hydration products in GC paste are highly vulnerable to pH=3 HCl attack. The most common Ca-containing hydration products present in GCs and alkali-activated cements are C-A-S-H and C-S-H, which are easily decomposed in acid media [41]. The incomplete leaching of Na from the acid exposed surface layer of GC is a sign of the presence of Na in the GC matrix not only in the form of charge balancing cation in geopolymer molecular structure, but also in a different chemically more stable form. The total Na content

of GC has two different main sources including alkali activator and RCBW powder. The Na in the alkali activator hydrates into  $\text{Na}(\text{H}_2\text{O})_n^+$  cation and makes a weak bonding to tetrahedral Al to charge balance it in the geopolymer molecular structure, based on charge-balancing models given for alkali cations in geopolymer molecular structure [42]. This type of alkali detaches from the geopolymer molecular structure and leaches away easily even when exposed to hydronium ion in distilled water [42]. The leaching of this type of alkali when exposed to acid media is expected to be much faster compared to distilled water.

Another Na in GC with a different type of chemical bonding originates from RCBW. The relatively larger RCBW particles react partially in the GC and the residue of nonreacted RCBW remained in the GC matrix includes some Na that is believed to strongly bound to the brick molecular structure through covalent bonding. This type of Na exhibits a much higher chemical stability in acid media and is leached away only in strong acid solutions. The partial leaching of Al from the GC matrix is in agreement with the partial aluminum removal from the geopolymer matrix confirmed in the results of FTIR spectroscopy (see Fig. 5 and Table 2). Therefore, almost complete leaching of Ca together with partial leaching of Na and Al from GC matrix during the 24-month course of pH=3 HCl attack, leaves behind a silica enriched matrix (see Table 3) which is highly micro-cracked due to leaching shrinkage (see Fig. 7).

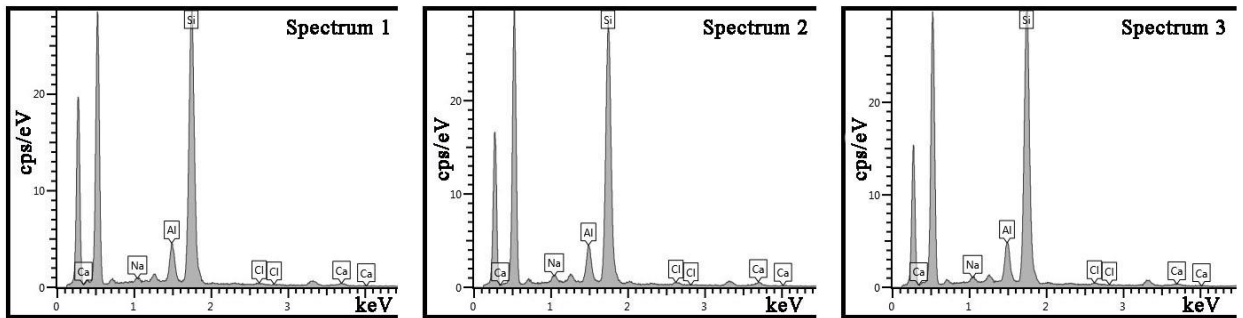
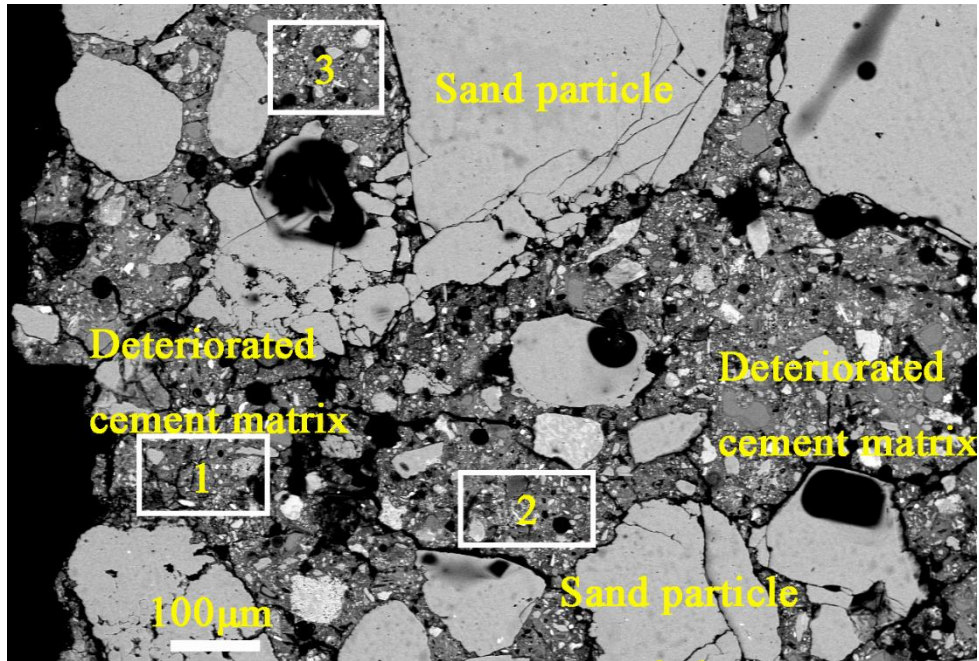
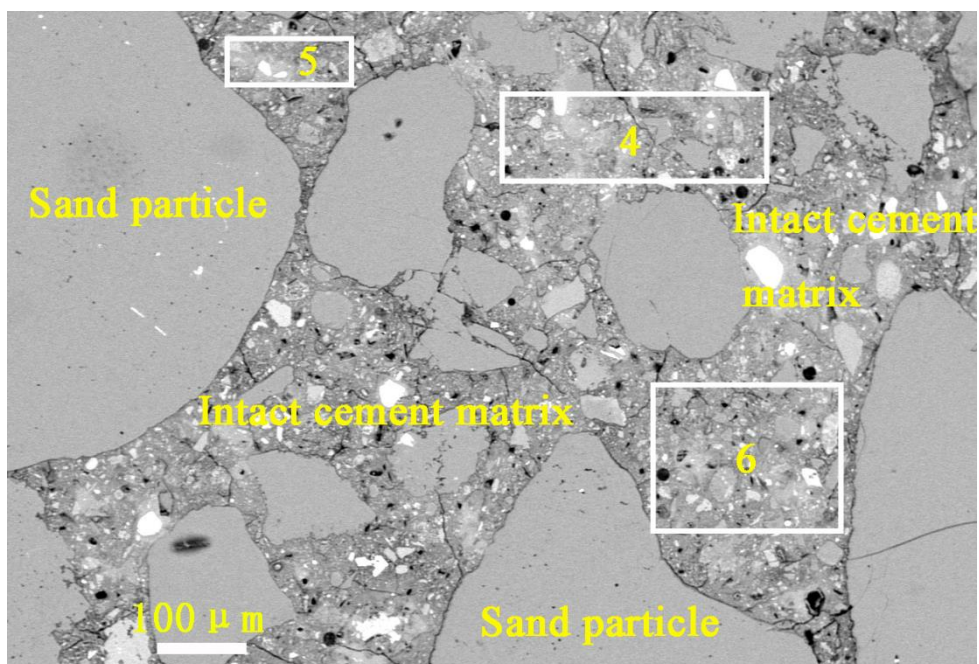


Fig. 7. SEM images from deteriorated surface layer of 24-month HCl (pH=3) exposed GC mortar with the corresponding EDS elemental profiles (the acid exposed surface is on the left side)



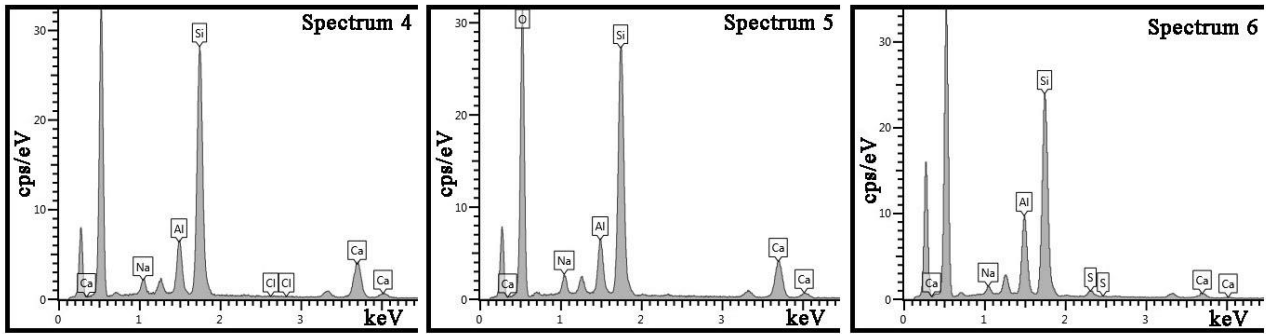


Fig. 8. SEM micrographs from intact GC mortar with the corresponding EDS elemental profiles

Table 3 Oxygen-free EDS elemental analysis (wt.%) of the boxes specified in SEM images displayed in Figs. 7 and 8

	Si	Ca	Al	Na	Cl
Spectrum 1 in Fig. 7	86.6	2.0	9.6	1.0	0.8
Spectrum 2 in Fig. 7	84.1	3.1	9.5	1.7	1.6
Spectrum 3 in Fig. 7	86.2	1.5	10.0	1.3	1.0
Deteriorated matrix (Average)	85.6	2.2	9.7	1.3	1.1
Spectrum 4 in Fig. 8	59.4	26.7	10.8	3.0	0.1
Spectrum 5 in Fig. 8	58.3	27.2	10.5	3.7	0.2
Spectrum 6 in Fig. 8	59.3	26.6	10.4	3.5	0.2
Intact matrix (Average)	59.0	26.8	10.6	3.4	0.2

Fig. 9 represents a typical SEM image from the deteriorated surface layer of GC mortar exposed to pH=3 H<sub>2</sub>SO<sub>4</sub> for 24 months and the corresponding EDS elemental profiles obtained from the boxes. The sulfuric acid attack changed the relatively dense and uniform microstructure of the GC matrix (as observed in Fig. 8) into a highly porous microstructure with a high number of microcracks partially filled with a precipitate that is brighter in color. The oxygen-free EDS compositions of the GC matrix and the precipitate inside the microcracks are collected in Table 4. As seen, the EDS elemental compositions obtained from the precipitate inside the microcracks is mainly composed of Ca and S (about 97% on oxygen-free basis)

confirming the formation and precipitation of gypsum inside the deteriorated GC matrix, as previously observed in XRD results (see Fig. 4).

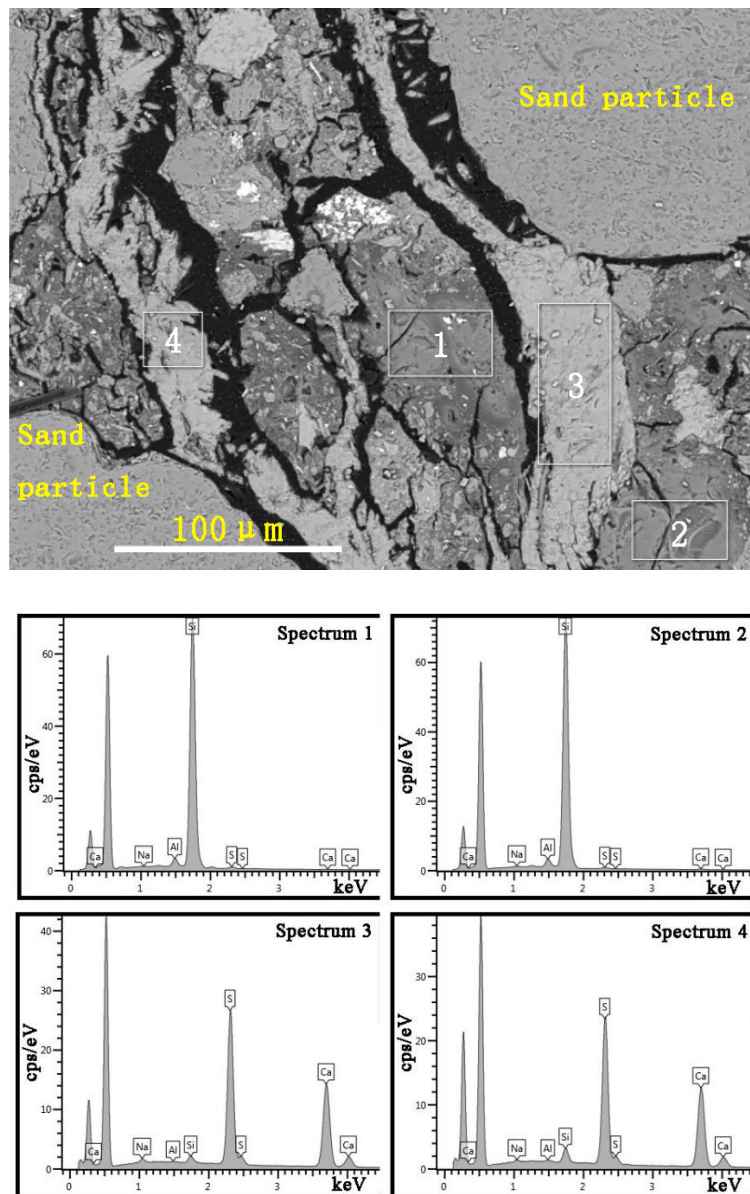


Fig. 9. SEM images from deteriorated surface layer of 24-month  $\text{H}_2\text{SO}_4$  (pH=3) exposed GC mortar with the corresponding EDS elemental profiles

A comparison of the oxygen-free compositions of the matrix deteriorated in pH=3  $\text{H}_2\text{SO}_4$  (Table 4, spectra 1 and 2) and the intact matrix (Table 3, spectra 4, 5, and 6) shows that Ca, Na, and Al were leached away into the acid solution by about 97%, 94%, and 77%, respectively. Such an extensive leaching of the main elements of the matrix accelerates the sulfate ions penetration into the matrix through the shrinkage pores and microcracks. Part of

the penetrating sulfate ions react with countercurrent diffusing Ca ions inside the microcracks bringing about the precipitation of gypsum crystals inside microcracks (Fig. 9, boxes and spectra 3 & 4) and the other part penetrate and react with Ca inside the matrix resulting in the precipitation of fine gypsum crystals (Fig. 9, boxes and spectra 1 & 2). It is believed that gypsum crystals precipitation and growth inside the matrix and the microcrack induce significant internal disintegrating stresses that lead to expansion, cracking and finally spalling of the deteriorated surface layers [43, 44]. The mechanism of deterioration of GC matrix due to pH=3 H<sub>2</sub>SO<sub>4</sub> attack, therefore, starts with leaching of alkali and alkali earth metals together with breakdown and dealumination of geopolymer molecular structure followed by expansion and spalling of surface layers caused by internal stresses induced by gypsum crystals growth. The results of this research work confirmed that attack by H<sub>2</sub>SO<sub>4</sub> is more aggressive than attack by HCl at the same pH value of 3. This can be attributed to role of gypsum resulting in expansion and spalling of deteriorated surface layers and in this way accelerating the total rate of deterioration.

Table 4 Oxygen-free EDS elemental compositions (mass%) of the boxes shown in in SEM micrograph displayed in Fig. 10

	Si	Ca	Al	Na	S
Spectrum 1	95.7	0.4	2.4	0.1	1.3
Spectrum 2	95.6	0.9	2.3	0.2	1.0
Deteriorated matrix (Average)	95.7	0.7	2.4	0.2	1.2
Spectrum 3	1.3	54.1	0.1	0.8	43.7
Spectrum 4	3.0	53.0	0.3	0.5	43.2
Gypsum deposit (Average)	2.2	53.6	0.2	0.7	43.5

#### 4. Conclusions

This study investigated the acid resistance of red clay brick waste/phosphorus slag-blended geopolymer cement mortar. The acid resistance experiments were performed by immersing the mortar specimens in hydrochloric and sulfuric acid solutions (pH=3). The acid immersion time was set up to 24 months. High alumina cement (Secar 80) and type II Portland cement mortars were used as reference. The geopolymer mortar experienced minimal loss of physical and mechanical properties upon prolonged acid solutions exposure. This excellent durability performance of geopolymer cement was found to be due to its relatively low calcium content and its high acid resistant aluminosilicate structure. Based on the results, pH=3 acid attack led to noticeable leaching of calcium and sodium content of geopolymer cement paste into the acid solution confirming the weak chemical bond of calcium and sodium cation in the paste matrix. The minor sodium content of the material resisting acid attack and exhibiting a strong bonding type originates from the non-reacted brick particles existed in the matrix.

By comparing the degradation results of the hydrochloric and sulfuric acid attack, it was found that sulfuric acid causes greater and faster degradation. It was due to the deposition of gypsum crystals in the geopolymer matrix which induced internal disintegrating stresses and consequently the formation of microcracking and surface spalling.

## **References**

1. Page, C.L. and M.M. Page, Durability of concrete and cement composites. 2007: Elsevier.
2. Scrivener, K. and J.F. Young, Mechanisms of chemical degradation of cement-based systems. 1997: CRC Press.
3. Zivica, V.r. and A. Bajza, Acidic attack of cement-based materials—a review Part 2. Factors of rate of acidic attack and protective measures. *Construction and Building Materials*, 2002. 16(4): p. 215-222.
4. Zivica, V.r. and A. Bajza, Acidic attack of cement-based materials—a review.: Part 1. Principle of acidic attack. *Construction and Building Materials*, 2001. 15(8): p. 331-340.

5. Davidovits, J., *Geopolymer Chemistry and Applications*. 2008: Geopolymer Institute.
6. Provis, J.L. and J.S.J. Van Deventer, *Geopolymers: structures, processing, properties and industrial applications*. 2009: Elsevier.
7. Jacek Kwasny, Timothy A. Aiken, Marios N. Soutsos, John A. McIntosh, David J. Cleland. Sulfate and acid resistance of lithomarge-based geopolymer mortars, *Construction and Building Materials*, Volume 166, 30 March 2018, Pages 537-553.
8. Francis N. Okoye, Satya Prakash, Nakshatra B. Singh, Durability of fly ash based geopolymer concrete in the presence of silica fume. *Journal of Cleaner Production*, Volume 149, 15 April 2017, Pages 1062-1067.
9. Mantong Jin, Fan Lian, Ruiqi Xia, Zhuohui Wang. Formulation and durability of a geopolymer based on metakaolin/tannery sludge. *Waste Management*, Volume 79, September 2018, Pages 717-728.
10. ALLAHVERDI, A. and F. SKVARA, Nitric acid attack on hardened paste of geopolymeric cements. Part 1. *Ceramics*, 2001. 45(3): p. 81-88.
11. ALLAHVERDI, A. and F. SKVARA, Nitric acid attack on hardened paste of geopolymeric cements. Part 2. *Ceramics*, 2001. 45(4): p. 143-149.
12. Allahverdi, A. and F. Skvara, Sulfuric acid attack on hardened paste of geopolymer cements-Part 1. Mechanism of corrosion at relatively high concentrations. *CERAMICS SILIKATY*, 2005. 49(4): p. 225.
13. Allahverdi, A. and F. Skvara, Sulfuric acid attack on hardened paste of geopolymer cements-part 2. Corrosion mechanism at mild and relatively low concentrations. *CERAMICS SILIKATY*, 2006. 50(1): p. 1.
14. Vafaei, M. and A. Allahverdi, Durability of Geopolymer Mortar Based on Waste-Glass Powder and Calcium Aluminate Cement in Acid Solutions. *Journal of Materials in Civil Engineering*, 2017. 29(10): p. 04017196.

15. E.P.M.J. Fest, E.J.M. Temminghoff, J. Griffioen, B. Van Der Grift, W.H. Van Riemsdijk, "Groundwater chemistry of Al under Dutch sandy soils: effects of land use and depth", *Appl. Geochem.*, 22, 1427-1438, 2007.
16. National Trends Network Annual Maps, NADP Program Office, Illinois State Water Survey, Champaign, IL (2014), <http://nadp.sws.uiuc.edu/ntn/maps.aspx> (accessed 17.08.16.).
17. Mostafa Vafaei, Ali Allahverdi. Strength development and acid resistance of geopolymer based on waste clay brick powder and phosphorous slag. *Structural Concrete*. 2019;1–11.
18. A. Allahverdi, E.N. Kani. Use of construction and demolition waste (CDW) for alkali- activated or geopolymer cements. *Handbook of recycled concrete and demolition waste*, Woodhead Publishing Series in Civil and Structural Engineering, 2013. 439-475
19. ASTM, C., 109/C 109M-02. Standard test method for compressive strength of hydraulic cement mortars (using 2-in. or [50-mm] cube specimens), 2002.
20. ASTM, C., 1437. Standard Test Method for Flow of Hydraulic Cement Mortar, 2001.
21. ASTM, C., 267. Standard test methods for chemical resistance of mortars, grouts, and monolithic surfacings and polymer concretes. American Society of Testing Materials, 2001.
22. Djobo, J.N.Y., et al., Mechanical properties and durability of volcanic ash based geopolymer mortars. *Construction and Building Materials*, 2016. 124: p. 606-614.
23. Duan, P., et al., An investigation of the microstructure and durability of a fluidized bed fly ash–metakaolin geopolymer after heat and acid exposure. *Materials & Design*, 2015. 74: p. 125-137.
24. Sata, V., A. Sathonsaowaphak, and P. Chindaprasirt, Resistance of lignite bottom ash geopolymer mortar to sulfate and sulfuric acid attack. *Cement and Concrete Composites*, 2012. 34(5): p. 700-708.
25. <http://www.kerneosinc.com/secar80.php>
26. Thokchom, S., Fly Ash Geopolymer Pastes in Sulphuric Acid. 2014.
27. Song, X., et al. Durability of fly ash based geopolymer concrete against sulphuric acid attack. in *Proceedings of the international conference on durability of building materials and components*, Lyon, France. 2005.
28. Ariffin, M., et al., Sulfuric acid resistance of blended ash geopolymer concrete. *Construction and Building Materials*, 2013. 43: p. 80-86.

- 29 A. Allahverdi and F. Skvara, "Sulfuric acid attack on hardened paste of geopolymer cements: Part 1. Mechanism of corrosion at relatively high concentrations", *Ceramics-Silikaty*, 49(4), 225- 229, 2005.
- 30 A. Allahverdi and F. Skvara, "Sulfuric acid attack on hardened paste of geopolymer cements: Part 2. Corrosion mechanism at mild and relatively low concentrations", *Ceramics-Silikaty*, 50(1), 1-4, 2006.
31. Baščarević, Z., et al., Effects of the concentrated  $\text{NH}_4\text{NO}_3$  solution on mechanical properties and structure of the fly ash based geopolymers. *Construction and Building Materials*, 2013. 41: p. 570-579.
32. Ahmari, S. and L. Zhang, Durability and leaching behavior of mine tailings-based geopolymer bricks. *Construction and Building Materials*, 2013. 44: p. 743-750.
33. Chukanov, N.V. and A.D. Chervonnyi, *Infrared Spectroscopy of Minerals and Related Compounds*. 2016: Springer International Publishing.
34. Zhang, M., et al., Durability of red mud-fly ash based geopolymer and leaching behavior of heavy metals in sulfuric acid solutions and deionized water. *Construction and Building Materials*, 2016. 124: p. 373-382.
35. Part, W.K., M. Ramli, and C.B. Cheah, An overview on the influence of various factors on the properties of geopolymer concrete derived from industrial by-products. *Construction and Building Materials*, 2015. 77: p. 370-395.
36. Perera, D., et al., Influence of curing schedule on the integrity of geopolymers. *Journal of Materials Science*, 2007. 42(9): p. 3099-3106.
37. Bakharev, T., Resistance of geopolymer materials to acid attack. *Cement and Concrete Research*, 2005. 35(4): p. 658-670.
38. Slaty, F., et al., Durability of alkali activated cement produced from kaolinitic clay. *Applied Clay Science*, 2015. 104: p. 229-237.
39. Tatsuya Koumoto, Production of High Compressive Strength Geopolymers Considering Fly Ash or Slag Chemical Composition. *Journal of Materials in Civil Engineering*, Vol. 31, Issue 8 (August 2019), [https://doi.org/10.1061/\(ASCE\)MT.1943-5533.0002788](https://doi.org/10.1061/(ASCE)MT.1943-5533.0002788).
40. D.S. Perera, O. Uchida, E.R. Vance, and K.S. Finnie, Influence of curing schedule on the integrity of geopolymers", *Journal of Materials Science*, 42(9), 3099-3106, 2007

41. Tero Luukkonen, Zahra Abdollahnejad, Juho Yliniemi, Paivo Kinnunen, Mirja Illikainen, One-part alkali-activated materials: A review, *Cement and Concrete Research*, Volume 103, January 2018, Pages 21-34.
42. F. Škvára, V. Šmilauer, P. Hlaváček, L. Kopecký, and Z. Cilová, “A weak alkali bond in (N, K)-A-S-H gels: evidence from leaching and modeling”, *Ceramics-Silikáty*, 56(4), 374-382, 2012.
43. T.G. Nijland, J.A. Larbi, Microscopic examination of deteriorated concrete, *Non-Destructive Evaluation of Reinforced Concrete Structures, Deterioration Processes and Standard Test Methods*, Volume 1 in Woodhead Publishing Series in Civil and Structural Engineering, 2010, Pages 137-179
44. V. Penttala, Causes and mechanisms of deterioration in reinforced concrete. Failure, Distress and Repair of Concrete Structures, *Woodhead Publishing Series in Civil and Structural Engineering*, 2009, Pages 3-31